Near-field Vortex Dynamics of Flows Emerging from a Rectangular Duct

by

Abbas Ghasemi

A thesis
presented to the University of Waterloo
in fulfillment of the
thesis requirement for the degree of
Doctor of Philosophy
in
Mechanical Engineering

Waterloo, Ontario, Canada, 2019

Examining Committee Membership

The following served on the Examining Committee for this thesis. The decision of the Examining Committee is by majority vote.

External Examiner: Chao Zhang
Professor, Dept. Mechanical and Materials Engineering,
Western University

Supervisor: Xianguo Li
Professor, Dept. of Mechanical and Mechatronics Engineering,
University of Waterloo

Internal Member: John Wen
Professor, Dept. of Mechanical and Mechatronics Engineering,
University of Waterloo

Internal Member: Serhiy Yarusevych
Professor, Dept. of Mechanical and Mechatronics Engineering,
University of Waterloo

Internal-External Member: Eric Croiset
Professor, Dept. of Chemical Engineering,
University of Waterloo

Author's Declaration

This thesis consists of material all of which I authored or co-authored: see Statement of Contribution included in the thesis. I hereby declare that I am the sole author of this thesis. This is a true copy of the thesis, including any required final revisions, as accepted by my examiners.

I understand that my thesis may be made electronically available to the public.

Statement of Contributions

The content of the different chapters in this thesis is adopted and reprinted from the list of publications given below:

Chapter 2:

Abbas Ghasemi, Aaron Pereira, and Xianguo Li. Large eddy simulation of compressible subsonic turbulent jet starting from a smooth contraction nozzle. Flow Turbulence and Combustion, 98(1):83108, 2017.

I prepared the numerical model set-up, carried out the simulations, post-processed the data, prepared the figures and wrote/revised the manuscript. The experimental data (not presented in this thesis) in the original manuscript were obtained by Aaron Pereira and used to validate the simulations. The manuscript was reviewed by Dr. Xianguo Li.

Chapter 3:

Abbas Ghasemi, Burak Ahmet Tuna, and Xianguo Li. Shear/rotation competition during the roll-up of acoustically excited shear layers. Journal of Fluid Mechanics, 844:831854, 2018.

I developed the experimental procedure according to the research objectives. Dr. Tuna and I carried out the hot-wire (HW) anemometry and particle image velocimetry (PIV) measurements, post-processed the data and prepared the figures. I wrote/revised the manuscript and it was reviewed by Dr. Xianguo Li.

Chapter 4:

Abbas Ghasemi, Burak Ahmet Tuna, and Xianguo Li. Curvature-induced deformations of the vortex rings generated at the exit of a rectangular duct. Journal of Fluid Mechanics, 864:141180, 2019.

I developed the experimental procedure according to the research objectives. Dr. Tuna and I carried out the hot-wire (HW) anemometry and particle image velocimetry (PIV) measurements, post-processed the data and prepared the figures. I wrote/revised the manuscript and it was reviewed by Dr. Xianguo Li.

Chapter 5:

Abbas Ghasemi, Burak Ahmet Tuna, and Xianguo Li. Viscous diffusion effects on the self-induced distortions of rectangular vortex rings. Physics of Fluids, 30(12):124101, 2018.

I set up the numerical model, carried out the large eddy simulation (LES), post-processed the data, prepared the figures and wrote/revised the manuscript. The experimental data is obtained by Dr. Tuna and used to validate the LES simulations. The manuscript was reviewed by Dr. Xianguo Li.

Chapter 6:

Abbas Ghasemi and Xianguo Li. Cross-sectional reshaping of perturbed/unperturbed rectangular jets. International Journal of Numerical Methods for Heat and Fluid Flow, VV(NN): AA-BB, 2019 (In Press).

I prepared the numerical model set-up, carried out the large eddy simulations (LES), post-processed the data, prepared the figures and wrote/revised the manuscript. The manuscript was reviewed by Dr. Xianguo Li.

Abstract

Shear layers and jets have motivated many researches to use experimental, theoretical and numerical methods for the better understanding of the fundamental physics and optimizing the flow characteristics that best suit practical applications such as mixing, heat/mass transfer, reacting flows, cleaning and combustion. Jet flows can be actively controlled using the acoustic forcing, while issuing the jet from non-circular openings can passively optimize the performance. Specifically, the dynamics of the rectangular vortex rings generated within the jet shear layer inspire this thesis for the in-depth experimental/numerical analysis of the underlying physics.

The shear layers separated from the longer edge of the rectangular opening at the Reynolds numbers $Re_{\theta_0} = U\theta_0/\nu = 85-945$ are studied using the hot-wire (HW) anemometry and particle image velocimetry (PIV), with a focus on the shear/rotation competition during the initial Kelvin-Helmholtz (KH) roll-ups. Velocity spectra and the spatial linear stability (LST) analysis characterize the fundamental (f_n) and its subharmonic ($f_n/2$) mode interacting due to the vortex pairing. For $276 \leq Re_{\theta_0} \leq 780$, the streamwise turbulence intensity shows a peculiar double-peaking phenomenon, i.e., major and minor peaks of the u_{RMS} coexist towards the high-speed (HS) and the low-speed (LS) sides of the shear layer, respectively. The single/double-peaked u_{RMS} profiles are found correlated with the scattered/organized distribution of the shear/rotation, in demonstrating a transitioning character with the downstream distance, Re_{θ_0} and the upstream turbulence levels. Excitation at f_n increases the vortex count by 21%, advances the location of the first KH roll-up and hence the minor peak formation. Due to the enhanced pairing at the $f_n/2$ forcing, the vortex count reduces by 23%. Before merging into the downstream rotation core, the upstream vortex is shifted towards the HS side and the major peak is accordingly augmented. Actuation advances the transition to the non-linear state, as well as the saturation of the amplification factor. The shearing and rotating loops are found associated with the thinning (elongation) and expansion (accumulation) of the vorticity, respectively.

The cross-section of the rectangular jets of aspect ratio 2 at $Re = UD_{\mathrm{h}}/\nu = 17,750$ deforms into the elliptic/circular shapes in the downstream due to the axis-switching. By enhancing the vortex pairing, excitation at $f_{\mathrm{n}}/2$ shortens the potential core, increases the jet spread rate, and eliminates the overshoot typically observed in the centreline velocity fluctuations. Unlike circular jets, the skewness and kurtosis of the rectangular jets demonstrate elevated anisotropy/intermittency levels before the end of the potential core. The axis-switching location is found variable by the acoustic control of the relative expansion/contraction rates of the shear layers in the top (TV: longer edge), side (SV: shorter edge) and diagonal (DV) views. The curvature-induced velocities are found to reshape the vortex ring by imposing non-linear azimuthal perturbations occurring at shorter wavelengths with time/space evolution. Eventually, the multiple high-curvature/high-velocity regions merge into a single mode distribution. In the TV plane, the self-induced velocity distribution evolves symmetrically while the tilted ring results in the asymmetry of the azimuthal perturbations in SV as the side closer to the acoustic source rolls up in more upstream locations.

Large eddy simulations (LES) of the isolated rectangular vortex rings at Reynolds numbers $Re_i = UD_h/\nu = 355, 877.5, 1775, 8775, 17750$ ($i = 1, ..., 5$) reveal the differences between their axis-switching and that of rectangular jets. At increased viscous effects, the rotational content of the vortices diffuse and grow in size. The high curvature corners of the rectangular vortex rings induce additional velocities which distort the topology until it appears to be rotated for 90^o, the so-called axis-switching phenomenon. Strong viscous effects (Re_1) diffuse the ring before the switching is completed while reduced viscous effects allow for the first (Re_2, Re_3) and second (Re_4, Re_5) switching. For Re_2 and Re_3, the rotated rectangular rings bifurcate into the pair of semi-circular topologies. Space-time mapping of the instantaneous streamwise velocity at the vortex ring axis reveals strong correlation spots for the occurrence of each axis-switching. Trajectories of the vortex cores in two orthogonal planes demonstrate contractions/expansions conforming to the Sine/Cosine waves associated with the varicose instability modes. The pair of orthogonal varicose modes interact with the phase lagging/leading equal to the quarter of a full cycle which is interestingly equal to the axis-switching frequency. Cross-sectional reshaping of the trailing shear layer in transitioning/starting rectangular jets is similar to that of steady jets while the axis-switching of the leading vortex ring is similar to the isolated rings. Dynamics of the leading vortex ring dominate the entrainment that are not significantly affected by inlet forcing. On the other hand, the near-field entrainment within the trailing vortex rings is promoted proportional to the amplitude of the controlled inlet oscillations.

Acknowledgements

First of all, I would like to thank my supervisor Professor Xianguo Li for his academic supervision, encouraging support and giving me the opportunity to explore various research projects in pursuing my scientific curiosity.

I would like to thank my Ph.D. examining committee, Professor Eric Croiset, Professor John Wen, Professor Serhiy Yarusevych from university of Waterloo, and Professor Chao Zhang as my external examiner from Western university for their time and contributions.

I would like to acknowledge the funding support from the Natural Sciences and Engineering Research Council of Canada (NSERC) via a Discovery Grant, and Ontario Centres of Excellence (OCE) TalentEdge Internship Program (TIP) under the Project Numbers 25398 and 25657.

I would like to thank the Fluid Mechanics Research Laboratory of Professor Serhiy Yarusevych for providing some of the measurement hardware and facilitating the experiments.

I would like to thank Dr. Burak Ahmet Tuna for his help with the experimental measurement and analysis.

Finally, I am thankful to my family, friends and all my colleagues from the Fuel Cell and Green Energy Laboratory at University of Waterloo. Without the love, help and support I received from them I would have not been able to make it this far.

Dedication

To my beloved parents.

Table of Contents

List of Tables

List of Figures

List of Symbols

a = Short side length of the rectangular opening;
$A(f_n)$ = Amplitude of the fundamental mode;
$A(f_n/2)$ = Amplitude of the subharmonic mode;
D = Round jet nozzle diameter;
D_h = Hydraulic diameter;
D_e = Equivalent diameter;
f_n = Fundamental frequency;
$f_n/2$ = Subharmonic frequency;
H = Shape factor;
K_u = Kurtosis of the streamwise velocity fluctuations;
$k_r = \frac{1}{2}\tau_{ii}^R$ = Residual kinetic energy;
L = Length of the rectangular duct;
M = Local streamwise mass flow rate;
M_o = Inlet streamwise mass flow rate;
$\tilde{p^*} = P/\rho U^2$ = Dimensionless filtered (resolved) pressure;
$p^{'*}$ = Dimensionless sub-grid scale (residual) pressure;
$\widetilde{p_m} = \widetilde{p} + \frac{2}{3}k_r$ = Pressure correction term;
Q = Q-criterion (second invariant of the velocity gradient tensor);
Re_{θ_0} = Reynolds number based on momentum thickness;
$St_a = fa/U$ = Dimensionless forcing frequency (Strouhal number);
S_u = Skewness of the streamwise velocity fluctuations;
$t^* = (Ut)/a$ = Non-dimensional time;
u_{RMS} = Streamwise turbulence intensity;
v_{RMS} = Transverse turbulence intensity;
w_{RMS} = Spanwise turbulence intensity;
${U^*}_{in}$ = Dimensionless inlet velocity;
U = Centreline velocity at the inlet;
U_j = Jet velocity;
$\tilde{u_i^*} = u_i/U$ = Dimensionless filtered (resolved) velocity components;
$u_i^{'*}$ = Dimensionless sub-grid scale (residual) velocity components;
$u^{'}$ = Amplitude of the inlet streamwise velocity oscillations;
$x_i^*(i = 1, 2, 3)$ = The non-dimensional coordinates x/a, y/a and z/a;

α_i = Growth rate;
δ^* = Displacement thickness;
Δ = LES filter width;
ε_{u} = Uncertainty in the PIV measurement of the streamwise velocity;
ε_{v} = Uncertainty in the PIV measurement of the spanwise velocity;
λ_2 = Vortex identification criterion;
Γ_2 = Vortex identification criterion;
λ_I = Integral length scale;
λ_K = Kolmogorov length scale;
λ_T = Taylor length scale;
ν = Kinematic viscosity;
ρ = Density;
$\tau_{ij}^R = \widetilde{u_i u_j} - \tilde{u}_i \tilde{u}_j$ = Residual or the subgrid-scale (SGS) stress tensor;
$\tau_{ij}^r = \tau_{ij}^R - \frac{2}{3} k_r \delta_{ij}$ = Anisotropic residual stress;
θ_0 = Momentum thickness;
Ω_{xy} = Vorticity in the side view (SV) plane;
Ω_{zy} = Vorticity in the top view (TV) plane;
$\Omega_{\mathrm{x}\zeta}$ = Vorticity in the diagonal view (DV) plane;
ω_x^* = Dimensionless streamwise vorticity;

Chapter 1

Introduction

1.1 Overview

Shaer layers are formed due to the velocity difference between the two layers of high speed and low speed fluid regions [1]. When the high speed fluid is issued into the low speed (quiescent or stagnant) ambient through the nozzle or orifice openings, jet flows are formed. Jet flows have significant fundamental and practical importance. They are extensively used in enhancing and controlling the mixing, heat/mass transfer, reacting flows and combustion processes [2]. For instance, characteristics of the single phase natural gas jets [3] injected into the combustion chamber are found to be similar to that of starting jets [4] evolving spatio-temporally [5]. The initial formation, transition, penetration and expansion of the starting fuel jets are important features associated with the entrainment and mixing. The jet characteristics are affected by the nozzle geometrical configuration as well as the flow regimes under various injection conditions [5]. Even though the jet flows are mostly issued with starting conditions, they eventually evolve/transition into steady state [6]. Therefore, their understanding is essential for a wide range of practical applications. In additon, dynamics of the single phase jets are important as they can be linked with the entrainment and mixing taking place in two-phase jets and sprays [7, 8].

1.2 Shear layer formation and vortex dynamics in jets

In addition to their practical importance, free (unbounded) jets are classified as shear flows with their own fundamental significance owing to the fascinating dynamics of the vortical structures [1]. Formation of rather organized vortex structures in the near-field influence the downstream transition into the chaotic, intermittent and well-mixed flow [9]. Appearance of these organized train of vortices can also be linked to the instability modes within the shear layer [10, 11]. Specifically, the Kelvin-Helmholtz (KH) instability governs the vortex formation and shedding in shear layers [10, 12]. Among various characteristics of the shear layers, the streamwise turbulence intensity (u_{RMS}) is perhaps one of the most commonly studied parameters [13]. The u_{RMS} profiles typically exhibit a single peak near the location at which the velocity gradient is maximum. Interestingly, in some cases the u_{RMS} profiles demonstrate a peculiar double-peaking phenomenon [14]. In spite of all the extensive literature on shear layers and jets, most of the earlier studies have not reported the double-peaking phenomenon. This is perhaps because the phenomenon takes place within the regions where both the numerical and experimental studies are challenging. While very few studies reported and/or attempted to describe the double-peaking [15, 16, 17, 18], a proper explanation for the underlying physics is still missing.

When the shear layers separate from the edges of a nozzle/orifice, jet flows are formed. The circular jets originated from axisymmetric nozzles or orifices, have been extensively studied for their fundamental and practical properties [19, 20, 13]. In circular jets, the KH mechanism generates axisymmetric vortex rings. The dynamics of these rings govern the global jet properties such as entrnment and spread rate. The wide range of applications require that the jet flows are controlled/optimized for improved mixing, heat/mass transfer, reacting flows and combustion. Active and passive forcing techniques are the two main strategies for jet control. Active forcing methods such as the acoustic excitation may lead into increased/reduced flow organization through their influence on vortex shedding and pairing [21]. As a consequence, the entrainment and mixing processes can be optimized for the desired applications [9]. Among different passive control stratgies, issuing the jets from non-circular openings of different shapes has drawn attention towards fundamental and applied research using different statistical [22], experimental [23] and numerical [24] techniques.

Fundamental complexities of the evolving non-circular jets are so rich that can be used to describe the organization and/or randomness in various natural phenomena [25]. The complex flow structure observed in the developing region of the non-circular jets are attributed to the near-field three-dimensional perturbations caused by the so-called "axis-switching" mechanism [26]. Axis-switching demonstrates the geometrical deformations in non-circular jets traditionally defined as the cross-sectional rotation along the downstream distance [27]. One of the important features to be further clarified on the non-circular jet dynamics is to describe the axis-switching phenomenon as a reshaping mechanism rather than a traditionally used rotational definition [26]. Axis-switching and the consequent jet deformations are the oucome of the self-induced dynamics of non-circular vortex rings [28]. Moreover, occurrence of the axis-switching phenomenon can be altered using various inflow conditions, namely, the momentum thickness at the nozzle lip, the upstream turbulence intensity level and Reynolds number [26, 29, 30]. All these factors determine the far field jet behaviour in the fully developed region.

As global characteristics, the near-field distortions of non-circular jets lead into the improved local entrainment [31, 32, 33, 34]. In addition, increased shear layer expansion and larger spread rates are commonly seen farther downstream [35, 32]. Such different behaviours from the round jets, are found coupled with the augmented instantaneous lateral oscillations in non-circular jets [36] also known to develop off-center peaks in the time-averaged streamwise velocity profiles [35, 37]. Likewise, high aspect ratio rectangular jets develop a saddle-back shape velocity profile [38]. The off-center peaks may rarely occur in round jets when the vena contracta effect is present [39]. Even though the time-averaged quantities of non-circular jets provide valuable information on the global jet characteristics, they cannot be used for unveiling the underlying physics. Therefore, it is essential to extract the instantaneous flow features and correlate them with the time-averaged observations.

The initial shapes of the non-circular vortex rings are constructed by the nozzle opening through which the jet is issued [26]. Unlike axisymmetric vortex rings, asymmetric rings exhibit a non-uniform curvature distribution. For instance, sharp corners of the rectangular and square rings show larger local curvature compared to that of their flat sides. In order to understand the vortex ring dynamics, it is important to first explain the concept of self-induced velocity. While the entire body of a vortex ring moves at the bulk flow velocity, any given point on the ring induces an additional component [26]. Two important factors affect the self-induced velocity component. The first factor is the local vortex core radius and the second is the local curvature on the ring. As predicted by the Biot-Savart Law (see Appendix A), the self-induced velocity inreases at high curvature regions and is reduced with vortex core growth [40, 41, 42]. A non-uniform velocity distribution distorts the non-circular vortex rings and generates the complex self-induced deformations resulting in the reshaping and axis-switching [12, 43, 42]. Owing to the coupled dynamics of the pressure and velocity fluctuations, reshaping of the non-circular jets have been theoretically interepreted based on the pressure variations [44]. Moreover, instability analysis suggests that the pressure perturbation modes in different regions govern the deformations [45]. Large eddy simulation (LES) of the square shaped vortex rings reveals how the corner pressure perturbations propagate in azimuthal direction and reshape the ring into 2D and 3D structures [28]. Very few numerical studies aimed at using the instantaneous vortex dynamics to describe the underlying physics [46, 26, 12, 28]. However, majority of the experiments focus on the time-averaged and global features of the non-circular jets.

Therefore, it is essential to conduct experiments capable of measuring the self-induced velocities and correlating them with the vortex dynamics.

Unlike round jets which have been studied more thoroughly in the literature, vortex dynamics in non-circular rings demand further attention due to the complex phenomena taking place. Above mentioned studies on non-circular jets mostly describe the jet characteristics in terms of the time-averaged quantities and the global jet characteristics such as entrainment. This is due to the fact that it is quite cumbersome to use experimental or numerical methods and properly extract the three-dimensional flow structures for several meaningful time instants. In many practical applications, jet flows are initiated with starting conditions and transition into the steady state. Therefore, it is also very important to study the starting jet characteristics, particularly for non-circular jets evolving in time/space.

1.3 Objective and scope of thesis

Above overview of the knowledge on shear layers and jet flows shows that some of the governing mechanisms need to be better explained to complete the existing literature. It is also worth to mention that majority of earlier studies have been carried out when the jet is issued from smooth contraction nozzles or orifice plates where the boundary layer at the separation edge (nozzle lip) is different from that of a straight duct with a certain length. It should also be noted that a more detailed and specific literature review is given within the individual following chapters. The objective of this PhD thesis research is to conduct different experimental and numerical analyses aimed at better understanding of the vortex dynamics outside rectangular ducts, specifically focused on the:

- Physical mechanisms governing the peculiar double-peaking phenomenon during the shear layer roll-up.
- Correlation between the local curvature on rectangular vortex rings, the self-induced velocity and jet reshaping.
- Viscous diffusion effects on the self-induced dynamics of isolated vortex rings.
- Transitioning behaviour of the vortex dynamics and entrainment in perturbed/unperturbed starting rectangular jets.

1.4 Thesis layout

In order to meet the above research objectives, the thesis layout is based on seven chapters. In chapter 1, a brief introduction of the vortex dynamics in shear layers and jets is provided to motivate the objectives of this thesis. Also, an overall layout of the thesis describes the content of each chapter with reference to the published work.

Chapter 2 provides an overview for the main features of the jet flows. Specifically, some of the results on the round jet vortex dynamics are selected and reprinted with permission from Flow Turbulence and Combustion journal [47]:

Abbas Ghasemi, Aaron Pereira, and Xianguo Li. Large eddy simulation of compressible subsonic turbulent jet starting from a smooth contraction nozzle. Flow Turbulence and Combustion, 98(1):83108, 2017.

The idea is to provide some opening discussions on the vortex dynamics in round jets. This can be beneficial for the readers when comparing the round jets with the rectangular jet vortex dynamics presented in the following chapters.

Chapter 3 presents the results obtained from the hotwire (HW) anemometry and particle image velocimetry (PIV) measurements conducted along the near-field shear layer on the longer side of the rectangular jet. The results characterizing the nearfield shear layer with a focus on the shear/rotation competion and the peculiar double-peaking in turbulence intensity profiles are reprinted with permission from Journal of Fluid Mechanics [48]:

Abbas Ghasemi, Burak Ahmet Tuna, and Xianguo Li. Shear/rotation competition during the roll-up of acoustically excited shear layers. Journal of Fluid Mechanics, 844:831854, 2018.

In chapter 4, HW and PIV results provide a comprehensive disucssion of the flow structure in rectangular jets with a focus on the curvature-induced vortex dynamics. The chapter content are reprinted with permission from Journal of Fluid Mechanics [49]:

Abbas Ghasemi, Burak Ahmet Tuna, and Xianguo Li. Curvature-induced deformations of the vortex rings generated at the exit of a rectangular duct. Journal of Fluid Mechanics, 864:141180, 2019.

Chapter 5 is written based on the large eddy simulation (LES) results to reveal the viscous diffusion effects on the self-induced dynamics of isolated rectangular vortex rings. The content is reprinted with permission from Physiscs of Fluids journal [50]:

Abbas Ghasemi, Burak Ahmet Tuna, and Xianguo Li. Viscous diffusion effects on the self-induced distortions of rectangular vortex rings. Physics of Fluids, 30(12):124101, 2018.

Chapter 6 is prepared from the LES simulations of the transitioning/starting rectangular jets to investigate the effect of the inlet forcing on vortex dynamics and entrainment. The content is reprinted with permission from International Journal of Numerical Methods for Heat and Fluid Flow [51]:

Abbas Ghasemi and Xianguo Li. Cross-sectional reshaping of perturbed/unperturbed rectangular jets. International Journal of Numerical Methods for Heat and Fluid Flow, VV(NN): AA-BB, 2019 (In Press).

In chapter 7, a summary of the discussions in the main body of the thesis is provided and recommendations are proposed for future research.

Chapter 2

Vortex ring dynamics in circular and non-circular jets

2.1 Circular vs. non-circular jet dynamics

Extensive experimental [52, 19] and numerical [20, 13] studies have been carried out on the jet flows issued into the quiescent ambient. The relative velocity between the high speed and low speed (stagnant ambient) sides of the jet creates a shear layer and the vortical structure are formed [1]. The shear layer evolves owing to the onset and growth of the Kelvin-Helmholtz (KH) instability. The transition of the linear KH instability into the non-linear state results in the shear layer roll-up and vortex formation. In round jets, the KH instability produces rather axisymmetric vortex rings which affect the shear layer dynamics depending on the inflow conditions of the jet [13]. Circular vortex rings expand in radius as they move farther downstream [20]. In addition, the vortex core radius grows due to the viscous diffusion [19]. The rings eventually break down at the end of the potential core beyond which the small scale structures promote the mixing. Beyond the potential core, the jet region further expands and the centreline velocity decays [13].

Different jet characterstics such as the entrainment mechanisms are highly influenced by the dynamics of the vortex rings as they emerge, evolve and eventually break down into smaller scales [53]. The dynamic motion and deformation of the vortices affect the entrainment and mixing processes that are important for many practical applications [54]. In circular vortex rings, the large scale roll-up of the shear layer causes the flow engulfment entrainment mechanism [55]. In addition, the low pressure zones caused by the rotating vortex cores also lead into the large scale flow induction into the jet region [1, 56].

Furthermore, the small scale nibbling entrainment may drag in the small patches of the non-turbulent fluid into the jet core [1]. In addition, the large and small scale entrainment mechanisms near the interface separating the turbulent and non-turbulent regions plays an important role [29, 53]. The contributions from these three mechanism and the overall entrainment into the circular jets can be altered by changing the inflow conditions such as the Reynolds number and inlet turbulence levels [13]. In addition, active control strategies such as acoustic forcing can be used to enhance the jet properties.

An alternative method for controlling the vortex dynamics and the consequent entrainment/mixing is to issue the jet through the non-circular openings. Unlike the axisymmetric vortex rings formed in circular jets, non-circular jets produce vortex rings according to the circumferential shape of the nozzle/orifice opening [22]. As a result, the different and more complex dynamics due to the presence of the non-circular rings results in the variations in the jet characteristics [36, 29]. Compared to round jets, more three dimensional shear layer dynamics emerge due to the so-called axis-switching phenomenon in jets issued from the non-circular nozzles. Moreover, non-circular jets demosntrate increased small scale entrainment compared to circular jets [57, 58]. These differences in the non-circular jet characteristics mainly arise from their self-induced dynamics and the elevated azimuthal instabilities [57, 58].

Another important factor in the study of circular or non-circular jets is their transitioning state. In many of the practical applications, jet flows are issued with starting characteristics and then transition into the fully developed steady state [59]. The vortex dynamics and entrainment of starting jet are significantly different from the fully developed steady jets because of the formation of a leading vortex ring [60]. Presence of the leading vortex ring alters the interaction of the jet with its surounding ambient. The leading vortex ring is followed by a quasi-steady shear layer. The leading vortex ring may break down or pinch off from the quasi-steady region under certain flow conditions [59]. Dynamics of the leading vortex rings are also influenced owing to their inetractions with the secondary trailing vortices [28, 47]. Formation, evolution and penetration of the leading vortex ring play a major role in the entrainment characteristics of starting jets [28]. In general, it is necessary to be familiar with the characteristics of the circular jets before studying the increased complexities in the dynamics of the non-circular jets (starting, transitioning or steady). To this end, the round jet vortex dynamics are explained below to be compared to that of non-circular jet flows in later chapters.

2.2 Vortex ring dynamics in round jets

Before moving on to the following chapters that are focused on the dynamics of rectangular jets, it is worth to explain some of the vortex dynamics in round jets. To this end, the results shown below are adopted and reprinted with permission from Flow Turbulence and Combustion journal [47]:

Abbas Ghasemi, Aaron Pereira, and Xianguo Li. Large eddy simulation of compressible subsonic turbulent jet starting from a smooth contraction nozzle. Flow Turbulence and Combustion, 98(1):83108, 2017.

Ghasemi et al. [47] conducted large eddy simulation (LES) to study the round turbulent starting jets at relatively large Reynolds number of significant practical importance. The jet was numerically started from a smooth contraction nozzle and entered the computational domain of truncated conical shape.

Figure 2.1 shows the iso-surface of vorticity magnitude obtained from the LES of the circular turbulent jet starting from a smooth contraction nozzle [47]. The non-dimensional time appearing in Figure 2.1 is defined as $t^* = tU_j/D$ where t, U_j and D denote time, jet velocity and nozzle diameter, respectively. The vorticity iso-surface is coloured from blue to red to characterize the low pressure (LP) and high pressure (HP) regions within the shear layer. The main characteristic of the starting jets differentiating them from steady jets is the presence of the leading tip vortex preceding the remaining jet that resembles a steady jet (the so-called quasi-steady region).

It can be seen that the jet shear layer demonstrates alternative variation of the LP and HP zones. This phenomenon can be explained through understanding the contraction and expansion taking place in shear layers. The contractions and expansions are associated with the inward and outward flow motions due to the presence of the passing vortex rings. This process occurs for the large leading vortex ring as well as smaller trailing vortex rings in the quasi-steady region. In general, the downstream advection of a vortex ring as well as its local direction of rotation pushes the downstream fluid outward creating a high pressure expansion zone. On the other hand, a low pressure contraction zone is formed in the upstream of the vortex ring. These low pressure cores entrain the ambient flow inward. It can also be seen that the lowest pressure (blue) occurs at the core of the larger vortex rings. The rotating vortex cores produce the strong recirculation leading into the local pressure drop. As a result, ambient flow is entrained inside the ring. The entrainment and viscous diffusion effects cause the ring to grow larger.

In the above discussion of contractions and expansions, LP and HP zones are associated with the vortex ring dynamics. These vortex rings are formed as a result of the onset and

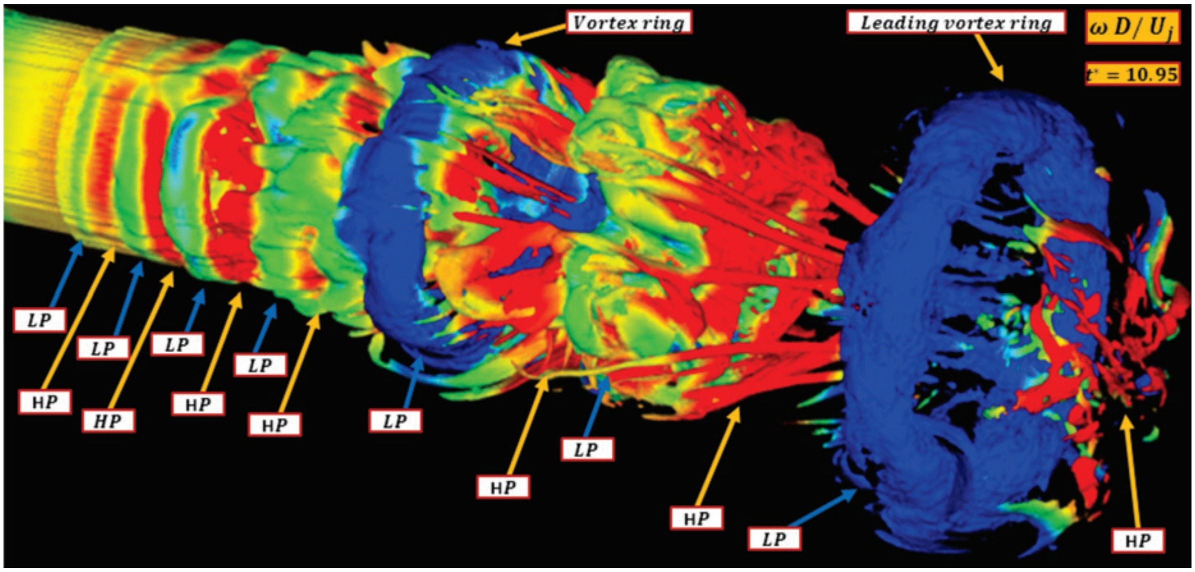

Figure 2.1: Iso-surface of vorticity magnitude coloured by pressure; low pressure (blue), high pressure (red).

growth of the KH instability within the shear layer. Even though the vorticty field properly visualizes the shear layer evolution, it does not necessarily characterize the vortex cores. This is because vorticity cannot distinguish between the pure rotation of the flow elements and irrotational shear. Therefore, λ_2 criterion is used to identify the vortex cores in figure 2.2. In λ_2 criterion [61], the gradient operator is applied to the Navier-Stokes equations to evaluate the acceleration gradient tensor. The symmetric component of the acceleration gradient tensor provides information associated with the local pressure extrema while the anti-symmetric component is related to the vorticity transport. Three real eigenvalues can be obtained for the symmetric part of the tensor. Negative portion of the second eigenvalue ($\lambda_2 < 0$) which is related to the local pressure minimum represents the vortex cores.

Compared to the vorticity iso-surfaces, it can be seen in figure 2.2 that the vortex cores are more distinguished from the other regions of the shear layer. It is shown how the leading vortex ring is first formed in starting jets and is then followed by the trailing vortex rings in the upstream quasi-steady shear layer. Vortex rings are formed at the nozzle exit and grow in radius and thickness due to the viscous diffusion effects with increased downstream distance. The initially axisymmetric rings become distorted and eventually break down farther downstream. After the vortex ring break-down, elongated and complex vortical structures as well as hairpin shape vortices are formed. The leading vortex ring is surrounded by fine scale secondary vortices.

In figure 2.3, iso-surfaces of λ_2 are used to identify the hairpin-shaped vortices in the jet shear layer. These hairpin vortices are characterized by a curved head hanging upstream and outward the jet shear layer. On the other hand, the legs of the hairpin have roots inward and downstream of the jet shear layer. The population of these small scale and elongated vortical structures increases at higher Reynolds numbers, hence they need to be properly resolved in the numerical simulations. Through changing the direction of streamwise momentum to transverse direction, flow is ejected outward inside the hairpins. On the other hand, some studies suggest that the flow is vertically entrained inward near the roots of the hairpins [19].

Figure 2.4 demonstrates the magnified view of the jet near-exit region to better visualize the vortex ring formation, growth and break-down. The shear layer emerged from the nozzle lip becomes unstable as a result of the KH primary instability. The resulting shear layer roll-up develops the axisymmetric vortex rings which are advected downstream while growing in ring radius and core thickness due to the viscous diffusion. As shown in figure 2.4, growth of azimuthal instabilities on the vortex ring can distort the ring into lobe shaped filaments. At this instant, the vortex ring has distorted into a more three dimensional shape. Due to this three-dimensionality the vortex ring is no longer axisymmetric and eventually breaks into finer elongated vortical structures with complex geometries.

While the KH instability results in the primary vortex rings, azimuthal instabilities formed on the ring vortices cause the secondary type of instability. This secondary instability results in the formation of counter-rotating streamwise vortex tube pairs in the braid region between two consecutive vortex rings. Figure 2.5 shows the iso-surface of λ_2 coloured by streamwise vorticity. Two braid regions are shown between the successive vortex rings (A) and (B) and the leading vortex ring. It can be seen that vortex ring (B) is about to collapse and break-down. Azimuthal instabilities deform the initially axisymmetric vortex rings into asymmetric shapes. The rib-shape streamwise vortex filaments emanate from the vortex rings in the braid region. Interaction of these secondary vortices (ribs) with primary vortical structures (rings) significantly enhances the entrainment in the near field of the jet.

The streamwise vorticity colouring of the rib-shape vortex filaments from -1.5 (blue) to 2 (red) is used to provide a sharper contrast between the counter-rotating rib pairs shown in figure 2.5. It is seen that the streamwise ribs appear as pairs of counter-rotating vortices. Larger spacing between the two neighbour vortex rings results in a wider braid region and consequently more stretched rib vortices. The number of streamwise vortex pairs does not significantly change with increased downstream distance. However, since the radius of the

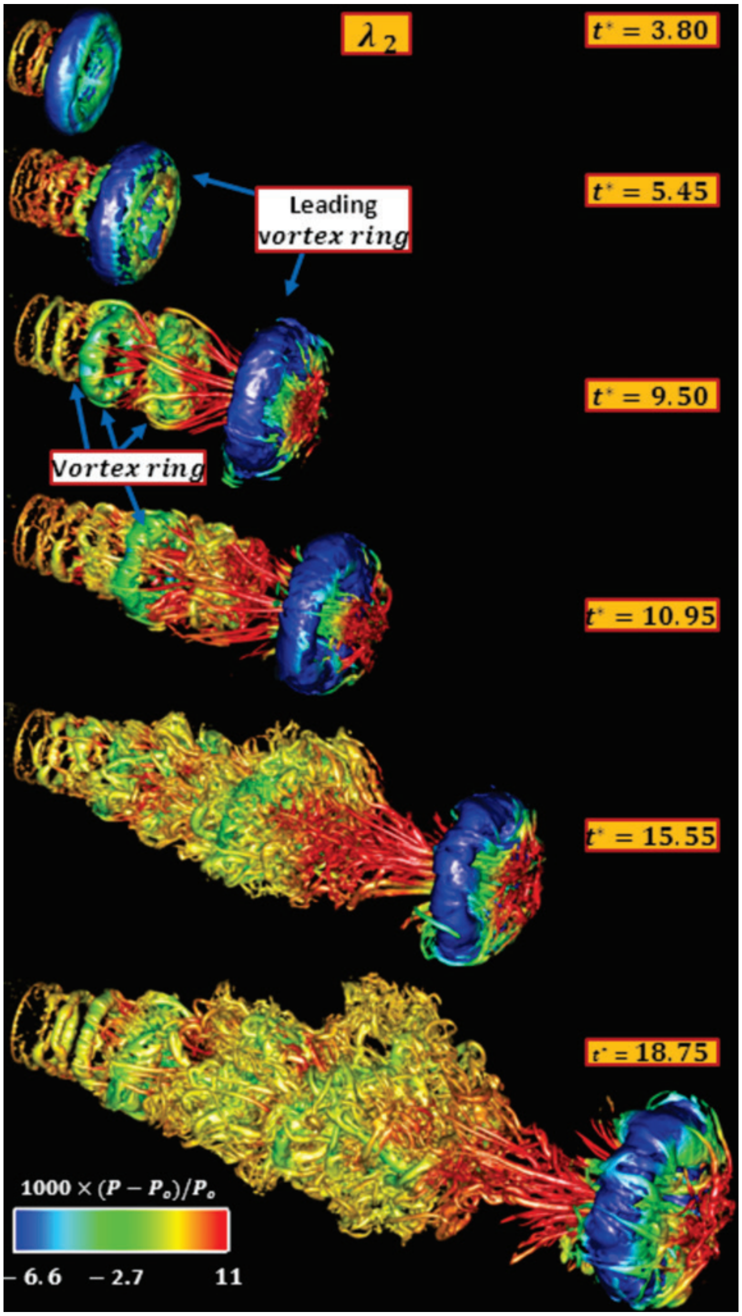

Figure 2.2: Iso-surface of λ_2 coloured by pressure; low pressure (blue), high pressure (red), at various nondimensional times t^*.

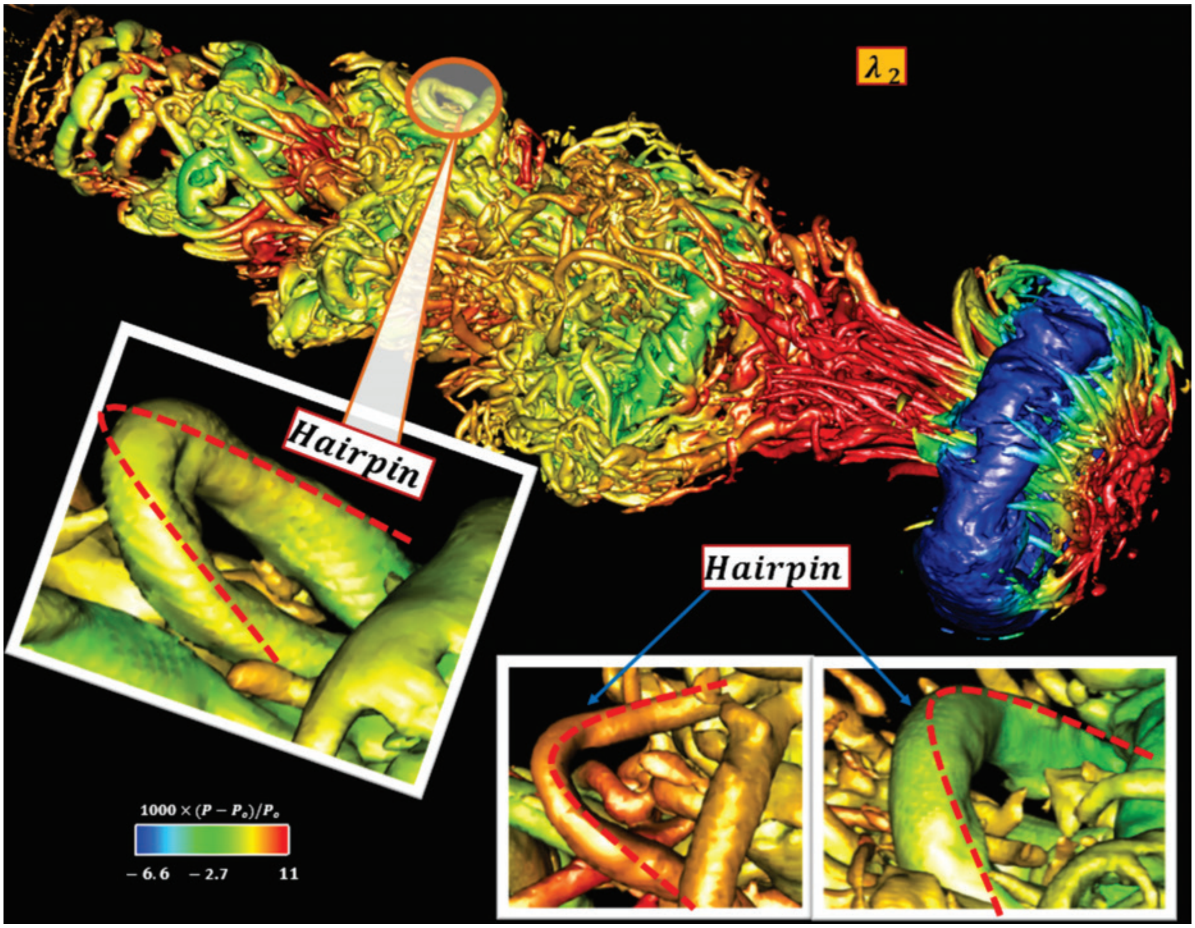

Figure 2.3: Iso-surface of λ_2 coloured by pressure; low pressure (blue), high pressure (red), at $t^* = 18.75$.

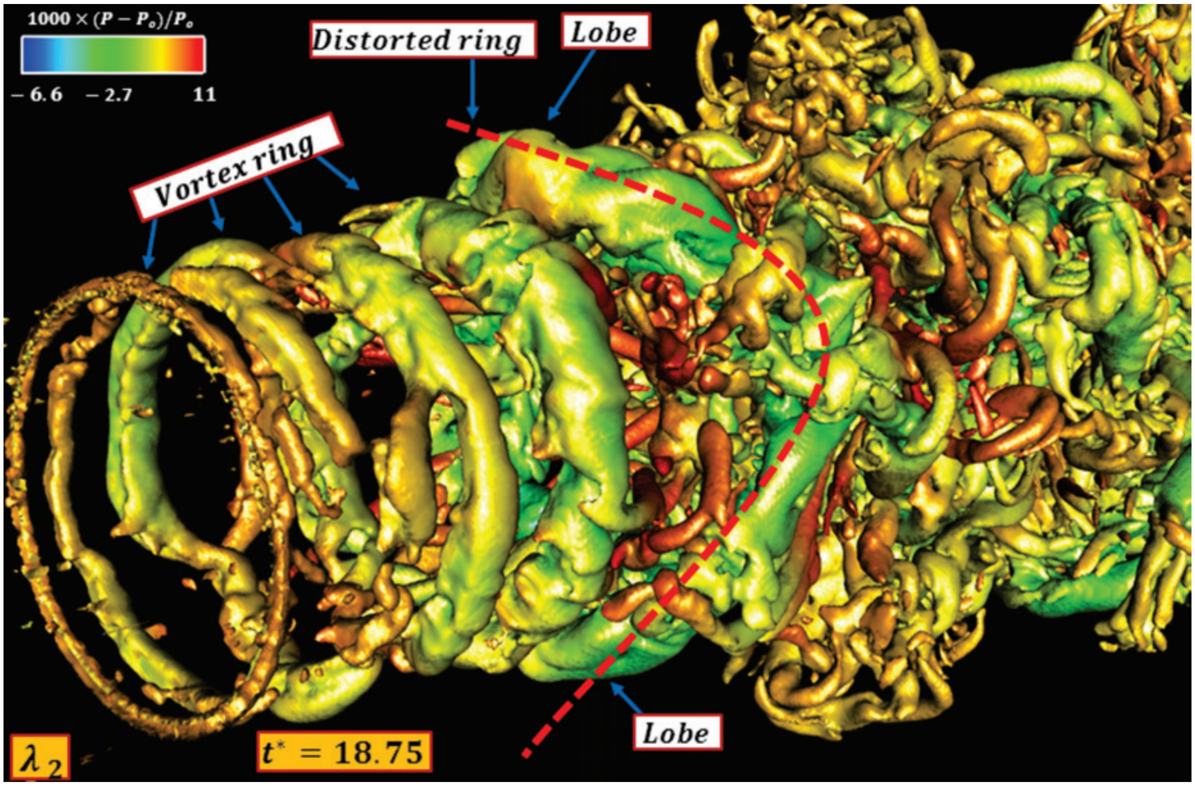

Figure 2.4: Iso-surface of λ_2 coloured by pressure; low pressure (blue), high pressure (red), at $t^* = 18.75$

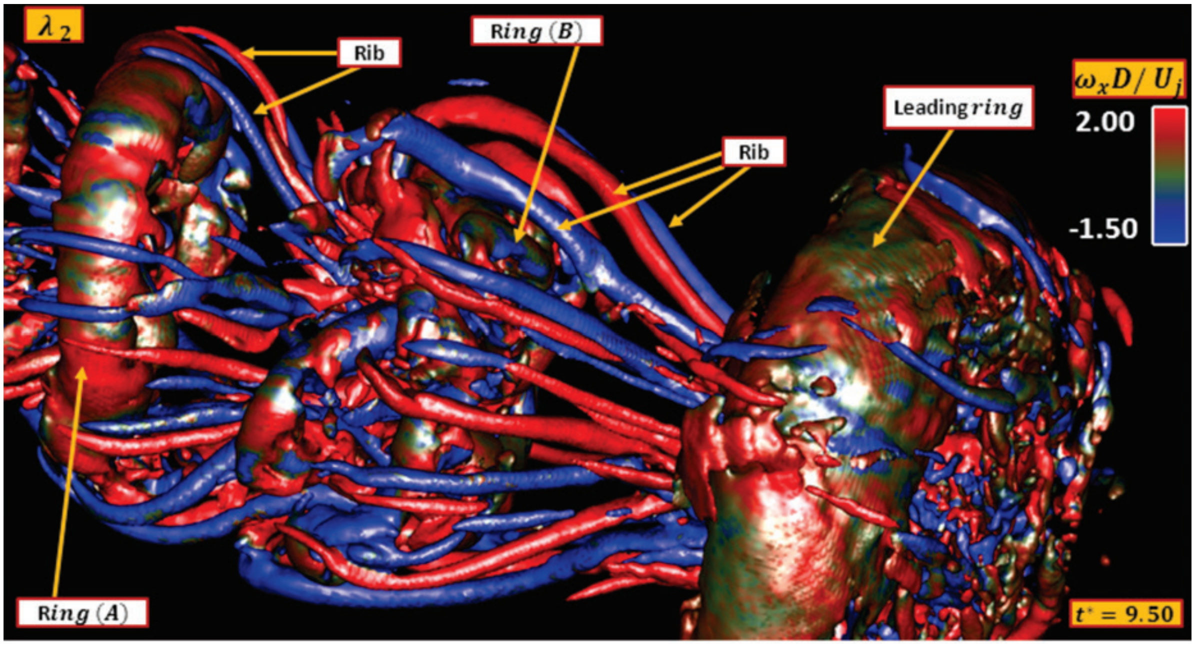

Figure 2.5: Iso-surface of λ_2 coloured by streamwise vorticity; blue (negative), red (positive).

rings increases with the downstream distance, wavelength of the azimuthal instabilities on the ring grow resulting in lower frequencies.

To summarize the vortex dynamics in starting round jets, the starting jet consists of a leading vortex ring followed by a quasi-steady jet. The jet shear layer exhibits contraction and expansion zones, corresponding to the high pressure (HP) and low pressure (LP) regions. These LP/HP regions are formed by the passing vortex rings generated owing to the Kelvin-Helmholtz instability and the shear layer roll-up. The thin boundary layer inside the smooth contraction nozzle evolves into a shear layer at the nozzle exit and develops with the downstream penetration of the jet. Formation and the spatio-temporal evolution of the vortical structures illustrate the distortion of the vortex rings into lobed shapes prior to break-down. Rib-shaped streamwise vortex filaments appear due to the growth of the secondary instabilities in the braid region between the pairs of consecutive vortex rings. In addition, formation and dynamics of the hairpin vortices in the shear layer have been identified. The following chapters of this thesis focus on the vortex dynamics outside of a rectangular duct with describing the difference between the rectangular jet shear layer and that of round jets.

Chapter 3

Shear/rotation and the peculiar double-peaking phenomena at the exit of a rectangular duct

This chapter presents the results obtained from the hot-wire (HW) anemometry and particle image velocimetry (PIV) measurements conducted along the near-field shear layer on the longer side of the rectangular jet. The results characterizing the near-field shear layer with a focus on the shear/rotation competition and the peculiar double-peaking in turbulence intensity profiles are reprinted with permission from Journal of Fluid Mechanics [48]:

Abbas Ghasemi, Burak Ahmet Tuna, and Xianguo Li. Shear/rotation competition during the roll-up of acoustically excited shear layers. Journal of Fluid Mechanics, 844:831854, 2018.

3.1 Introduction

Shear layers belong to an important class of the fluid flows both fundamentally and practically. Their practical importance lies in their high turbulent fluctuations arising from the velocity gradient within the shear layers that greatly enhance the fluid mixing, and heat/mass transfer, such a characteristic is significantly important for many practical applications such as reacting flows [62]. Shear layers also exhibit rich fundamental phenomena related to fluid flows, and knowledge of them helps better understand mechanisms behind various fluid flow phenomena.

Shear layers are formed due to the velocity difference between the two streams of high speed (HS) and low speed (LS) fluids [1], and this velocity difference is the cause for the instabilities to develop within the shear layers, or the so-called Kelvin-Helmholtz (KH) instability, leading to the growth of perturbations in space and/or time. Shear layers occur frequently in many flow situations, for instance, when the incoming boundary layer from the upstream of a backward-facing step separates from the wall, a shear layer is formed in the downstream of the separation edge [63]. Another example is the flow separation occurring after a bluff body resulting in the shear layer formation [64]. Shear layers can also develop due to the injection of the high momentum jet flow ejected through an opening (orifice or nozzle) into the stagnant ambient [65]. In all these cases, the no-slip wall boundary condition imposed on the flow is suddenly eliminated allowing for the formation of shear layers with free evolution in both space and time. The abrupt exclusion of the incoming boundary layer at the separation edge and the associated characteristics such as the shape of the velocity profile, the momentum thickness and the upstream fluctuation levels play an important role on the initial state of the shear layer formation [66]. After all, the near-separation flow characteristics are governed by the transition of the boundary layer to shear layer [67].

The onset of the linear Kelvin-Helmholtz (KH) instability destabilizes the near-separation region of the shear layers [68]. Near the separation edge, the shear layer produces a friction zone between the HS and the LS flows, and the vorticity field is elongated. Due to the linear KH instability, the elongated region starts a wavy motion in the form of the traverse meandering. Farther downstream, the non-linear instabilities set in and a roll-up is formed with a strong rotational content. The roll-up region is comprised of the strong accumulation of the vorticity. Transition of these vorticular motions into the non-linear state produces instabilities also in the traverse direction as the vortex loops advect farther downstream in the streamwsie direction [53]. These traverse perturbations eventually disintegrate the large structures into smaller scales of shorter wavelengths [65]. These high-frequency small-scales contribute to the enhanced mixing. Shear layers are commonly studied in three distinct regions. In the near-field, the KH roll-ups and the resulting large-scale motions govern the dynamics of the flow structures. Consequently, the large-scale mechanisms such as the engulfment and the flow induction dominate the entrainment of the ambient fluid in the near-field region [1]. Farther downstream in the developing region, where the large-scale structures break down, the shear layer tends to evolve into a fully-developed condition. However, the fully-developed state is accomplished in the far-field where the small-scales dominate the entrainment through the nibbling of the small patches of the non-turbulent flow into the turbulent zone [1].

In the developing and the fully-developed regions, which are studied extensively, a single-peaked streamwise turbulence intensity (u_{RMS}) is commonly observed [13]. The single peak in the u_{RMS} is associated with the fluctuations of the local vortical structures and its magnitude is related to the length-scale of the vortices. On the other hand, in the near-separation region, where the initial roll-ups take place, the double-peaking phenomenon may occur in the u_{RMS} profiles, and some limited studies have attempted to explore the potential causes of the phenomenon. For instance, the formation of a sub-shear layer in the near-separation region is described by [69]. The study however does not observe the double-peaked u_{RMS} profiles, perhaps due to presenting the fluctuations of the velocity magnitude rather than the streamwise component. The double-peaking of the u_{RMS} as well as the phase-reversal of the velocity fluctuations with respect to the HS and the LS sides of the shear layer has been roported in [14]. These observations are associated with the high intermittency, non-linear distortions, secondary instabilities, and growth of the subharmonic oscillations. The subharmonic dynamics, which are known to originate from the vortex pairing phenomenon, are also previously observed by [15, 16, 17]. The phase-reversal observed in the measurements is not found predictable by the temporal linear stability theory, while it is inferred from conducting a spatial analysis by [70]. This is due to the fact that the perturbations in a shear layer mostly grow in space rather than time. In search for the origin and cause of the double-peaking phenomenon, [18] investigates the possible role of three different mechanisms. The first is the low-frequency transverse flapping of the shear layer, introduced as a mere kinematic event, and it is ruled out since the corresponding effects are not found sufficiently large. The second mechanism considered is the modulation of the growth rate, and is also precluded due to its small effect that is within the order of experimental error. The third is the modulation of the amplitude of the initial instability near the separation edge, or more specifically, the modulation of the receptivity occurring through the feedback mechanism is proposed to drive the occurrence of the double-peaking phenomenon. It is suggested that the governing mechanism is related to the low-frequency jet column mode and its association with the shear layer mode. The vortex passage frequency at the end of the potential core is proposed to develop receptivity through the feedback mechanism and modulate the upstream initial instability. Nonetheless, the proposed mechanism is limited to laminar inlet boundary layers where the vortex pairing consequences are different from those due to the transitioning/turbulent inlet boundary layers. [71] attempt to control the resonance/suppression of the subharmonic and its non-linear interactions with a wave. Finding the most unstable Strouhal number from the experiments smaller than the theoretical value is interpreted by the effect of the feedback mechanism. The study also suggests that the configuration (strength, spacing) of the vortices during the roll-up governs the downstream vortex pairings. The rotating cores are advected with the main flow velocity and an additional component is added due to the self-induced velocity of the vortex [41]. For a vortex tube, the self-induced velocity can be related to the local curvature on the tube, the inverse of the core radius and the local circulation. Assuming the vortex tubes as straight cylinder, the curvature effect can be ruled out. The vortex core located farther downstream attains a larger radius due to the viscous diffusion process. Consequently, it has a smaller self-induced velocity and slows down while growing in time/space. Given the proper conditions, the faster moving upstream vortex catches up with the slower downstream tube and merges into it [72, 73]. If the two vortices rotate in the same sense, the pairing takes place, the subharmonic effects appear and the double-peaking may occur in the u_{RMS}. Prior to the present measurements, our recent large eddy simulation (LES) results are reprocessed and demonstrate the occurrence of the double-peaking for both the round and square jets at different Reynolds numbers [28, 47].

Interesting findings above regarding the sub-harmonic effects on the double-peaking phenomenon in the u_{RMS} profiles provide valuable information in the role of the feedback mechanism and the vortex pairing. Thus, the importance of the vortex dynamics in the near-separation region of the shear layers becomes evident. The two main parameters influencing the vortex dynamics in this region are the initial KH roll-ups and their counteraction with the vortex pairing process occurring farther downstream. A vortex can be characterized by a rotating core and its association with the peripheral shear zones. Therefore, the objective of this chapter is to investigate shear layers in the near field, both naturally developing and acoustically excited, by using hot-wire (HW) anemometry and particle image velocimetry (PIV), and to explore the occurrence and mechanism of the double-peaking phenomenon in the u_{RMS} profiles, with a focus on the shear/rotation counteraction during the roll-up of the shear layers. The dynamics of the shear/rotation zones are studied to further describe the physical phenomena governing the double-peaking in the u_{RMS} profiles. After the description of the problem and the regions of interest, a wide range of Reynolds numbers are analysed to suggest the natural flow regimes within which the double-peaking may occur or be suppressed. In addition, its correlation with the time-averaged shear/rotation regions is investigated. Then, a case presenting the double-peaking behaviour is selected to investigate the instantaneous vortex dynamics and the corresponding shear/rotation counteractions to further describe the phenomenon. Moreover, the vortex dynamics are actively altered using the acoustic control to discover the behaviour of the individual peaks under the actuation of the fundamental or the subharmonic modes.

3.2 Experimental setup and measurement procedure

The schematic of the experimental set-up including the regions of interest, the flow channel geometry, as well as the measurement components are presented in figure 3.1. Experiments are conducted at the outlet of a rectangular 20×40 mm^2 duct with the length $L = 300$ mm. The flow is supplied by a blower and passes through a flow conditioning unit consisting of a honeycomb insert and a set of three wire screens, followed by a 9:1 contraction. The flow enters the duct at turbulence intensities below 0.9% and the mean flow uniformity within 0.25% in the inviscid core. The flow rate is varied at the centreline velocities of $U = 1, 2, 5, 10, 12.5, 16, 17.5, 19, 20$ m/s corresponding to the Reynolds numbers of $Re_{\theta_0} = U\theta_0/\nu = 85, 135, 276, 470, 616, 713, 780, 860, 945$ where ν and θ_0 denote kinematic viscosity and momentum thickness, respectively. The spatial dimensions are scaled using the θ_0 value which is evaluated 20 mm downstream of the separation edge. It should be noted that, the velocities presented above are selected out of the measurements conducted for the range $U = 1 - 40$ m/s and found sufficient to represent the transitioning characteristics of the phenomena under study.

Point-wise measurements are conducted using a Dantec 55P11 straight, general purpose single hot-wire (HW) probe oriented normal to the flow direction and connected to a Dantec Streamline Constant Temperature Anemometry system. The HW sampling rate is set to 16 kHz. The HW measurements are conducted over a time span of 32.8 seconds, corresponding to a total of $524, 288$ samples. Spectral analysis of the streamwise velocity fluctuations measured by the hot-wire is performed, with a frequency resolution bandwidth of at least 0.03 Hz. Following the HW, planar particle image velocimetry (PIV) is employed. The origin of the coordinate system is located at the center of the duct with the x-axis oriented in the streamwise direction. The y-axis normal to the duct wall characterizes the span of the shear layer. The major components of the system include a dual pulsed Nd:YAG laser with a maximum output of 70 mJ/pulse, a $1,600 \times 1,200$ pixel 14-bit Imager Pro X 2M CCD camera, and a programmable timing unit. Laser sheet is formed using a combination of the cylindrical and spherical lenses, with a thickness of about 1 mm at its waist. The flow is seeded using a glycol-water based fog with a mean particle diameter of 3 μm. The camera is equipped with a 60 mm fixed focal length lens and a 532 nm $\mp$ 10 nm band-pass filter. The camera is synchronized with the laser by means of a timing unit controlled through the LaVisions DaVis 8 software. PIV images are acquired in the $x - y$ planes located at several z/θ_0. The camera sensor is cropped to 800×1200 pixels and the imaged field of view (FOV) is set to 24×36 mm. The velocity fields are computed by using the cross-correlation of pairs of the successive images. The captured images are processed in the LaVisions DaVis 8 software using an advanced multi-pass method where

	Tunnel-OFF (dB)	Tunnel-ON actuation amplitude (dB)
Natural	76.33	91.2
Low amplitude (LA)	79.11	91.5
Mid amplitude (MA)	88.04	92.9
High amplitude (HA)	95.55	96.87

Table 3.1: Characterization of the low (LA), mid (MA) and high (HA) amplitudes for the acoustic actuations at the fundamental and subharmonic frequencies. See Appendix B for details.

the initial and the final correlation passes are the 64×64 pixels with 50% overlap and the 24×24 pixels with 75% overlap, respectively. This technique results in a vector pitch of 0.18 mm (measurement in the shear layer region), and the effective magnification of 0.38 in the camera provides a pixel scale factor of 33 pixels/mm. For the PIV measurement of the boundary layer at the separation edge, a vector pitch of 0.045 mm is achieved. The results are post-processed using the universal outlier detection [74] technique and the spurious vector removal with vector replacement. To produce time-averaged vector fields for each case, 3000 image pairs are acquired at a rate of 14.73 Hz. The convergence of the results for the mean velocity, the RMS of the streamwise velocity fluctuations and the $< Q >$ criterion are checked using 1000, 1500, 2000, 2500 and 3000 instantaneous fields, and the 3000 snapshots are found more than sufficient for the time-averaged results. The random errors in the PIV measurements are evaluated using the particle image disparity method [75], with the associated average in the velocity fields estimated to be less than 2% within 95% confidence for the free-stream region.

Volume reconstruction of the flow fields is accomplished by performing the phase-locked PIV [76] measurements at multiple planes between $-10 \leq z/\theta_0 \leq 10$ spaced by $z/\theta_0 = 1.25$. Acoustic excitation is provided by a sub-woofer placed at the outlet of the test section and the excitation signal served as the phase-locking reference signal for the PIV timing unit. Characterization of the low (LA), mid (MA) and high (HA) amplitudes for the acoustic actuations at the fundamental and subharmonic frequencies are presented in table 3.1 (See Appendix B for details.). The natural/unperturbed case is characterized by a sound pressure level (SPL) of 91.2 dB at the center of the channel exit. The effect of the acoustic excitation is characterized as 79.1 dB (LA), 88.1 dB (MA), and 95.5 dB (HA) at the same location when the tunnel is off. Based on these, each case can be defined as in table 1 by adding the free stream noise level with the acoustic excitation noise level.

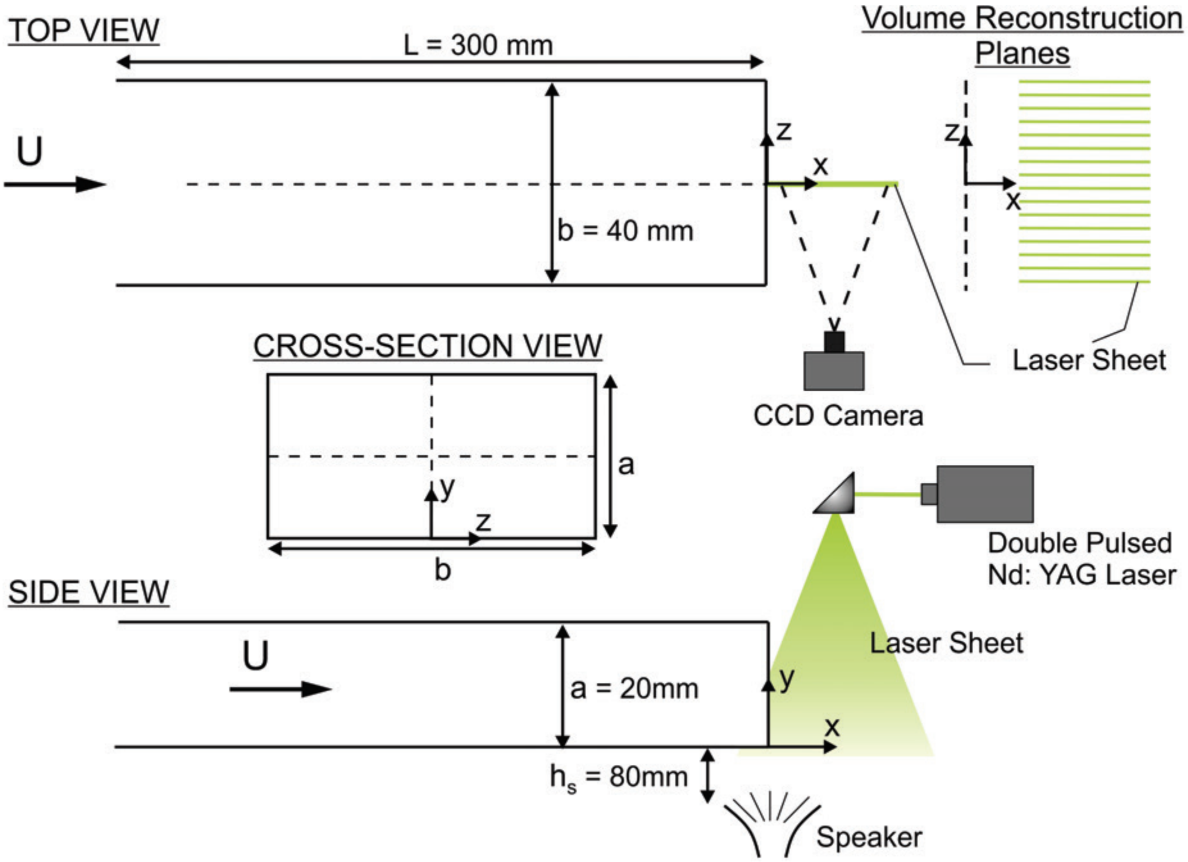

Figure 3.1: Experimental set-up: The schematic of the flow channel geometry and dimensions; The measurement components; Planes of measurement.

3.3 Results and discussion

3.3.1 Problem definition

The general features of the present problem are introduced in figure 3.2 by illustrating the time-averaged streamwise velocity ($< u > /U$), the RMS of the streamwise velocity fluctuations (u_{RMS}/U), as well as the vorticity component (Ω_Z) normal to the plane of measurement for $Re_{\theta_0} = 470$. In figure 3.2a, the time-averaged streamwise velocity contour is presented with the horizontal and the vertical axes characterizing the streamwise (x/θ_0) and the spanwise directions (y/θ_0), respectively. The spanwise variation of the velocity at the location of the vertical dashed line ($x/\theta_0 = 25$) is shown with the profile at the upper-right corner. The high-speed (HS) and low-speed (LS) sides of the shear layer in the downstream of the separation edge are identified in the contour plot. They are also detectable on either side of the inflection point in the velocity line plot. The existence of an inflection point implies that the present flow-field is prone to instabilities. In figure 3.2b, the u_{RMS}/U contour is displayed with the corresponding line-plot. It can be seen that two distinguishable peaks are detectable for the u_{RMS}. Hereafter, the peaks located towards the LS and the HS side are referred to as the minor and the major peaks, respectively. We emphasize that, the LS and HS terms characterize the sides towards which the structures are oriented and not necessarily their exact location. As will be elaborated in the following sections, the individual peaks in the u_{RMS} react independently to the various active/passive flow control strategies. On the other hand, the shape of the vorticity profiles as shown in figure 3.2c remain unresponsive. Knowing the fact that the shearing and rotating fluid elements are not distinguishable by the vorticity field, the following sections of the study are motivated by the analysis of the shear/rotation interactions in the vicinity of the double-peaking.

3.3.2 Incoming boundary layer at the separation edge

Before starting the main discussion of the results, a brief note on the incoming boundary layer characteristics at the separation edge would be beneficial. This is particularly important, since the double-peaked u_{RMS} profiles may also be observed in the wall-bounded flows [77, 78]. Therefore, one would suggest this observation as the root for the occurrence of the double-peaked u_{RMS} in the separated shear layer formed in the downstream. Accordingly, the characteristics of the incoming boundary layer are presented in figure 3.3 for the $Re_{\theta_0} = 470$ case which displays the double-peaking phenomenon for the naturally

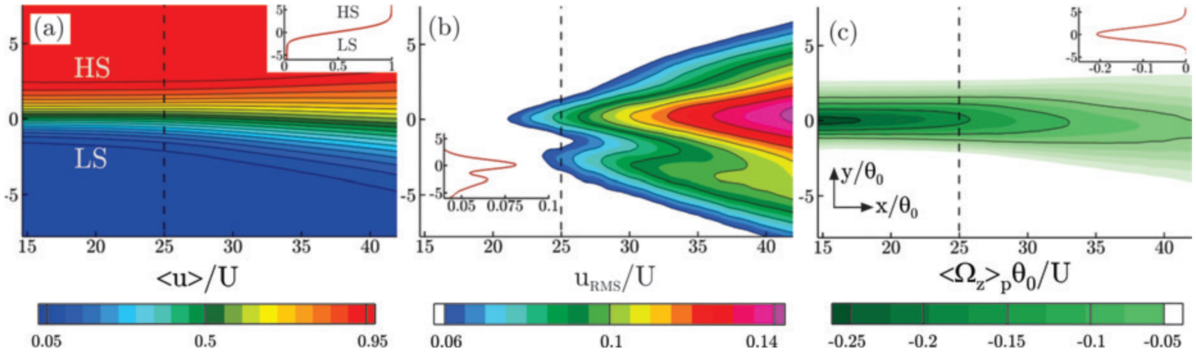

Figure 3.2: (a) Time-averaged streamwise velocity ($< u > /U$); (b) RMS of the streamwise velocity fluctuations (u_{RMS}); (c) Time-averaged vorticity (Ω_Z). Profiles are extracted at the location of the vertical dashed line ($x/\theta_0 = 25$). The low-speed and the high-speed sides of the shear layer are denoted as LS and HS, respectively.

developing shear layer. The boundary layer velocity profile obtained from the PIV measurement is included in figure 3.3a. The wall normal distance (y) is normalized by the local displacement thickness δ^*. The measured velocity profile has a shape factor of $H = 2.58$ and resembles the Blasius boundary layer with $H = 2.59$. This characterizes a laminar incoming boundary layer at the separation edge. In addition, the streamwise turbulence intensity profile u_{RMS} shown in figure 3.3b depicts a single peak, and tends to diminish towards the free stream and near the wall region. This information rules out the possibility of the role of the boundary layer on the double-peaking phenomenon in the downstream shear layer.

3.3.3 Transitioning character of the double-peaking with the shear and rotation

To investigate the correlation between the double-peaking in the u_{RMS} and the competing effects of the shearing and the rotating regions of the flow, the $< Q >$ criterion [79] is calculated from the time-averaged flow field. The advantage of the $< Q >$ criterion to the vorticity is its capability of distinguishing between the purely shearing and rotating fluid elements. It should be noted that an instantaneous vortex dynamics analysis is carried out using the information obtained from the phase-locked PIV measurements and proper orthogonal decomposition (POD) in the following sections of the article. The $< Q >$ criterion identifies the core of a vortex where the second invariant ($< Q >$) of the velocity gradient tensor is positive [61]. Therefore, the $< Q >$ criterion exhibits the local balance

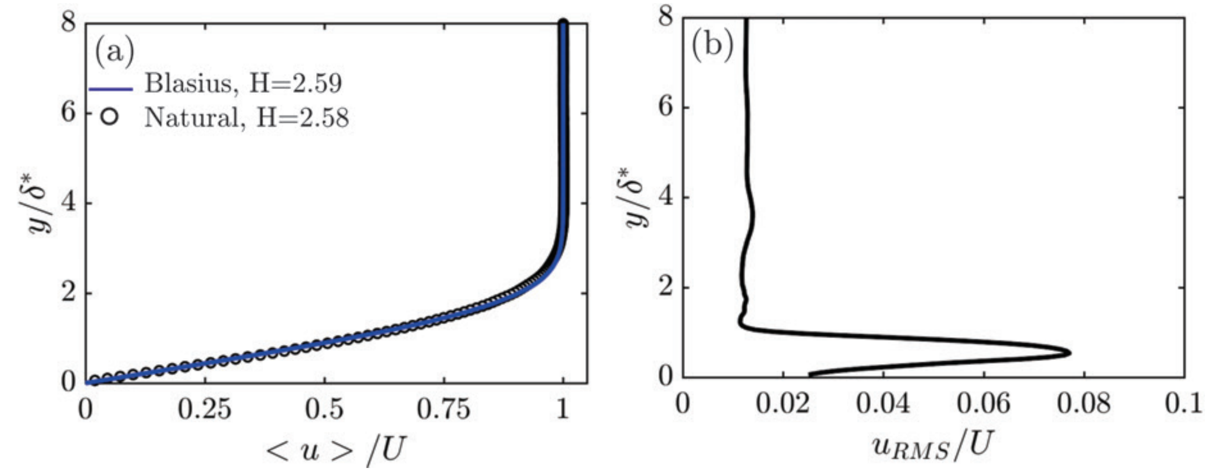

Figure 3.3: Boundary layer characteristics at the separation edge for $Re_{\theta_0} = 470$: (a) Time-averaged streamwise velocity ($< u > /U$); (b) RMS of the streamwise velocity fluctuations (u_{RMS}). The wall normal distance (y) is normalized by the local displacement thickness δ^*.

between the shear strain rate and the vorticity magnitude [61]. Before investigating the hypothesis for the role of the shear/rotation dynamics on the double-peaking phenomenon, it would be beneficial to determine the flow regimes within which they occur. To this end, a range of Reynolds numbers can be inspected through which the shear/rotation competition correlates with the double-peaking in the u_{RMS}.

Selected from our measurements for a wide range of Reynolds numbers, the contours of the $< Q >$ criterion superimposed by the iso-lines of $0.05 \leq u_{RMS} \leq 0.15$ for $Re_{\theta_0} = 85, 135, 276, 470, 616, 713, 780, 860, 945$ are illustrated in figure 3.4. It should be noted that the panels in figure 3.4 are restrained to the downstream locations where the initial KH roll-ups are more likely to take place. Negative (blue) clusters of the $< Q >$ are associated with the shearing regions. On the other hand, the positive (red) spots represent the regions where the rotation of the fluid elements dominate. For the $Re_{\theta_0} = 85$ and 135 cases, the iso-lines show a single major peak with a tendency towards the high-speed side. For these two cases of the low Reynolds number, small-scale intermingled patches of the shear/rotation spots present a sporadic distribution. A second minor peak appears and develops near the low-speed side for $Re_{\theta_0} = 276, 470, 616, 713, 780$. This minor peak in the u_{RMS} profile seems to form at a certain streamwise location downstream of the separation edge. Subsequently, the minor peak tends to diminish and eventually disappear with farther downstream distances. Furthermore, the minor peak disappears for the Reynolds

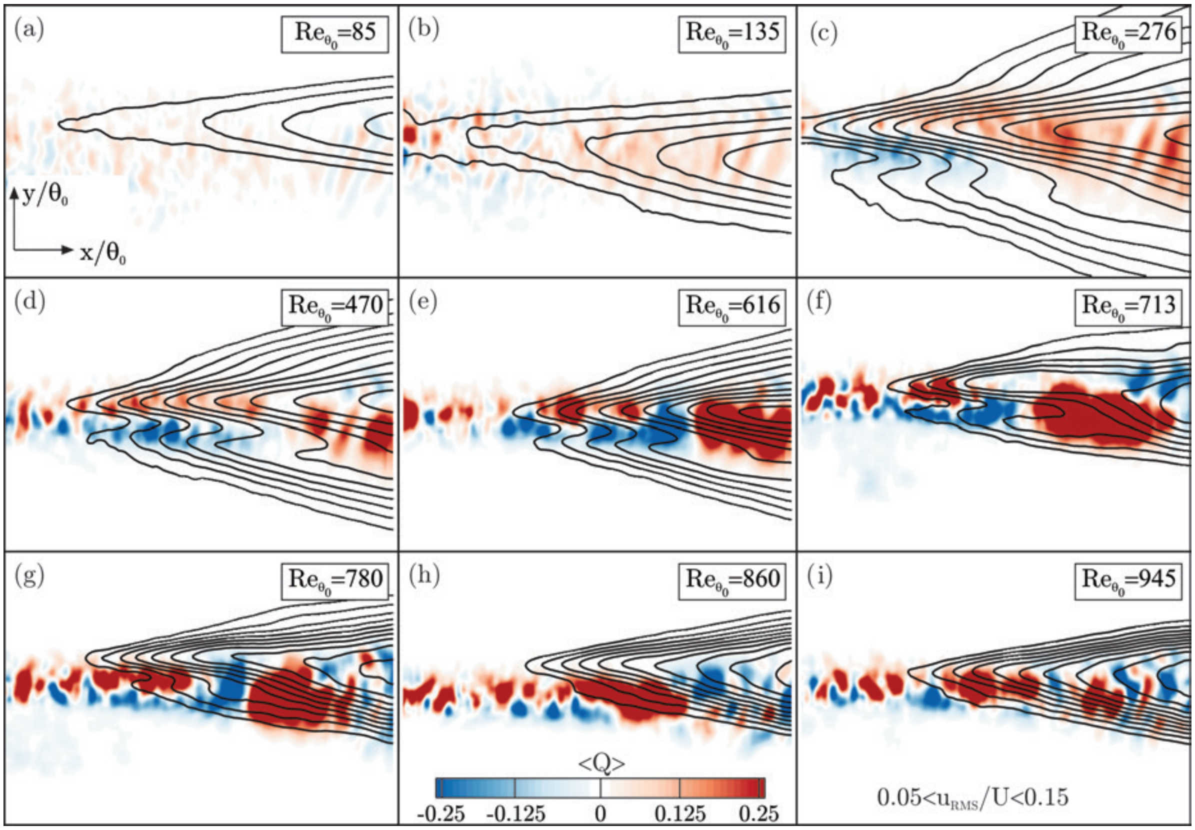

Figure 3.4: Time-averaged $< Q >$ criterion superimposed by the iso-lines of the streamwise turbulence intensity ($0.05 \leq u_{RMS}/U \leq 0.15$) for the naturally developing shear layer at $Re_{\theta_0} = 85 - 945$.

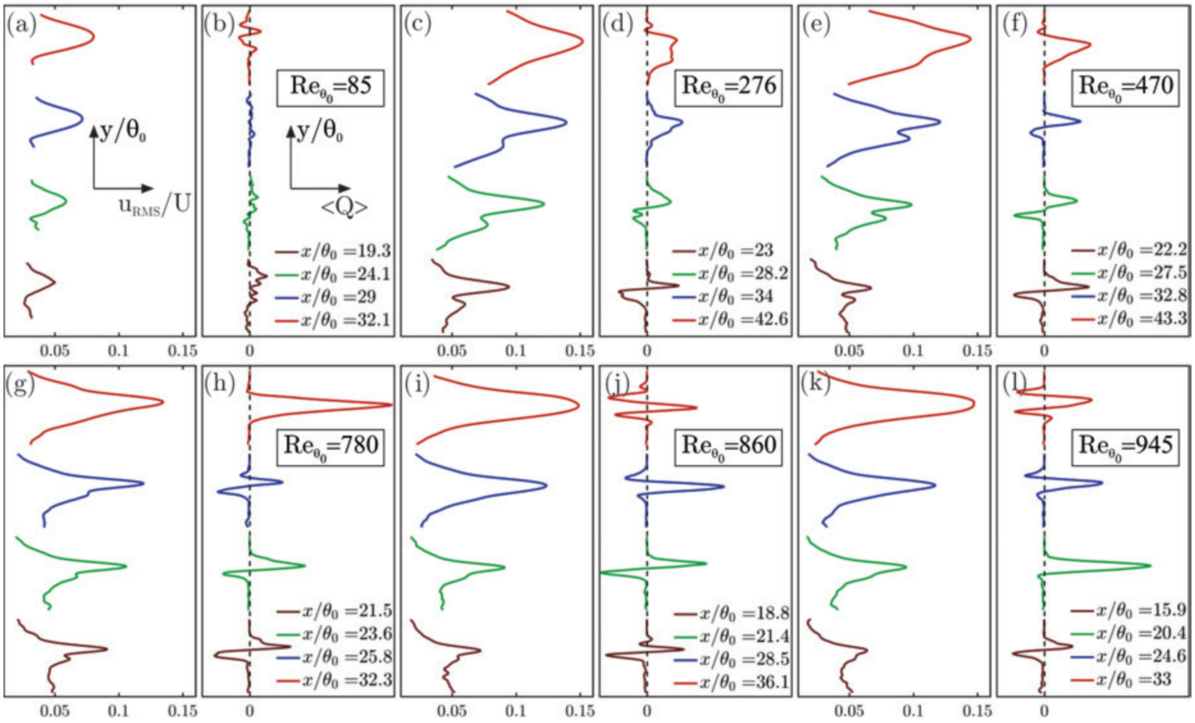

Figure 3.5: Streamwise turbulence intensity (u_{RMS}/U) correlated with the $< Q >$ criterion at different streamwise locations ($x/\theta_0 = 19.3, 24.1, 29, 32.1$) in the naturally developing shear layer for $Re_{\theta_0} = 85, 276, 470, 780, 860, 945$.

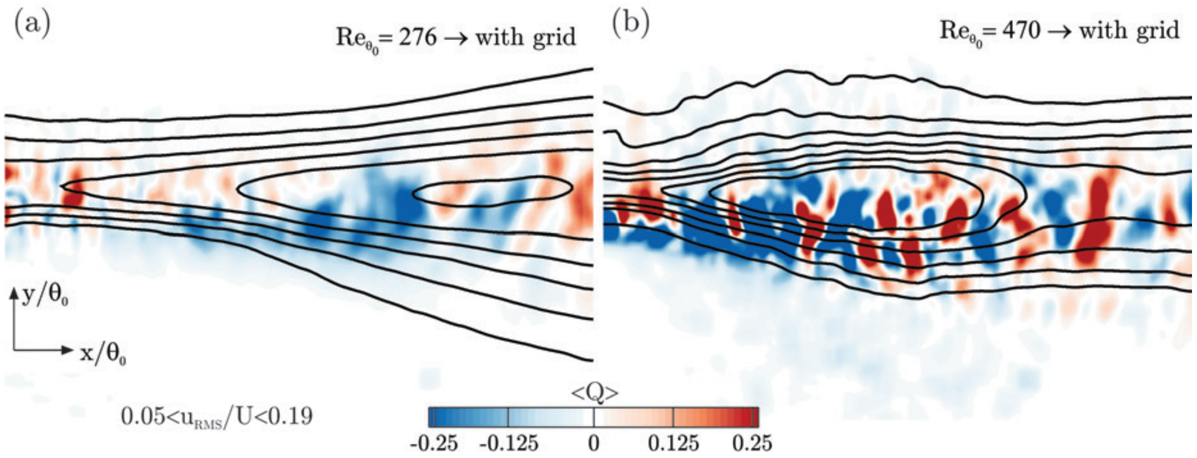

Figure 3.6: Time-averaged $< Q >$ criterion superimposed by the iso-lines of the streamwise turbulence intensity ($0.05 \leq u_{RMS}/U \leq 0.19$) for the naturally developing shear layers at: (a) $Re_{\theta_0} = 276$; (b) $Re_{\theta_0} = 470$ cases subjected to the upstream grid turbulence.

numbers larger than the $Re_{\theta_0} = 860$. Another interesting observation is regarding the shear/rotation distribution obtained from the time-averaged flow fields at the presence of the minor peak. Either within the downstream locations or the Reynolds number ranges within which the double-peaked u_{RMS} occurs, the shear/rotation zones are not composed of the intermingled small spots. Instead, they portray two distinguished and well-organized layers (ribbons) of shear and rotation. Towards the low-speed side (not exactly on the LS side), a blue layer of shearing flow is observed at the vicinity of the minor peak of the u_{RMS}. On the contrary, the red ribbon of rotating zone appears at the proximity of the major peak of the u_{RMS} leaning towards the high-speed flow. It should be noted that, when we refer to the low-speed (LS) and the high-speed (HS) sides, the intention is not to specify the exact location of the structures. It is rather to indicate the side towards which a certain phenomenon is leaning to occur.

In accordance with the formation and disappearance of the minor peak, the shear rotation distribution can also be associated with the transitional characteristics of shear layers. To further correlate the formation and decay of the minor peak with the shear/rotation distribution, figure 3.5 presents the spanwise variation of the u_{RMS} correlated with the $< Q >$ criterion for different streamwise locations (x/θ_0) for $Re_{\theta_0} = 85, 276, 470, 780, 860, 945$. For the lowest Reynolds number ($Re_{\theta_0} = 85$), a single major peak is observed in the u_{RMS} profile at all streamwise locations. This is accompanied with the random small scale variations of the shear (negative)/rotation (positive) quantities in the corresponding $< Q >$

profiles. For the larger Reynolds numbers of $Re_{\theta_0} = 276, 470, 780$, a negative peak (shear) forms in the $< Q >$ profiles and decays with the downstream distance. This co-occurs with the growth and the disappearance of the minor peak in the u_{RMS} profiles. For the higher ends of the transitioning locations or at the larger Reynolds numbers, the minor peaks in the u_{RMS} disappear and the organized correlation with the shear-characterizing peak in the $< Q >$ is lost. As an example, the correlation is lost beyond the $x/\theta_0 = 21.4$ location for the $Re_{\theta_0} = 860$. Also, the profiles of the $Re_{\theta_0} = 945$ are uncorrelated for all the streamwise locations.

Another important factor in forming the structure of the shear layers in the near-separation region is the level of the upstream turbulence and consequently the shape of the incoming boundary layer [80]. To this end, the grid turbulence is introduced at the inlet of the channel for the above cases of the $Re_{\theta_0} = 276$ and 470. As a result, the incoming boundary layer transitioned from the laminar ($H = 2.59$) to turbulent ($H = 1.5$). The contours of the $< Q >$ criterion superimposed by the iso-lines of $0.05 \leq u_{RMS} \leq 0.19$ are presented in figure 3.6. As a consequence of the grid turbulence, the above cases of the $Re_{\theta_0} = 276$ and 470 with the previous demonstration of the double-peaking (in figures 3.4c, d), now transition to the single-peaked u_{RMS} profiles. Likewise, the layered shear/rotation regions are dispersed and replaced by the more disorganized intermingling spots. Up to this point, three important observations suggest the transitioning character of the double-peaking phenomenon and the corresponding shear/rotation distributions. This transitioning behaviour is commonly attributed to the nature of the shear layer formation and the associated phenomena. First, the double-peaking in the u_{RMS} profile occurs and correlates with the shear/rotation distribution within a certain range of the Reynolds numbers below and above which the correlation/occurrence is lost. Second, the formation, evolution and the decay of the double-peaking and the corresponding organization of the shear/rotation starts at a certain downstream location, maintains its character up to a distance farther downstream after which it disappears. Third, development of the separated boundary layer into the transitioning/turbulent states as well as the elevated upstream turbulence levels due to the grids, alters the transition of the double-peaking and the organization of the shear/rotation spots.

3.3.4 Frequency considerations

The literature survey presented in the introduction section suggests the phenomenon under investigation to be associated with the interaction of the fundamental and the subharmonic modes. Therefore, the corresponding frequencies should be first determined for the naturally developing shear layer. Afterwards, the frequencies characterizing the fundamental and the subharmonic modes can be used to acoustically actuate the flow at different amplitudes. To this end, HW measurements are utilized to obtain the streamwise velocity spectrum at different downstream locations ($x/\theta_0 = 0 - 300$) for the $Re_{\theta_0} = 470$ which portrayed the double-peaking behaviour. Figure 3.7 presents the frequency spectra of the streamwise velocity fluctuations obtained from the HW measurements at different axial locations. The vertical dashed and solid lines characterize the frequencies associated with the subharmonic ($f_n/2 = 175$ Hz) and the fundamental ($f_n = 350$ Hz) modes, respectively. At $x/\theta_0 = 0$ location seen in figure 3.7a, the natural case maintains the upstream boundary layer characteristics without any frequency preference. It should be noted that the high frequency spike at this location is associated with the apparatus noise which is significantly larger than the natural frequency of interest. On the other hand, forcing the shear layer at the subharmonic (figure 3.7b) and the fundamental (figure 3.7c) modes create the sharp spikes in the velocity spectrum at ($x/\theta_0 = 0$) for the corresponding frequency. At $x/\theta_0 = 16.7$, the naturally developng shear layer forms a broadband peak, which is commonly seen in shear layers [81, 82]. The highest peak almost located in the middle of the broadband characterizes the dominance of the fundamental mode and accordingly the roll-up frequency. The equivalent dimensionless frequency, is determined based on the Strouhal number ($St_{\theta_0} = f_n\theta_0/U = 0.026$) which is close to the reported value of 0.024 [81]. Farther downstream at $x/\theta_0 = 33.3$, the higher harmonic peaks start to appear. This is the consequence of the non-linear perturbations setting in [81]. Beyond this streamwise location, the energy content of the fundamental mode starts to diminish until it vanishes within the range of $x/\theta_0 = 50 - 66.7$ streamwise locations. This is also accompanied by the formation and growth of the subharmonic peak. This phenomenon appearing as the shifting of the peak towards the lower frequencies with the downstream distance follows the previous observations by [81]. The frequency associated with the subharmonic demonstrates the value half of the fundamental mode. This occurs because the passage frequency of the vortices is halved due to the vortex pairing in the downstream of the roll-up location. For the case of the subharmonic actuation, a sharp spike is observed for the $f_n/2$ frequency. Accordingly, the corresponding mode tends to dominate the fundamental mode earlier. On the other hand, actuating the fundamental mode advances the formation of the non-linear effects and the appearance of the higher harmonic spikes. In the far-field region at $x/\theta_0 = 300$, none of the cases show a frequency preference and hence the isotropic fully-developed turbulence introduces wide ranges of frequencies. In this region, the contribution of the high-frequency (short-wavelength) small-scale eddies is increased and the mixing is consequently enhanced.

In figure 3.8, the amplitude ratios corresponding to the fundamental and the subharmonic modes are extracted from the velocity spectra and presented as ($A(f_n)/A(f_n/2)$)

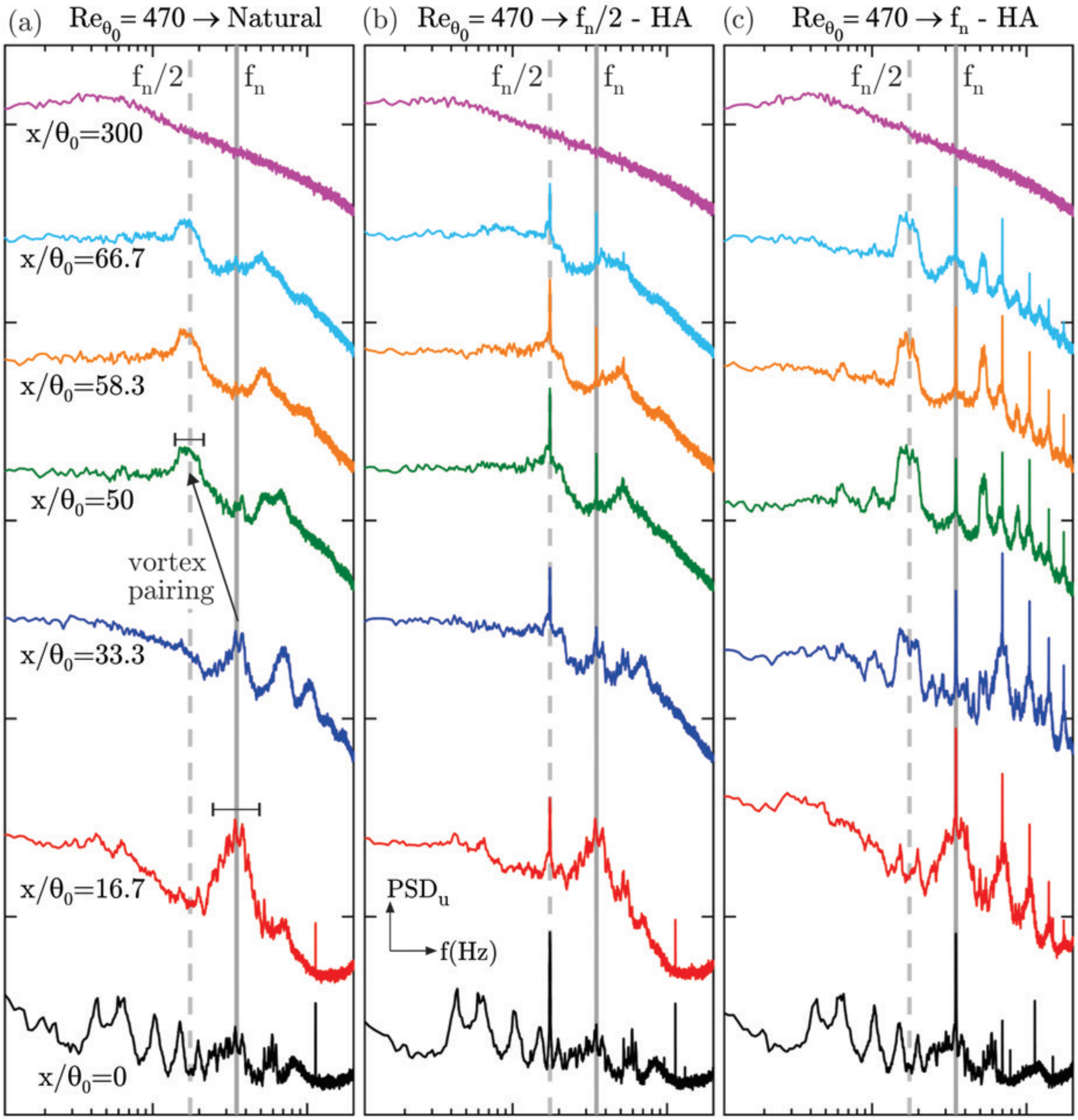

Figure 3.7: Spectra of the streamwise velocity fluctuations at different streamwise locations ($x/\theta_0 = 0-300$) obtained from the HW measurements at $Re_{\theta_0} = 470$ for: (a) Natural case; (b) Actuation of the subharmonic mode ($f_n/2$) at the high amplitude (HA); (b) Actuation of the fundamental mode (f_n) at the high amplitude (HA).

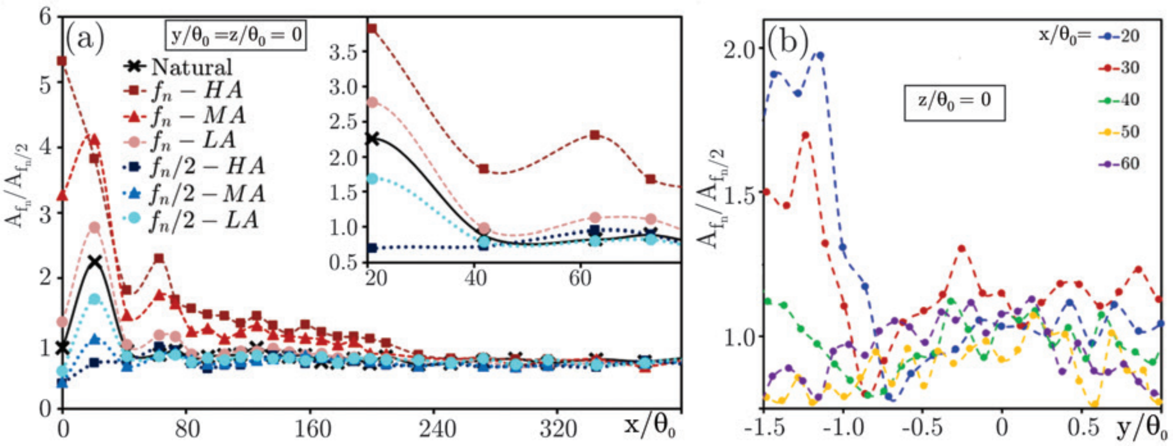

Figure 3.8: Fundamental (f_n) to subharmonic ($f_n/2$) amplitude ratio of the velocity spectra obtained from the HW measurements for the $Re_{\theta_0} = 470$: (a) Streamwise variation at ($y/\theta_0 = z/\theta_0 = 0$) for the fundamental and subharmonic forcing of the shear layers at the low (LA), mid (MA) and the high (HA) amplitudes; (b) Spanwise variation at ($x/\theta_0 = 20, 30, 40, 50, 60$) streamwise locations and ($z/\theta_0 = 0$) for the natural case.

for the $Re_{\theta_0} = 470$. The streamwise variation of the amplitude ratio shown in figure 3.8a confirms the dominant effect of the fundamental mode near the separation region for the natural case. With the downstream distance, the amplitude ratio is decreased as the fundamental mode declines and the subharmonic effects dominate due to vortex pairing. Excitation at low (LA), mid (MA) and high (HA) amplitudes amplifies the energy content of the corresponding f_n or $f_{n/2}$ frequency. Beyond $x/\theta_0 = 240$, none of the modes dominate as the shear layer demonstrates fully-developed characteristics where the high-frequency small scales become important. This observation limits the focus of our study to the near-field region where the competing effects of the fundamental and the subharmonic modes are strong. The traverse distribution of the amplitude ratio is presented in figure 3.8b at the streamwise locations $x/\theta_0 = 20, 30, 40, 50, 60$ in the $z/\theta_0 = 0$ plane for the naturally developing shear layer. At $x/\theta_0 = 20 - 30$, the fundamental mode prevails with a stronger domination on the low-speed side. This is a verification of the KH roll-ups occurring towards the low-speed outside region as also reported in the velocity spectra by [81]. Up to $x/\theta_0 = 40$, which is located within the vortex pairing region, the fundamental mode loses its energy content until the subharmonic dominates beyond $x/\theta_0 = 50$.

The fundamental and the subharmonic frequencies detected above, for the naturally developing shear layers and their behavior under the actuation, are obtained owing to

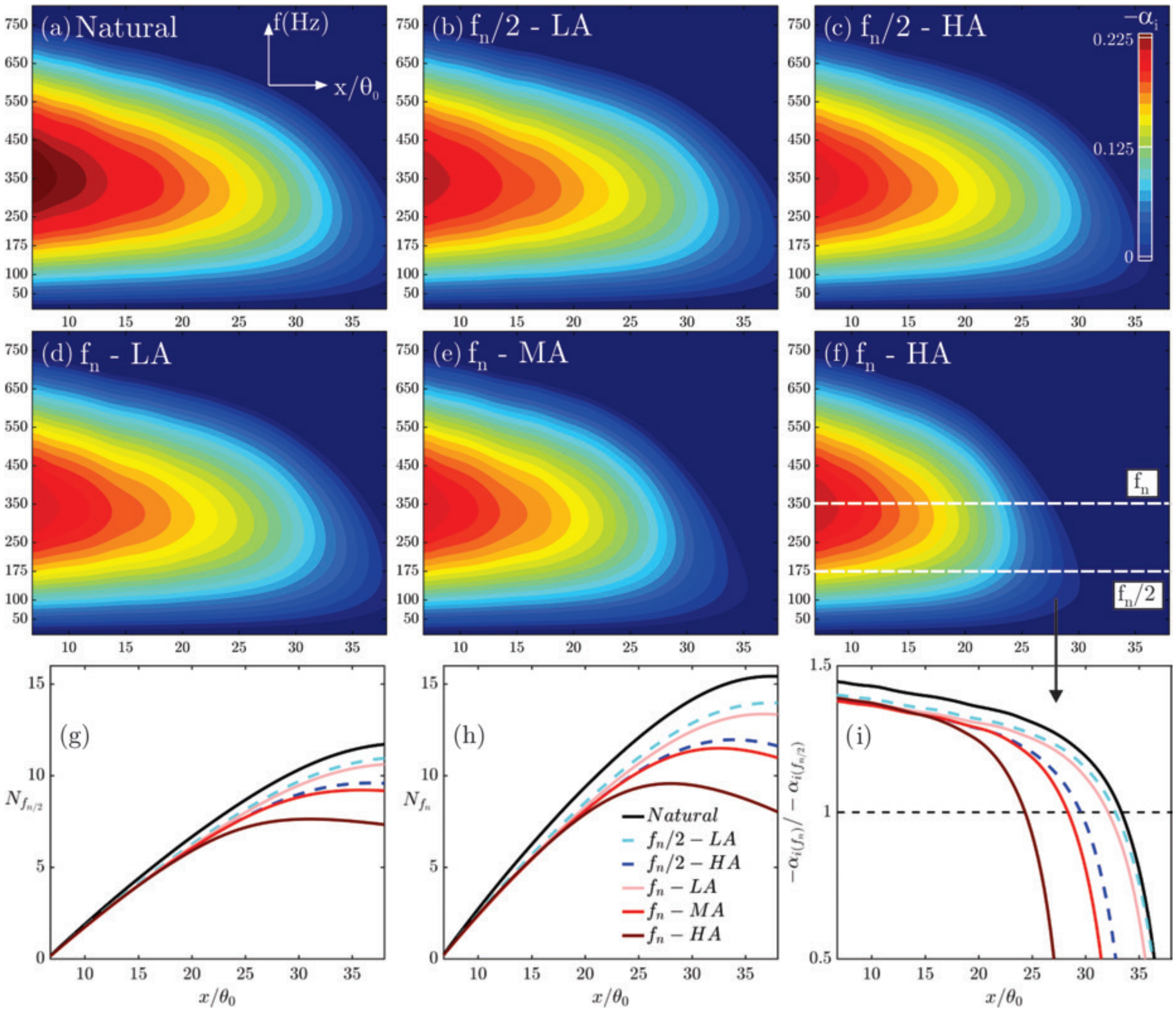

Figure 3.9: Spatial theory of the linear stability (LST) analysis based on the PIV measurements for the natural, fundamental (f_n), and subharmonic ($f_n/2$) actuations at low (LA), mid (MA) and high (HA) amplitudes: (a-f) Growth rate ($-\alpha_i$) variation of the range of frequencies with the downstream distance; (g-h) The cumulative integral of the growth rate (N-factor) associated with the fundamental and the subharmonic modes; (i) Fundamental to subharmonic growth rate ratios ($-\alpha_i(f_n)/-\alpha_i(f_n/2)$).

the temporally high-resolution HW velocity measurements. To verify this analysis, spatial linear stability (LST) analysis is conducted based on the spatially-resolved PIV measurements. In the hydrodynamic theory of stability, the shear layer is then treated as the counteraction among the ensemble of propagating instability waves [83, 84, 85]. Each of the waves, the amplitude of which may grow/decay in time/space as they advect downstream, are associated with the flow structure of a certain length scale (wave length). This concept is achieved by the analysis of the flow in a Fourier space rather than in a physical time/space domain. In the spatial analysis, the perturbations are only allowed to grow/decay in space. The disturbances may only be convected in time without amplification/damping. To this end, the least squares method is implemented for the curve fitting of the local velocity profiles obtained from the PIV measurements according to [86]. The hyperbolic-tangent velocity profile is typically used to conduct the spatial linear stability analysis, namely in the study of the effect of the shear layer velocity ratio on the growth of the perturbations in space [87]. The Orr-Sommerfeld equation can be derived by introducing perturbations to the linearized incompressible Navier-Stokes equations assuming the normal-mode disturbances [88]. It should be noted that for individual natural or actuated cases, different base flows are considered. More specifically, the time-averaged velocity field measured by the PIV are extracted at certain locations and used for the LST. It should also be noted that, the spatial LST is previously used for actuated flows, namely [89] and [90]. For each downstream location, implementation of the time-averaged streamwise velocity profile as the base flow, signifies a local LST analysis of the spatial perturbations. After implementing the proper homogeneous boundary conditions, the resulting eigenvalue problem needs to be solved. The Orr-Sommerfeld equation is then solved by the spectral colocation approach, where the Chebyshev polynomials provide the approximation of the eigen-functions. The non-linearity issue in the eigenvalue system is resolved by means of the companion matrix according to [91]. Compared to the other traditional methods such as the finite difference schemes, implementing the spectral method based on the Chebyshev polynomials provides enhanced accuracy [92]. The higher order spectral methods converge faster and are computationally more affordable as they demand less processing power and physical memory.

LST results are presented in figure 3.9 for the natural and the forced cases at the fundamental (f_n) and the subharmonic ($f_n/2$) frequencies for the low (LA), medium (MA) and high (HA) excitation amplitudes. The contour plots in figures 3.9(a-f) display the downstream variation of the growth rates ($-\alpha_i$) associated with a range of frequencies obtained from the LST for $Re_{\theta_0} = 470$. In the near-separation region of the natural case, a range of frequencies contribute to the growth of the instabilities. However, the fastest growing wave is associated with the 350 Hz frequency characterizing the fundamental (f_n)

mode at which the roll-up occurs. This verifies the broadband peak previously discussed for the velocity spectra. Another interesting observation is that the LST contours illustrate meaningful results almost up to $x/\theta_0 = 30$ beyond which the velocity spectra detected the emergence of the non-linear effects. This is more evident by the shrunk contour region in the $f_n - HA$ actuation case for which the LST validity deteriorates earlier. This is a meaningful observation when restating that the high amplitude actuation at the fundamental frequency depicts advanced location of the non-linear peaks in the velocity spectra.

A common way of presenting the downstream variation of the growth rate is by calculating its cumulative integral over the streamwsie distance known as the N-factor. This parameter is also called the amplification factor and is a measure of the flow transition [93, 94, 95]. Figures 3.9(g-h) depicts the N-factor profiles corresponding to the fundamental and the subharmonic modes obtained for the naturally developing and the actuated shear layers. The profiles characterize an initial linear increase with the downstream distance. After reaching its critical value at the maxima, the N-factor profile start a decreasing trend. This reduction after the critical value demonstrates the saturation of the instabilities and characterizes the start of the transition [89]. The occurrence of the transition precedes for the forced cases as they earlier reach a non-linear state.

In addition, the N-factor is related to the amplitude of the disturbances (a) through the equation $a/a_0 = e^N$, where a_0 is the reference value. Accordingly, the critical value of the N-factor is equivalent to the saturation limit of the perturbations beyond which the transition occurs. By visual inspection of the slope in the linear region of the N-factor, the rates at which the perturbations grow with the downstream distance can be analysed. Comparing the naturally developing shear layers within this linear region, it becomes evident that the fundamental mode grows at a higher rate with respect to the subharmonic frequency. The actuated shear layers tend to saturate earlier and hence the transition is advanced. Particularly, actuation at the fundamental frequency reaches the transition earlier due to the advanced roll-up. Similarly, increasing the amplitude of the excitations advances the transition as the earlier domination of the non-linear effects reach up to the transition state earlier. In figure 3.9i, the fundamental to the subharmonic growth rate ratios ($-\alpha_i(f_n)/-\alpha_i(f_n/2)$) are presented. Within the expected range of validity of the linear stability analysis, the fundamental mode dominates in the near-separation region. With the farther downstream distances, the subharmonic mode tends to grow faster. This is also in accordance with the previous observations in the HW-based velocity spectra. The fundamental to the subharmonic growth rate ratios tends to fall below unity at certain streamwise locations for each of the natural and the actuated cases. These locations coincide with the point of the saturation in the N-factor profiles discussed above.

3.3.5 Acoustic control of the shear/rotation

The discussions up to this point reveal the transitioning character of the double-peaking phenomenon, with the Reynolds number, the downstream distance and the upstream grid-induced turbulence. It is also shown that the double-peaking in the RMS of the streamwise velocity fluctuations is correlated with the shear/rotation distribution obtained from the time-averaged flow field. However, the time-averaged analysis conducted earlier, only provides the global aspects of the shear/rotation dynamics. For a better understanding of the local features, the shear/rotation is analysed in the context of the instantaneous vortex dynamics presented in this section. The intention is to control a case with the existence of the double-peaking through the acoustic altering of the vortex dynamics. The instantaneous speculations are then generalized using the statistical analysis of the vortex core locations.

Proper orthogonal decomposition (POD) is implemented to reconstruct the flow-field of the natural and the actuated cases at $Re_{\theta_0} = 470$ using the five most energetic modes. This is achieved by recovering the 79%-85% of the total energy in the flow. The mean of the snapshots are subtracted prior to conducting the POD. Afterwards, the RMS of the streamwise velocity fluctuations ($\tilde{u}_{RMS}/U$) are calculated using the POD field and displayed in figures 3.10(a, e, i) for the natural, subharmonic and the fundamental actuation cases, respectively. At the first glance, the RMS field obtained from the POD demonstrates a cleaner image with the peaks displayed more clearly compared to that of the originally presented data. POD reproduces the time-averaged PIV results with clearly defined double-peaks by filtering out the small scale high frequency modes. It can be seen that the actuation of the shear layer at the fundamental mode amplifies the minor peak, which tends to form near the low-speed region. In addition, the formation location of the minor peak in the streamwise distance is advanced under the actuation of the fundamental mode. On the other hand, excitation at the subharmonic frequency amplifies both the major and the minor peaks. However, the major peak located towards the high-speed region is more significantly affected. The vortex pairing mechanism and the associated subharmonic effect, are known to expand the shear layer [70, 96] in the traverse direction. This is also evident in figure 3.10e where the $\tilde{u}_{RMS}/U$ field corresponding to the subharmonic forcing, covers a broader traverse region compared to the natural and the fundamental actuation cases.

In figures 3.10(b, f, j), the instantaneous streamwise velocity fluctuations ($\tilde{u'}/U$) coloured from blue (-0.2) to red (0.2) are given for the natural, subharmonic and the fundamental actuation cases, respectively. The corresponding spanwise velocity fluctuations ($\tilde{v'}/U$) are presented as dashed (-0.24) and solid (0.24) lines. The local direction associated with each of the fluctuating regions is depicted by a horizontal or vertical arrow for the streamwise and spanwise directions, respectively. As stated earlier, the Kelvin-Helmholtz instability initiates the growth of the disturbances in the shear layer. That would be the case of having only two horizontal arrows, generating a differential of the streamwise velocity with respect to the traverse direction. This generates an elongated layer between the pair of horizontal arrows and a friction (shear) region is formed. Farther downstream, as the instabilities grow, another pair of the vertical arrows appear and create a differential of the spanwise velocity with respect to the streamwise direction. The resulting four-arrow configuration is illustrated in figures 3.10(b, f, j), where the two pairs of the streamwise and spanwise shear arrows create a spinning around a center of rotation. This observation clearly characterizes a shear/rotation cell which we know as the vortex core. In other words, the coupling between the shear and rotation is the engine to the formation of a vortex through the roll-up process.

This observation translates into the instantaneous vorticity $\tilde{\Omega}_Z$ dynamics in the corresponding POD reconstructions presented in figures 3.10(c, g, k). The case of the pair of horizontal arrows is basically the near-separation region where the elongated (stretched) voricity layer is formed. Farther downstream, the accumulated vorticity field is associated with the angular velocity of the flow the direction of which is depicted by the four-arrow arrangement described above. Another observation is recognized as the phase-reversal phenomenon which is described by [15, 16, 17] and [14]. They found that the amplitude of the fluctuations reduce to zero at a certain traverse location and then grows on the other side with the opposite phase. The four-arrow arrangement of the present study and its correlation with the shear/rotation zones explain this phenomenon by the straightforward visualization of the flow features. Each pair of the parallel arrows with the opposite directions simply portray the phase-reversal of the fluctuations. Also, the fluctuations vanish at a traverse location between the two horizontal arrows. The traverse location is found near the center of rotation which is detected slightly towards the low speed side. This finding is in accordance with [97], who stated that the traverse location does not fall on the critical layer and it is rather located towards the low speed side.

The POD reconstruction of the $\tilde{Q}$-criterion clearly describes the rotating vortex core in figures 3.10(d, h, l). With the aid of the vertical dashed lines, the rotation of the vortex core is correlated with the center of rotation of the four-array arrangement as well as the accumulated vorticity region. In addition, the instantaneous $\tilde{Q}$-criterion distinctively represents the shear and the rotation areas. The shear regions in the $\tilde{Q}$-criterion can be associated with the thinning in the stretched (elongated) vorticity layer. The streamwise location of the first KH roll-up is advanced under the actuation of the fundamental mode. Accordingly, the minor peak of the $\tilde{u}_{RMS}$ is also augmented and appears at more upstream

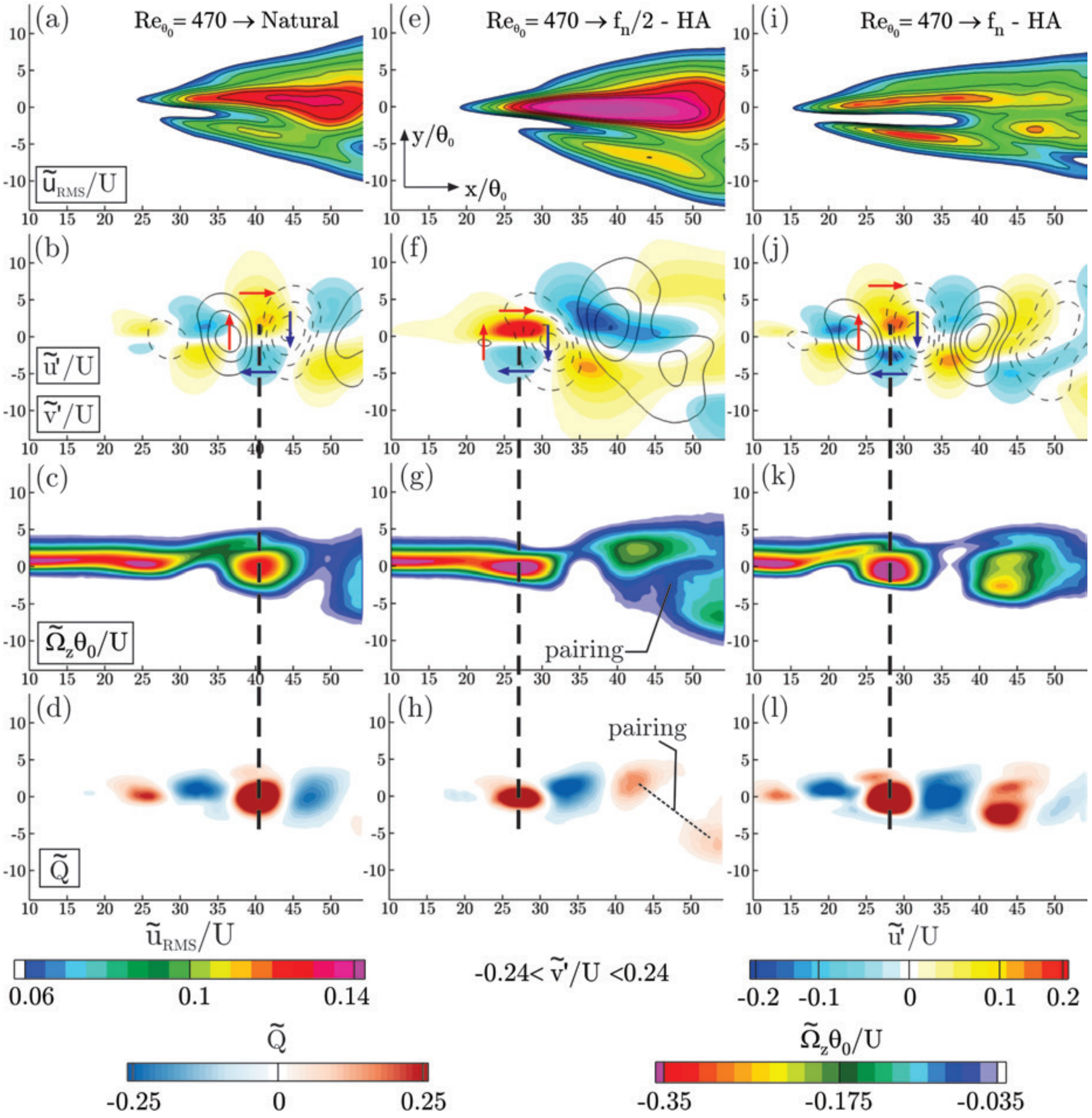

Figure 3.10: Proper orthogonal decomposition (POD): Streamwise turbulence intensity $\tilde{u}_{RMS}/U$; Streamwise ($\tilde{u'}/U$, blue to red) and spanwise ($\tilde{v'}/U$, dashed-solid lines) fluctuations; Vorticity $\tilde{\Omega}_Z$ and $\tilde{Q}$: (a, b, c, d) Natural; (e, f, g, h) Subharmonic forcing at the high amplitude (f_n/2-HA); (i, j, k, l) Fundamental forcing at the high amplitude (f_n-HA); Arrows show the direction of the local shear and the sense of rotation of the corresponding vortex core.

locations. It should be noted that the KH roll-ups occur towards the low-speed side where the minor peak of the $\tilde{u}_{RMS}$ is also observed. Actuation of the subharmonic mode enhances the occurrence of the vortex pairing. As illustrated in figures 3.10(g, h) during the pairing, the upstream vortex core accelerates and shifts towards the high-speed side and catches up with the decelerated downstream rotation core. Concurrently, the downstream vortex core is pushed towards the low-speed region. As a result, both the major and the minor peaks are amplified. However, the major peak which leans towards the high-speed side is more strongly intensified. In addition, organization of the pair of the merging rotating cores in a wider traverse region is accompanied by a larger RMS field of the streamwise velocity fluctuations.

Above observations in the instantaneous flow field, shed more light on the role of the vortex dynamics on the double-peaking and their association with the roll-up and the pairing processes. However, it is important to determine whether the occurrence of these phenomena are statistically sufficient to affect the RMS values. To this end, a vortex core detection algorithm is utilized based on the Γ_2 criterion introduced by [98]. This method is found to identify the vortex core more precisely as the center of rotation [98]. The total number of the detected vortices in the measurement frames are counted over 3000 time instants and used for the statistical examination. The spatial statistics of the vortex locations are presented in terms of the probability density function (PDF) in figure 3.11 for the natural and the actuated shear layers. The PDF associated with the natural case demonstrates the majority of the vortices detected within the $x/\theta_0 = 30 - 40$ streamwsie locations. The vortex count increase with the downstream distance due to the roll-up and then drops due to the pairing. The subharmonic actuation does not demonstrate a major difference compared to the naturally evolving shear layer. On the other hand, the PDF is evidently shifted upstream for the shear layer actuated at the fundamental frequency. This observation reveals the advanced location of the KH roll-ups for the shear layers forced under the fundamental frequency. In addition, the total number of the vortices is found to increase by 21% due to the actuation of the fundamental mode. Since the KH roll-ups tend to occur towards the low speed side of the shear layer, the outcome is observed in the augmentation of the minor peak in the u_{RMS}. Moreover, the minor peak location is also advanced in accordance with the KH roll-ups.

The PDFs presented in figure 3.11b exhibit the traverse distribution of the vortex core locations within the range of the downstream locations in which the pairing is expected to happen according to the velocity spectra shown earlier. The PDFs associated with the actuation at the fundamental mode displays a flatness similar to that of the natural case. However, the PDF peak is shifted towards the low-speed side in accordance with increased KH roll-ups when forcing the shear layer at the fundamental frequency. Also,

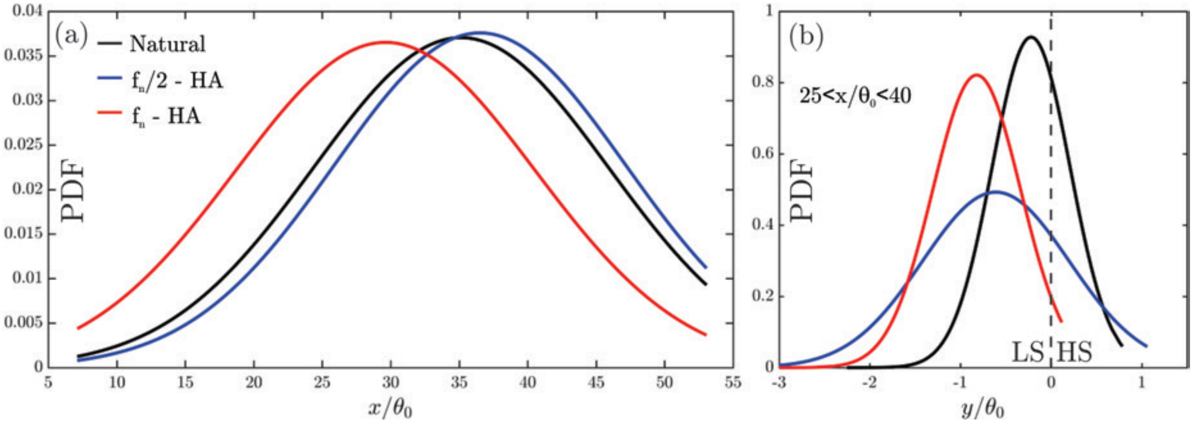

Figure 3.11: Probability density function (PDF) of the spatial statistics of the vortex core locations for the natural and actuated cases: (a) Streamwise distribution; (b) Traverse distribution within the $x/\theta_0 = 30 - 40$ streamwsie locations. The vortex core locations are detected using the Γ_2 criterion for the natural, fundamental (f_n), and subharmonic ($f_n/2$) actuations at the high amplitude (HA).

this PDF is clustered around its mean traverse location. On the other hand, actuation at the subharmonic mode generates a wider PDF where the vortex locations are more deviated from the mean and are more uniformly distributed in the traverse direction. The wider PDF under the subharmonic actuation is a sign of the shear layer expansion which is known to occur due to the vortex pairing [96]. Traverse statistics of the $f_n/2$ excitation case reveals occurrence of more vortex cores near both the high-speed and the low-speed sides compared to the fundamental mode actuation. This verifies our discussions in the instantaneous analysis of the vortex pairing. The upstream vortex is shifted towards the high-speed side during the merging and the major peak of the u_{RMS} is amplified. In contrast, the downstream vortex is shifted towards the low-speed side and the minor peak of the u_{RMS} is augmented. Even though both of the u_{RMS} peaks are affected, the peak on the high-speed side is more strongly intensified. It should also be noted that the total number of the vortices drops by 23% when the shear layer is actuated at the subharmonic mode. This signifies the vortex pairing enhancement when forcing the flow under the subharmonic mode.

As discussed, the vorticity field provides a realistic visualization of the shear layer elongated regions, accumulated rotating vortex roll-ups as well as the pairing phenomenon [40, 99, 100]. However, it would be more beneficial to distinguish between the shear/rotation regions and correlate them with the vorticity distribution. Spatio-temporal formation/advection

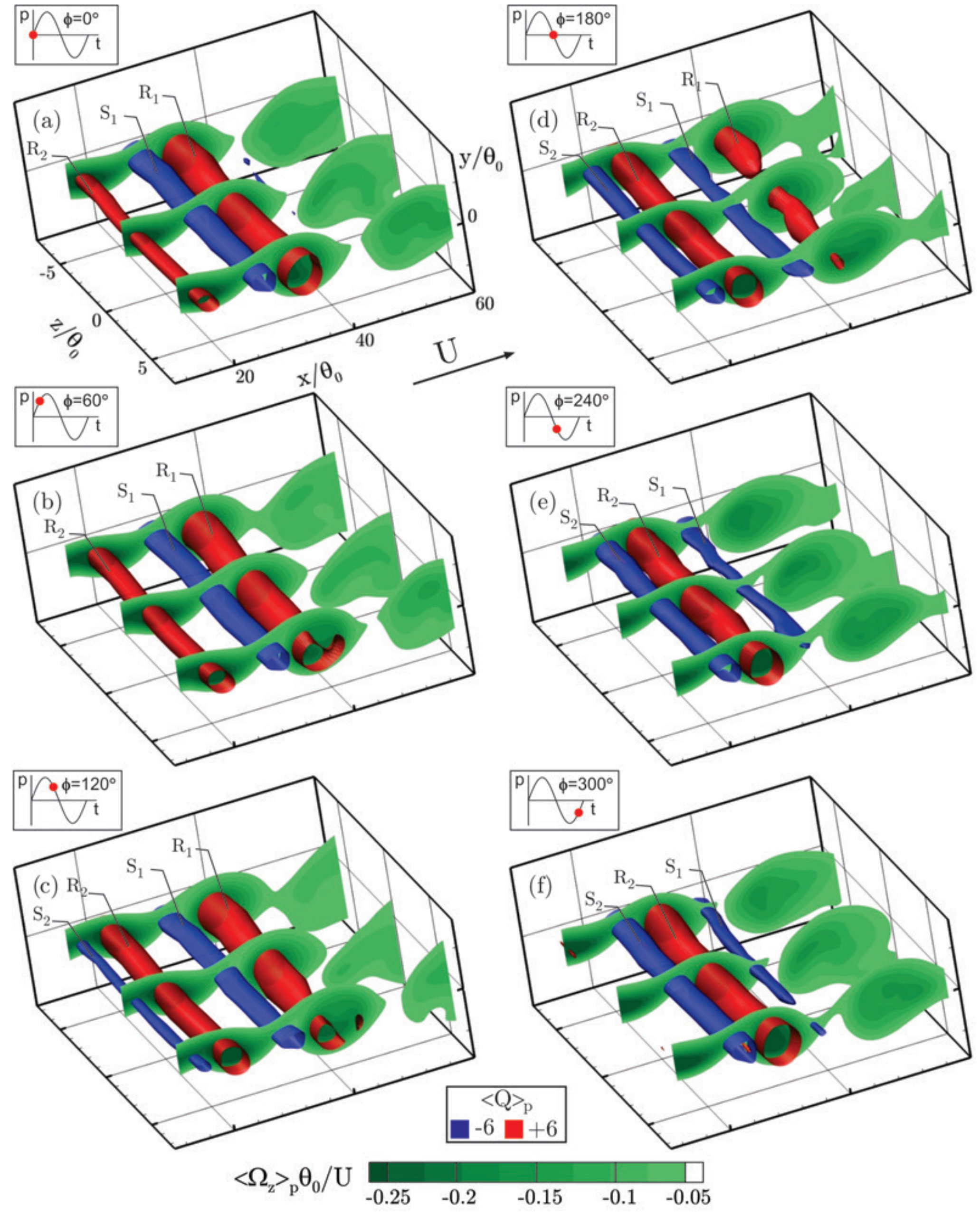

Figure 3.12: Volumetric topologies of the shear/rotation loops from the phase-locked PIV measurements. Instantaneous phases ($\phi = 0^o$, 60^o, 120^o, 180^o, 240^o, 300^o) of the shear (blue) and rotation (red) loops of the $< Q >_p$-criterion passed through the vorticity cut-planes (green) at for the fundamental actuation at high amplitude (f_n-HA).

of the distinguished shear(blue)/rotation(red) loops are animated in figure 3.12. After conducting the phase-locked PIV measurements in multiple planar fields of view, the three-dimensional topologies are obtained by interpolating the FOVs into the volumetric information. The resulting $< Q >_p$-criterion obtained for the high-amplitude actuation of the fundamental mode, during the period of the acoustic excitation, are presented at the phases $\phi = 0^o, 60^o, 120^o, 180^o, 240^o, 300^o$. The rotation loops are formed near the separation edge, entrain the ambient fluid and grow in time/space due to the viscous diffusion while convecting downstream. The shear loops are identified with the shear layer thinning in the stretched vorticity zones while the rotating loops intersect with the expansion/accumulation in the vorticity cut-planes. The first rotating loop (R_1) is followed by the shear loop (S_1) and the second vortex loop (R_2) during the phases $\phi = 0^o - 60^o$. During $\phi = 120^o - 180^o$, the shear loop S_2 enters the domain while the previous loops are advected farther downstream and grown in radius. The rotation core R_1 exits the domain during $\phi = 240^o - 300^o$ and the expected phase $\phi = 360^o$ to complete a cycle is equivalent to $\phi = 0^o$.

The radial expansion of the vortex cores with the downstream distance is due to the influence of the friction, through the viscous diffusion process in the vorticity field. Initially, when the vorticity is accumulated in the vortex core, it is subjected to high gradients. At the presence of such high vorticity gradients, the viscous diffusion effects are stronger. As a result, while conserving the total vorticity, its region of effectiveness is expanded. Accordingly, the strength of the vortex core is gradually diminished as the vorticity field becomes smooth (diffused). It should be noted that with the appearance of the small scales, the viscous diffusion occurs at smaller time scales and hence the dissipation dominates. Another important aspect of the viscous diffusion phenomenon is its indirect effect on the velocity at which the rotating vortex cores travel downstream. The first component of this velocity is due to its translation with the mean flow. The second component is due to the self-induced velocity of the rotating vortex core [41]. For any spot on a long vortex tube, the self-induced velocity is proportional to the local curvature of the tube, the inverse of the core radius and the local circulation. The vortex tubes presented in our region of interest, appear as rather straight cylinders and hence the curvature effect can be neglected. However, the core radius grows in time/space due to the viscous diffusion process discussed above. This results in the smaller self-induced velocity of the vortex tubes located farther downstream. Consequently, the faster moving vortices located more upstream, may catch up with the decelerated downstream vortex tubes. Under certain scenarios, this process results in the merging of the two tubes [72, 73]. It should be noted that this process known as the vortex pairing occurs only when the two vortex cores have the same sense of rotation.

3.4 Summary

Hot-wire (HW) anemometry and particle image velocimetry (PIV) results are presented within the near separation region of the naturally developing shear layers as well as the acoustically actuated flows. Selected out of a wider range of measurements, Reynolds number effects are presented for $Re_{\theta_0} = 85, 135, 276, 470, 616, 713, 780, 860, 945$. The focus is to better understand the shear/rotation competition throughout the initial Kelvin-Helmholtz (KH) roll-ups and the subsequent vortex pairing. In addition to the well-known high-speed (HS) side major peak in the RMS of the streamwise velocity fluctuations (u_{RMS}), a second minor peak may appear with a tendency towards the low-speed (LS) side of the shear layer. The minor peak appears as long as $276 \leq Re_{\theta_0} \leq 860$, and vanishes otherwise. Also, the minor peak starts to form at a certain streamwise location, grow and eventually decay with the downstream distance. Moreover, when introducing the grid-induced turbulence, the incoming boundary layer transitions from the laminar (shape factor: $H = 2.58$) to turbulent ($H = 1.5$). Accordingly, the case with the double-peaking in (u_{RMS}) transitions into a single one.

This transitioning character of the double-peaking phenomenon with the Reynolds number, the downstream distance and the upstream grid-induced turbulence is found correlated with the time-averaged shear/rotation distribution obtained by the $< Q >$ criterion. This evolution of the double-peaking is found co-occurred with the distribution of the $< Q >$, such that the small scale intermingled patches of the shear/rotation spots are observed for the cases with the single major peak in (u_{RMS}). On the other hand, the shear/rotation spots are not scattered at the presence of the double-peaks. Instead, they describe two distinguished layers (ribbons) of shear (towards the LS side) and rotation (towards the HS side). Within this layered region, the minor peak in the u_{RMS} nicely coincides with a shear-characterizing peak in the profiles of the time-averaged $< Q >$ criterion. Moreover, the upstream grid-induced turbulence transitions the separation edge boundary layer from laminar to turbulent, promotes the sporadic shear/rotation pattern and the minor peak vanishes.

The HW-based spectra of the streamwise velocity fluctuations and the PIV-based spatial theory of the linear stability (LST) identify the fundamental (f_n) and its subharmonic ($f_n/2$) mode in the naturally developing shear layer. The shear layer is then forced acoustically by the corresponding frequencies at low (LA), medium (MA) and high (HA) amplitudes. The fundamental mode which is formed due to the KH instability interacts with its subharmonic through the vortex pairing mechanism. The amplification factor (N-factor) saturates to its critical value and undergoes earlier transitions as the effect of the non-linear perturbations grow earlier. The linear region of the N-factor associated with the naturally developing shear layers, shows a larger slope under the actuation of the fundamental mode when compared to the subharmonic forcing. The fundamental mode is found predominant in the near-separation region and the subharmonic prevails with the downstream where the vortex pairing takes place. Accordingly, the fundamental to the subharmonic growth rate ratio becomes lower than unity at certain streamwise locations found coincident with the saturation point of the N-factor, i.e., the subharmonic effects become dominant.

Using a four-arrow arrangement characterising the peripheral fluctuations of the vortex core, the shear/rotation regions are coupled and the corresponding phase-reversal is described. Under the actuation of the fundamental mode, the streamwise locations of the first KH roll-ups are advanced. Due to the tendency of the roll-ups towards the low-speed side, the minor peak leaning towards the same side, is augmented and appears earlier. In addition, the count of the vortex cores demonstrates a 21% increase when actuating the flow at $f_n - HA$. On the other hand, the subharmonic forcing is found to reduce the vortex count by 23% which indicates the enhanced vortex pairing. During the vortex pairing, the accelerated upstream rotating core and the decelerated downstream vortex tend to shift towards the high-speed and the low-speed sides, respectively. Therefore, the subharmonic forcing expands the lateral span of the shear layer, the u_{RMS} profile and the vortex core traverse distribution. Moreover, both the u_{RMS} peaks are augmented and the major one located towards the high-speed side is more strongly influenced. Finally, the spatio-temporal advection of the three-dimensional topologies of the shear/rotation loops are monitored at different instantaneous phases. After separating from the edge, the structures grow in time/space due to the viscous diffusion. Subsequent to this radial growth, the vortices located farther downstream attain a smaller self-induced velocity compared to the upstream rotating cores. The shear loops are found correlated with the shear layer thinning in the stretched (elongated) vorticity zones. On the other hand, the rotating vortex loops pass through the expansion regions in the accumulated vorticity fields.

Chapter 4

Curvature-induced vortex dynamics and jet characterization at the exit of a rectangular duct

In this chapter, hot-wire (HW) anemometry and particle image velocimetry (PIV) results are provided to explain the flow structure in rectangular jets with a focus on the curvature-induced vortex dynamics. The chapter content is reprinted with permission from Journal of Fluid Mechanics [49]:

Abbas Ghasemi, Burak Ahmet Tuna, and Xianguo Li. Curvature-induced deformations of the vortex rings generated at the exit of a rectangular duct. Journal of Fluid Mechanics, 864:141180, 2019.

4.1 Introduction

Jet flows are an important member of the shear flow family [1, 9, 10, 11]. Whether originated from axisymmetric or nonaxisymmetric nozzles or orifices, they have both fundamental and practical significance with rich flow phenomena [19, 20, 13, 47]. They are extensively involved in applications associated with mixing, heating/cooling, cleaning and combustion, etc., and require proper implementation of the passive/active control strategies to suit the needs of the particular applications. One of the efficient passive control mechanisms is to issue the jet from the non-circular openings of different shapes. Non-circular jets are practically beneficial due to their enhanced mixing, improved heat/mass transfer, and the regulated noise levels [22, 24, 23]; their different and richer dynamics also improve and expand our fundamental understanding of the mechanisms behind jet flows [25].

The non-circular jets have their near flow field to the developing regions dynamics that are dominated by the three-dimensional perturbations arising from the so-called axis-switching phenomenon. Axis-switching represents the shape change of the non-circular jets as the cross section visually appears to rotate with the downstream distance. However, this conventional reference to axis-switching as a rotational phenomenon should be replaced by the cross-sectional evolution towards more round shapes farther downstream. This phenomenon is initiated by the dynamics of the non-circular vortex rings shedding and their evolutions, and results in the cross-sectional deformations and the increased level of complexity compared to the axisymmetric shear layers [28]. Changing the nozzle shape produces different jet flow dynamics, which are often implemented to passively control the jet flows [27]. Further, axis-switching is also influenced by the inlet flow conditions such as the momentum thickness, the turbulence level and the Reynolds number [26, 29, 30]. In the far field (developed region), the non-circular jets evolve towards the more axisymmetric cross sections, in a way similar to that of the circular jets.

Due to the increased near-field three-dimensionality, the non-circular jets develop a wider near-field and have a larger spread rate compared to their round counterparts [35, 32]. As a result, the non-circular jets entrain more ambient fluid into the jet core, enhancing the fluid mixing process [31, 32, 33, 34]. Further, the non-circular jets experience increased instantaneous lateral oscillations involving axis-switching phenomenon [36], leading to the occurrence of off-center peaks in the time-averaged streamwise velocity profiles [35, 37]. This is uncommon for circular jets (unless due to the vena contracta effect [39]). Similarly, the high aspect ratio rectangular jets are known to demonstrate the saddle-back distribution of the time-averaged velocity [38]. It is inferred that the time-averaged analysis of the non-circular jets, mainly reflects the outcomes of the axis-switching rather than describing the underlying physics. In order to identify the governing mechanisms associated with the observed phenomena, the instantaneous vortex dynamics should be explored.

The Kelvin-Helmholtz (KH) instability produces vortex rings shed from the jets, whether circular or non-circular cross sections [10, 12]. The dynamics and complexities of the vortex rings, however, are determined by the curvature of the rings imparted initially by the shape of the nozzle [26]. The circular vortex rings have a uniform radius of curvature, the sharp corners of the rectangular/square rings attain a higher local curvature relative to their flat sides. The vortex rings travel with the advection velocity of the main flow, which is almost the same for the entire vortex rings, plus the additional self-induced velocity, which varies locally on the vortex rings, hence responsible for the deformation and rich dynamics of the rings [26].

The additional self-induced velocity on the vortex rings is, based on the Biot-Savart Law (see Appendix A), proportional to the local curvature of the ring, the inverse of the vortex core radius and the vortex circulation [40, 41, 42]; and hence it is higher near the high-curvature (sharp) regions of the non-circular vortex rings. As a result, the orientation of the non-circular vortex rings appears to be rotating around their streamwise axis [12, 43, 42]. This is however merely a visual impression caused by the fascinating three-dimensionality of the ring deformations [12, 28]. The curvature-induced vortex ring deformations initiate the axis-switching in the near field, and the interactions among the streamwise rib-shaped vortex loops, the corner hairpin vortices and the primary KH rings dominate the subsequent downstream dynamics [28, 26]. The axis-switching phenomenon may be amplified or prevented by the upstream conditions, through changes in the formation of the streamwise vorticity [101, 102]. Consequently, single or multiple switching may take place until the ring attains a rather symmetric geometry and/or eventually breaks down into smaller scales.

In addition to the mechanism of the self-induced velocity, the axis-switching of the non-circular jets is theoretically related to the pressure distribution [44]. Three instability modes for the pressure perturbations have been identified in rectangular jets [45], the first and the third modes relate to the pressure fluctuations at the corners while the second governs the central region and is dominant over the other two modes with increasing downstream distance. Large eddy simulation (LES) study by [28] indicates that the corner pressure perturbations propagate towards the central region, and deform the initially 2-D ring into a 3-D shape; then after the axis-switching, flatten the ring and recover its 2-D character. These perturbation mechanisms are responsible for the enhanced small-scale entrainment, while the axis-switching for the enhanced large-scale entrainment of the rectangular jets [46, 12].

It is clear from the preceding literature review that the axis-switching in non-circular jets is useful for the enhanced entrainment and noise control. However, majority of the experimental studies are described in terms of the time-averaged flow features, while some numerical simulations have attempted to explore the underlying physics by characterizing the instantaneous vortex dynamics [46, 26, 12, 28]. Capturing/quantifying the self-induced (curvature-induced) velocities experimentally is required to correlate them with the spatio-temporal dynamics of the vortical structures in the non-circular jet flows. Therefore, the objective of the present study is to experimentally quantify the self-induced velocities due to the curvature variations on the vortex rings generated during the axis-switching of a rectangular jet, with and without acoustic excitation. Phase-locked and conventional particle image velocimetry (PIV) measurements are conducted for a rectangular jet of aspect ratio 2 at the Reynolds number $Re = UD_\mathrm{h}/\nu = 17,750$ where U, D_h, and ν denote the centerline velocity at the nozzle exit, the hydraulic diameter and the kinematic viscosity. This condition is selected for in-depth characterization in the present study, because our recent study [48] investigated a wide range of flow conditions, equivalent to the Reynolds number of 1,775 to 71,000, for double-peaking phenomena of the turbulence intensity in shear layers via competition between fluid rotation and shearing; during that study it is noticed that at this flow condition, rich dynamic phenomena exist with relation to the curvature-induced velocities around the sharp corners of the rectangular rings. For active control, the flow is also acoustically actuated at the fundamental and subharmonic modes associated with the naturally evolving jet for different amplitudes. Acoustic control of the vortex ring generation, advection, self-induced deformations, and the axis-switching are explored by the spatio-temporal tracking of the three-dimensional vortex structures.

4.2 Experimental setup and measurement procedure

4.2.1 Air flow tunnel

Measurements are carried out at the outlet of the air flow tunnel shown in figure 4.1a. The blower fan forces the air flow through the circular inlet which transitions into a rectangular cross-section. The air is then passed through the diffuser section. The conditioning section displays the space in which the honeycomb insert and a set of three wire screens are placed. After the $9:1$ smooth contraction region which reduces the turbulence intensity to less than 0.9% and a mean flow uniformity within 0.25% inside the inviscid core, the air flow passes through the $L = 300$ mm duct and exits into the jet region from the rectangular opening with the dimensions of the side length $a = 20$ mm by the top edge $b = 40$ mm (figure 4.1b). At the exit of the duct, the centreline velocity is maintained at $U = 10$ m/s corresponding to the Reynolds number $Re = UD_\mathrm{h}/\nu = 17,750$ where $D_\mathrm{h} = 26.67$ mm is the hydraulic diameter.

It is important to mention the boundary layer characteristics at the separation edge. As shown in figure 4.2a in the side view (SV: $z/a = 0$) plane, the measured velocity matches the Blasius profile with the shape factor $H = \frac{\delta^*}{\theta} = 2.59$ where δ^* and θ denote displacement and momentum thickness, respectively. The boundary layer velocity at the exit of the duct is characterized as laminar flow. The corresponding root mean squared (RMS) of the streamwise inlet velocity fluctuations is given in figure 4.2b. It can be seen that the centreline turbulence intensity is less than 0.02 with a peak value of nearly 0.08 in the boundary layer which decays near the wall region.

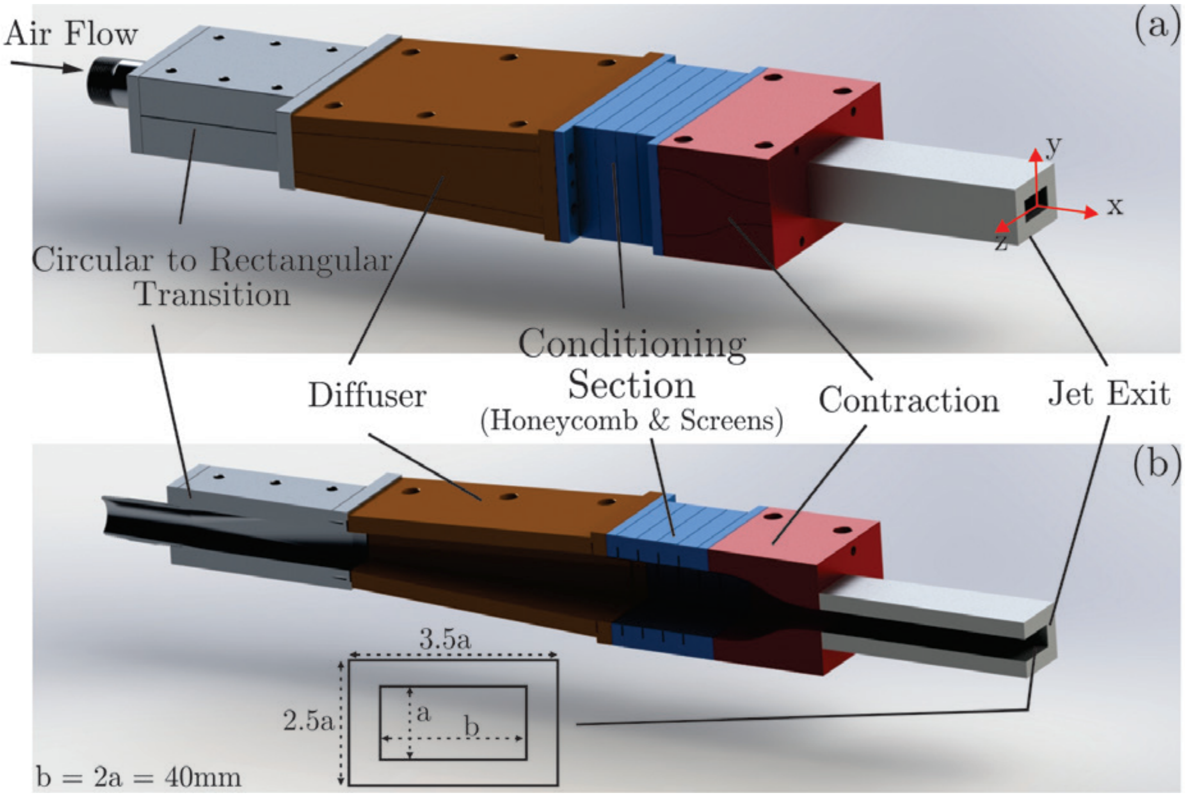

Figure 4.1: Air flow tunnel for producing the rectangular jet: The blower fan forces the air flow through the circular inlet which transitions into the rectangular cross-section. The air is then passed through the diffuser section. The conditioning section displays the space in which the honeycomb insert and a set of three wire screens are placed. After the 9 : 1 smooth contraction region, the air flow passes through the $L = 300$ mm duct and exits to the jet region from the rectangular opening with the dimensions of the side length $a = 20$ mm by the top edge $b = 40$ mm.

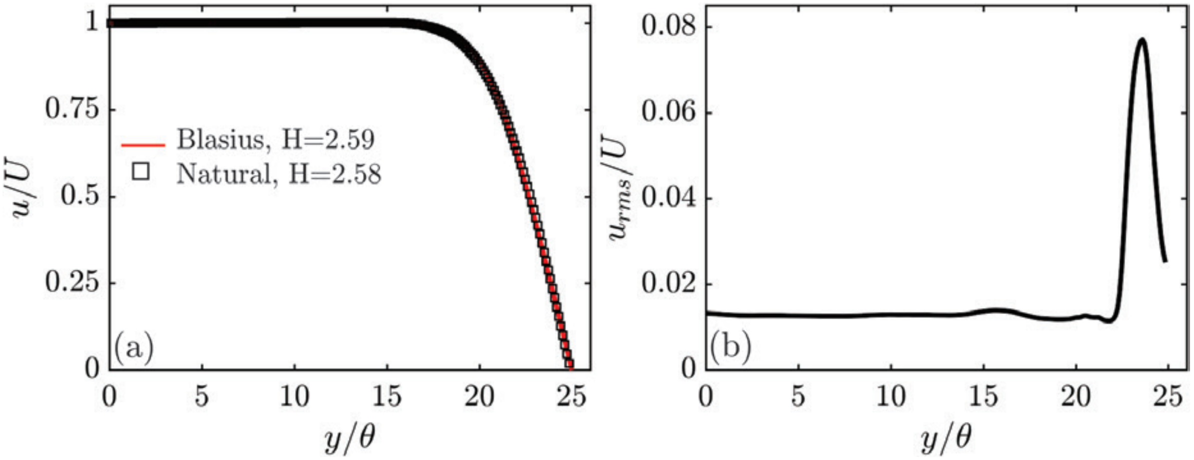

Figure 4.2: Boundary layer at the separation edge in the side view (SV: $z/a = 0$) plane of the naturally developing jet: (a) The measured velocity (u/U) matching the Blasius profile characterizes the laminar flow with the shape factor $H = \frac{\delta^*}{\theta} = 2.59$ where δ^* and θ denote the displacement and momentum thickness, respectively. (b) Streamwise turbulence intensity (u_{rms}/U).

4.2.2 Hot-wire (HW) anemometry and particle image velocimetry (PIV)

First, the hot-wire (HW) anemometry is conducted using an automatically traversed single probe oriented normal to the flow direction. A Dantec 55P11 straight general-purpose probe connected to a Dantec Streamline Constant Temperature Anemometry system is utilized to carry out the measurements. HW data are sampled at a 16 kHz frequency producing a total number of $524,288$ samples for the time period of 32.8 seconds. Spectral analysis is conducted for the fluctuating velocity obtained from the HW at a frequency resolution of 0.03 Hz. After the HW, planar particle image velocimetry (PIV) is conducted with the origin of the coordinate system fixed at the channel exit $(x, y, z) = (0, 0, 0)$ in the centroid of the rectangular exit cross-section in the $y - z$ plane. The x-axis is oriented along the streamwise direction while the y and z axes stand normal to the longer ($b = 40$ mm) and shorter walls of the duct ($a = 20$ mm), respectively (figure 4.3). The main components of the system consist of a dual pulsed Nd:YAG laser producing an output of up to 70 mJ/pulse, a $1,600 \times 1,200$ pixel 14-bit Imager Pro X 2M CCD camera, and a programmable timing system. The laser beam is generated by the combination of the cylindrical and spherical lenses. The laser beam light sheet thickness at its waist is in the

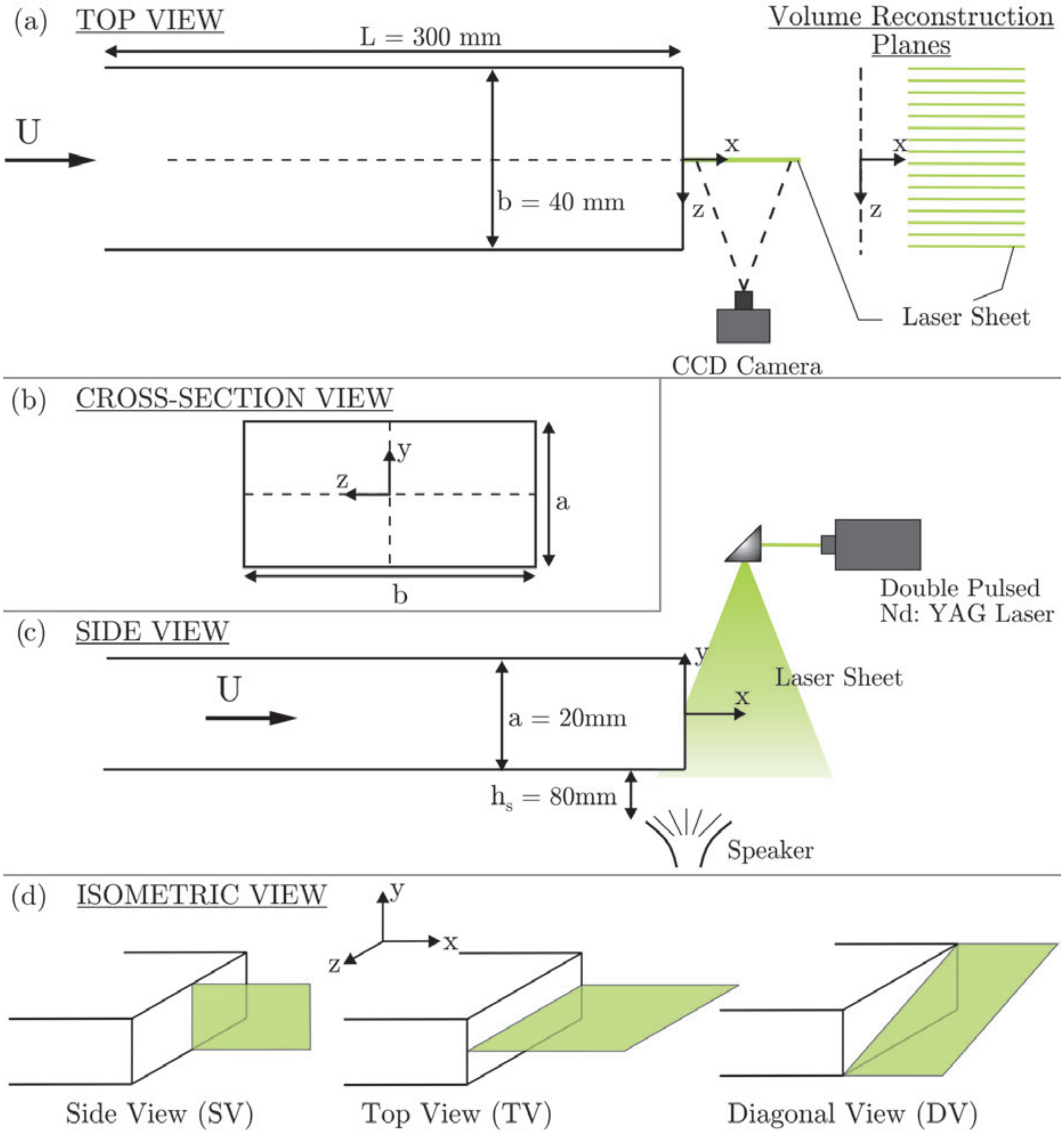

Figure 4.3: Experimental set-up for the PIV measurements in: (a) Top; (b) Side; (c) Cross-section; (d) Isometric views of the rectangular duct with the relative positioning of the camera, laser and the speaker. Sample mid-planes are illustrated for the top view (TV: $y/a = 0$) or the $x - z$ plane, the side view (SV: $z/a = 0$) or the $x - y$ plane and the diagonal view (DV: $y/z = 0.5$) or the $x - \zeta$ plane.

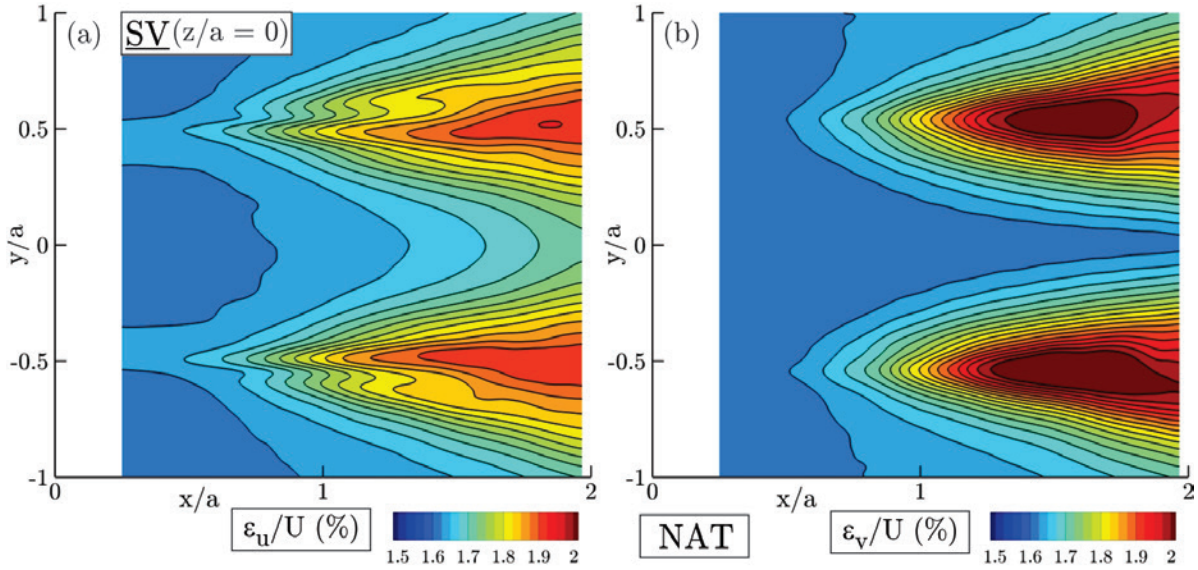

Figure 4.4: Spatial distribution of the uncertainties associated with the PIV measurements of the streamwise ($\varepsilon_{\mathrm{u}}/U$) and spanwise ($\varepsilon_{\mathrm{v}}/U$) velocity components in the side view (SV: $z/a = 0$) plane.

order of 1 mm.

The glycol-water based fog is produced to form the flow seeding particles at an average diameter of 3 μm. Care is taken to uniformly seed the flow at the outlet of the duct. The 60 mm fixed focal length lens and a 532 nm $\mp$ 10 nm band-pass filter are used along with the camera. The camera and the laser pulse are synchronized by a timing control system using the LaVisions DaVis 8 software. The camera/laser set-ups optimized for the field of view (FOV) are translated together by using a set of servo-driven traverses to obtain various locations/orientations desired for the PIV. Images acquired in multiple $x - y$ planes provide the side view (SV) information for two FOVs that are overlapped with 10% and then stitched at various z locations. Also, the $x - z$ planes capture the top view (TV) flow field for the two FOVs that are also overlapped with 10% and then stitched at different y locations. In addition, PIV measurements are conducted in a diagonal view (DV: $y/z = 0.5$) or the $x - \zeta$ plane to provide a complete set of time-averaged data associated with the three-dimensionality of the rectangular jet. Accordingly, the above information obtained at the planar FOV spacing of $0.05a$ are interpolated to reconstruct the phase-averaged, three-dimensional flow field by using the phase-locked PIV measurement technique [76].

The jet is acoustically excited by a sub-woofer which is located at the outlet and near the longer edge of the rectangular opening (near the $y/a = -0.5$ edge). It is oriented normal to the top view (TV) or the $x - z$ planes, as shown in figure 4.3c, and the acoustic waves are emitted in the y-axis direction. The sinusoidal excitation signal from the sub-woofer serves as a reference for the synchronised data acquisition in phase-locked PIV. The frequency/amplitude characteristics of the acoustic forcing signal are given in table B.1 with the detailed information given in Appendix B. It should be noted that sufficiently strong driving pressure (excitation amplitude) is required so that the flow behaviour (vortex shedding) synchronizes with the driving signal's frequency and results into robust phase-locking measurements. After cropping the camera sensor to 960×1200 pixels, each FOV for different views covers a 50×39 mm (SV), 50×39 mm (TV), 62×50 mm (DV) area. The velocity field calculations are conducted by cross-correlating pairs of successive images in LaVisions DaVis 8 software. An advanced multi-pass technique is adopted resulting in the initial and final correlation passes of the 64×64 pixels with the 50% overlap and the 24×24 pixels with the 75% overlap, respectively.

This also leads to the vector pitches of 0.246 mm(SV), 0.248 mm(TV) and 0.313 mm (DV) with the camera pixel scale factors of 24.4, 24.2 and 19.1 pixels/mm for the side, top, and diagonal views, respectively. Post-processing of the results are achieved by the universal outlier detection [74] and removal with vector replacement. Time-averaged quantities are obtained using the $1000, 1500, 2000, 2500$ and 3000 instantaneous image pairs acquired at a rate of 14.73 Hz, and the 2000 snapshot are found more than sufficient to provide the converged fields. The PIV random errors are estimated according to the particle image disparity method [75], resulting in the corresponding average uncertainties evaluated to be less than 2% within 95% confidence in the core region of the jet. The local distribution of the uncertainties associated with the PIV measurements corresponding to the streamwise ($\varepsilon_{\mathrm{u}}/U$) and spanwise ($\varepsilon_{\mathrm{v}}/U$) velocity components in the side view (SV: $z/a = 0$) plane are presented in figure 4.4. It can be seen that the higher uncertainty levels are evaluated within the shear layer region and found more significant for the spanwise ($\varepsilon_{\mathrm{v}}/U$) velocity components.

4.2.3 Characterization of the fundamental and subharmonic frequencies used for the acoustic excitation

As shown in figure 4.5, HW measurements of the streamwise velocity are used to obtain the spectra of the fluctuations at different locations of the naturally (NAT) evolving rectangular jet. The measurements points ($x/a = 1, 1.5, 2, 2.25, 2.75, 3.5, 5.5$ and 18.75) are located

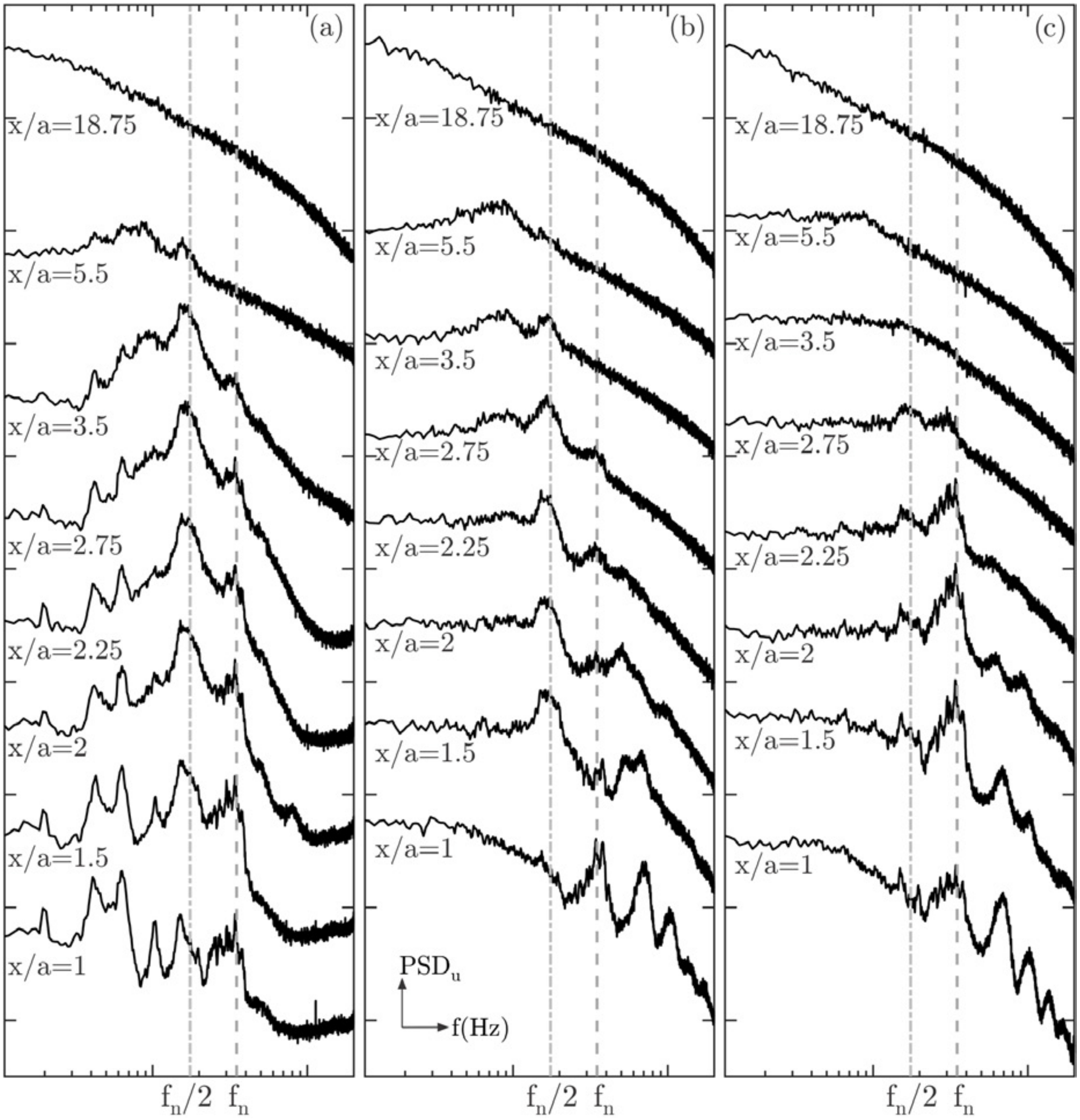

Figure 4.5: Streamwise velocity spectra obtained as the power spectral density (PSD) from the HW measurements along the three lines parallel to the x-axis for ($x/a = 1$, 1.5, 2, 2.25, 2.75, 3.5, 5.5 and 18.75): (a) Centreline (along the x-axis at $y/a = z/a = 0$); (b) Long edge (along the x-axis at $y/a = 0.5, z/a = 0$); (c) Short edge (along the x-axis at $y/a = 0, z/a = 1$)

along the three lines parallel to the x-axis as the centreline (along the x-axis at $y/a = z/a = 0$), the long edge line (along the x-axis at $y/a = 0.5, z/a = 0$) and the short edge line (along the x-axis at $y/a = 0, z/a = 1$). At $x/a = 1$, a broadband peak, typically seen in the near-field of the shear layers, characterizes the fundamental frequency ($f_\mathrm{n} = 350$ Hz). This fundamental mode, which is more distinguishable at the edges, is associated with the shear layer roll-up due to the initial KH instability.

The corresponding dimensionless frequency can be obtained in terms of the Strouhal number as $St_\mathrm{a} = f_\mathrm{n}a/U = 0.7$, or alternatively as $St_\mathrm{h} = f_\mathrm{n}D_\mathrm{h}/U = 0.93$ and $St_\mathrm{e} = f_\mathrm{n}D_\mathrm{e}/U = 1.12$ where D_h and D_e are the hydraulic and equivalent diameters, respectively. The corresponding values for D_h and D_e can be calculated using $D_\mathrm{h} = 4ab/(2(a+b))$ and $D_e = \sqrt{4ab/\pi}$). The Strouhal numbers presented here are larger than that of round jets ($0.3 - 0.7$) reported by [103, 9, 22]. They rather conform to the values observed by [46, 22] for rectangular jets. The higher dominant frequencies in rectangular jets suggest a more unstable near-field compared to circular jets, which can be attributed to the more complex vortex dynamics. Earlier studies on non-circular jets [22] report the shifting of the spectral dimensionless frequency (Strouhal number) of the fluctuations towards higher values. This suggests the increased presence of small scale perturbations. Axisymmetric vortex rings are formed in circular jets due to the low-frequency Kelvin-Helmholtz (KH) instability transitioning from the linear to the non-linear state. On the other hand, non-circular vortex rings experience additional modes of the high-frequency instability due to the azimuthal perturbations resulting from the curvature-induced instabilities.

The subharmonic mode ($f_\mathrm{n}/2 = 175$ Hz) is due to the vortex pairing farther downstream and modulates the initial KH instability through the feedback mechanism [104]. The non-linear effects first set in due to the transition of the initially linear KH instabilities. Afterwards, these non-linear trends are intensified during the vortex pairing which result in the appearance of the higher harmonic peaks in the spectra. The centreline spectra ($y/a = z/a = 0, x/a = 1 - 18.75$) portray both the f_n and $f_\mathrm{n}/2$ frequencies of comparable energy content where the subharmonic dominates with the downstream distance. The long ($y/a = 0.5, z/a = 0$) and short ($y/a = 0, z/a = 1$) edges initiate with a dominant f_n frequency as well as the higher harmonics and again the $f_\mathrm{n}/2$ frequency prevails in the downstream. The higher harmonics are mostly detectable near the edges where the shear layer is present, while the corresponding peaks are not strong in the centreline spectra. Beyond $x/a = 18.75$, there is no frequency preference and the jet approaches a fully-developed isotropic state. In this far-field region, small scales are ubiquitous and contribute to the enhanced mixing.

To verify the fundamental frequency (f_n) and its subharmonic ($f_\mathrm{n}/2$) mode obtained above from the HW measurements, linear stability (LST) analysis is conducted (see Ap-

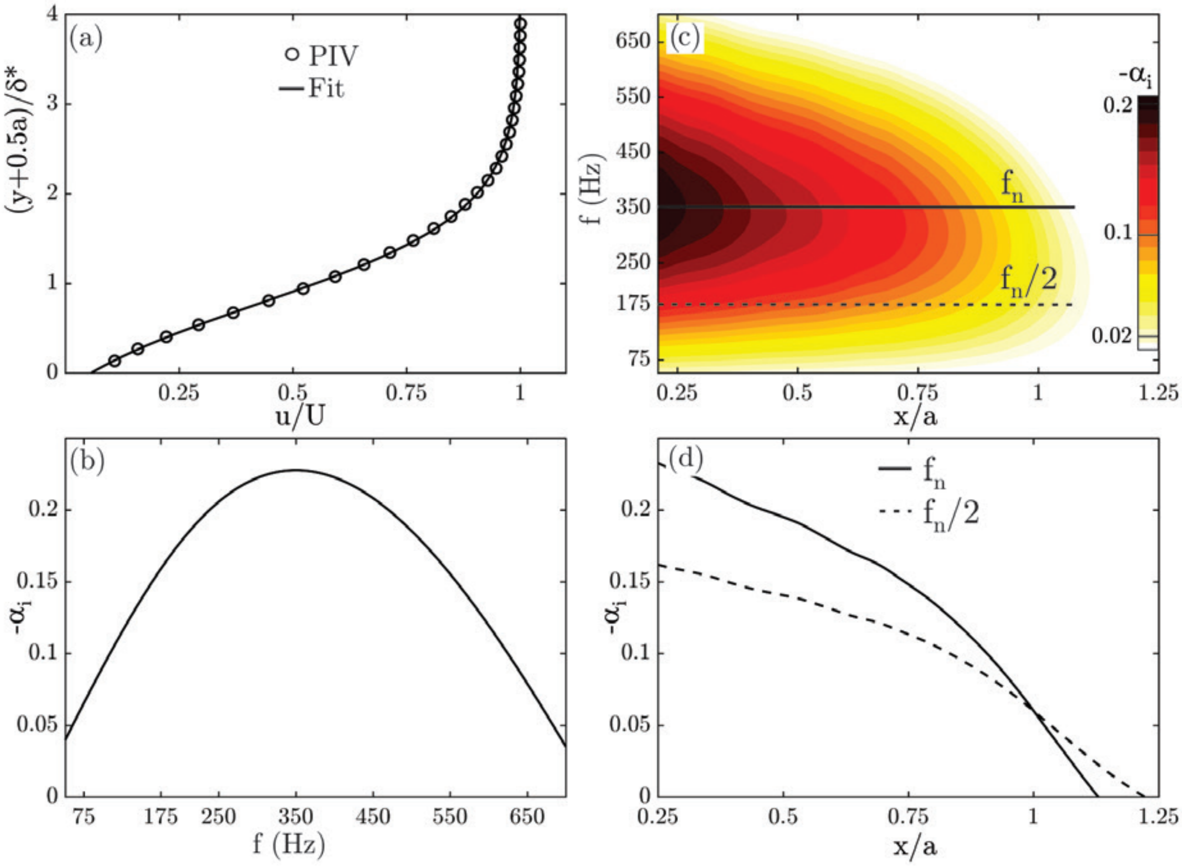

Figure 4.6: Spatial theory of the linear stability (LST) analysis obtained from the PIV: (a) Typical measured velocity profile vs. the data fit at a given arbitrary axial location (for $0.25 < x/a < 1.25$) and (b) its corresponding growth rate ($-\alpha_\mathrm{i}$) characterizing the fundamental frequency ($f_\mathrm{n} = 350$) Hz; (c) Streamwise distribution of the growth rates associated with the different perturbation frequencies; (d) Streamwise variation of the growth rates associated with the fundamental (f_n) mode and its subharmonic ($f_\mathrm{n}/2$) frequency.

pendix C for details). According to the hydrodynamic theory of stability, shear layers can be described by the interaction of the ensemble of propagating instability waves [83, 84, 85]. The amplitudes corresponding to individual propagating instability modes, the wave lengths of which characterize the length scale of a particular flow structure, may amplify/fade while evolving in time/space. Such an interpretation becomes convenient by analysing the flow in the Fourier space rather than in the physical time/space. The present spatial LST predictions allow the perturbations to grow/decay in space and only advect in time without amplification/damping.

To this end, the method of the least squares is implemented for the curve fitting [86] of the velocity profiles obtained from the PIV with a typical representation shown in figure 4.6a. It should be noted that the panel (a) of the figure 4.6 is just an arbitrary velocity profile obtained from PIV to demonstrate how the curve-fitting is carried out. The velocity profiles are fitted to a hyperbolic tangent (Tanh) which is the commonly used function in the spatial LST analysis [87]. The Orr-Sommerfeld equation derived from introducing the normal mode perturbations to the linearised incompressible Navier-Stokes equations [88] is then solved by implementing the Chebyshev polynomials for the spectral approximation of the eigen-functions. The spatial LST provides the corresponding growth rates ($-\alpha_{\mathrm{i}}$) associated with a range of frequencies. For instance, the typical growth rate profile corresponding to the arbitrary velocity in figure 4.6a is presented in figure 4.6b. Afterwards, panel (c) of the figure 4.6 incorporates all the velocity profiles at several streamwise locations within the PIV field of view to obtain the colour map of the growth rates associated with the different frequencies as they change with the downstream distance. The planar PIV data used for the LST calculations are taken in the near-exit region of the side view (SV) plane to verify the fundamental and sub-harmonic modes obtained from the HW.

The growth rate associated with the fundamental frequency ($f_{\mathrm{n}} = 350$ Hz) is found dominant (figure 4.6b) for this particular location. Similar information is reproduced for all the streamwise locations and presented as a contour plot in figure 4.6c. The near-exit colourmap shows that the strength of the fundamental mode shifts towards lower frequencies with the downstream distance and fades eventually. Beyond certain downstream locations where the non-linear perturbations set in the linear assumption deteriorates. For a direct comparison, the streamwise variation of the growth rates identifying the fundamental (f_{n}) mode and its subharmonic ($f_{\mathrm{n}}/2$) are presented in figure 4.6d. The fundamental mode is dominant in the near-exit region where the KH instabilities tend to roll-up the shear layer. With increased downstream distance, the subharmonic effects dominate as the local passage frequency of the vortices are reduced due to the smaller self-induced velocity of the vortices. Care must be taken when discussing the subharmonic frequency in the context of the linear stability theory. The subharmonic frequency appears because of vortex pairing, which is a nonlinear mechanism. This is inferred from our streamwise velocity spectra obtained as the power spectral density (PSD) from HW measurements. Even though such a similar conclusion may not be directly drawn from the linear theory of stability, some underlying physics can be justified. The vortex pairing phenomenon occurs due to the deceleration of the vortex as a result of the smaller self-induced velocities associated with the larger core radius. Consequently, the upstream vortices which move faster may catch up with the downstream cores. Even before the pairing occurs, the reduced velocity of the vortices with the downstream distance reduces their passage frequency. This may explain why the LST results reveal the shifting towards the lower frequencies with the downstream distance even before the linear assumption deteriorates.

The modes f_n and $f_\mathrm{n}/2$, respectively referred to as the high (HF) and low(LF) frequencies, are used to acoustically force the jet at low (LA), mid (MA) and high (HA) amplitudes. The characteristics of the excitation amplitudes and the corresponding sound pressure levels (SPL) are presented in table B.1 with the detailed descriptions given in Appendix B. The objective is to specify a reference signal for the phase-locked PIV measurement as well as investigating the effect of the acoustic excitation on the jet characteristics. For instance, the jet excited at the f_n frequency and mid-amplitude is referred to as HFMA. The natural/unperturbed case (NAT) is characterized by the sound pressure level (SPL) of 76.3 and 91.2 dB at the center of the channel exit when the tunnel air flow is OFF or ON, respectively. The effect of the acoustic excitation is characterized as 79.1 dB (LA), 88.1 dB (MA), and 95.5 dB (HA) at the same location when the tunnel air flow is OFF. Based on these, each case can be described as shown in table B.1 by adding the free stream SPL to the acoustic excitation level (see Appendix B for details).

4.3 Results and discussion

First, the qualitative representation of the rectangular jet cross-sectional evolution is described as an overview of the overall flow behaviour. Afterwards, the flow characteristics obtained from the point-wise HW and the planar PIV measurements are presented to provide interpretations for the time-averaged behaviours resulting from the axis-switching as well as the acoustic forcing. Finally, the three-dimensional vortex dynamics are focused on the identification of the curvature-induced velocity of the vortex rings to shed more light on the instantaneous dynamics causing the time-averaged observations.

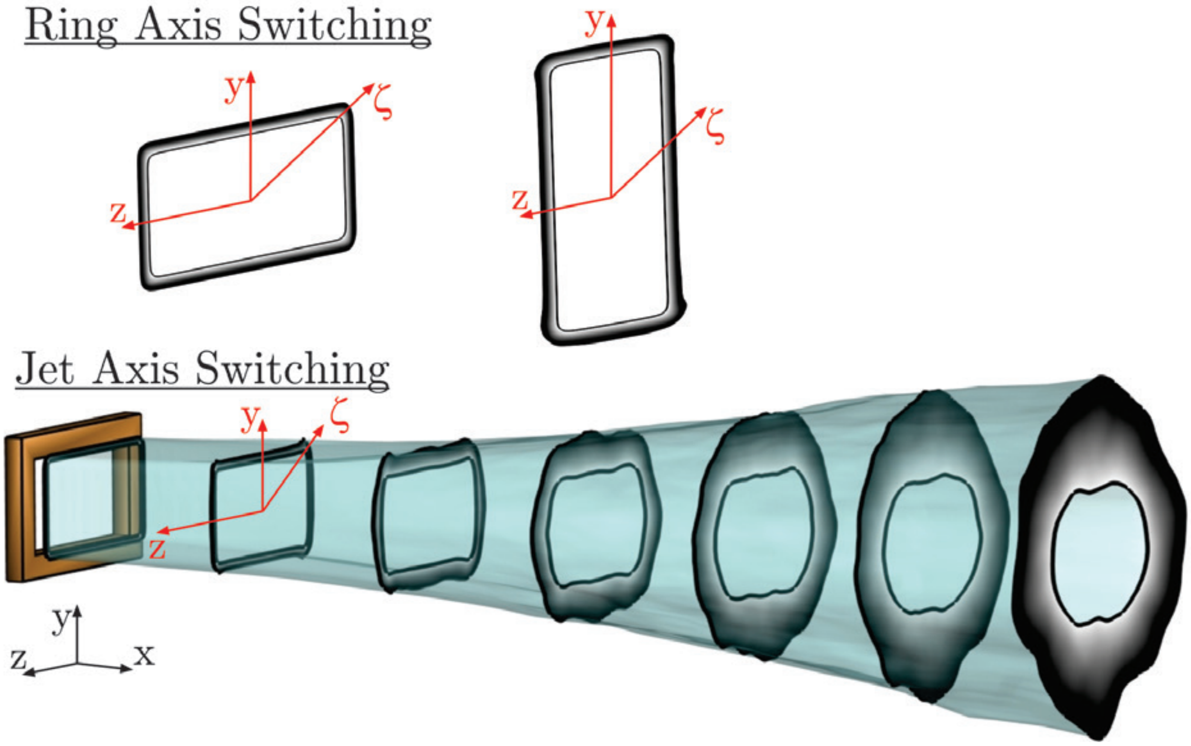

Figure 4.7: Schematic definition of the axis-switching in isolated vortex rings versus rectangular jets. For isolated rectangular vortex rings, axis-switching is accomplished when the ring appears to be rotated for 90^o around its streamwise axis, while the initial rectangular shear layer of the jet may mildly reshape towards the rounder cross-sections.

4.3.1 Qualitative description of the axis-switching in rectangular jets and isolated vortex rings

Before presenting the actual data, Figure 4.7 provides a schematic description of the differences between the "axis-switching" of rectangular jets and isolated vortex rings. Even though the present study is focused on rectangular jets and not the isolated vortex rings, it is important to define the axis-switching phenomenon for both cases and explain the differences. While the cause of axis-switching for both cases is the self-induced vortex ring deformations, the outcomes are different for isolated rings and continuous jets. For isolated rectangular vortex rings, axis-switching is traditionally defined when the ring rotates for 90^o around its streamwise axis. We emphasize that this is merely a visual observation, hence the present study suggests that a definition based on the deformation/reshaping is more appropriate. On the other hand, neighbouring vortex rings interacting within the initially rectangular shear layers (jets) do not demonstrate this apparent 90^o rotation. Instead, the diagonal width contracts while the SV and TV planes mildly expand at different rates and result in the cross-sectional reshaping from rectangular to the more round geometries.

The phase-averaged streamwise velocity displayed in figure 6.4, qualitatively describes the cross-sectional evolution of the rectangular jet. The cross-sectional planes are obtained from the interpolation of the phase-locked measurements in multiple side view (SV) planes. The first observation is the rectangular cross-section of the jet in the near-field at $x/a = 0.7$. The edges show a slower velocity as they are subjected to the low speed ambient, while the central region forms the high velocity potential core. Farther downstream at $x/a = 1.5$, the jet boundaries become more distorted. While the SV $x - y$ plane expands with the downstream distance, the diagonal (DV) span shrinks. Eventually at $x/a = 3.9$, the jet cross-section evolves into rather elliptic/circular shapes due to the axis-switching. The relevant underlying physics governing the axis-switching phenomenon are described in the following sections by exploring the spatio-temporal vortex dynamics. It should be noted that the shifted high-velocity region at $x/a = 1.5$ and 2.3 are due to the directional effect of the acoustic excitation on the tilting of the vortex rings as discussed later in figures 4.16 and 4.17. In addition, beyond $x/a = 3.1$ the jet core starts to bifurcate into the pair of high-speed zones which are commonly observed in elliptic [105] and rectangula [12] jets.

4.3.2 Jet evolution along the centreline and the higher order moments

In figure 4.9, HW data are presented along the jet centreline ($y/a = z/a = 0$) for different acoustic excitations (LFLA, LFHA, HFLA, HFMA HFHA, NAT). The shaded band regions

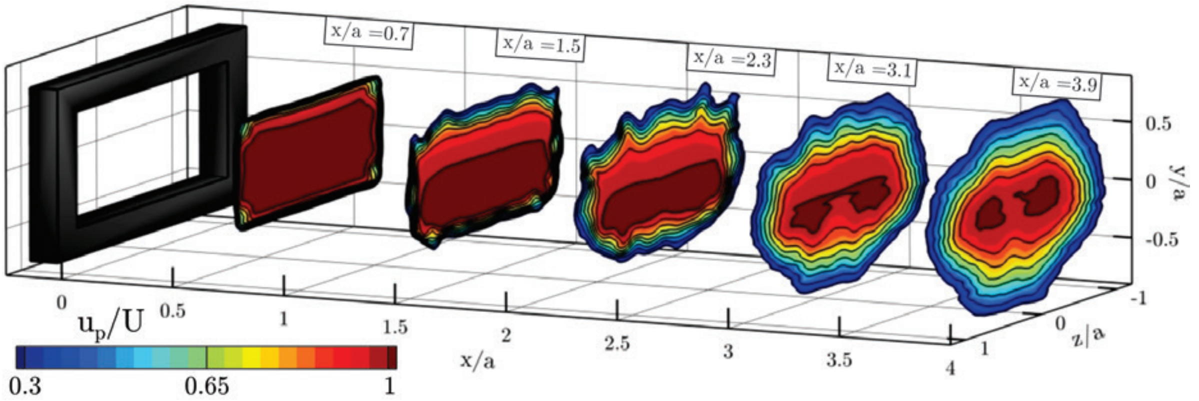

Figure 4.8: Phase-averaged streamwise velocity in the cross-sectional views ($y - z$ planes at $x/a = 0.7,\ 1.5,\ 2.3,\ 3.1,\ 3.9$) of the rectangular jet acoustically actuated at the high-frequency and high-amplitude (HFHA).

overlaid on the line plots are associated with the uncertainty levels of the HW. As seen in figure 4.9a, the time-averaged streamwise velocity decays (when $u/U < 0.98$) after the potential (unmixed) core $x/a = 2.5 - 3$ (or $x/D_\mathrm{h} = 1.9 - 2.25$). Similar to the non-circular jets of different shapes ($x/D_\mathrm{h} = 1 - 3.5$), the present rectangular jet develops a shorter potential core compared to the round jets issued from the smooth contraction nozzles ($x/D_\mathrm{h} = 5.5$) and orifice plates ($x/D_\mathrm{h} = 4$) [22]. This is a consequence of the axis-switching which results in enhanced entrainment of the ambient fluid as well as the earlier shear layer merging/break-down [12]. The subharmonic (LF) forcing at the high amplitude (HA) or the LFHA case, which is known to promote the vortex pairing [48], results in the shortest potential core length. Therefore, in the fully developed region of the jet where the velocity profiles are self-similar, the larger spreading rate implies a higher rate of entrainment.

The root-mean-square (RMS) of the streamwise velocity fluctuations (u_rms) in the natural case, shown in figure 4.9b, develops an overshoot due to the wobbling of the large-scale structures, which fades away after the potential core break-down. This "wobbling" is associated with the unsteady fluctuations of the large scales mostly taking place in the lateral direction due to the vortex pairing and break-down which result in the lateral expansion of the jet near the end of the potential core. In addition, they are correlated with increased local anisotropy and intermittency. [22] suggest that the overshoot (hump) after the linear increase of the u_rms does not occur for the circular, square, cross and star-shaped jets which have an aspect ration of one. On the other hand, the overshoot is observed in the triangular, rectangular and elliptic jets. For both the fundamental and subharmonic frequencies,

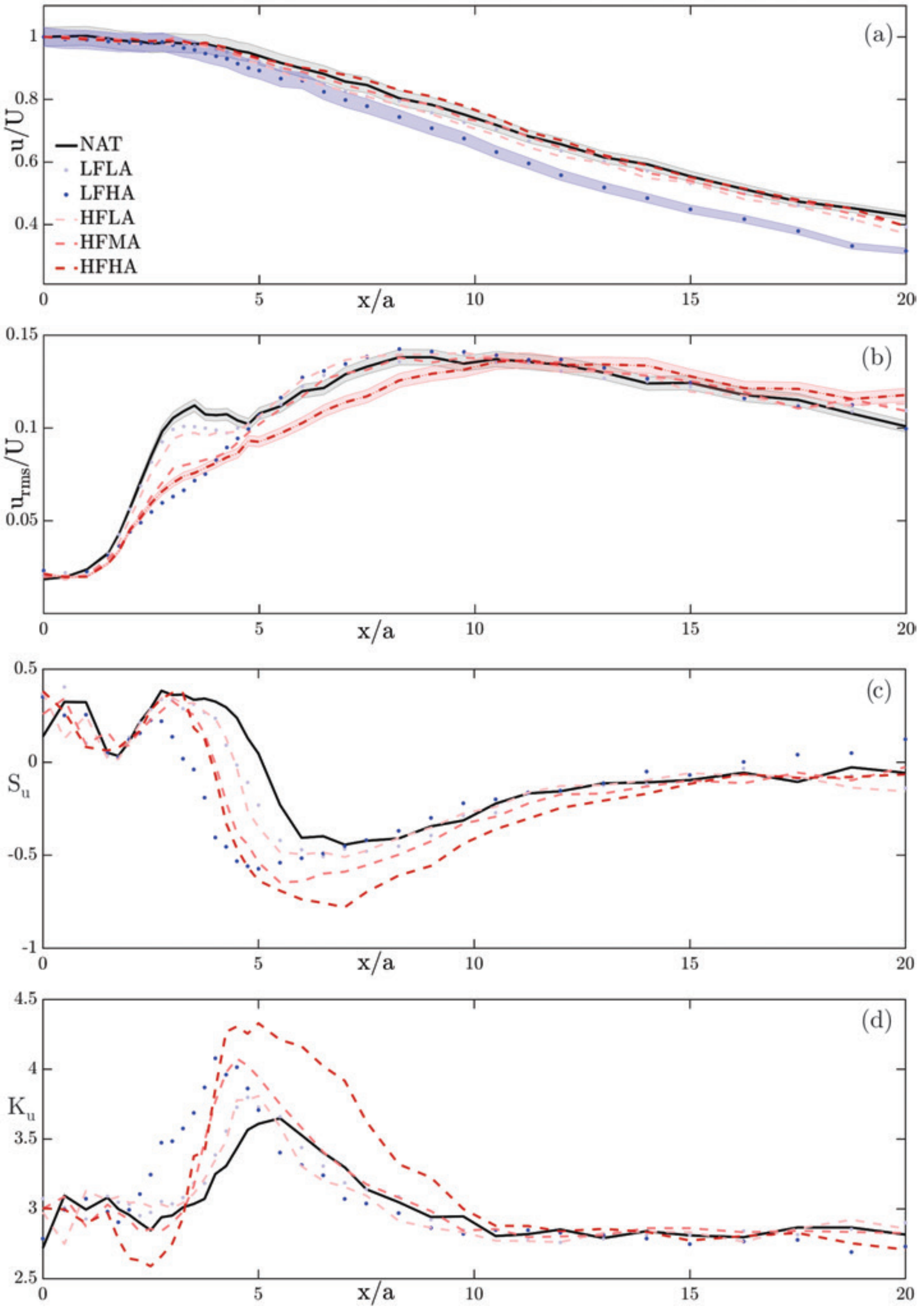

Figure 4.9: HW measurements along the jet centreline (along the x-axis at $y/a = z/a = 0$): (a) Time-averaged streamwise velocity (u); (b) Root-mean-square (RMS) of the streamwise velocity fluctuations (u_{rms}); (c) Skewness of the streamwise velocity fluctuations (S_u); (d) Kurtosis of the streamwise velocity fluctuations (K_u).

increasing the excitation amplitude weakens the overshoot. The centreline u_{rms} overshoot disappears completely for the subharmonic LFHA case.

The higher order moments of the statistics are presented in terms of the skewness (S_u) and kurtosis (K_u) of the streamwise velocity fluctuations in figures 4.9c and 4.9d, respectively. The typical values of the skewness ($S_u = 0$) and kurtosis ($K_u = 3$) characterize a normal Gaussian distribution of the statistics and hence are associated with the isotropic fluctuations. For the round jets, the centreline ($S_u = 0$) and ($K_u = 3$) demonstrate an isotropic state in the near-exit and the far-field regions while they deviate from these values near the end of the potential core. It should be noted that the far-field skewness and kurtosis approach isotropy, but never attain the exact isotropic values. This continually occurs by the small-scale entrainment mechanisms nibbling the non-turbulent patches of the fluid into the far-field jet. Conversely, the large-scale entrainment mechanisms such as the engulfment and the flow induction in the near-field eventually result in the shear layer merging and vortex break-down at the end of the potential core and hence intensify the anisotropy. As also seen here, for non-circular jets the anisotropic values start before the end of the potential core due to the axis-switching [28, 22].

The negative skewness in the time signal implies dominance of the values smaller than the mean compared to the larger ones. Also, the large values of the kurtosis are an indication of the higher probability of finding large peaks (either smaller or larger than the mean) in the time signal, which are associated with the elevated intermittency [106] levels replacing the orderly oscillations. The large value of the kurtosis at the end of the potential core suggests the intermittent nature of the flow due to the shear layer merging and vortex break-down. In addition, the negative skewness can be associated with the interference of the slower vortical structures abruptly entrained inward [107, 108]. Acoustic excitation is found to increase the intermittency level and broaden its region of effectiveness. The high amplitude (HA) subharmonic excitation (LF), which develops the shortest length of the potential core, demonstrates earlier intermittency generation. The positive skewness observed near the exit can be associated with the local curvature-induced velocities of the perturbed corners of the rectangular vortex ring increasing the occurrence of the fluctuations larger than the mean value.

The centreline u/U and u_{rms} from the PIV (lines) nicely align with the HW (symbols) in figure 4.10. In addition, the transverse and spanwise velocity fluctuations (v_{rms} and w_{rms}) in y and z directions respectively presented in figures 4.10b and 4.10d reveal interesting information. While the centreline variation of the v_{rms} is significantly augmented under the acoustic excitation, the w_{rms} is not strongly affected. This observation reveals the directional effectiveness of the acoustic waves being emitted in the y-direction aligned with the v_{rms}. Further, the subharmonic (LFHA) excitation is found to intensify the spanwise

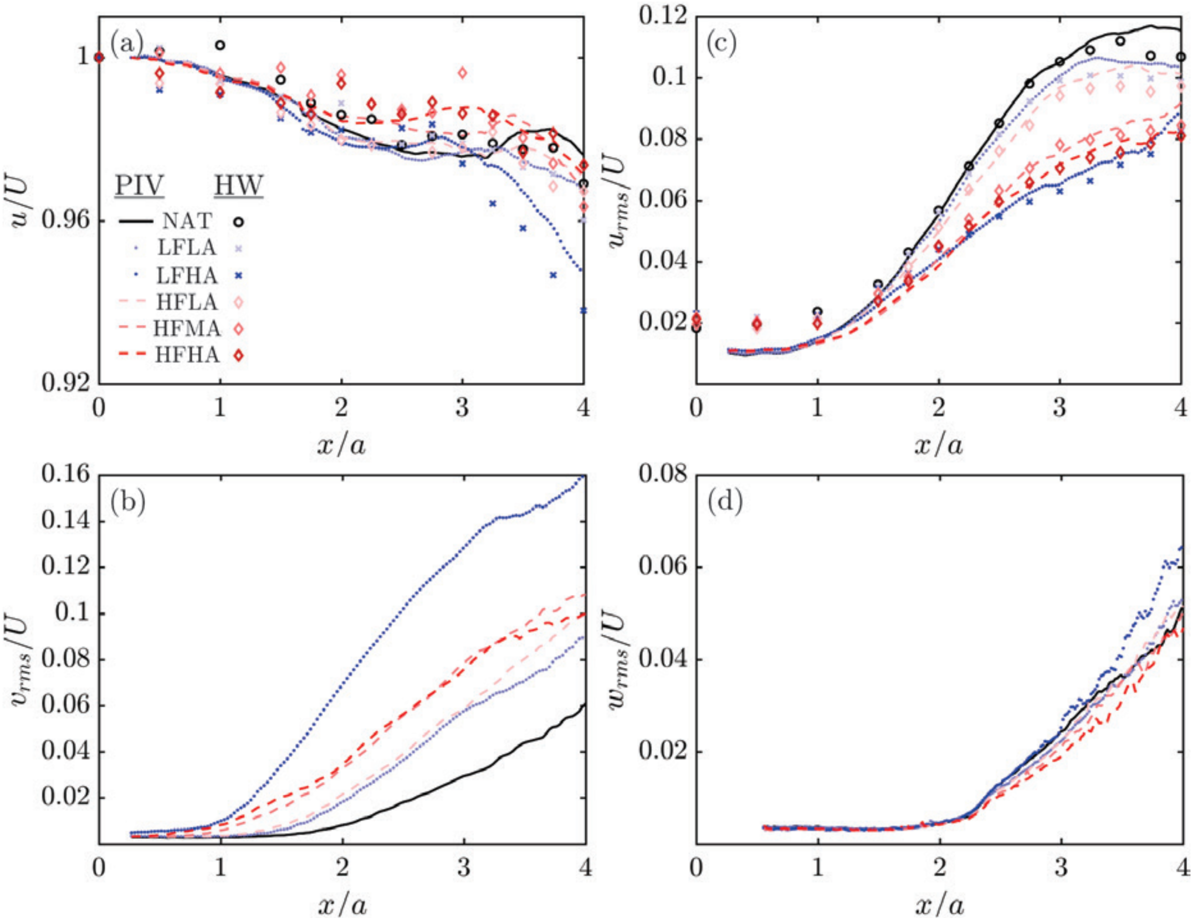

Figure 4.10: PIV measurements along the jet centreline (along the x-axis at $y/a = z/a = 0$): (a) Time-averaged streamwise velocity (u); (b) RMS of the spanwise velocity fluctuations (v_{rms}) in the side view (SV: $z/a = 0$) or the $x - y$ plane; (c) RMS of the streamwise velocity fluctuations (u_{rms}); (d) RMS of the transverse velocity fluctuations (w_{rms}) in the top view (TV: $y/a = 0$) or the $x - z$ plane.

velocity fluctuations while it decreases the streamwise component. This is a justifiable observation as the subharmonic forcing is suggested [48] to enhance the vortex pairing and results in the lateral expansion of the jet.

4.3.3 Time-averaged flow-field in the side (SV), top (TV) and diagonal (DV) views

The mean velocity (u/U) and the vorticity ($\Omega = \Omega_{\mathrm{xy}}, \Omega_{\mathrm{zy}}, \Omega_{\mathrm{x\zeta}}$ component normal to each plane of view (SV, TV or DV in figure 4.3d) obtained from the PIV are respectively presented in figures 4.11(a, b, c) and 4.11(d, e, f) for the naturally developing jet (NAT). Out of the multiple FOVs, one sample mid-plane is illustrated in figure 4.3d for each of the SV (the $x-y$ plane at $z/a = 0$), TV (the $x-z$ plane at $y/a = 0$) and DV (the $x-\zeta$ plane at $y/z = 0.5$) views. If otherwise the SV (the $x-y$ plane at $z/a = 1$) and TV (the $x-z$ plane at $y/a = 0.5$) views are shifted to the edges of the jet, it is stated in the figure captions as well as the text. The high velocity near the centreline describes the potential core while the jet is decelerated near the edges as shown in figures 4.11(a, b, c). While the vorticity is negligible inside the potential core, the largest values occur near the edges subjected to the low speed ambient (figure 4.11 d, e, f). The opposite signs of the vorticity on either sides of the jet describe the sense of rotation of the passing vortices. This sense of rotation describes the roll-up of the shear layer from the high-speed side (potential core) towards the low-speed side (ambient fluid). Therefore, the near-field vorticity field describes the time-averaged evolution of the shear layer in different planar views. In the SV plane (figure 4.11d), the shear layer clearly grows in thickness and expands outward. On the other hand, the shear layers go through a contraction in the DV plane as seen in figure 4.11e. The TV shear layers start with an expansion, which declines with the downstream distance. These differences in the relative evolution of the shear layers in the SV, TV and DV planes are the outcomes of the instantaneous vortex dynamics during the axis-switching reflected in the time-averaged flow fields [26, 12, 28].

In the figures 4.12, 4.13 and 4.14, the line plots obtained from the PIV measurements are extracted at different streamwise locations ($x/a = 1, 2, 3$) in the SV, TV and DV planes for the NAT, LFLA, LFHA, HFLA, HFMA and HFHA excitations. The traverse origins of the profiles are shifted to the local in-plane half-width of the jet ($y_{0.5}, z_{0.5}, \zeta_{0.5}$). The half-width values at each streamwise location in the corresponding planes of view are defined as the lateral locations at which the local velocity is 50% of the centreline value. In figures 4.12 a,d,g, the u profiles start with a rather top-hat shape at $x/a = 1$ and almost maintain the incoming laminar boundary layer characteristics at the separation edge. The half-width locations ($y - y_{0.5} = z - z_{0.5} = \zeta - \zeta_{0.5} = 0$), approximately coincide with the inflection point in the velocity profiles which can be interpreted as the location of the critical layer in the shearing region. The presence of the inflection point in the velocity profiles suggests that the flow is prone to the onset of the instabilities. According to the "Rayleigh's inflection-point theorem", a necessary condition for the instability is the presence of an inflection point in the base flow velocity profile [85]. Even if the boundary layer profile at the separation edge does not have an inflection point, it appears eventually due to the shear layer instability.

Interestingly, the velocity profiles located in the diagonal plane (figure 4.12g) demonstrate an extra inflection point indicating an additional destabilizing mode near the corners of the jet. This observation further motivates the following sections in search for the peculiar phenomena taking place at the high-curvature corners of the jet. Farther downstream, the streamwise velocity profiles evolve into rather Gaussian shapes with a tendency towards a fully-developed distribution [35, 26, 12, 28]. This is in accordance with the jet expansion due to the increased entrainment with the downstream distance. As it can be seen, the acoustic forcing does not result in the significant variation of the time-averaged streamwise velocity. However, there is a minor effect at $x/a = 1$ where forcing the jet at the fundamental frequency (HFHA) results in the slightly more developed velocity profile in the SV plane (figure 4.12a). At $x/a = 2$ and 3, the subharmonic excitation (LFHA) results in an advanced development in the SV and DV planes while the TV view shows a delayed evolution.

The PIV data for the lateral variation of the u_{rms} are presented in figure 4.13 in the SV (a, b, c), TV (d, e, f) and DV (g, h, i) planes for the NAT, LFLA, LFHA, HFLA, HFMA and HFHA excitations at $x/a = 1, 2, 3$. The u_{rms} attains high values within the shear layer region due to the fluctuating motion of the large-scale vortical structures. The fluctuations decrease towards the outer low-speed flow as well as within the potential core. At $x/a = 1$, the double-peaked u_{rms} profiles are observed with a major peak near the high-speed side and a minor one located towards the low-speed region (figure 4.13 a,d,g). This peculiar double-peaking of the u_{rms} appears due to the shear/rotation counteractions due to the interaction of the fundamental and subharmonic modes as elaborated by [48]. The fundamental mode is associated with the shear layer roll-up due to the Kelvin-Helmholtz (KH) instability which produces the vortex rings. Farther downstream, the vortex rings tend to merge where the subharmonic mode dominates. At $x/a = 1$, the double-peak is more evident in the SV plane (figure 4.13a) and it transition to a single one with the downstream distance ($x/a = 2, 3$). Especially in the SV plane, the acoustic excitation at the fundamental frequency (HFHA) amplifies the minor peak which is located near the low speed side. This is because the HFHA excitation causes the more upstream occurrence of

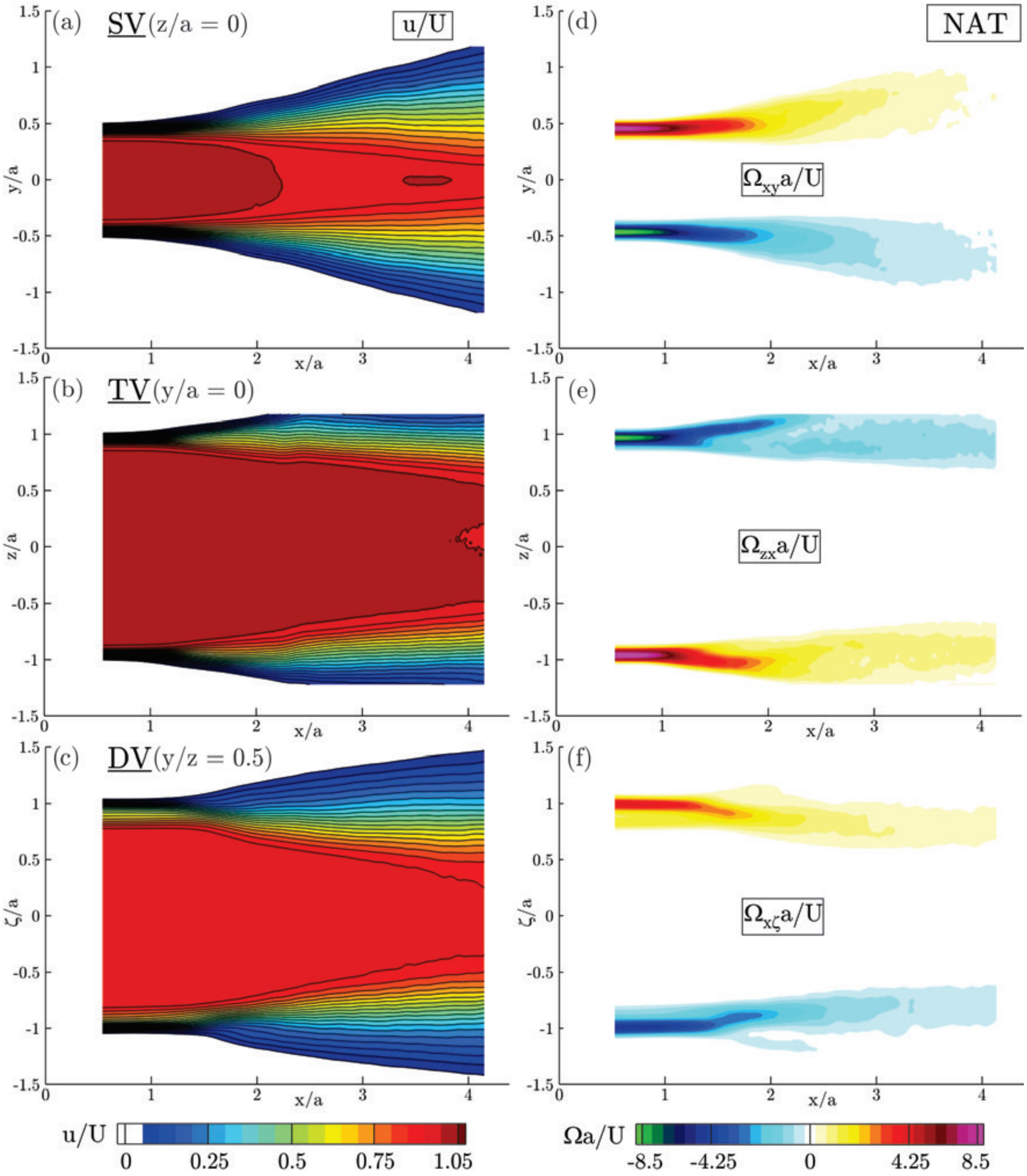

Figure 4.11: Time-averaged PIV measurements for the natural (NAT) or unexcited jet. Streamwise velocity (a, b, c) and plane-normal vorticity (d, e, f) in the side view (SV: $z/a = 0$) or the $x - y$ plane; top view (TV: $y/a = 0$) or the $x - z$ plane and diagonal view (DV: $y/z = 0.5$) or the $x - \zeta$ plane.

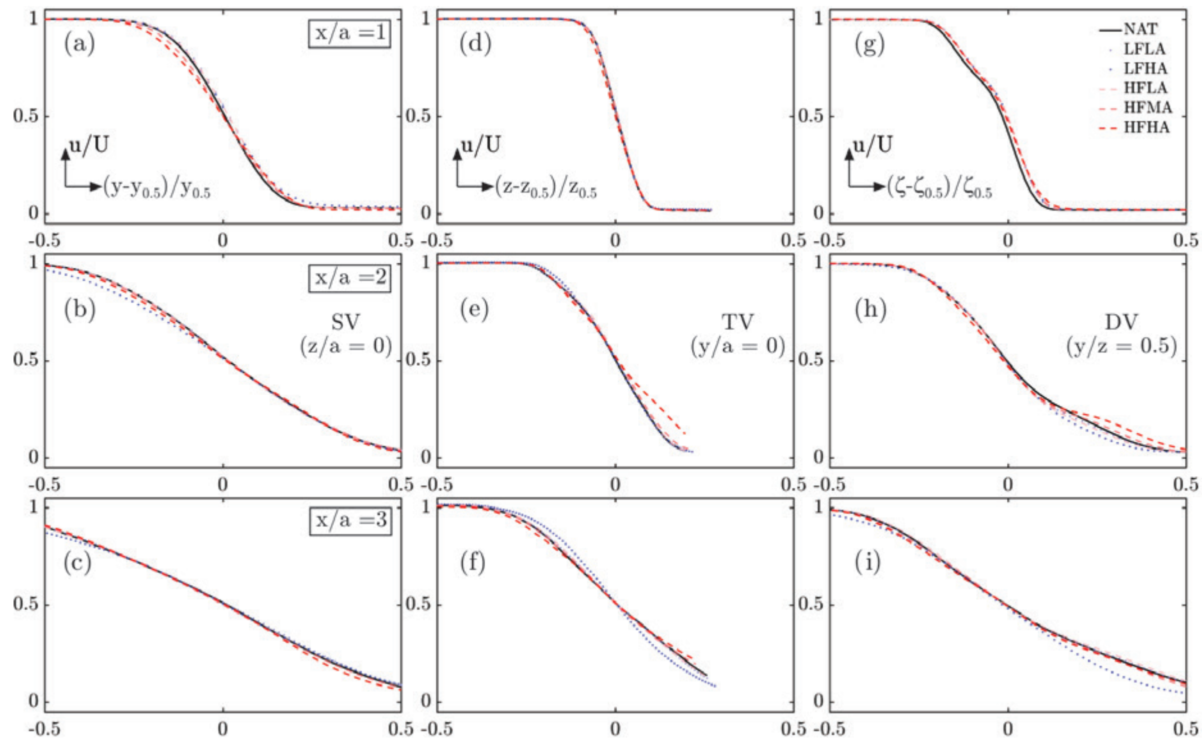

Figure 4.12: Time-averaged streamwise velocity (u) from the PIV for the NAT, LFLA, LFHA, HFLA, HFMA and HFHA excitations: (a,b,c) the side view (SV: $z/a = 0$) or the $x-y$ plane; (d,e,f) the top view (TV: $y/a = 0$) or the $x-z$ plane and (g,h,i) the diagonal view (DV: $y/z = 0.5$) or the $x-\zeta$ plane.

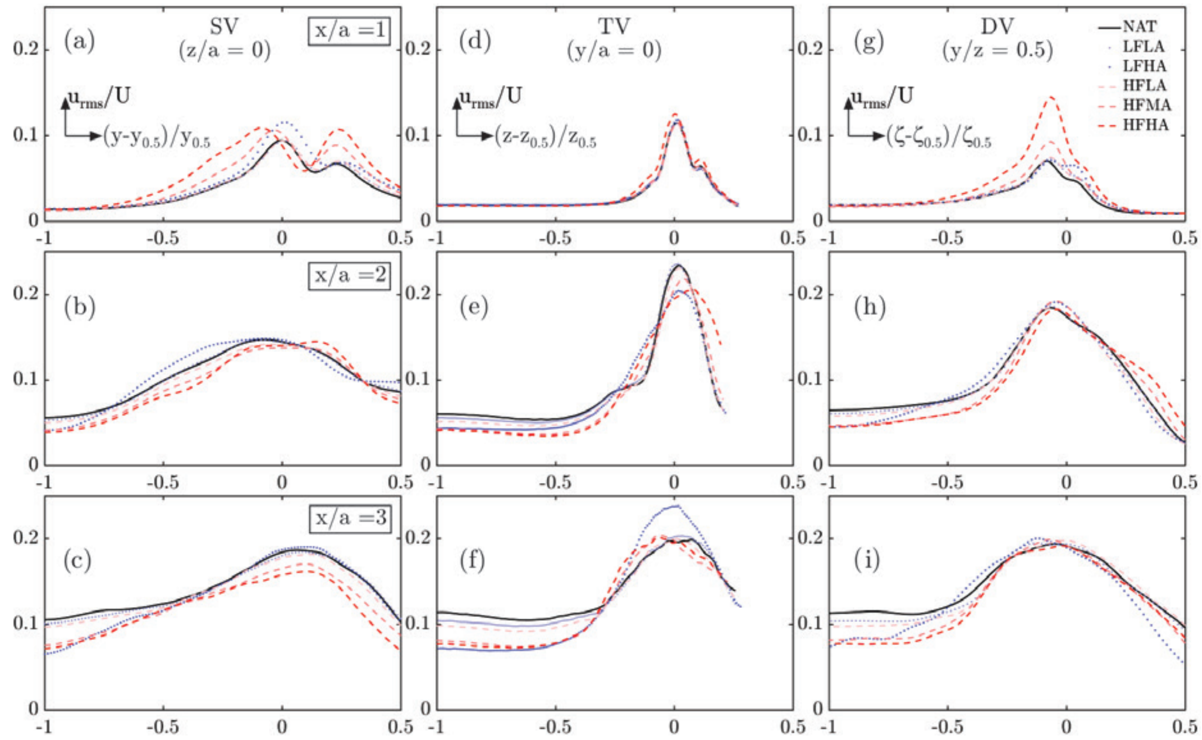

Figure 4.13: RMS of the streamwise velocity fluctuations u_{rms} measured by the PIV for the NAT, LFLA, LFHA, HFLA, HFMA and HFHA excitations: (a,b,c) the side view (SV: $z/a = 0$) or the $x-y$ plane; (d,e,f) the top view (TV: $y/a = 0$) or the $x-z$ plane and (g,h,i) the diagonal view (DV: $y/z = 0.5$) or the $x-\zeta$ plane.

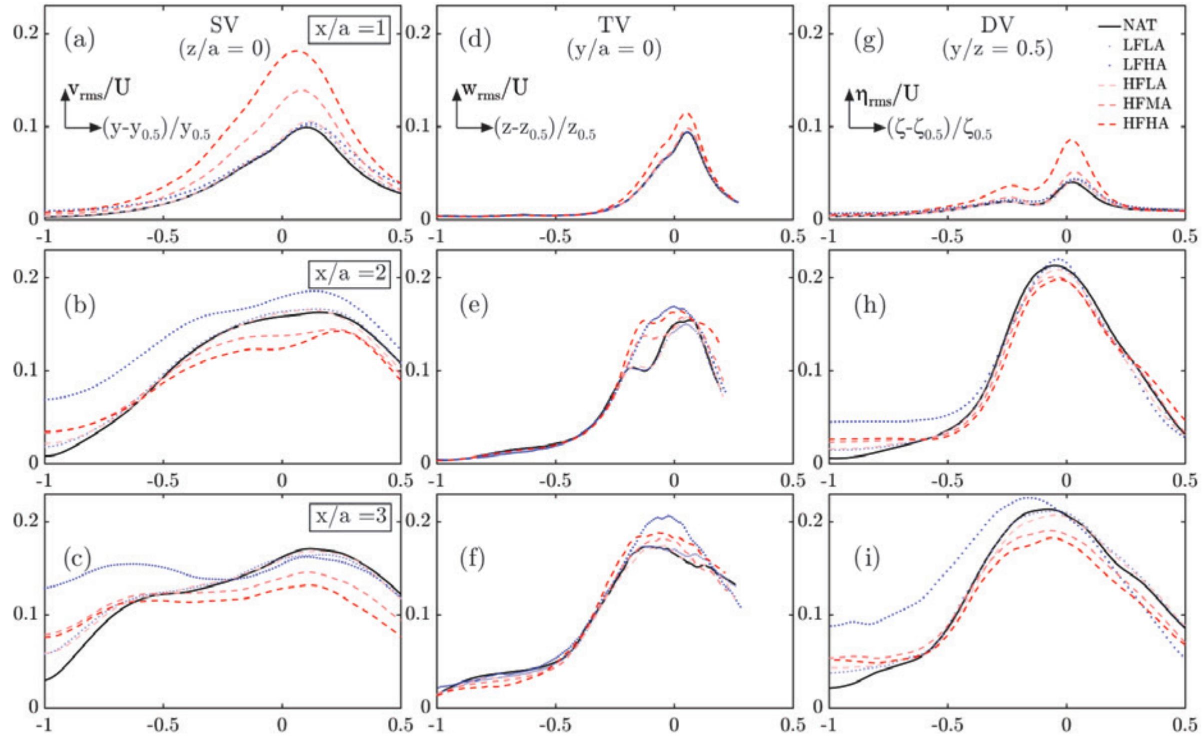

Figure 4.14: RMS of the spanwise velocity fluctuations (v_{rms}, w_{rms}, η_{rms}) measured by the PIV for the NAT, LFLA, LFHA, HFLA, HFMA and HFHA excitations: (a,b,c) the side view (SV: $z/a = 0$) or the $x - y$ plane; (d,e,f) the top view (TV: $y/a = 0$) or the $x - z$ plane and (g,h,i) the diagonal view (DV: $y/z = 0.5$) or the $x - \zeta$ plane.

the KH roll-ups which tend to lean outside towards the low-speed ambient [48]. On the other hand, the high-speed side major peak is augmented under the subharmonic excitation which is found to contract more vortices inward due to enhanced vortex pairing [48]. The RMS profiles laterally expand with the downstream distance. This is in accordance with the growth of the vortical structures and the consequent thickening of the shear layer due to the viscous diffusion.

In figure 4.14, the lateral variation of the spanwise velocity fluctuations corresponding to the SV (a, b, c), TV (d, e, f) and DV (g, h, i) planes are presented as v_{rms}, w_{rms} and η_{rms}, respectively. At $x/a = 1$, the peaks of the spanwise fluctuations are augmented proportional to the forcing amplitude of the fundamental mode (HFHA, HFMA) in the SV (figure 4.14a), TV (figure 4.14d) and the DV (figure 4.14g) planes. This occurs due to the advanced upstream location of the KH roll-ups which laterally undulate the shear layer. It should be noted that the effect of the subharmonic forcing is not significant at $x/a = 1$ since this region is dominated by the KH instability and the shear layer roll-ups. On the other hand, at $x/a = 2$ where the subharmonic (LFHA) excitation enhances the vortex pairing [48], the RMS peak of the spanwise velocity fluctuations tend to become stronger. Eventually, the peak of the spanwise velocity fluctuations associated with the subharmonic forcing dominate at $x/a = 3$. In parallel with the aforementioned observations (figure 4.10) for the centreline values, the spanwise fluctuations are stronger in the SV plane due to the fact that the acoustic source emits along the y-axis which is aligned with the direction of the v_{rms}.

4.3.4 Axis-switching and vortex dynamics under various acoustic forcing

According to the schematic definition given in figure 4.7, the outward expansion and the inward contraction of the velocity/vorticity fields observed in different planes of view describe the axis-switching phenomenon. In order to quantify the streamwise locations within which the axis-switching is initiated and completed, the relative expansion/contractions among different planar fields are determined. To this end, the streamwise evolution of the spanwise locations ($y_{\Omega_{\mathrm{max}}}, z_{\Omega_{\mathrm{max}}}, \zeta_{\Omega_{\mathrm{max}}}$) at which the maximum vorticity occurs in the shear layer are detected. The obtained locations for the SV ($y_{\Omega_{\mathrm{max}}}$), TV ($z_{\Omega_{\mathrm{max}}}$) and DV ($\zeta_{\Omega_{\mathrm{max}}}$) planes are shown in figure 4.15 for the NAT, LFLA, LFHA, HFLA, HFMA and HFHA excitations. It should be noted that these locations are normalized by their corresponding near-exit values ($y_{\Omega_{\mathrm{max},0}}, z_{\Omega_{\mathrm{max},0}}, \zeta_{\Omega_{\mathrm{max},0}}$) so that they all start from unity. Therefore, in all the cases the peak vorticity location remains constant (unity) almost up to the downstream

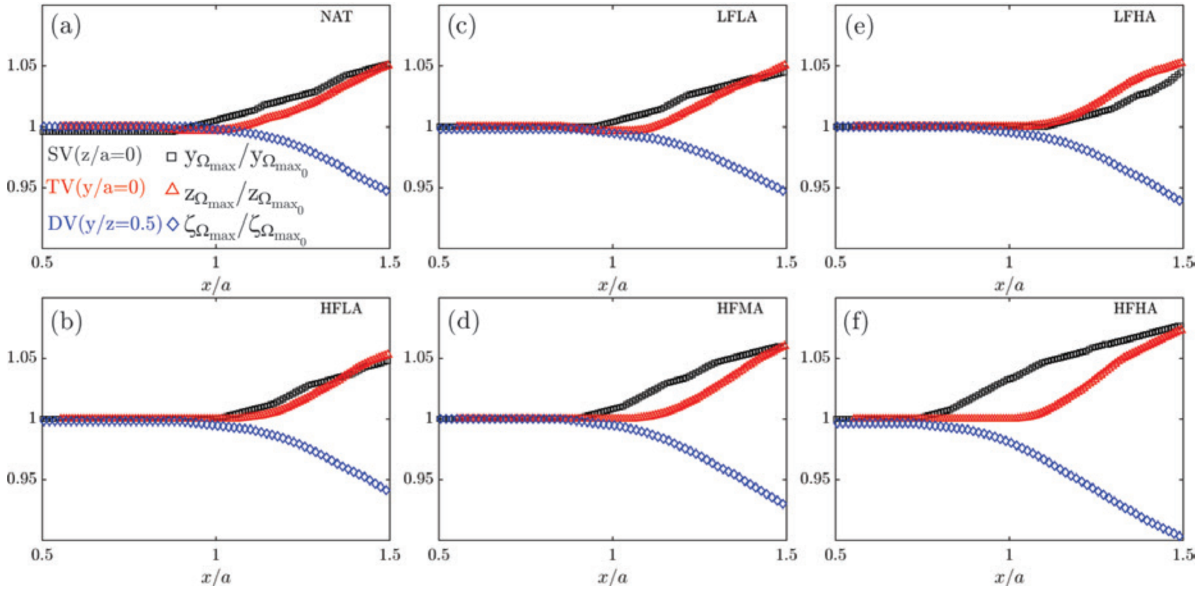

Figure 4.15: Streamwise evolution of the traverse locations of the maximum vorticity ($y_{\Omega_{\max}}$,$z_{\Omega_{\max}}$, $\zeta_{\Omega_{\max}}$) respectively shown in the side view (SV: $z/a = 0$) or the $x - y$ plane, the top view (TV: $y/a = 0$) or the $x - z$ plane and the diagonal view (DV: $y/z = 0.5$) or the $x - \zeta$ plane. (a) NAT, (b) HFLA, (c) LFLA, (d) HFMA, (e) LFHA and (f) HFHA excitations.

location $x/a = 1$. This implies that the shear layers neither expand nor contract from their original positions located near the edges. Then, beyond certain downstream distance the locations of the peak vorticity in the diagonal view (DV) drops below unity meaning that the shear layer is contracting in this plane.

On the other hand, the SV and TV planes show an increase to larger than unity characterizing the outward expansion of the shear layer. This characterizes the region within which the first axis-switching is started between the DV plane with respect to the SV and TV views. The first axis-switching is known to occur mostly due to the self-induced deformation of the initially non-circular (rectangular here) KH vortex rings [26, 28]. Even though weaker, a second axis-switching may be characterized between the SV and TV planes by the crossover observed in the peak vorticity locations. This weak cross-over means that one side of the jet becomes slightly wider than the other one [26, 28]. This second axis-switching is known to be associated with the interaction of the primary KH vortex ring with the secondary streamwise vortex loops as well as the corner hairpin vortices [26, 28].

The expansions/contractions in different view planes and the consequent axis-switching characteristics are not significantly influenced under the low amplitude (LFLA and HFLA) excitations. However, the streamwise locations of the second axis-switching observed in figures 4.15b and 4.15c are slightly advanced. Under the subharmonic excitation (LF) at high amplitude (HA), the expansion rate in the SV is decreased while it is increased in the TV plane. In addition, the contraction of the DV plane is somewhat enhanced. Unlike the subharmonic, the fundamental excitation (HF) increases the expansion in the SV with respect to the TV. Furthermore, increasing the amplitude of the HF excitation results in the faster contraction in the DV plane. Therefore, increasing the excitation amplitude from LA to HA at the fundamental (HF) frequency, advances the location of the first axis-switching by earlier expansion of the SV shear layer and the contraction in the DV plane. On the other hand, it postpones the second axis-switching by delaying the expansion of the TV plane.

Above discussed jet dynamics reflected into the time-averaged flow features are associated with the axis-switching. Instantaneously, the axis-switching phenomenon is initiated by the deformations of the non-circular (e.g. rectangular) vortex rings due to the self-induced velocity [12, 43, 42, 28]. To further investigate the governing mechanisms of the axis-switching in rectangular jets, the spatio-temporal dynamics of the initially rectangular ring needs to be explored. To this end, planar phase-locked PIV conducted in multiple SV and TV planes are interpolated into the volumetric structures constructing the three-dimensional vortical structures. The Q_{p}-criterion [61] is calculated to identify the vortex cores where the second invariant (Q) of the velocity gradient tensor is positive. For in-

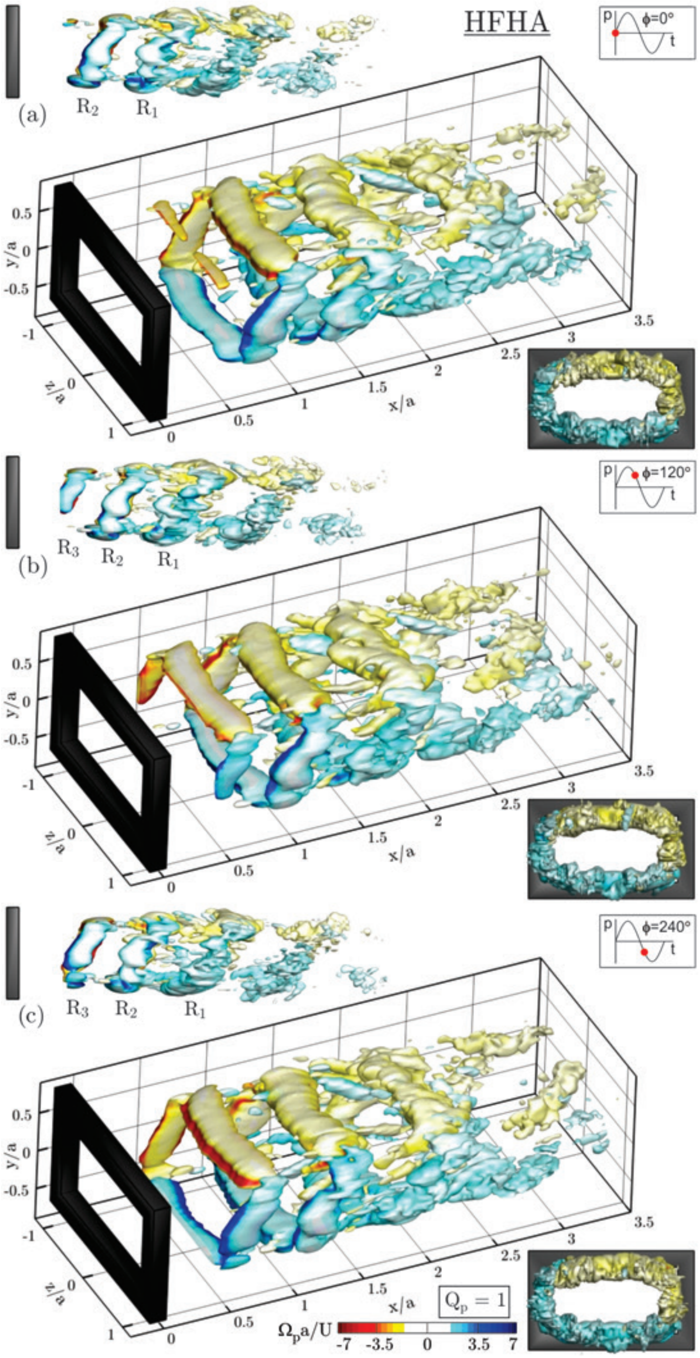

Figure 4.16: Iso-surfaces of the instantaneous Q_p-criterion during the phases ($\phi = 0^o$, 120^o, 240^o) for the acoustic forcing at HFHA. Vortical structures are coloured by the vorticity component corresponding to the roll-up sense of rotation.

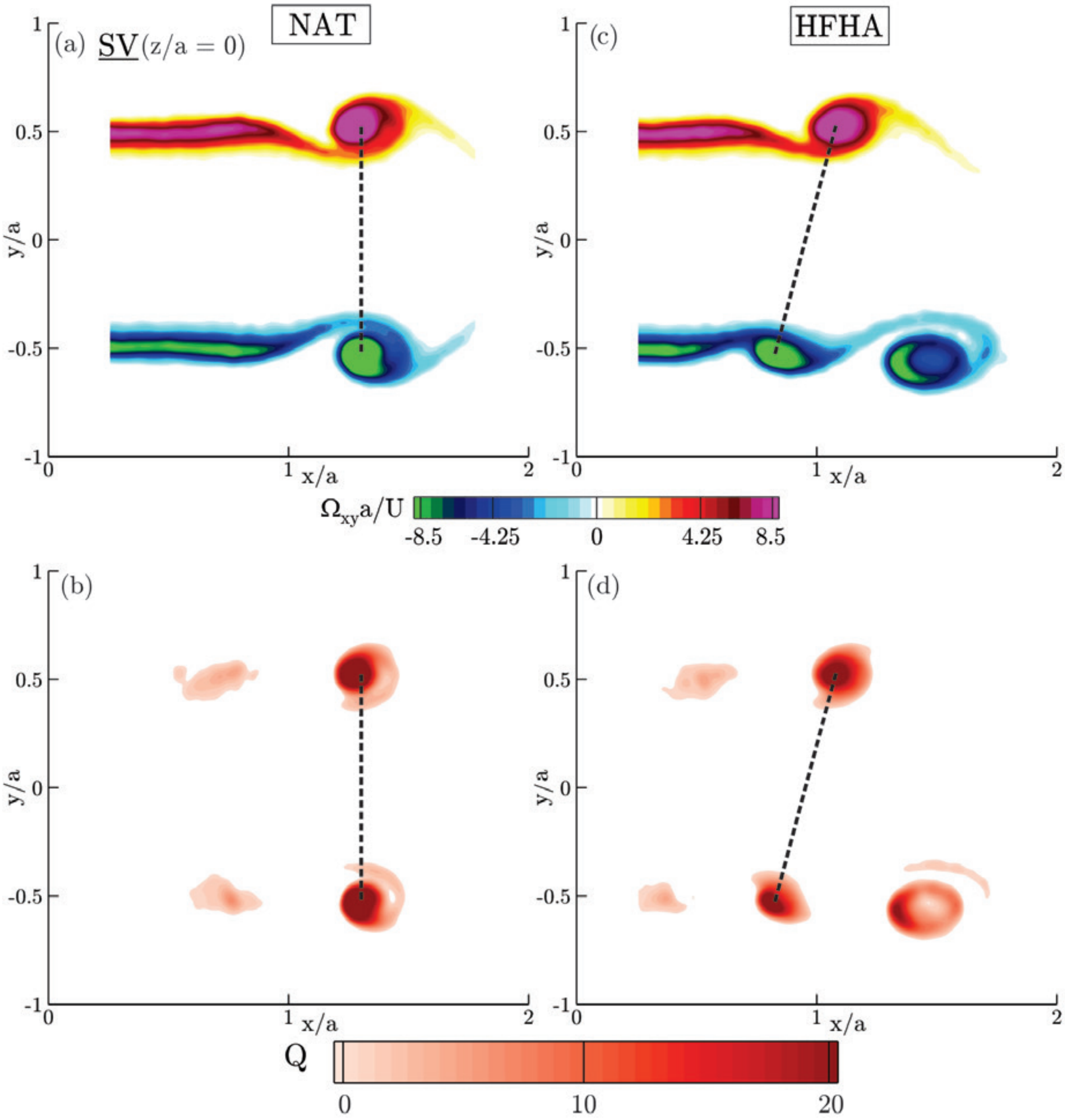

Figure 4.17: Sample side view (SV: $z/a = 0$) instantaneous snapshots of the vorticity ($\Omega_{\mathrm{xy}}a/U$) and the Q-criterion to compare the symmetric and non-symmetric (tilted) vortex shedding for the natural and the acoustically forced (HFHA) jets, respectively. The side near the acoustic source demonstrates roll-up and vortex shedding at more upstream locations compared to the farther shear layer.

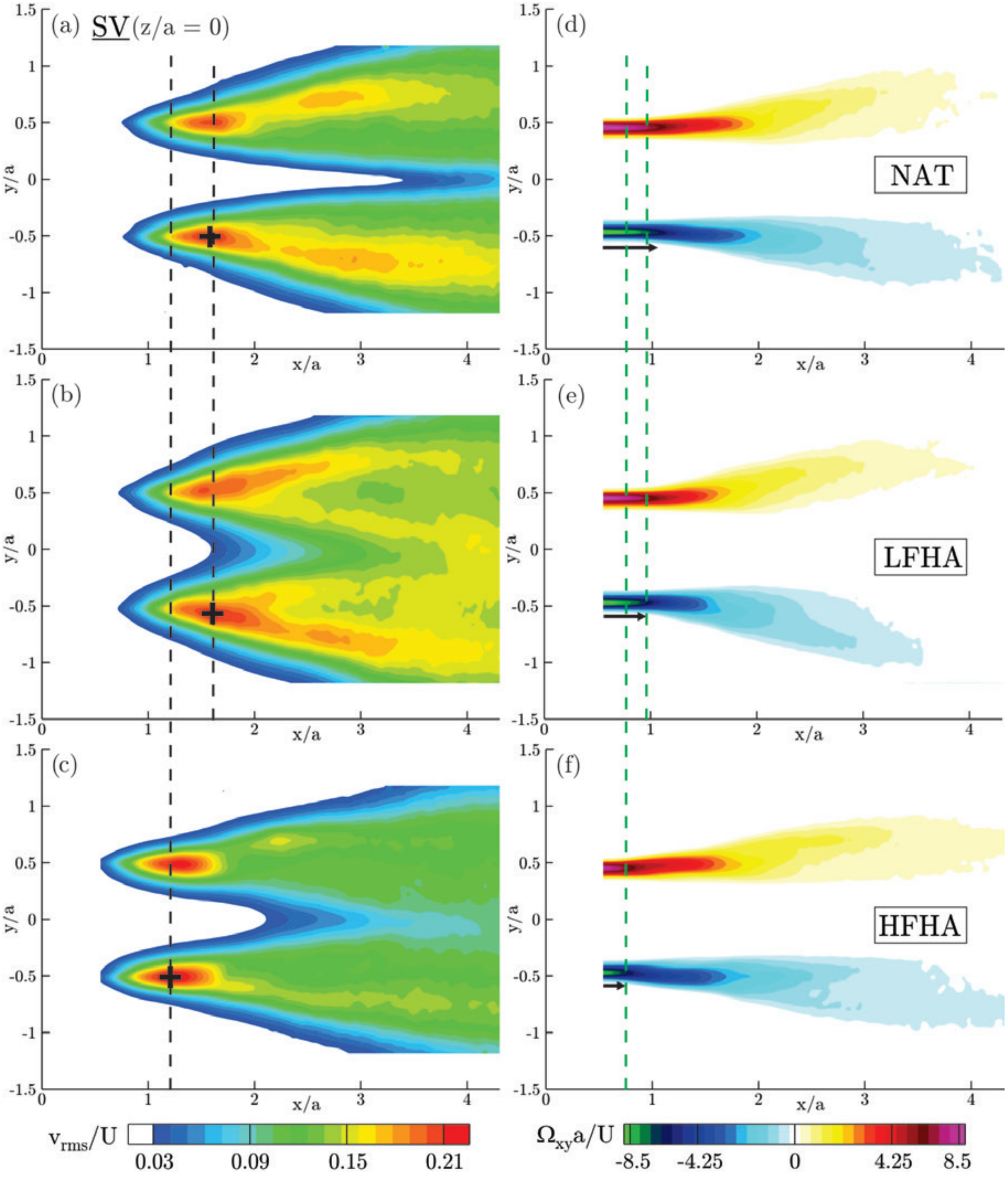

Figure 4.18: Side view (SV: $z/a = 0$) or the $x - z$ plane coloured by: (a, b, c) the transverse velocity fluctuations (v_{rms}) and (d, e, f) time-averaged vorticity ($\Omega_{\mathrm{xy}}a/U$) for the NAT, LFHA and HFHA cases.

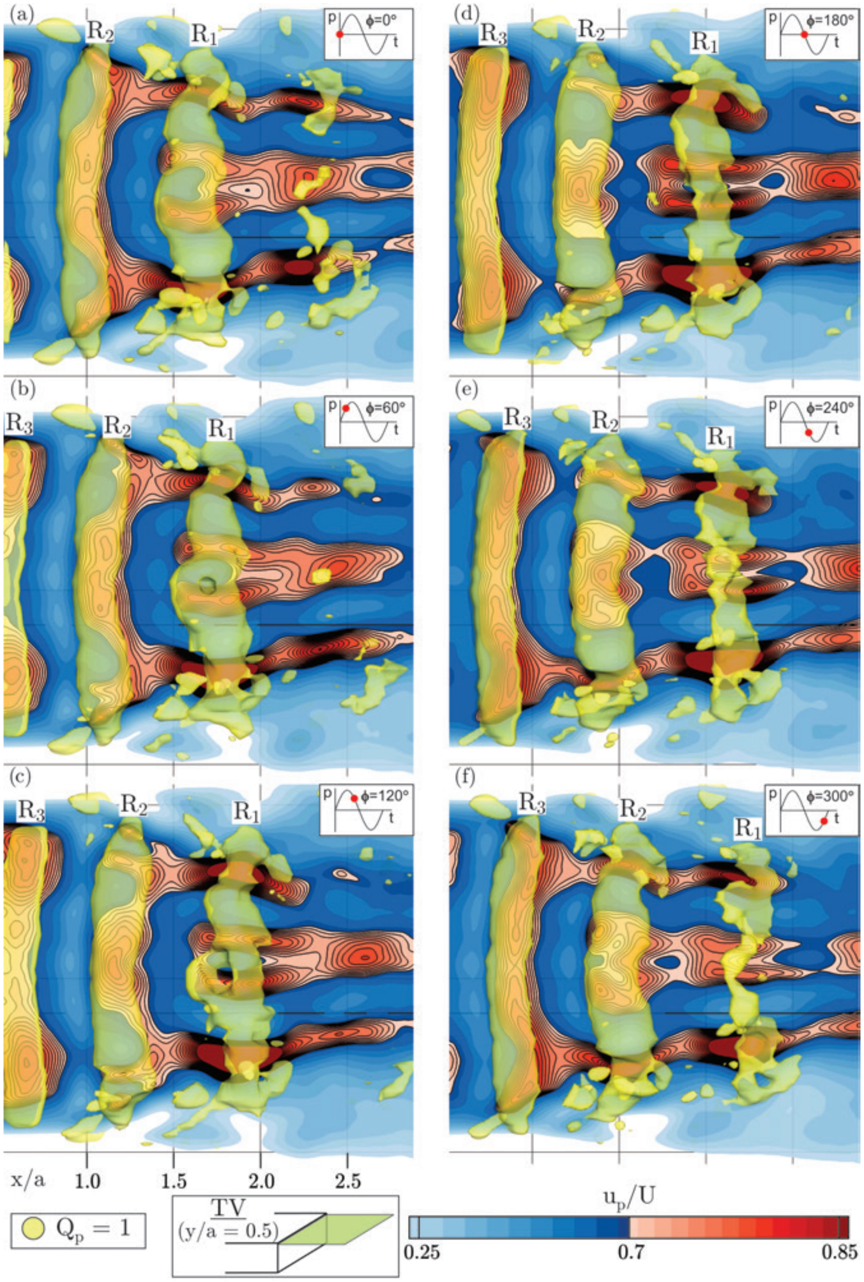

Figure 4.19: Top view (TV: near the $y/a = 0.5$ edge) or the $x - z$ plane coloured by the phase-averaged streamwise velocity. The TV plane is passed through the local vortex loop demonstrated by the yellow-coloured iso-surface of the instantaneous Q_p-criterion. The vortex loop is isolated from the longer side of the initially rectangular vortex ring. Instantaneous snapshots are presented for the acoustic forcing at HFHA during the phases ($\phi = 0^o$, 60^o, 120^o, 180^o, 240^o,300^o).

stance, the iso-surfaces of the instantaneous Q_p-criterion are presented in figure 4.16 to visualize the three-dimensional vortical structures during the phases of HFHA excitation. The vortex loops constructing each of the four sides of the rectangular ring are coloured by the vorticity component which characterizes their roll-up sense of rotation. The volumes are presented for the three phases of $\phi = 0^o, 120^o, 240^o$ during the period of the acoustic excitation. Three viewpoints are presented for each phase. The side view (SV) is located at the upper-left corner and the cross-sectional view in the lower-right corner. The middle large volume is then viewed at an angle best illustrating the three-dimensional structures.

In the spatial point of view, the rectangular vortex ring of the figure 4.16 is formed due to the KH instability in the near-exit region. With increased downstream distance, the originally rectangular shape turns into the more distorted geometry. Any given point on the vortex ring moves by the advection velocity of the main flow as well as the local self-induced velocity [40, 41]. The self-induced velocity is related to the local curvature in that point, the inverse of the vortex core radius and the local circulation [40, 41]. The major factor for the self-induced velocity of the rectangular vortex rings is the presence of the sharp corners. Therefore, the additional curvature-induced velocity on top of the convective velocity of the vortex ring generates the local acceleration at the corners with respect to the flat sides.

According to the Biot-Savart law [42], higher velocities are induced at the high curvature regions of a vortex filament. See Appendix A for further details on the Biot-Savart integral and its correlation with the curvature induced velocity. Farther downstream, the deformed vortex rings tend to break down and the small-scale vortical structures appear in the shear layer. It is worth to mention that the self-induced velocity of an axisymmetric vortex ring is mostly related to the radii of the circular ring and the vortex core since the curvature distribution is uniform. A circular structure is decelerated while evolving in time/space as a result of the increased radii of the vortex ring as well as the core thickening due to the viscous diffusion.

In a temporal point of view, one could track the vortex rings of the figure 4.16 in time/phase. At the phase $\phi = 0^o$, the vortex ring R_1 which emerges first is advected farther downstream compared to its following ring R_2. At this instant, R_1 appears to be more distorted while R_2 still maintains its rather rectangular shape. At the phase $\phi = 120^o$, the vortex ring R_3 starts to form and enter the domain. Also, the rings R_2 and R_1 are now advected farther downstream compared to the previous phase ($\phi = 0^o$). Also at $\phi = 120^o$, the ring R_1 is surrounded by the small-scale vortices shedding from the primary KH ring due to the growth of the perturbations. The ring R_1 does not maintain its intact shape at $\phi = 240^o$ and the upstream R_2 and R_3 rings go through the deformations. Observing the vortex cores from the downstream towards the upstream, reveals the formation of a rather elliptic shape of the cross-section. This elliptic shear layer recognized from the downstream demonstrates the small-scale vortices near the jet boundaries. The spatio-temporal evolution of the volumetric vortical structures reveals the deformations of the rings due to the axis-switching. The near-exit rectangular shape is found to evolve into the rather elliptic shape accompanied with the increased small-scale activities with the downstream distance.

Another interesting observation in figure 4.16 is that the vortex rings appear to be tilted when looking from the side view (SV). This is due to the directional effect of the excitation observed earlier in the lateral velocity fluctuations (v_{rms}) in figure 4.10. Since the acoustic source, which is located near the $y/a = -0.5$ edge, emits the pressure waves along the y-axis (normal to the TV or the $x - z$ planes), the shear layer closer to the acoustic source ($y/a = -0.5$) tends to roll-up in more upstream locations compared to the farther edge ($y/a = 0.5$). To better visualize and clarify the occurrence of the KH roll-ups in more upstream locations at the vicinity of the acoustic source, figure 4.17 presents the sample side view (SV: $z/a = 0$) snapshots of the instantaneous vorticity ($\Omega_{\mathrm{xy}} a/U$) and the Q-criterion. The symmetric and non-symmetric (tilted) vortex shedding for the natural and the acoustically forced (HFHA) jets are observed in both the vorticity and the Q-criterion fields. The side near the acoustic source demonstrates KH roll-ups and vortex shedding taking place at more upstream locations compared to the farther side of the shear layer. [48] used a vortex tracking algorithm to obtain the probability density function (PDF) of the vortex core locations and suggest that the KH roll-ups are statistically shifted upstream when the shear layer is forced at its fundamental frequency. Observation of the vortex ring tilting could also be interpreted in terms of the earlier transition from the shear layer varicose (symmetric) mode of instability into the sinusoidal (anti-symmetric) undulations.

In the sinusoidal mode, the lateral undulations of the vortices are expected to play an important role. Also, the directional effects of the acoustic source described instantaneously above need to be analysed in a time-averaged manner. To this end, figure 4.18 shows the RMS of the spanwise velocity fluctuations (v_{rms}) and the time-averaged vorticity ($\Omega_{\mathrm{xy}} a/U$) in the side view plane under the effect of the fundamental and the subharmonic excitation. The peak values of the vorticity and v_{p} are found shifted to more upstream locations and decay earlier for the excitation of the fundamental (HFHA) mode compared to the the natural (NAT) shear layer. This suggests the advanced upstream location of the shear layer roll-up while the tilting of the vortex rings are not reflected in the time averaged results. On the other hand, excitation of the subharmonic (LFHA) mode does not affect the streamwise location of the roll-ups. Instead, a thicker v_{rms} region is formed due to the enhanced vortex pairing at LFHA. In addition, the v_{rms} peaks are sustained farther downstream and appear earlier in the centreline region.

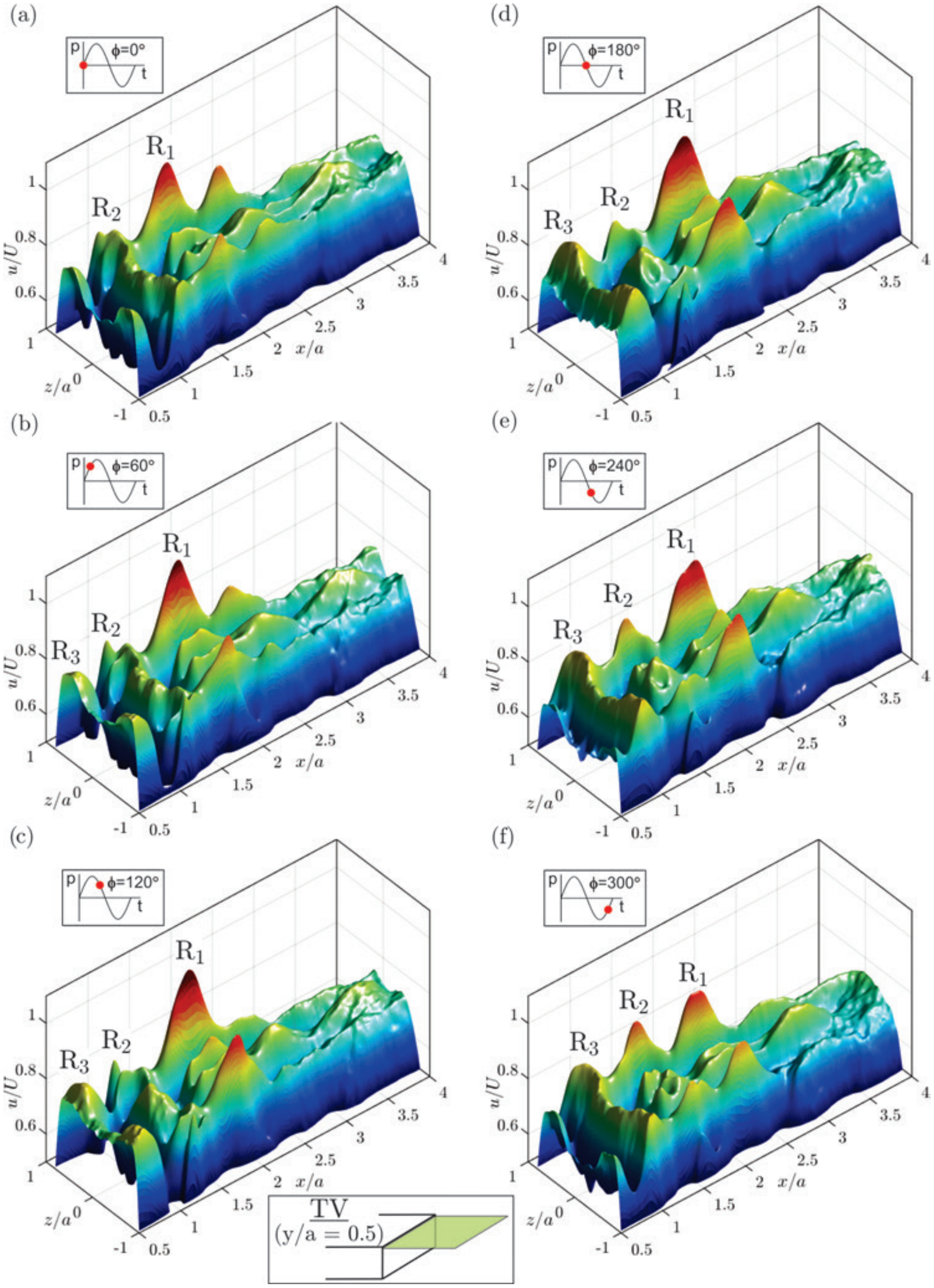

Figure 4.20: Phase-averaged streamwise velocity spikes characterizing the curvature-induced velocity. Instantaneous information are extracted from the top view (TV: near the $y/a = 0.5$ edge) or the $x - z$ plane. Instantaneous snapshots are presented for the acoustic forcing at HFHA during the phases ($\phi = 0^o$, 60^o, 120^o, 180^o, 240^o, 300^o).

4.3.5 Curvature-induced perturbations in rectangular vortex rings

To enhance the understanding of the driving mechanisms of the axis-switching phenomenon, the local variation of the self-induced velocity on the vortex ring, needs to be characterized. To this end, the shorter and longer sides of the rectangular vortex ring shown earlier in figure 4.16 are considered as individual vortex loops under curvature-induced deformations. The $x - z$ plane shown in figure 4.19 is passed through the vortex loop constructing the longer side of the initially rectangular vortex (see figure 4.16). This vortex loop, which is demonstrated by the yellow-coloured iso-surface of the instantaneous Q_{p} criterion, is aligned with the z-axis and advects downstream in the x-direction. The intersecting top view (TV: the $x - z$ plane at $y/a = 0.5$ edge) is coloured by the instantaneous streamwise velocity. The snapshots are presented for the acoustic forcing at HFHA during the phases $\phi = 0^o, 60^o, 120^o, 180^o, 240^o, 300^o$.

During the phases $\phi = 0 - 60^o$, the segment of the vortex ring R_3, which is just entering the domain, clearly shows two high-velocity spots near the high-curvature corners ($z/a = \mp 1$). These local accelerations at the sharp corners with respect to the flat sides in the middle, characterize the additional curvature-induced velocity. During this stage, the newly formed vortex loop R_3 viewed from the top maintains its rather straight geometry. However, its faster moving sharp corners initiate the deformations as predicted by the Biot-Savart law [42] described in Appendix A. After the fast motion of the corners, the initially flat mid part which is now left behind, attains a high-curvature. Therefore, another high-velocity spot is induced in the middle part of the vortex loop. This stage is nicely visible during the phases $\phi = 60^o - 180^o$ through which the ring R_2 demonstrates development of a slightly arced shape. Accordingly, the three high-velocity spots on the corners and the middle of the R_2 can be correlated with the local curvature. The vortex loop associated with the ring R_1, which is evolved further in time/space, appears to be more distorted compared to R_2 and R_3.

This wavy shape characterizes the increased number of the high-curvature regions on the loop. Accordingly, the high-velocity spot in the middle splits into two. The outcome is the formation of the four high-velocity zones over the span of the vortex segment which are associated with the two corners and the two high-curvature regions in the middle. Alternative variations of the high/low velocity spots along the span of the vortex loop describe the formation of the azimuthal instabilities over the ring. Likewise, the increased number of the high-velocity regions, suggests the shorter wavelength (higher frequency) of the azimuthal instability. By further evolving in time and correspondingly with the downstream distance, the two high-velocity spots at the corners tend to decay. On the other hand, the high-velocity pairs in the middle tend to merge into one where a single mode prevails. The self-induced deformations and the resulting distortions of the vortex loop, finely correlate with the curvature distribution on the vortex loops. This wavy shape of the ring is the consequence of non-linear growth of the azimuthal perturbations on top of the initial KH instability. These perturbations grow in time and space until the ring starts to disintegrate into the smaller scales.

The curvature-induced velocity over the vortex loop and its correlation with the spatio-temporal evolution of the azimuthal perturbations can be further elucidated by the surface plot given in figure 4.20. The phase-averaged streamwise velocity information are extracted from the top view (TV: the $x-z$ plane at $y/a = 0.5$ edge) plane passed through the vortex loop located on the longer side of the rectangular opening. The surface height and colour account for the local magnitude of the phase-averaged streamwise velocity. Near the nozzle exit, two small spikes appear which describe the curvature-induced velocities at the corners of the ring R_3. These two spikes grow in magnitude through the phases $\phi = 0 - 60^o$ and advect downstream with time. The ring R_2, which is located farther downstream during the phases $\phi = 0^o - 60^o$, develops an additional spike corresponding to its high curvature in the middle. Further in time and the downstream distance, the ring R_1 forms larger spikes at the corners. In addition, the two smaller spikes are formed in the middle. Increased number of these spikes on the span of the vortex loop demonstrates the formation of multiple high-curvature regions at shorter wavelengths. These peaks and valleys characterize a spatial instability at each specific downstream location. In addition, the spatial perturbations are monitored as they advect downstream, grow or decay spatio-temporally. For instance between $x/a = 2.5 - 3$, while there is still a spike in the middle, the corner spikes have almost decayed. Furthermore, beyond $x/a = 3$, the curvature gradient becomes negligible on the ring and the ring does not remain intact due to the break-down into the smaller scales. Therefore, no preference in the self-induced velocity is observed.

Another important observation in the TV plane is the symmetry of the self-induced velocity spikes with respect to the mid plane ($z/a = 0$). This accordingly suggests that the perturbations within this plane propagate symmetrically. It should be noted that the corner and the middle spikes of the self-induced velocity characterized and discussed in figure 4.20 can be associated with the corner and center modes of the pressure perturbations described by [45]. In their vortex sheet model, the center instability modes of the pressure perturbations are found to prevail over the corner modes with the downstream distance. In addition, the large eddy simulations (LES) by [28] correlates the corner pressure perturbations with the self-induced velocity during the axis-switching of the square-shaped vortex rings. The present measurements verify the findings of the above theoretical/numerical efforts by explaining the growth of the corner instabilities, their decay in time/space and the domination of the middle spikes with the downstream distance.

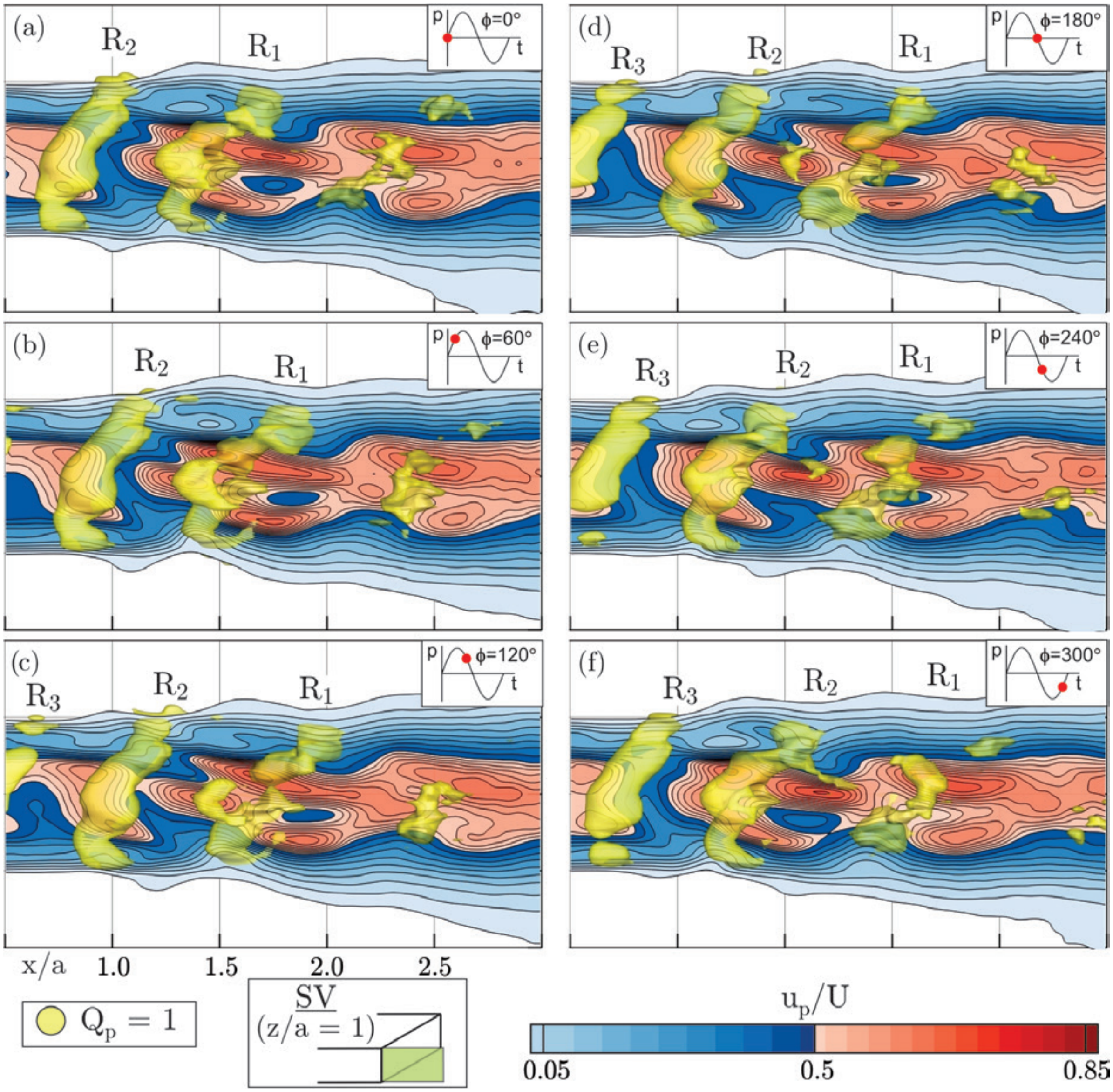

Figure 4.21: Side view (SV: near the $z/a = 1$ edge) or the $x - y$ plane coloured by the phase-averaged streamwise velocity. The plane is passed through the local vortex loop demonstrated by the iso-surface of the instantaneous Q_p-criterion. The vortex loop is isolated from the shorter side of the initially rectangular vortex ring. Instantaneous snapshots are presented for the acoustic forcing at HFHA during the phases ($\phi = 0^o$, 60^o, 120^o, 180^o, 240^o, 300^o).

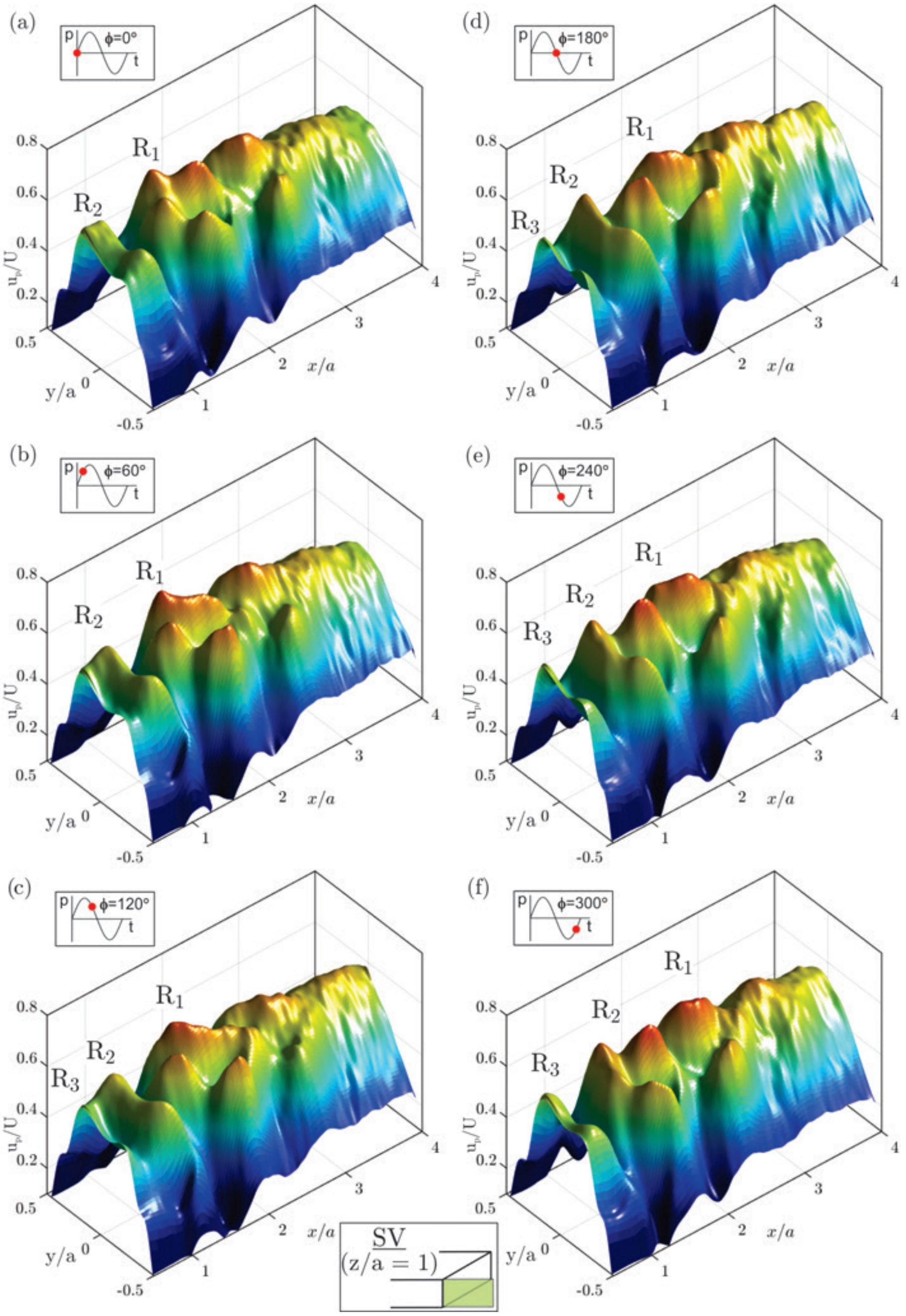

Figure 4.22: Phase-averaged streamwise velocity spikes characterizing the curvature-induced velocity. Instantaneous information are extracted from the side view (SV: near the $z/a = 1$ edge) or the $x - y$ plane. Instantaneous snapshots are presented for the acoustic forcing at HFHA during the phases ($\phi = 0^o$, 60^o, 120^o, 180^o, 240^o, 300^o).

The corresponding curvature-induced velocity information displayed for the top view (TV) in figures 4.19 and 4.20, are also presented for the side view (SV) plane in the figures 4.21 and 4.22. The $x-y$ plane displayed in figure 4.21 passes through the vortex loop constituting the shorter edge of the initially rectangular vortex ring. The vortex loop which is illustrated by the yellow-coloured iso-surface of the instantaneous Q_{p} criterion, is oriented along the y-axis and travels downstream in the x-direction. The intersecting side view (SV: near the $z/a=1$ edge) or the $x-y$ plane is coloured by the phase-averaged streamwise velocity. The phase-averaged images are shown for the acoustic forcing at HFHA during the phases $\phi = 0-60^o, 120^o, 180^o, 240^o, 300^o$. The main observation is the tilting of the shorter segment of the vortex ring viewed from the side. As discussed earlier for the figures 4.16 and 4.17, this happens because of the more upstream KH roll-ups in the shear layer located near the acoustic source. Accordingly, the curvature-induced velocity in the SV plane exhibits the asymmetric pattern for either of the sharp corners ($y/a=\mp0.5$). The high-velocity spots are present again in accordance with the curvature variations over the vortex loop. However, they are not distinguished as clearly as in the TV vortex loop. This could be explained by the shorter length of the SV vortex loop where the spanwise (azimuthal) perturbations behave differently.

The dynamics of the vortex loop constructing the shorter edge in the side view (SV: the $x-y$ plane near the $z/a=1$ edge) can be further clarified by exploring the curvature-induced velocity spikes presented in figure 4.22. At the phase $\phi=0^o$, the two spikes near the edges ($y/a=\mp0.5$) of the R_2 loop characterize the curvature-induced velocity. Unlike the top view (TV), the self-induced velocity spikes at the corners of the side view plane are not significantly larger relative to the middle of the loop. In addition, the count of the spikes on the span of the SV loop never grows beyond three while it reaches up to four on the vortex loop along the longer edge top view (TV: the $x-z$ plane near the $y/a=0.5$ edge). On this shorter side of the rectangular vortex ring, the middle spike does not split into two. Instead, the middle spike is shifted away from the acoustic source which is located near the $y/a=-0.5$ edge. After the shifting, the middle spike eventually merges into the corner spike passing near the $y/a=0.5$ edge. As the flow develops further in time and in the downstream of the merging point, the self-induced velocity spikes are again only present at the two corners. Ultimately, these two corner spikes also approach the center and coalesce. Beyond this coalescence, the center mode prevails as previously observed for the longer side TV vortex loop.

4.4 Summary

Particle image velocimetry (PIV) and the hot-wire (HW) anemometry measurements are employed to study the curvature-induced deformations of the vortex rings generated in the jet flows emerging from the rectangular duct of the aspect ratio 2. At the Reynolds number of $Re = UD_\mathrm{h}/\nu = 17,750$, the near-exit of the naturally evolving jet demonstrates the fundamental (f_n) frequency due to the Kelvin-Helmholtz (KH) instability as determined by the HW-based velocity spectra and the PIV-based spatial theory of linear stability (LST). With increased downstream distance, the passage frequency of the vortices drop until the subharmonic ($f_\mathrm{n}/2$) mode dominates due to the vortex pairing. The characterized fundamental and subharmonic modes are then used to acoustically excite the jet at different amplitudes. The PIV measurements of the jet shows that the near-field rectangular cross-section evolves into the more elliptic/circular shapes farther downstream. This observation, which is accompanied with the contraction of the jet diagonal as well as the mild expansion of the longer and shorter sides, is attributed to the axis-switching phenomenon. By means of the acoustic forcing, the relative expansion/contraction of the jet in the top (TV), side (SV), and diagonal (DV) views are found controllable. This alters the occurrence of the first (stronger) and second (weaker) axis-switching and their corresponding locations.

Excitation of the subharmonic mode results in the shorter length of the potential core and larger spread rates due to the enhanced vortex pairing. Furthermore, the overshoot commonly formed in the centreline streamwise velocity fluctuations (u_rms) is suppressed under the excitation at $f_\mathrm{n}/2$. On the other hand, excitation of the fundamental mode advances the first KH roll-up to more upstream locations. It is found that the acoustic excitation imposes directional effects on the jet flow. The lateral velocity fluctuations aligned with the direction of the acoustic waves are significantly increased. In addition, the instantaneous KH roll-ups occur at the more upstream locations within the shear layer located near the acoustic source. As a result, the vortex rings viewed from the side appear to be tilted. The u_rms profiles demonstrate a peculiar double-peaking phenomenon due to the interaction of the fundamental and subharmonic modes which can be altered by applying the different acoustic forcing strategies. The skewness and kurtosis of the fluctuations in the near-separation region of the rectangular jets demonstrate increased anisotropy/intermittency, in contrast to that of circular jets which only become anisotropic near the end of the potential core. Such a deviation from the round jet behaviour can be associated with the local curvature-induced velocities at the perturbed corners of the rectangular vortex ring. Under the effect of the acoustic excitation, the intermittency levels grow and take place in a broader region. In addition, the high amplitude (HA) subharmonic excitation (LF), which results in the shortest length of the potential core, causes the earlier production of the intermittent flow.

The global observations in the time-averaged flow-fields are better interpreted by exploring the instantaneous three-dimensional vortex dynamics. The phase-locked spatio-temporal tracking of the three-dimensional flow structures exhibits the formation of initially rectangular vortex rings due to the KH instability. As the vortex rings are advected along with the bulk flow motion, they deform and eventually break down as a result of the curvature-induced velocity. Due to the additional self-induced velocities, the high-curvature corners of the initially rectangular KH rings are found to move faster relative to the initially flat regions of the ring. Therefore, the rectangular ring loses its two-dimensionality and develops a three-dimensional structure due to the increased number of the high-curvature regions (at shorter wavelengths) and the consequent self-induced velocity. This results in the formation of non-linear azimuthal perturbations over the distorted ring which eventually breaks down into the smaller scales. The corner modes of the curvature-induced velocity eventually coalesce into a single mode in the middle. Unlike the isolated rectangular vortex rings, those formed in continuous jets do not demonstrate a rotation-like deformation. Instead, the vortical structures reshape into the more round geometry due to the axis-switching.

Propagation of the perturbations produced by the curvature-induced velocities are found also influenced by the directional effect of the acoustic source. The small curvature-induced velocity spikes appear symmetrically in the TV plane passing through the longer vortex loop near the separation edge. Due to the normal orientation of the acoustic source with respect to the top view plane, the first KH roll-up and the self-induced velocity distributions occur symmetrically. This symmetric shedding of the vortices resembles the varicose mode of instability. While propagating farther downstream, these two small spikes grow in magnitude. Later, an additional spike appears in the middle of the vortex loop corresponding to the formation of the local high curvature. Increased waviness of the vortex loop is found correlated with the appearance of the more spikes and high-curvature regions suggesting the higher frequency (shorter wavelength) perturbations. Eventually, the middle spike dominates while the corner spikes decay. Since the acoustic source emits along the shorter loops, the shear layer closer to the source rolls up in more upstream locations compared to the farther side. Consequently, the vortex rings observed from the SV appear to be tilted. Accordingly, a non-symmetric curvature-induced velocity distribution takes place along the vortex loop. This non-symmetric shedding of the vortices appears similar to the sinusoidal mode of the instability. Unlike the TV loop, the middle spike associated with the SV loop is shifted away from the acoustic source and merges into the corner spike located in the farther edge.

Chapter 5

Effect of the viscous diffusion on the self-induced dynamics of isolated rectangular vortex rings

This chapter is written based on the large eddy simulation (LES) results to reveal the viscous diffusion effects on the self-induced dynamics of isolated rectangular vortex rings. The content is reprinted with permission from Physiscs of Fluids journal [50]:

Abbas Ghasemi, Burak Ahmet Tuna, and Xianguo Li. Viscous diffusion effects on the self-induced distortions of rectangular vortex rings. Physics of Fluids, 30(12):124101, 2018.

5.1 Introduction

Unbounded shear flows are formed after the solid boundary is eliminated and they freely evolve in space/time [1, 9, 10, 11]. The dynamics of the shear layers which are destabilized through the Kelvin-Helmholtz (KH) mechanism, are dominated by the formation, distortion and break-down of the vortical structures [20, 13]. If the shear layer separates from circular openings (nozzles, pipes or orifices), axisymmetric vortex rings are produced [19, 47]. On the other hand, non-circular vortex rings are issued from openings of different shapes (e.g., elliptic, square, rectangular, triangular, etc.) [25]. Generating vortex rings through the non-circular openings serves as a passive control strategy while active control techniques such as the acoustic excitation can also be used [102]. Jet flow control is important for many applications where mixing, heat/mass transfer, noise suppression, fuel injection, combustion and pollutant dispersion are involved. Furthermore, non-circular vortex rings exhibit more complex and rich dynamics, hence receive attention for their fundamental and practical importance.

The velocity at any point on a vortex loop has two components due to the bulk flow motion and the local self-induced velocity [40, 41]. The self-induced velocity depends on the vortex curvature, core radius and local circulation [40, 41]. The self-induced velocity of axisymmetric vortex rings (constant curvature) reduces as they evolve in time/space and both the core and ring radii increase. On the other hand, non-circular vortex rings (non-uniform curvature) exhibit high curvature at the sharp corners. As predicted by the Biot-Savart law [42], non-circular rings attain larger velocities induced near the high-curvature regions resulting in three-dimensional distortions and consequent axis-switching[12, 28, 43, 42]. Depending on the upstream conditions [101, 26, 29, 30], axis-switching may be influenced by the formation of streamwise rib-shape vortex loops and the corner hairpin vortices [28, 26]. While both originated from the self-induced dynamics, outcomes of the axis-switching appear to be different for isolated vortex rings and those generated in continuous jets [101, 28, 26]. For isolated vortex rings or the leading vortex of starting jets, axis-switching is traditionally defined as the apparent rotation of the ring around its streamwise axis [28, 26]. On the other hand, axis-switching of non-circular jets demonstrates a deformation of the cross-section into round shapes [101] also interpreted in terms of the azimuthal pressure perturbations [44, 45, 28].

In jet flows, three-dimensional distortions of non-circular vortex rings improve the near-field entrainment and mixing [46]. Rectangular vortex rings exhibit improved entrainment due to the axis-switching and corner fluctuations acting as the large and small scale mechanism, respectively [12]. As a result, non-circular jets become wider in the near-field, develop larger spread rates [35, 32] and exhibit enhanced entrainment/mixing[31, 32, 33, 34, 27]. Majority of the earlier studies on the axis-switching are focused on the global time-averaged features such as the spread rate, entrainment and increased anisotropy of the non-circular jets [22, 36, 35, 37, 38]. In addition, some experimental [23] and numerical [46, 26, 12, 28] studies aim at describing the instantaneous dynamics of the vortex rings in steady/starting jets as well as isolated vortex rings.

Earlier studies suggest that self-induced deformations initiated by the curvature-induced velocity of non-circular vortex rings play important roles in passive flow control and consequent processes such as heat/mass transfer, mixing, combustion and noise regulation. However, fundamental understanding of the vortex ring deformations should be further enhanced by focusing on the underlying physics such as viscous diffusion effects. Particularly, self-induced velocities due to the vortex core radius and local curvature demand further attention. Therefore, the present study aims at understanding the viscous diffusion effects during the self-induced deformations of rectangular vortex rings. Since it is difficult to obtain the three-dimensional structures of isolated vortex rings experimentally, stereoscopic particle image velocimetry (SPIV) and hotwire (HW) anemometry measurements are conducted for rectangular jets. Then, large eddy simulation (LES) is performed and the cross-sectional reshaping of the rectangular jet is compared to SPIV for validation. The turbulence length scales obtained from HW verify the grid resolution of LES. Finally, LES of isolated vortex rings are conducted at the Reynolds numbers $Re_{D_h} = Re_i = U_i D_h/\nu = 355, 877.5, 1775, 8775, 17750$ ($i = 1, ..., 5$) where U_i, D_h, and ν denote centreline velocity at the exit, hydraulic diameter and kinematic viscosity, respectively.

5.2 Experimental setup and measurement procedure

Stereoscopic particle image velocimetry (SPIV) measurements are carried out in order to acquire the three-component two-dimensional (3C2D) velocity fields outside of a rectangular duct with the length of $L = 300$ mm and cross-section dimension of side length $a = 20$ mm by the top edge $b = 40$ mm. The experimental set-up for the SPIV measurements illustrated in figure 5.1 demonstrates the top, cross-sectional and the isometric views of the rectangular duct with the relative positioning of the two cameras with the laser. The jet exits the rectangular opening by means of a blower fan forcing the air through a conditioning enclosure encompassing a honeycomb insert and a set of three wire screens. Afterwards, the air stream is passed through a $9:1$ contraction, in order to diminish the turbulence intensity below 0.9% and a mean flow uniformity within 0.25% in the inviscid core. The centreline exit velocity is characterized as $U = 10$ m/s associated with the Reynolds number $Re = UD_h/\nu = 17,750$ based on the hydraulic diameter $D_h = 26.67$ mm. This Reynolds number is selected for the measurements as it is the highest value used for the simulations and represents the most similar flow features desired for the practical applications.

The glycol-water based fog particles, with approximate mean diameter of 3μm, are used for seeding the air flow. The particles are then illuminated within the laser sheet generated by a double-pulsed Evergreen 70 mJ/pulse Nd: YAG laser. The laser beam is passed through the -10 mm cylindrical lens combined with a right-angle mirror to form an approximately 1.5 mm thick sheet oriented into the jet cross-section. The two Photron SA4 high-speed cameras with the 63 degree angle between them are synchronized with the laser pulse using the LaVision high-speed timing unit controlled by the LaVisions DaVis 8 software. Using the Nikon 200 mm fixed focal length macro lens, images are captured at the resolution of 1024×1024 pixels with a numerical aperture value of $f^{\#} =$

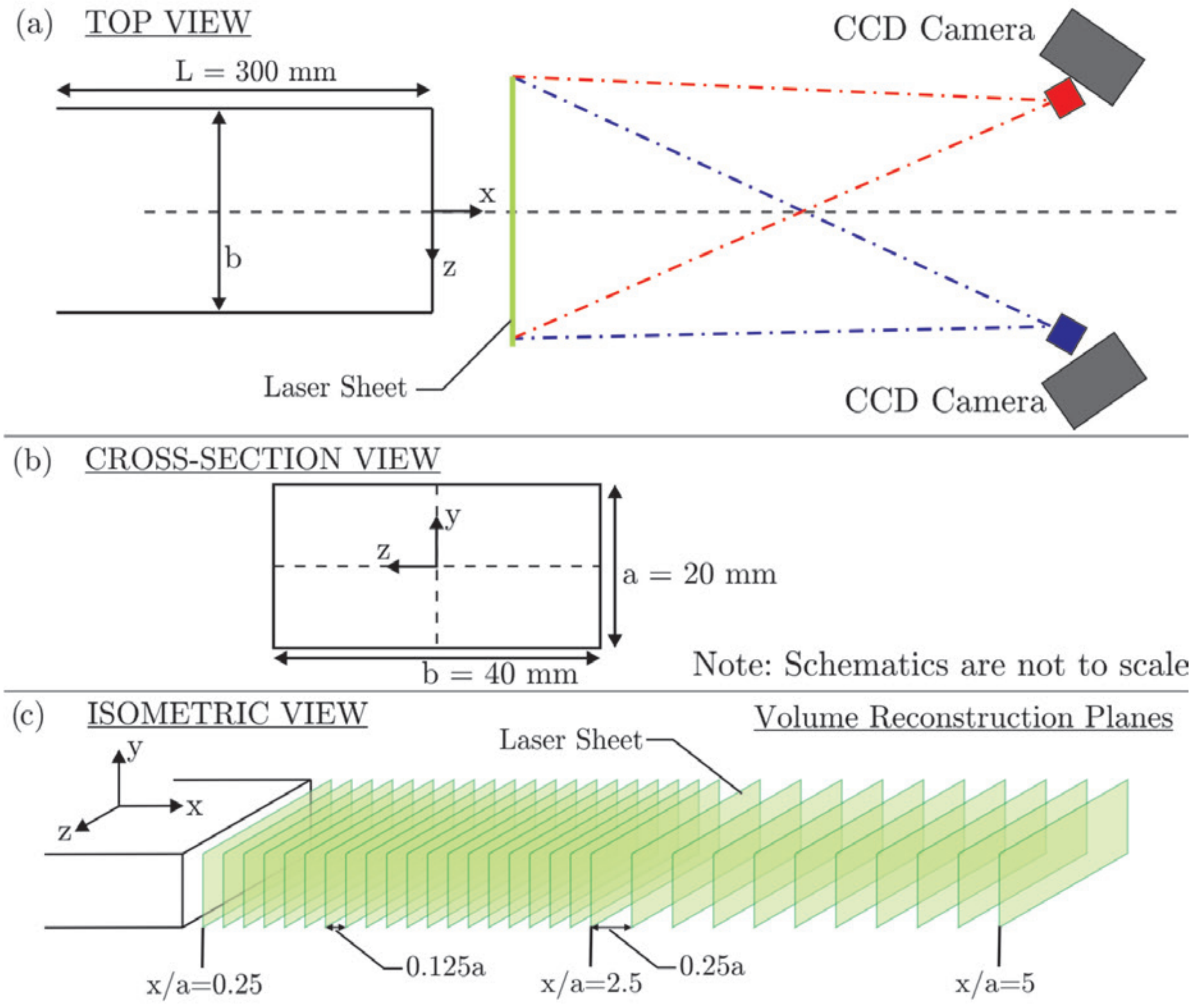

Figure 5.1: Experimental set-up for stereoscopic particle image velocimetry (SPIV): (a) Top; (b) Cross-section; (c) Isometric views of the rectangular duct with relative positioning of two cameras with the laser. Multiple measurement planes ($x/a = 0.25 - 5$) used to generate the 3D flow-field.

11. Images are acquired in double-frame mode at 15 Hz. Total of 1500 image pairs are collected for each set of experimental conditions. Cameras and the laser are translated along the x-axis to conduct the measurements within the cross-sectional planes ($y - z$) located at different streamwise locations ($x/a = 0.25 - 5$). Measurement planes are placed in streamwise increments of $0.125a$ in the jet near-exit (i.e. $x/a = 0 - 2.5$) and in $0.25a$

spacings for the farther downstream regions (i.e. $x/a = 2.5 - 5$). The time-averaged data from the individual planar measurement are interpolated to generate the three-dimensional (3D) flow-field. Images are processed by the Lavision Davis 8 multi-pass, iterative cross-correlation algorithm with decreasing window size to provide the three-component velocity (u, v, and w). The final window width is 24 × 24 pixels, with 75% overlap resulting in the vector pitch of 0.35 mm. The post-processing of the results is achieved by the universal outlier detection and removal with vector replacement [74]. After the calculation of the vector fields, the mean velocity fields obtained from each of the cameras are cross-correlated in the overlap region to align with the field of views (FOV). Furthermore, the time delay between the successive laser pulses is set to 50μs. For a pixel scale factor of 16.7 pixel/mm, the corresponding uncertainty of the out-of-plane (u) and in-plane velocity vectors (v and w) is not more than ±0.65 m/s and ±0.34 m/s, respectively. In order to characterize the streamwise evolution of the length scales, high-frequency hot-wire (HW) anemometry is conducted along the jet centreline. An automatically traversed single probe oriented normal to the flow direction is utilized. A Dantec 55P11 straight general-purpose probe connected to a Dantec Streamline Constant Temperature Anemometry system is implemented for the HW measurements. The HW data are sampled at the frequency of 16 kHz yielding a total number of $524,288$ samples for the time period of 32.8 seconds. The fluctuating velocity measured by the HW at a minimum frequency resolution bandwidth of 0.03 Hz is used for the spectral analysis.

5.3 Numerical set-up

Non-dimensional form of the filtered incompressible Navier-Stokes equations for large eddy simulation (LES) are given below [109]

$$\frac{\partial \tilde{u}_i^*}{\partial x_i^*} = 0 \tag{5.1}$$

$$\frac{\partial \tilde{u}_i^*}{\partial t^*} + \frac{\partial \tilde{u}_i^* \tilde{u}_j^*}{\partial x_j^*} = -\frac{\partial \tilde{p}^*}{\partial x_i^*} + \frac{1}{Re_a}\frac{\partial^2 \tilde{u}_i^*}{\partial x_j^* x_j^*} - \frac{\partial \tau_{ij}^r}{\partial x_j^*} \tag{5.2}$$

where $x_i^*(i = 1, 2, 3)$ represent the non-dimensional coordinates x/a, y/a and z/a. The non-dimensional time, Reynolds number, dimensionless filtered velocity components and pressure are denoted as $t^* = (Ut)/a$, $Re_a = Ua/\nu$, $\tilde{u}_i^* = u_i/U$ and $\tilde{p}^* = P/\rho U^2$, respectively. Flow quantities are decomposed into the resolved (filtered) and sub-grid scale (residual) fields, denoted respectively as $(\tilde{u}_i^*, \tilde{p}^*)$ and $(u^{'*}_i, p^{'*})$ for velocity and pressure. For instance, the instantaneous velocity and pressure can be evaluated as $u_i^* = \tilde{u}_i^* + u'^*_i$ and $p^* = \tilde{p}^* + p'^*$, respectively. Also, time-averaged quantities are denoted with an over-bar as $\bar{u}^*$.

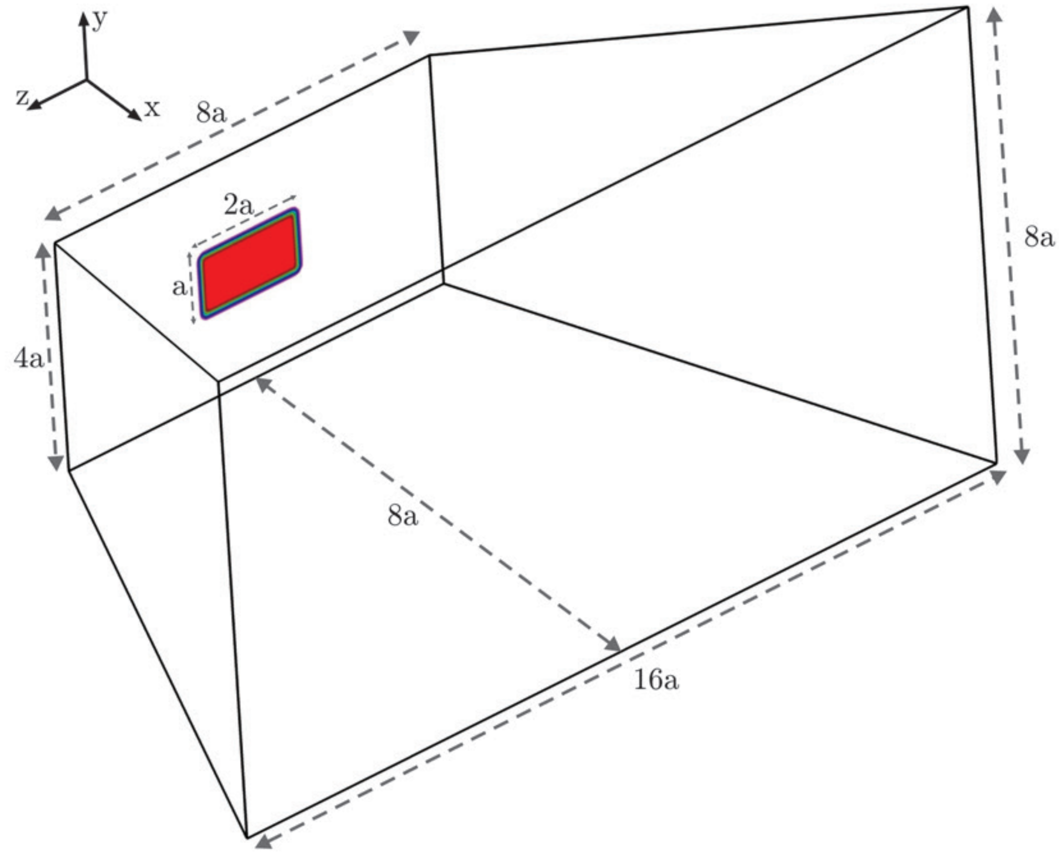

Figure 5.2: Characteristic dimensions of the computational domain. The origin of the coordinate system is placed at the centroid of the $2a$ by a rectangular opening.

The residual or the subgrid-scale (SGS) stress tensor is defined as $\tau_{ij}^R = \widetilde{u_i u_j} - \tilde{u}_i \tilde{u}_j$ from which the anisotropic residual stress $\tau_{ij}^r = \tau_{ij}^R - \frac{2}{3} k_r \delta_{ij}$ can be extracted. The isotropic content within the residual kinetic energy $k_r = \frac{1}{2}\tau_{ii}^R$ can be accounted for in the pressure correction term $\tilde{p}_m = \tilde{p} + \frac{2}{3}k_r$. In the original Smagorinsky-Lilly model, the anisotropic component of the residual stress tensor τ_{ij}^r is evaluated by obtaining the SGS turbulent viscosity using a fixed model constant [110]. To prevent the resulting numerical damping of the large-scale fluctuations, Germano[111] and Lilly [112] proposed the dynamic Smagorinsky-Lilly model in which the Smagorinsky model constant is continuously updated based on the calculations of the resolved fields. The dynamic approach is used in the present LES. The solutions are obtained using the coupled solver with a second-order fully implicit time marching scheme [113]. The finite volume approach is implemented to spatially discretize the equations with second-order central differencing for the diffusion terms and the third-order MUSCL scheme for the convective terms in the momentum equations.

5.3.1 Inflow and boundary conditions

The computational domain in figure 5.2 expands with the downstream distance to account for the growth of vortical structures [28]. The flow enters the computational domain at $x/a = 0$, where the origin of the coordinate system $(x, y, z) = (0, 0, 0)$ is placed at the centroid of the rectangular opening, and exits the domain at $x/a = 8$ subjected to the outflow conditions. The surrounding planes located at the traverse directions of the jet considered as symmetric boundaries start from $y/a = \pm 2$ and $z/a = \pm 4$ with expansion to $y/a = \pm 4$ and $z/a = \pm 8$.

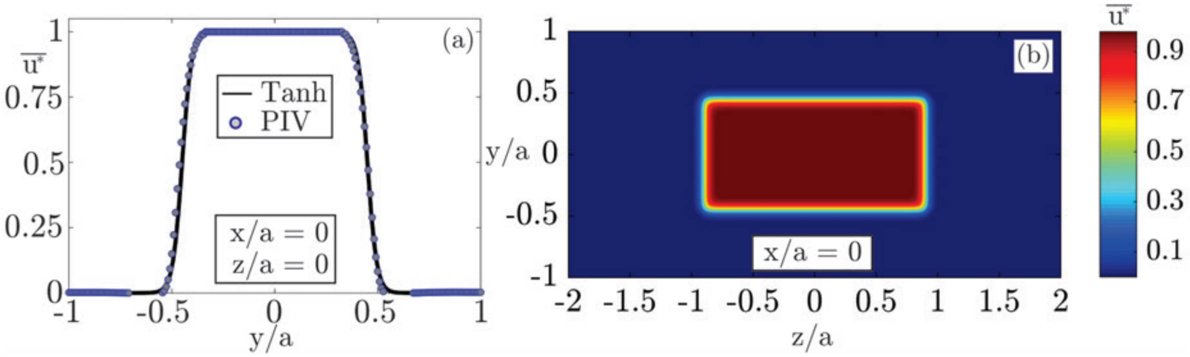

Figure 5.3: Inflow velocity condition: (a) Streamwise velocity profile obtained from particle image velocimetry (SPIV) measurement at the inlet $(x/a = 0, z/a = 0)$ overlaid by the hyperbolic Tangent function (Tanh) fit; (b) inlet velocity at the rectangular opening obtained from the Tanh fit.

To generate the inlet velocity, SPIV results are fitted to the hyperbolic Tangent function (Tanh). Figure 5.3a shows a typical top-hat velocity profile measured at the inlet $(x/a = 0, z/a = 0)$ overlaid by the corresponding Tanh fit. The Tanh fit is used to generate the rectangular inlet velocity by interpolating the values over the grid (Figure 5.3b). Present study is focused on the dynamics of isolated vortex rings. Therefore, the above velocity inlet is applied as a pulsed injection at a fixed flow rate during $t^* = 0 - 1$ after which the flow is stopped. To verify that the inlet velocity is properly defined, time-averaged flow

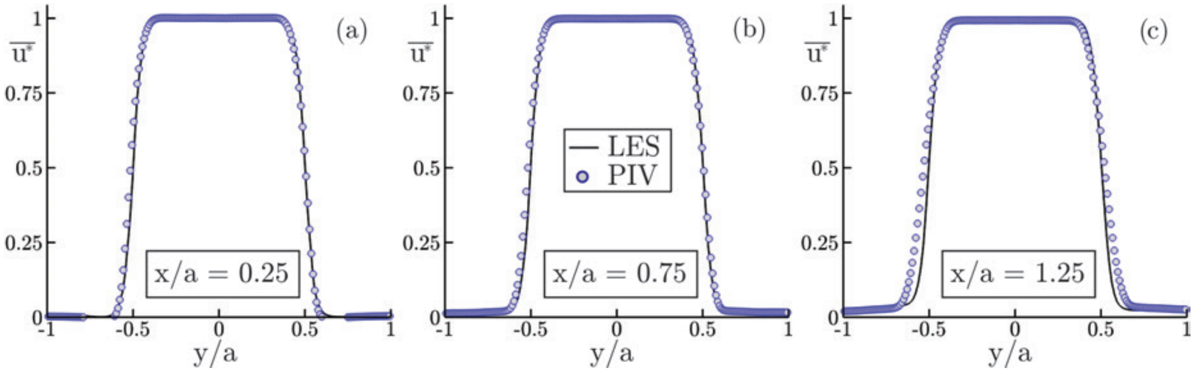

Figure 5.4: The time-averaged streamwise velocity profiles obtained from the SPIV compared to the LES simulations at $x/a = 0.25$ (a), 0.75 (b) and 1.25 (c).

Table 5.1: Reynolds numbers (Re_1, Re_2, Re_3, Re_4 and Re_5) defined using the centreline inlet velocity (U), hydraulic diameter (D_h), nozzle shorter edge (a) and the momentum thickness (θ).

Reynolds number	Re_1	Re_2	Re_3	Re_4	Re_5
$Re_{D_h} = UD_h/\nu$	355	877.50	1775	8775	17750
$Re_a = Ua/\nu$	266.25	658.12	1331.25	6581.25	13312.50
$Re_\theta = U\theta/\nu$	5.99	14.81	29.95	148.08	299.53

field is calculated in the near exit region for the continuous jet injection. The time-averaged velocity profiles obtained from the SPIV compare well with the LES results in figure 5.4 at $x/a = 0.25, 0.75, 1.25$. The inlet velocity profile produced here is used to define the five different Reynolds numbers (Re_1, Re_2, Re_3, Re_4 and Re_5) summarized in Table I. For convenience, these Reynolds numbers are shown as $R1$, $R2$, $R3$, $R4$ and $R5$ on the figures in this chapter.

5.3.2 LES grid considerations

The computational set-up is improved/refined from an earlier model [28] that used $4, 7, 15$ million cells to resolve the small scales of square jets at Reynolds number of 50000. Present study is conducted using nearly 30 million cells at lower Reynolds numbers of $350 - 17750$ that produce larger length scales. To further verify this, the integral (λ_I), Taylor (λ_T) and Kolmogorov (λ_K) length scales are evaluated in the continuous rectangular jet of $Re_5 = 17750$ using the HW data following Fellouah and Pollard [114]. In figure 5.5, the

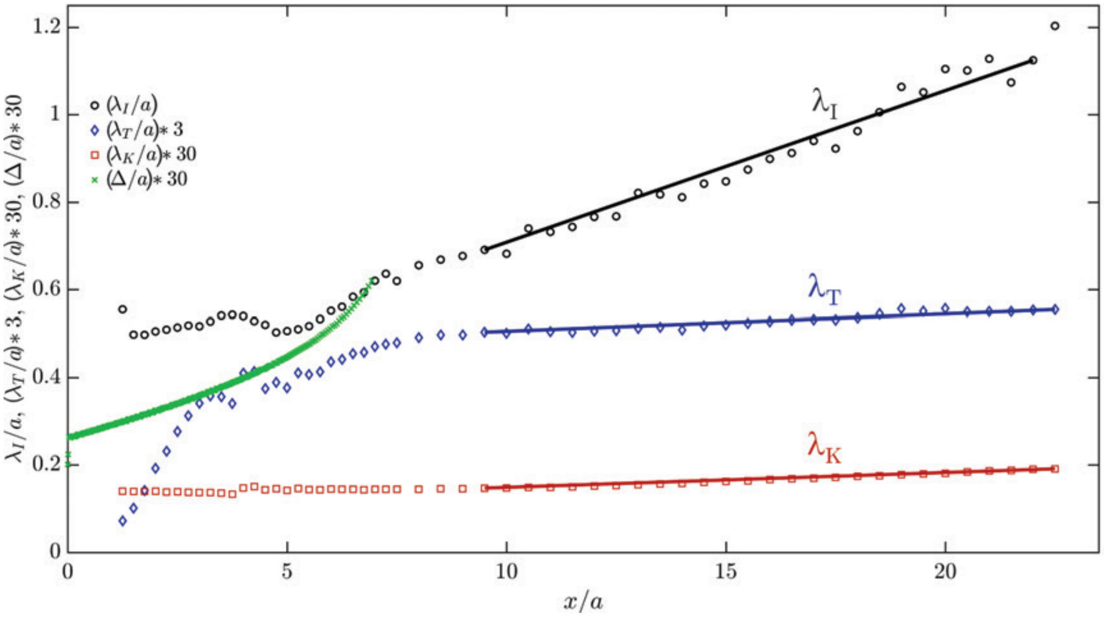

Figure 5.5: Integral (λ_I), Taylor (λ_T) and Kolmogorov (λ_K) length scales (from HW) compared to the local LES filter width (Δ) for $Re_5 = 17750$.

length scales are compared to the streamwise variation of the LES filter width Δ. All the scales grow with the downstream distance and reach linear trend in the fully-developed region. Within the near-field, the LES filter width ratio to the Kolmogorov scale varies between $1.7 - 4.3$. Considering a single vortex ring producing less small scales compared to a continuous jet [46, 12], the present grid is found very reliable. In addition, this grid evaluation is conducted for the highest Reynolds number of $Re_5 = 17750$ expected to produce the smallest length scales. Accordingly, it can be inferred that the quality of the present simulation is comparable to direct numerical simulations (DNS) for the lower Reynolds number cases (Re_1, Re_2, Re_3).

5.4 Results and discussion

Complex dynamics of the self-induced vortex distortions and the axis-switching phenomenon under various viscous diffusion effects can be better understood when focusing on the isolated rings. It is also important to distinguish the consequences of the axis-switching for isolated vortex rings and those continuously interacting within jet flows. To this end,

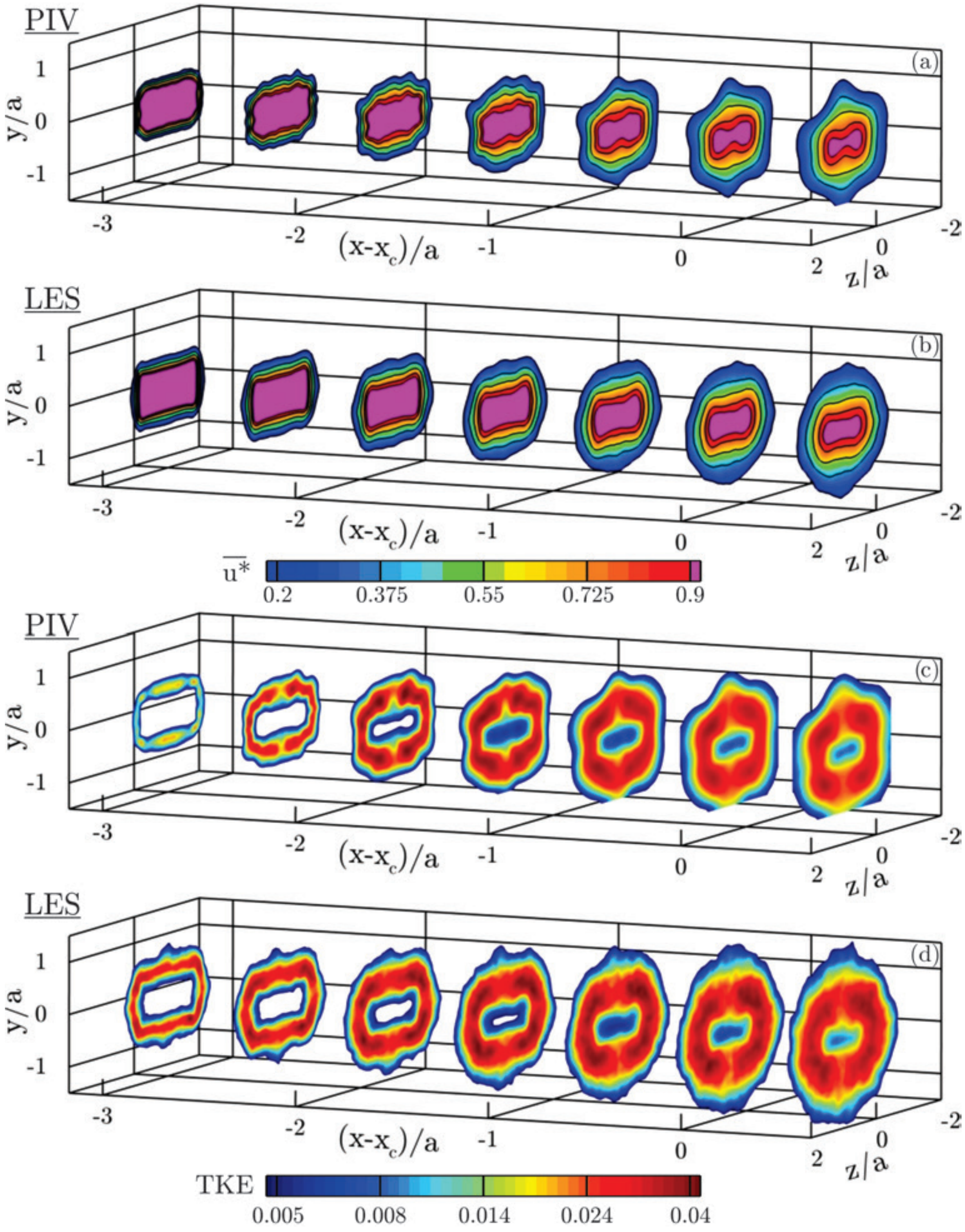

Figure 5.6: Axis-switching of the R_5 rectangular jet: Cross-sectional planes of the time-averaged streamwise velocity ($\bar{u}^*$) and turbulent kinetic energy (TKE): (a,c) SPIV (b,d) LES.

axis-witching is first defined for the time-averaged flow-field of the rectangular jets (from SPIV and LES). Afterwards, the study is focused on the definition and dynamics of the axis-switching in isolated rectangular vortex rings.

5.4.1 Experimental and numerical observation of the axis-switching consequences in rectangular jets

In figure 5.6, the time-averaged flow-fields in the cross-sectional planes of the Re_5 rectangular jet are presented where X_c defines the length of the potential core. The mean streamwise velocity $\bar{u^*}$ and the turbulent kinetic energy ($TKE = 0.5\left[(u^*_{rms})^2 + (v^*_{rms})^2 + (w^*_{rms})^2\right]$) obtained from the present SPIV measurements and the LES simulations characterize a rectangular shape of the near-exit jet cross-section at $(X - X_c)/a = -3$. With farther downstream distances approaching the end of the potential core at $(X - X_c)/a = 0$, the jet cross-section deviates from its rectangular shape. In accordance with the increased distortions near the corners and edges, the jet cross-sectional aspect ratio is reduced from 2 and approaches unity beyond the potential core $(X - X_c)/a = 2$. In the near-exit region, the large values of the TKE are concentrated within the rather rectangular shear layer. With increased downstream distance the shear layer becomes thicker, reshapes into the rounder geometries and the TKE levels increase near the jet centreline.

In the latter stage of the cross-sectional transformation from the rectangular to elliptic/circular shapes, there is a sharpening or peak developing at the vertical symmetry axes. This phenomenon is due to the instantaneous deformation of the vortex rings described in the following sections. For improved volumetric illustration of the cross-sectional reshaping, iso-surfaces of the mean streamwise velocity ($\bar{u}^* = 0.25, 0.5, 0.9$) are obtained from the interpolation of multiple cross-sectional SPIV planes compared with the LES in figure 5.7. In jet flows, the continuous generation of the vortex rings and their interactions could prevent the complete observation of the axis-switching. In the following sections, it is shown that the isolated vortex rings appear to be rotated due to the axis-switching [28, 26]. However, it will be emphasized that the rotation is merely a visual observation, and the axis-switching should be defined as a deformation or reshaping phenomenon.

5.4.2 Preliminaries on the axis-switching and viscous diffusion in isolated rectangular vortex ring

Results presented in the following sections focus on the self-induced deformations of the isolated rectangular vortex rings under variable viscous effects imposed by the Reynolds

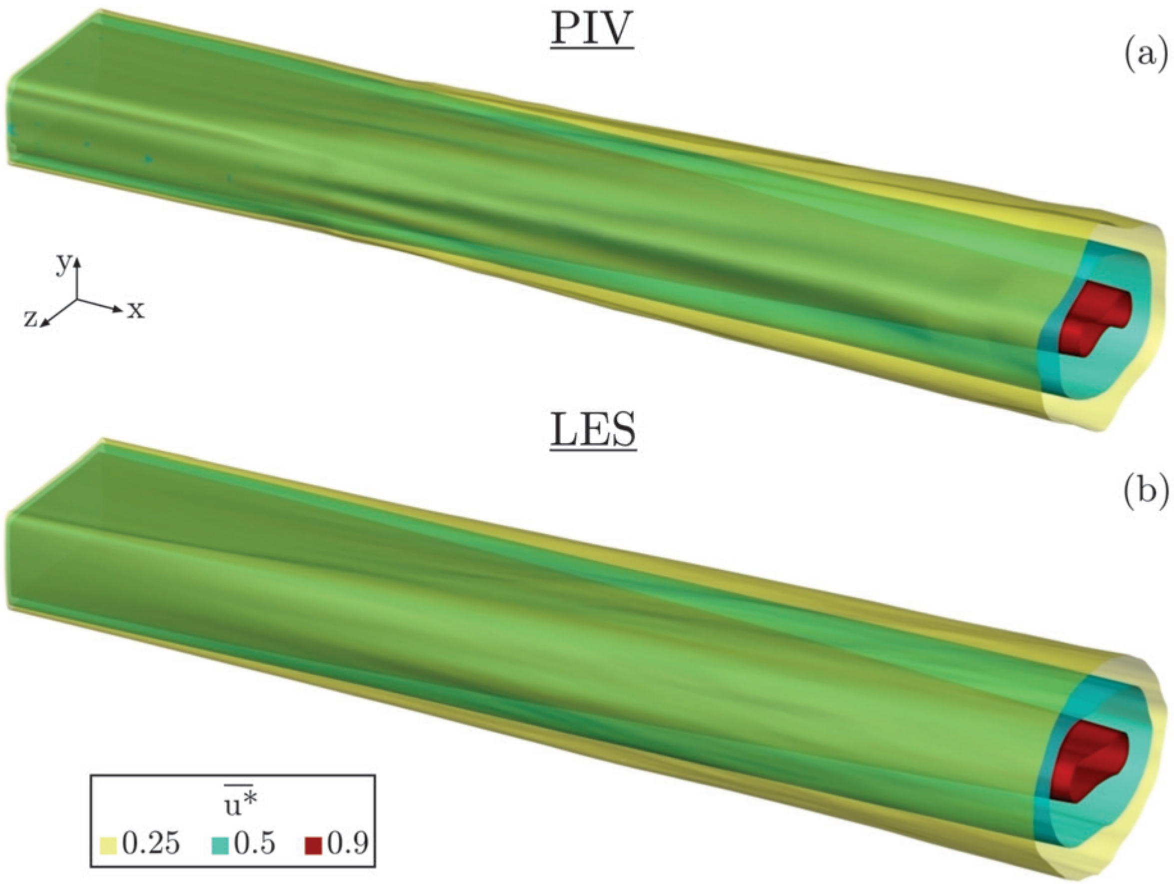

Figure 5.7: Axis-switching of the R_5 rectangular jet: Iso-surfaces of the mean streamwise velocity ($\bar{u}^* = 0.25, 0.5, 0.9$): (a) SPIV (b) LES. See figure 5.6 for the streamwise length of the iso-surfaces.

numbers $Re_i = UD_h/\nu = 355, 877.5, 1775, 8775, 17750$ ($i = 1, ..., 5$). The process of the rectangular vortex ring generation within the computational domain is first described. Also, the term "axis-switching" is clearly defined for isolated vortex rings. Effect of the viscous diffusion is first explored for the vortex core dynamics and then for the vortex ring curvature-induced deformations. Early state of the rectangular vortex ring is illustrated in figure 5.8.

During the time $t^* = 0 - 1$, the flow is continuously injected using the velocity profile generated in the earlier sections. Therefore, the inlet momentum thickness is identical for all the cases. The injection is stopped after $t^* = 1$ resulting in the formation of a single

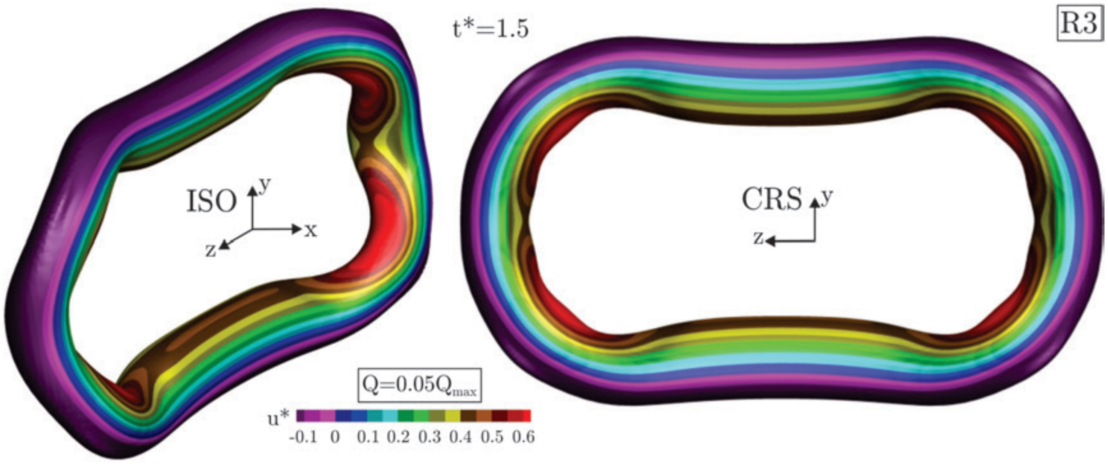

Figure 5.8: Early stage of the rectangular vortex ring obtained from LES, visualized by the Q-criterion ($Q = 0.05Q_{max}$) and coloured by the instantaneous streamwise velocity (u^*) at $t^* = 1.5$ for the case R_3: (a) isometric (ISO) view; (b) cross-sectional (CRS) view.

vortex ring. The vortex topologies visualized by the iso-surface of the Q-criterion [61] ($Q = 0.05Q_{max}$) are coloured by the instantaneous streamwise velocity (u^*). For each case, Q_{max} is the maximum value of the Q-criterion at $t^* = 1$. For instance, figure 5.8 illustrates the initial stage ($t^* = 1.5$) of the vortex ring formed for the Re_3 case. Also, figure 5.8 can be used as a reference for the isometric (ISO) and cross-sectional (CRS) orientations used in the following discussions. As seen in figure 5.8, the highest velocity occurs at the sharp corners of the initially rectangular vortex ring. This higher velocity is induced due to the larger local curvature of the ring as predicted by the Biot-Savart law [42].

In figure 5.9, axis-switching of an isolated rectangular vortex ring is illustrated. The phosphoric-green colour iso-surfaces of the Q-criterion ($Q = 0.05Q_{max}$) identify the Re_5 vortex ring topologies at the early stage ($t^* = 1.5$) as well as the time of the axis-switching ($t^* = 8.5$). The side (SV), top (TV) and diagonal (DV) view planes are used as the reference for the vortex ring deformations. According to the illustrations, the rectangular vortex ring appears to be rotated 90 degrees around the x-axis. However, we emphasize that the observation of such a rotational behaviour is merely from a visual point of view. In the following sections, the spatio-temporal evolution of the vortex ring describes the underlying mechanisms for the axis-switching. Another important phenomenon is the effect of the viscous diffusion on vortex cores as presented in figure 5.10. To this end, the top view (TV) plane ($y/a = 0$) is passed through the cores of the rectangular vortex ring at $t^* = 2.5$ for Re_1, Re_2, Re_3, Re_4 and Re_5. Using the Q-criterion the shearing (blue)

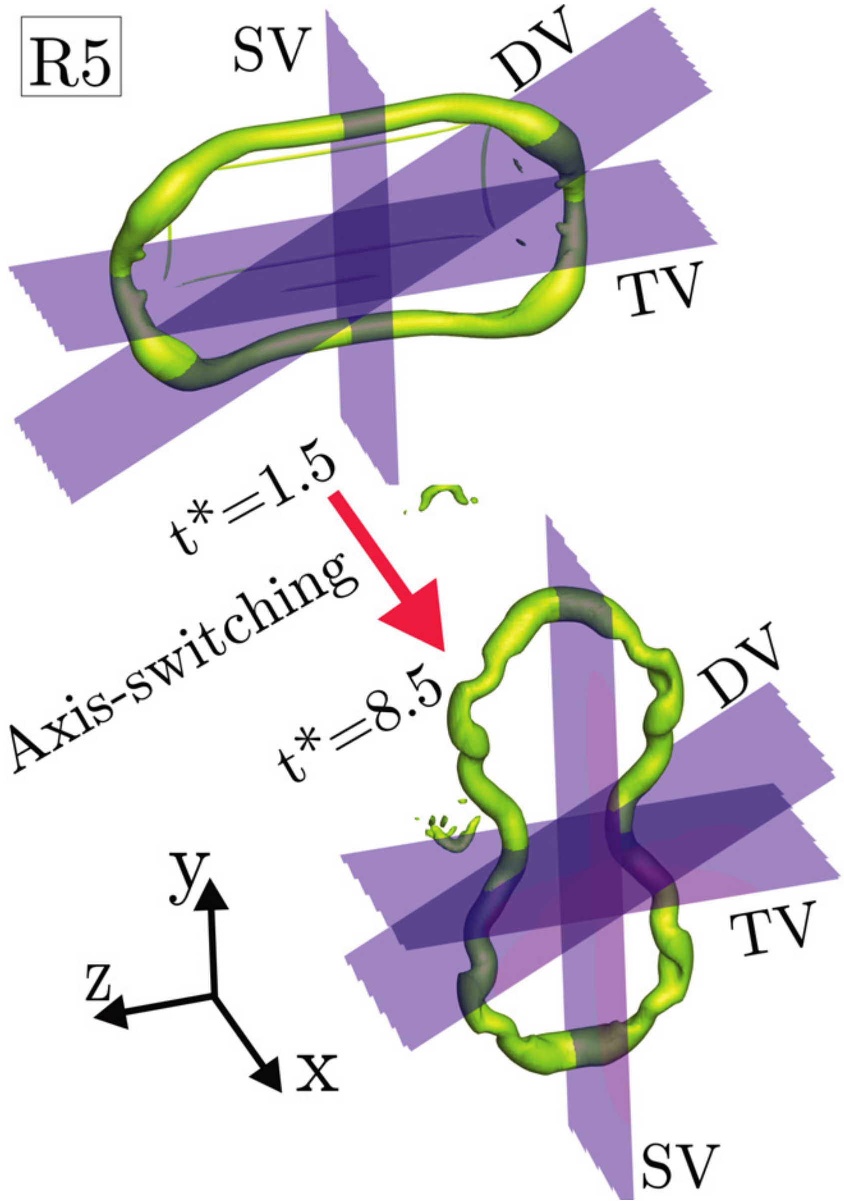

Figure 5.9: Axis-switching of the R_5 isolated vortex ring (from LES) and identified by the phosphoric-green colour iso-surfaces of the Q-criterion ($Q = 0.05Q_{max}$) at $t^* = 1.5$ and $t^* = 8.5$. The side (SV), top (TV) and diagonal (DV) view planes are used as the reference for the deformations.

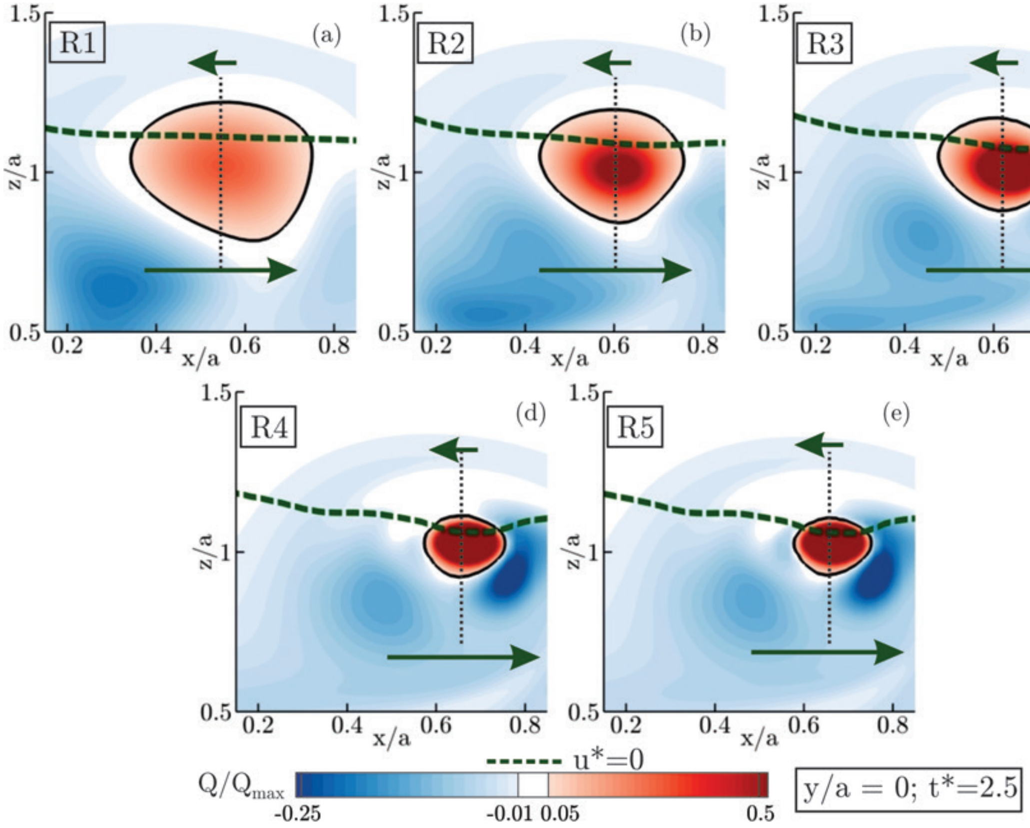

Figure 5.10: Q-criterion (from LES) for shearing (blue) and rotating (red) regions of the vortex cores in $y/a = 0$ planes passed through the (a) R_1, (b) R_2, (c) R_3, (d) R_4 and (e) R_5 rectangular vortex rings at $t^* = 2.5$. The horizontal dashed line separates the high-speed and the low-speed regions. Arrows schematically show the direction of streamwise velocity on either side of the critical layer.

and rotating (red) regions are isolated by the black solid line. Unlike vorticity, using the Q-criterion can distinguish between the pure shearing and rotating flow elements [48]. The horizontal dashed line separates the high-speed and the low-speed regions and hence it represents the critical layer. The arrows schematically show the direction of the streamwise velocity on either side of the critical layer. Larger vortex cores with a diffused rotational content are formed under the strongest viscous diffusion effects ($Re_1 = 355$). On the other hand, smaller vortex cores exhibiting accumulation of the rotational fluid are formed at higher Reynolds numbers.

In figure 5.11, the line plots of the Q-criterion (figure 5.11a) and the corresponding

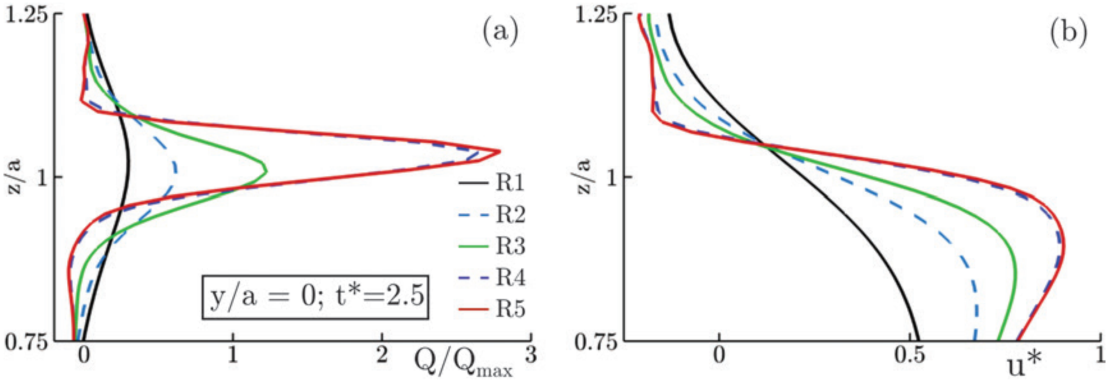

Figure 5.11: (a) Q-criterion and (b) streamwise velocity (u^*) near the R_1, R_2, R_3, R_4, R_5 vortex cores (from LES) in $y/a = 0$ plane passed through the rectangular vortex ring at $t^* = 2.5$. Line plots are extracted along the vertical dotted lines on the vortex cores shown in figure 5.10.

(figure 5.11b) streamwise velocity (u^*) are presented at the vicinity of the vortex cores visualized earlier in figure 5.10. The profiles are extracted along the vertical dotted lines passed through the vortex cores shown in figure 5.10. Above observations regarding the rotational content of the vortex cores can be verified by the line plots of the Q-criterion (figure 5.11a). The rotation line plots demonstrate a narrowed distribution (accumulation) with a larger peak value for the high Reynolds number cases and found almost identical for the Re_4 and Re_5 Reynolds numbers. Conversely, the peak values drop and the profiles become wider with increased viscous diffusion effects (lower Reynolds numbers). Smaller self-induced velocities are found near the larger vortex cores due to the stronger viscous diffusion effects (figure 5.11b).

5.4.3 Spatio-temporal vortex deformations

In this section the spatio-temporal deformations of initially rectangular vortex rings are presented for the Re_1, Re_2 and Re_5 cases. The rectangular vortex ring topologies are visualized by calculating the Q-criterion [61]. The $Q = 0.05Q_{max}$ iso-surfaces of the vortex structures are coloured by the instantaneous streamwise velocity and presented in isometric (ISO) and cross-sectional (CRS) views. Figure 5.12 illustrates the vortex rings developed at the lowest Reynolds number $Re_1 = 355$ with the strongest viscous diffusion effects. At $t^* = 1.5$, the vortex ring maintains its rather rectangular shape. The corners of the ring which have a larger curvature produce higher self-induced velocities as stated by the

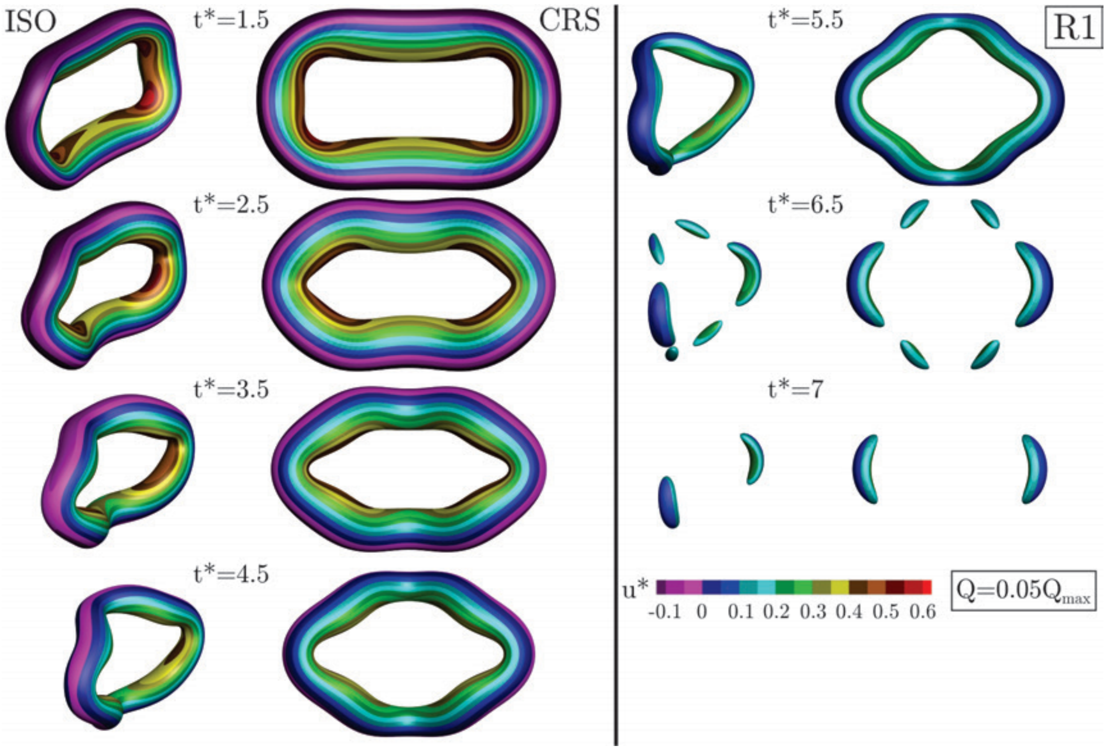

Figure 5.12: Topologies of the R_1 vortex ring (from LES) visualized by $Q = 0.05Q_{max}$ and coloured by the instantaneous streamwise velocity (u^*) during $t^* = 1.5 - 7$.

Biot-Savart law [42]. This higher velocity is observed at the corners of the ring by the streamwise velocity colour-map at $t^* = 1.5$. The four corners of the ring tend to move faster with respect to its flat sides. This results into the deformation of the ring from its initial rectangular shape. In addition, the ring topology deviates from two-dimensionality and becomes more three-dimensional. From a visual point of view, the ring appears to go through a contraction along its longer edge while the shorter edge tends to expand. However, the Re_1 ring starts to break down and diffuse during the times $t^* = 6.5 - 7$ before more distortions occur. Therefore, the Re_1 vortex ring does not accomplish the axis-switching process described earlier.

When increasing the inertial effects in the case $Re_2 = 877.5$, a similar curvature-induced velocity mechanism distorts the ring as seen in figure 5.13. Again, the faster moving corners initiate the deformations and move ahead of the flat sides. During this stage, the ring topology deviates from two-dimensionality and becomes three-dimensional. Later during the times $t^* = 3.5 - 5.5$, the previously flat sides attain high-curvatures

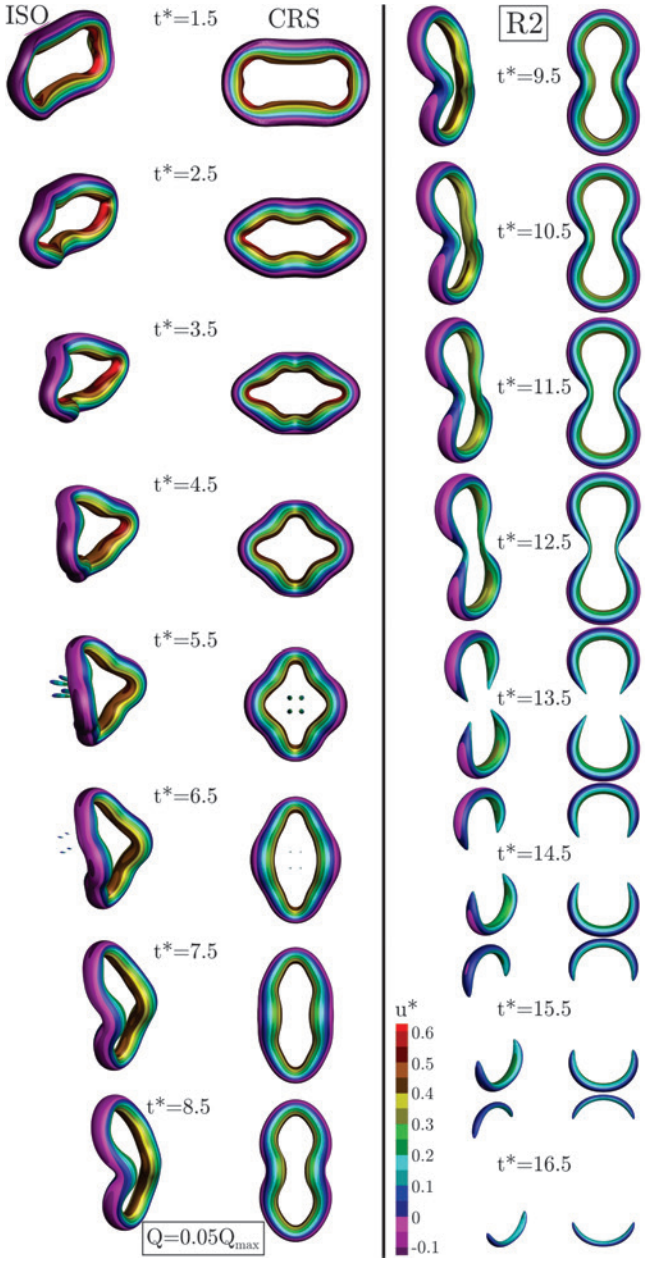

Figure 5.13: Topologies of the R_2 vortex ring (from LES) visualized by $Q = 0.05Q_{max}$ and coloured by the instantaneous streamwise velocity (u^*) during $t^* = 1.5 - 16.5$.

compared to the corners and consequently start to move faster. Converse to the initial three-dimensionality, this process tends to flatten the ring back to the two-dimensions. The above mentioned curvature-induced three-dimensionality followed by the recovering back into the two-dimensionally flat ring can also be interpreted by the azimuthal pressure perturbations described in detail by Ghasemi et al. [28] in terms of the local pressure differences in the back and front of the ring. Eventually at $t^* = 8.5$, the ring seems to be 90^o rotated around the x-axis. This is when the first axis-switching is completed by the dominance of the self-induced deformations over the viscous diffusion. To emphasize that, the ring is not actually rotating while earlier studies classically define "axis-switching" as a rotational phenomenon observed from the time-averaged fields of the non-circular jets. Very few studies [28, 115, 116] such as the present work focus on the distortions of isolated non-circular vortex rings to describe that axis-switching is a reshaping/deformation phenomenon. During the times $t^* = 9.5 - 12.5$, the ring demonstrates a bifurcation into a pair of semi-circular topologies. Throughout this phase until $t^* = 16.5$, the self-induced deformations are not sufficiently strong to overcome the viscous diffusion and hence the ring tends to decay rather than going through the second axis-switching. Similarly, there is only a single axis-switching accomplished for Re_3 occurring slightly earlier than Re_2.

With reduced viscous effects, Re_4 and Re_5 vortex rings demonstrate very similar Reynolds number independent dynamics. Compared to the lower Reynolds number cases, thinner and hence more distorted/unstable vortex topologies are formed. Spatio-temporal deformations of the vortex ring Re_5 are presented in figure 5.14. From $t^* = 1.5$ to $t^* = 7.5 - 8.5$, the first axis-switching is accomplished for the Re_5 vortex ring. The vortex ring topology demonstrates more distortions associated with the high-frequency (short-wavelength) azimuthal instabilities. Further in time/space, a second axis-switching is detected accomplishing nearly at $t^* = 18.5$. Another observation for high Reynolds numbers (Re_4 and Re_5) compared to the viscous dominated cases (Re_1, Re_2 and Re_3), is the formation of small scale vortical structures in the wake of travelling rings. It is worth mentioning that the above explained vortex ring dynamics (self-induced deformations, bifurcation, breakdown, reconnection) are very similar to the evolution of the vortices in the wake of an aircraft as visualised by engine contrails [117, 118, 119, 120]. The formation mechanism of the ring shape vortices from a pair of counter-rotating straight loops are different from the vortex rings of the present study. However, the evolved vortex rings demonstrate very similar dynamics as nicely represented by Misaka et al. [121].

Domination of inertial effects and the more unstable nature of thinner vortex rings result in the azimuthal perturbations [28]. Accordingly, the rib-shape vortices are occasionally accompanied with the hairpin shape structures. Hairpin vortices develop more commonly in the continuous formation of the train of interacting vortex rings. First axis-switching

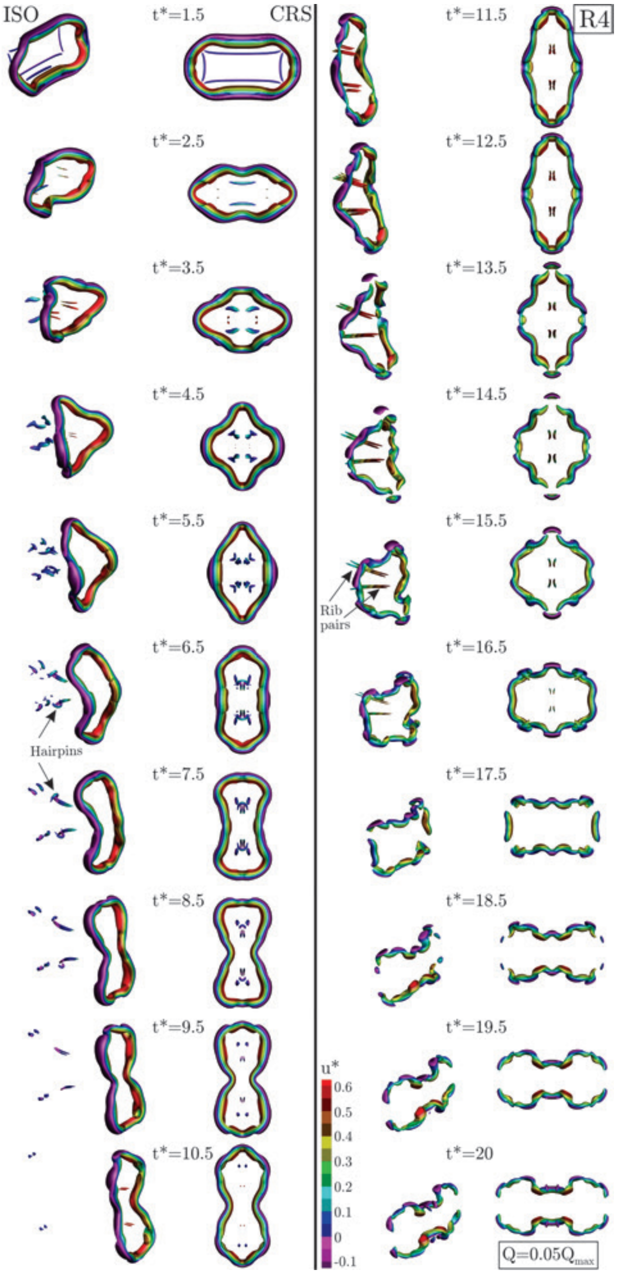

Figure 5.14: Topologies of the R_5 vortex ring (from LES) visualized by $Q = 0.05Q_{max}$ and coloured by the instantaneous streamwise velocity (u^*) during $t^* = 1.5 - 20$.

is mostly attributed to the vortex ring self-induced (curvature-induced) deformations and azimuthal pressure perturbations [12]. The second axis-switching is influenced by the azimuthal perturbations as well as the appearance of ribs and hairpin vortices. Therefore, increased presence of these secondary instabilities and the corresponding rib and hairpin shape vortices in the wake of the ring, advances the occurrence of the second axis-switching. During the second axis-switching, the Re_5 ring topology exhibits waviness associated with these high-frequency azimuthal perturbations.

Azimuthal perturbations near the Re_5 ring are presented in figure 5.15 at $t^* = 1.5$, 2.5, 4.5 and 8.5 using the cross-sectional planes of streamwise vorticity (ω_x^*) coloured from blue (-3) to red (3). The negative (blue) and positive (red) regions of the streamwise vorticity characterize the local clockwise (CW) and counter-clockwise (CCW) senses of rotation with respect to the x-axis. The general observation is the formation of counter-rotating (CW/CCW) streamwise vorticity pairs. This is due to the superposition of secondary instabilities on top of the primary Kelvin-Helmholtz (KH) mechanism acting on the vortex rings. At the early stage of $t^* = 1.5$, streamwise vorticity pairs are rather large and located near the edges of the vortex ring. At $t^* = 2.5$ where the ring is more distorted, the CW/CCW pairs emerge near the axis of the vortex ring. At this time, two pairs of the counter-rotating rib-shaped vortex loops appear. Later at $t^* = 4.5$, the streamwise rib vortices approach each other near the axis. Eventually at the time of the first axis-switching ($t^* = 8.5$) where the ring topology demonstrates spiral distortions, the frequency of the small scale (reduced wavelength) counter-rotating pairs significantly increases.

5.4.4 Space-time mapping of the vortex ring axis

Since the spatio-temporal evaluation of the vortex rings demand cumbersome post-processing of the large scale data, we propose a simple space-time mapping technique to predict the overall axis-switching characteristics. To generate a space-time map during the times $t^* = 0 - 20$, the axis of each vortex ring (along the $x - axis : y/a = z/a = 0$) is monitored by extracting 2000 line samples of the solution data. Space-time map of the streamwise velocity on the vortex axis is presented as a contour in figure 5.16. The overlaid cross-sectional (CRS) views of the vortex topologies are correlated with the space-time map to interpret the vortex deformation phenomena. We call the colourful region of the contours in figure 5.16 the "space-time band". In accordance with the formation of the larger structures due to the viscous diffusion effects, a wider "space-time band" is formed for the low Reynolds number cases. In addition, the slope of the "space-time band" increases at larger Reynolds numbers. This implies that it takes longer times for the deceleration of the vortex rings while inertia dominates the viscous dissipation. In other words, the larger

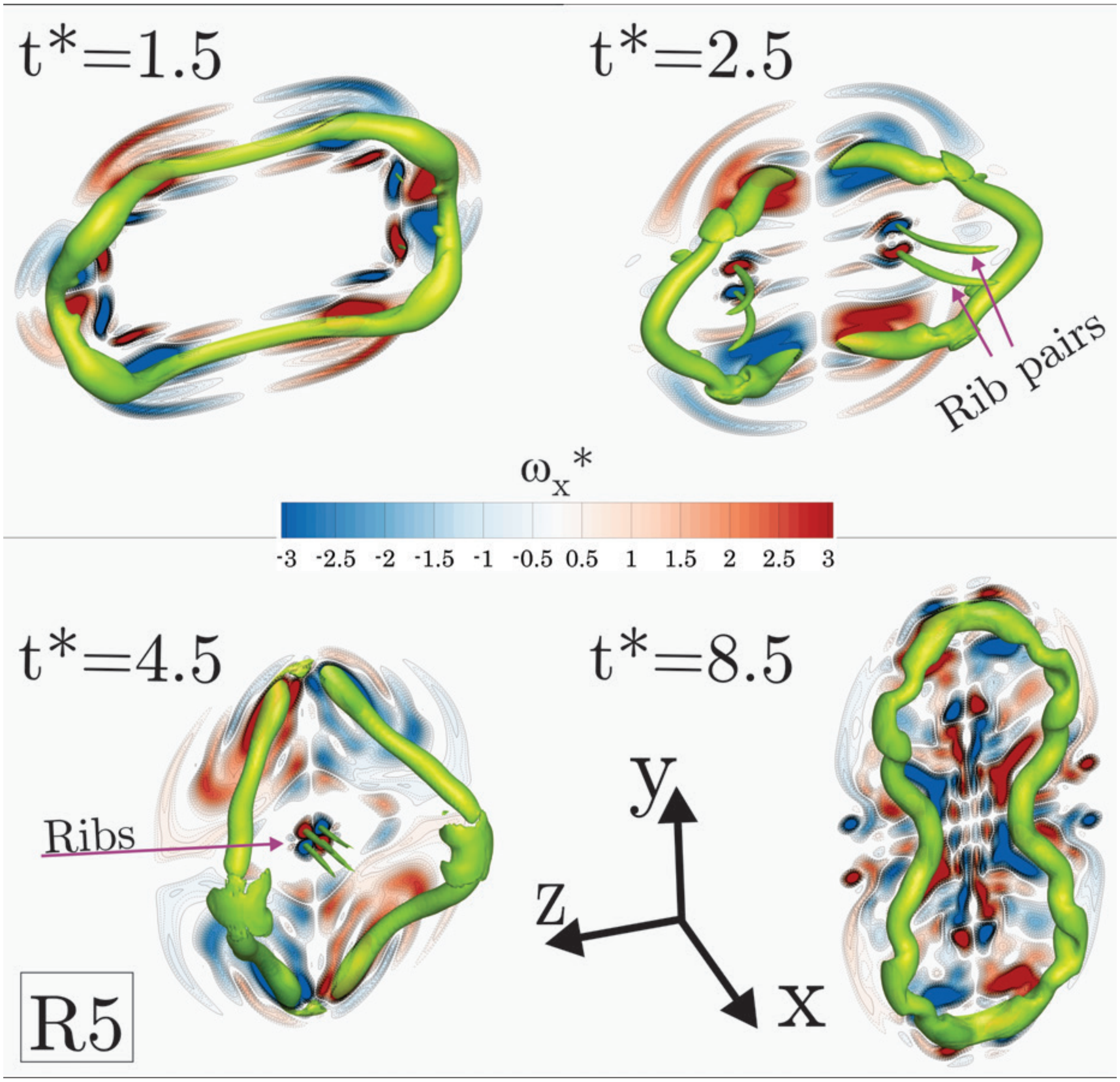

Figure 5.15: R_5 vortex ring ($Q = 0.05Q_{max}$ from LES) at $t^* = 1.5$, 2.5, 4.5 and 8.5. Cross-sectional planes of streamwise vorticity (ω_x^*) coloured from blue (-3) to red (3) are passed through the ring. The negative (blue) and positive (red) regions of the streamwise vorticity respectively characterize the clockwise (CW) and counter-clockwise (CCW) senses of rotation with respect to the x-axis.

vortex cores formed due to the viscous diffusion attain smaller self-induced velocities and are hence decelerated earlier.

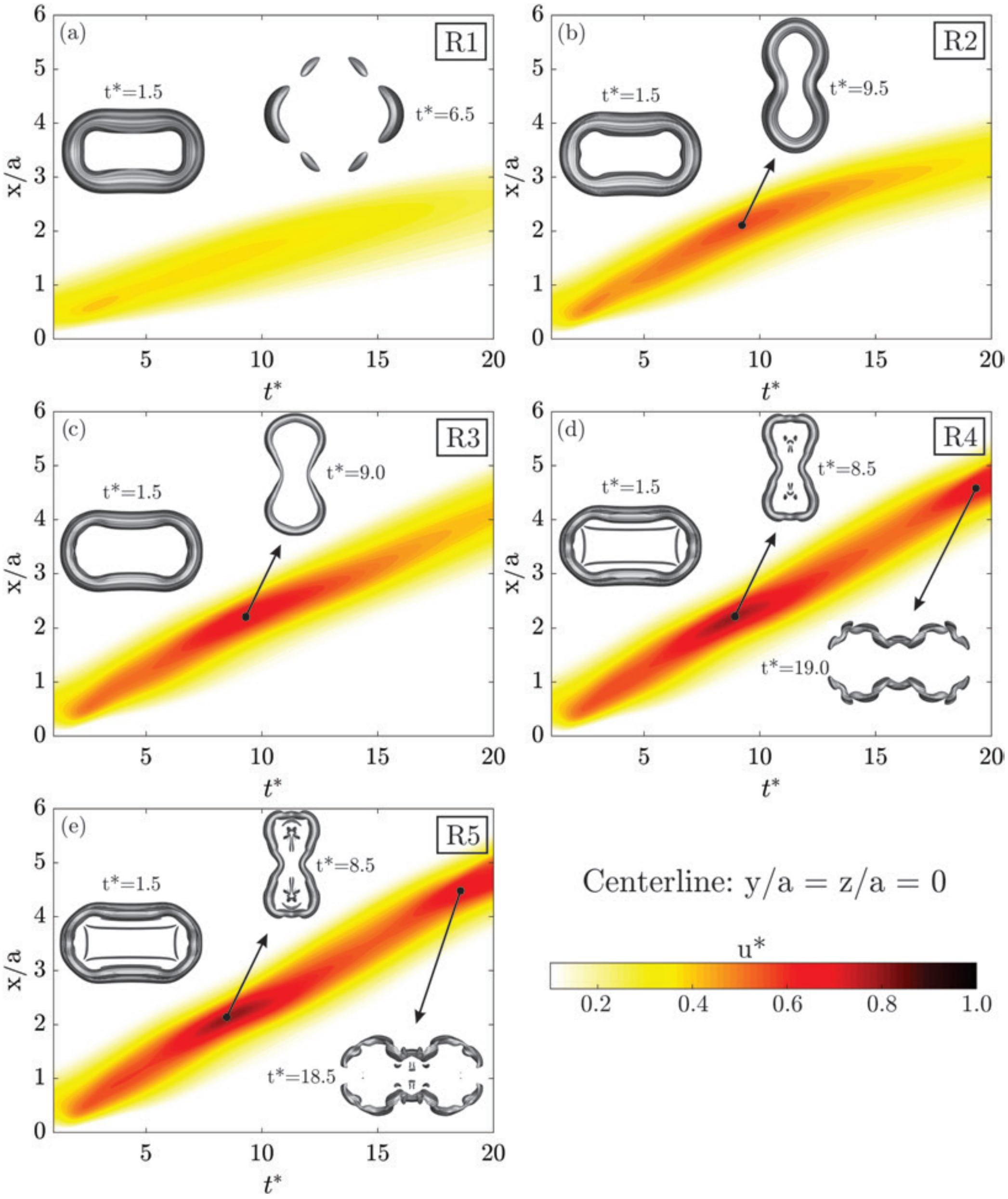

Figure 5.16: Space-time map (from LES) of the instantaneous streamwise velocity (u^*) along the vortex axis ($y/a = z/a = 0$) for (a) R_1, (b) R_2, (c) R_3, (d) R_4 and (e) R_5.

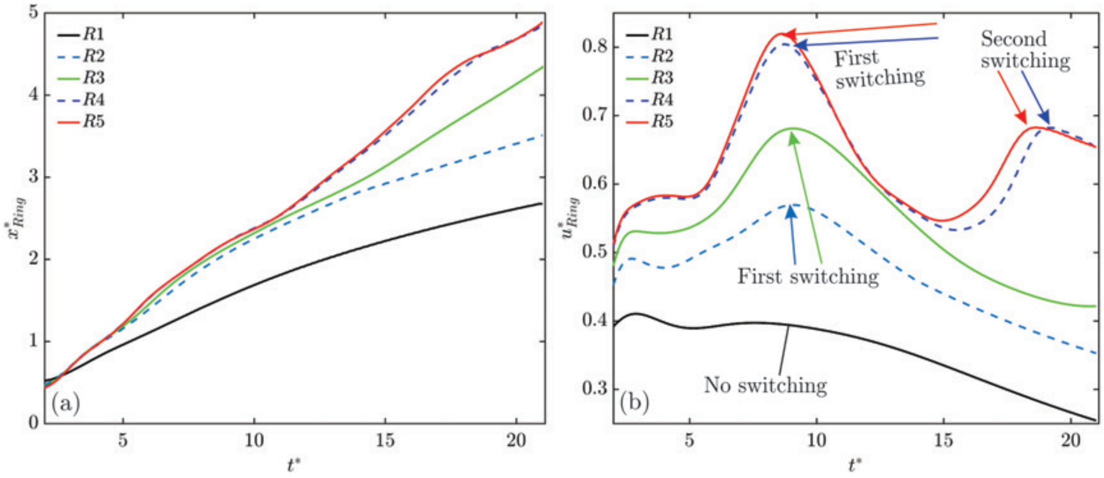

Figure 5.17: Temporal variation of the vortex ring (from LES): (a) penetration (x^*_{Ring}) and (b) advection velocity (u^*_{Ring}) for R_1, R_2, R_3, R_4 and R_5.

For Re_1 with no axis-switching, the “space-time band” exhibits a rather uniform (diffused) velocity distribution. On the other hand, Re_2 and Re_3 vortex rings develop a region of strong space-time correlation in the instantaneous streamwise velocity (u^*). This high velocity spot is associated with the time/space of the occurrence of a single axis-switching for Re_2 and Re_3. Likewise, Re_4 and Re_5 demonstrate very similar space-time maps with two high velocity zones associated with the times/spaces at which the first and second axis-switching take place. The vortex topologies corresponding to the first and second axis-switchings are displayed on the figure near the high velocity spots. This analysis can easily provide the information regarding the deformations of non-circular vortex rings if proper experimental/numerical data are available. From the space-time mapping of the vortex ring axis, it can be inferred that the localized flow accelerations take place due to the minimized cross-sectional area encompassed by the ring at the time/location of the axis-switching.The space/time map can be used to determine the penetration rate and the advection velocity of the vortex ring.

At each instant, the maximum velocity on the vortex ring axis defines the advection velocity (u^*_{Ring} in figure 5.17b) and the location it occurs determines the penetration (x^*_{Ring} in figure 5.17a). Interestingly, the time and number of the major peaks in u^*_{Ring} plots correspond to the axis-switching. Vortex rings initially penetrate rather linearly followed by an asymptotic deceleration. The Re_1 ring quickly decelerates (lowest penetration) due to the strong viscous effects and shows no major peaks in u^*_{Ring} as no axis-switching is accomplished. On the other hand, Re_2 and Re_3 penetrate farther and demonstrate one

u^*_{Ring} peak correlated with a single axis-switching. The rings Re_4 and Re_5 exhibit nearly identical (Reynolds number independent) penetration and advection velocity trends. In general, the completion of the axis-switching phenomenon is found delayed with increased viscous diffusion effects.

5.4.5 Correlation between the axis-switching and the varicose mode of instability

Above discussions regarding the axis-switching of rectangular vortex rings reveal that the phenomenon is initiated by the curvature-induced deformations. As a result, the longer/shorter edges of the initially rectangular vortex ring go through the contractions (inward motion) and expansions (outward motions) constructing the axis-switching phenomenon. To better understand these contractions/expansions, three planes of view are passed through the initially rectangular vortex rings (refer to figures 5.7 and 5.8 for orientation). The side (SV) and the top view (TV) planes are defined as $z/a = 0$ and $y/a = 0$, respectively. The diagonal view (DV) is the $y/z = 0.5$ plane passed through the corners of the rectangular ring. Using the positive content of the Q-criterion, the rotating vortex cores are extracted and presented in figure 5.18. The time line in the bottom left of the figure represents the time instants at which the vortex cores travel from left to right during $t^* = 1 - 20$. Each panel defines the streamwise location x/a as well as the spanwise locations z/a, y/a or ζ/a in SV, TV and DV planes, respectively. For each panel, the horizontal solid lines characterize the location of the nozzle edge from which the shear layer separates. Also, the vertical dashed lines characterize the occurrence of the axis-switching at that time/space. The first observation is that the vortex cores become smaller with increased Reynolds number due to the declined influence of the viscosity. In the SV plane, vortex cores move outward with respect to their original location at the nozzle edge (expansion). On the other hand, in the TV and DV planes vortex cores move inward (contraction). This expansion in the SV plane and the contraction in the TV and DV planes co-occurs until the first axis-switching is finalized. If a second axis-switching takes place, this process is reversed with expansion in the SV planes versus the contraction in the TV and DV planes.

Interestingly, these contractions/expansions resemble the varicose mode of instability, seen earlier in the symmetric/axisymmetric oscillations in planar/circular jets [122]. To quantify this for rectangular rings, coordinates of the maximum Q-criterion in figure 5.18 are identified in SV, TV and DV planes and presented in figure 5.19. The extracted points are fitted to the Sine functions of the form $\frac{y}{a} = A * Sin\left[\frac{2\pi}{\lambda}\left(\frac{x}{a}\right) - \beta\right] + B$. Here,

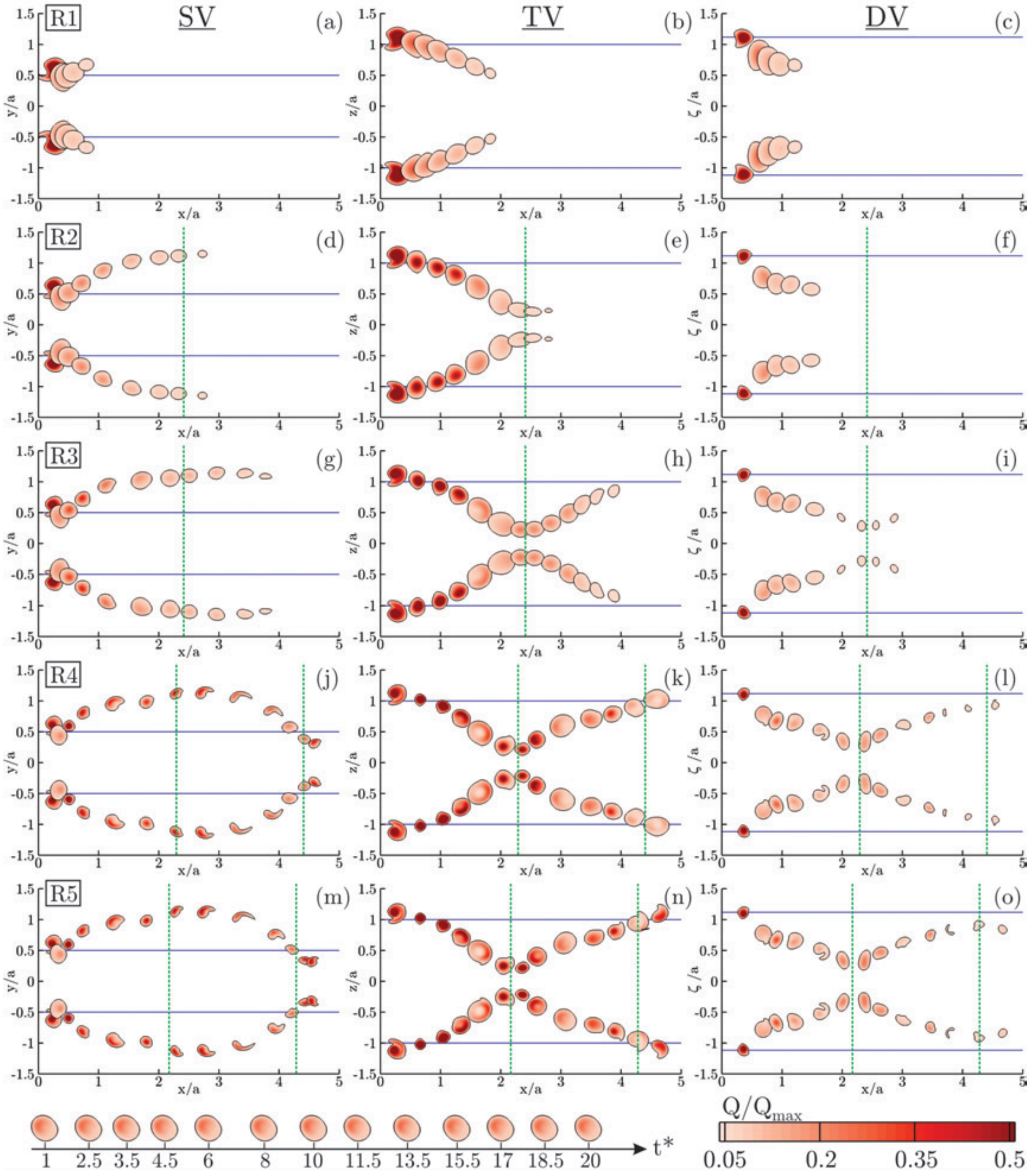

Figure 5.18: Trajectory of the vortex cores (from LES) displayed using the Q-criterion in the side (SV: $z/a = 0$), top (TV: $y/a = 0$) and diagonal (DV: $y/z = 0.5$) views during $t^* = 1 - 20$.

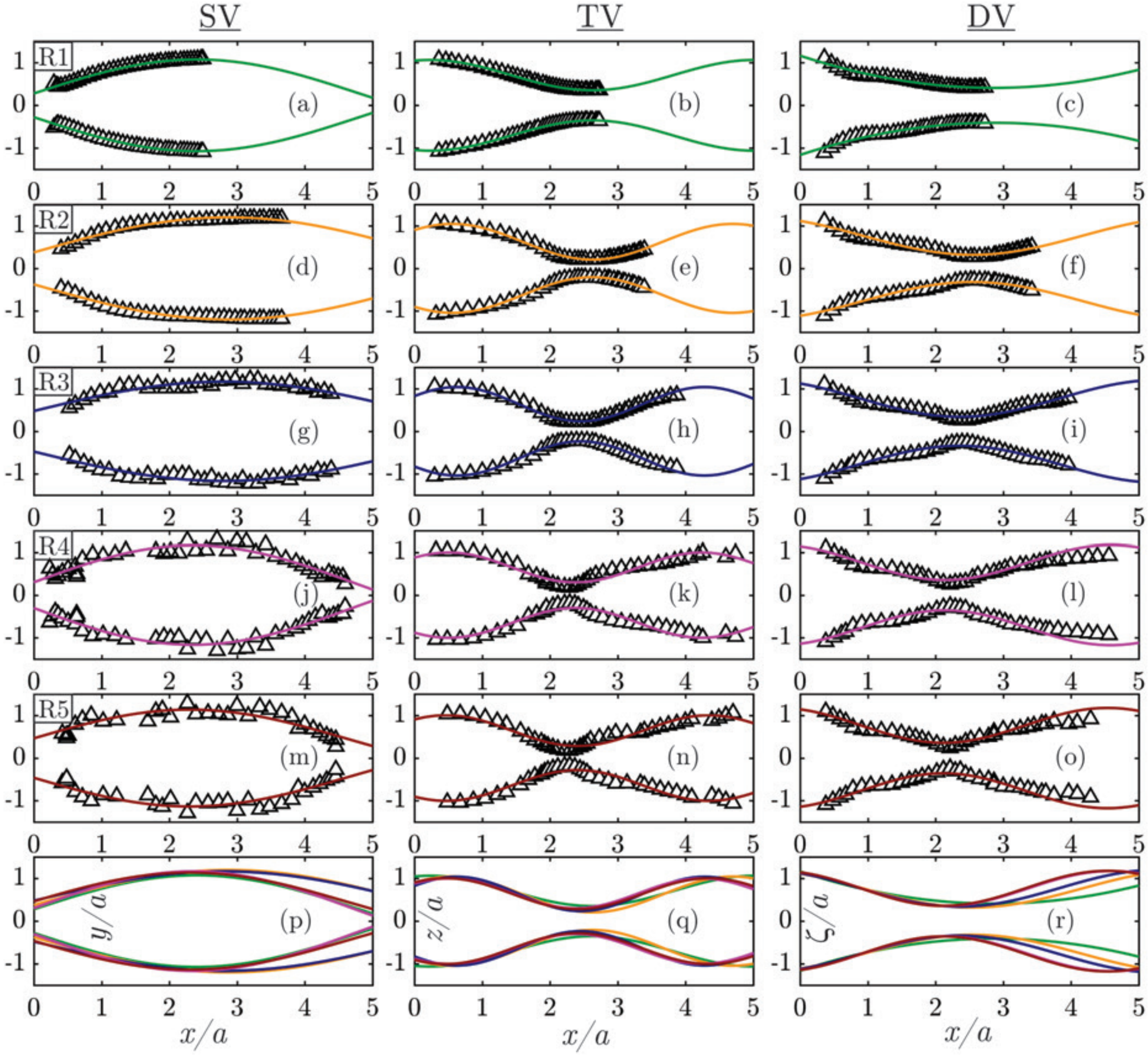

Figure 5.19: Vortex core trajectories (from LES) in SV, TV and DV planes fitted to the Sine functions of the form $\frac{y}{a} = A * Sin\left[\frac{2\pi}{\lambda}(\frac{x}{a}) - \beta\right] + B$ during $t^* = 1 - 20$.

A, B, λ and β denote the amplitude, interception with the vertical axis, wavelength and the phase difference, respectively. The wavelength associated with the Sine functions can be approximated as $\lambda = 10a$ equivalent to the axis-switching length of $\frac{\lambda}{4} = 2.5a$. The contractions/expansions in the SV plane shape the Sine function with $\beta = 0$ while $\beta = \frac{\pi}{2}$ forms the Cosine function in TV and DV planes. This quarter ($\beta = \frac{\pi}{2}$) cycle of phase lagging/leading found in the varicose modes between the orthogonal SV and TV planes is remarkably equivalent to the frequency of axis-switching. Therefore, axis-switching of rectangular vortex rings is governed by the counteraction of two orthogonal varicose modes of instability propagating with the phase leading/lagging equivalent to the quarter of a cycle.

5.5 Summary

Viscous diffusion effects on the self-induced distortions of the aspect ratio 2 rectangular vortex rings are studied using large eddy simulation (LES), high-frequency hot-wire (HW) anemometry and stereoscopic particle image velocimetry (SPIV). It is shown that the consequences of the the axis-switching phenomenon, which is initiated by the self-induced vortex deformations, are different for the isolated vortex rings and rectangular jets. Various viscous diffusion effects are accounted for by generating single vortex rings pulsed at five Reynolds numbers $Re_i = UD_h/\nu = 355, 877.5, 1775, 8775, 17750$ $(i = 1, ..., 5)$. Vortex cores developed under elevated viscous effects exhibit more diffused rotational content and larger core radius. As a result, the first self-induced velocity component is reduced.

The second self-induced velocity component deforms the rectangular ring through the faster motion of the high-curvature regions. The resulting three-dimensional deformations reshape the ring and cause axis-switching. The strong viscous effects diffuse the $Re_1 = 355$ vortex ring in a short time before the switching is completed. With reduced viscous effects, the $Re_2 = 877.5$ and $Re_3 = 1775$ vortex rings demonstrate a single axis-switching occurring slightly earlier for Re_3. In addition, the Re_2 and Re_3 rings tend to bifurcate into the pair of semi-circular topologies after the completion of the axis-switching. At $Re_4 = 8775$ and $Re_5 = 17750$ for which the inertial effects are dominant, two switchings are completed and instantaneous vortex dynamics are almost identical. The second axis-switching occurs slightly earlier for Re_5 and more small scale vortices are formed in the wake of the ring.

The space-time map along the vortex ring axis demonstrates strong high-speed correlation spots corresponding to the number of accomplished axis-switchings. Vortex rings subjected to larger viscous diffusion exhibit deceleration in shorter times and hence demonstrate declined penetration rates. Trajectories of the vortex cores in the side (SV), top (TV) and the diagonal (DV) views, display contractions and expansions resembling the varicose mode of instability. In the SV plane, the contractions and expansions follow the Sine wave trajectory while TV and DV harmonize with the Cosine form. The exact quarter of a full cycle phase lagging/leading between the Sine and Cosine functions is interestingly found identical with the frequency of the axis-switching. Accordingly, the axis-switching of the aspect ratio 2 rectangular vortex ring can be defined in terms of the interaction between the two orthogonal varicose modes of instability with a phase difference of quarter of a cycle.

Chapter 6

Reshaping, vortex dynamics and entrainment of perturbed and unperturbed transitioning rectangular jets

This chapter is prepared from the large eddy simulation (LES) of the transitioning/starting rectangular jets to investigate the effect of inlet forcing on vortex dynamics and entrainment. The content is reprinted with permission from International Journal of Numerical Methods for Heat and Fluid Flow [51]

Abbas Ghasemi and Xianguo Li. Cross-sectional reshaping of perturbed/unperturbed rectangular jets. International Journal of Numerical Methods for Heat and Fluid Flow, VV(NN): AA-BB, 2019 (In Press).

6.1 Introduction

Shear layers (also known as mixing layers) are formed when the interface between the high-speed and low-speed fluid regions becomes unstable. The initiating mechanism is the so-called Kelvin-Helmholtz (KH) instability which sets in linearly and transitions to non-linear state. Vortical strutures formed owing to these instabilitis grow in space/time and govern the consequent shear/rotation processes [48]. When originated from circular orifices/nozzles, axisymmetric shear layers develop in the form of round jets with both fundamental and practical significance [20]. In round jets, the important near-field mechanism is the formation of axisymmetric vortex rings due to the KH instability [20]. Axisymmetric vortex rings expand with downstream distances while the core radius grows due to viscous diffusion effects [19]. These vortices are shed rather orderely at the fundamental frequency associated with the KH instability [10, 9]. Subharmonic instability modes can appear due to the reduced passage frequency of vortex rings with increased downstream distance and the eventual vortex pairing [11].

For variety of applications where processes such as mixing, heating, cooling and combustion are involved, it is essential to control the jet flow dynamics. The first control strategy is the passive alteration of jet flows. For instance, inflow conditions such as momentum thickness and turbulence intensity can result in shear layer evolution of round jets [13]. Another interesting passive control approach is to issue the jets from non-circular openings which demonstrate richer dynamics leading to enhanced mixing, heat and mass transfer processes [22, 23, 29]. Increased three-dimensionality of non-circular jets, arising from the cross-sectional reshaping, promotes the flow complexity [27, 46, 102] compared to that of round jets. Non-circular jets demonstrate increased spread rates compared to round jets [37]. Hence, more ambient fluid is entrained into the jet core and mixing is enhanced [35, 34, 31]. In addition, near-field instantaneous lateral oscillations of non-circular jets contribute to improved mixing and entrainment [36]. These lateral oscillations result in the formation of off-center velocity peaks in non-circular jets not commonly seen for round jets [35, 38]. Another source to enhanced entrainment of non-circular jets is the increased azimuthal perturbations emerging due to the self-induced distortions of initially non-symmetric vortex rings [45]. These additional self-induced velocities occur near the high-curvature regions of non-circular vortex rings [28]. Velocity [26] and pressure [28] perturbations of initially non-symmetric vortex rings formed in non-circular jets deform the cross-section into more symmetric shapes farther downstream [25, 33]. The large (egulfment, flow induction) and small (nibbling) scale entrainment mechanisms are commonly observed in shear flows [1]. Non-circular jets exhibit an additional small scale entrainment component owing to the perturbations taking place at high-curvature regions of vortex rings [12].

In addition to passive perturbations, shear flows can be actively forced to control the jet dynamics and entrainment [104]. Active forcing results in the more organized shedding and pairing of the vortices [21], hence greatly affects the entrainment and mixing processes [9]. Active inlet forcing can be introduced in terms of the combined streamwise and azimuthal perturbation effects [123, 124]. In non-circular jets, the azimuthal component is passively accounted for by the geometrical configuration while the streamwise component can be introduced actively [24, 12]. While majority of earlier studies focus on the active/passive forcing of steady jets [104, 13, 12, 27], transient effects of the inlet forcing on transitioning (starting) non-circular jets need to be explored. In circular [47] and non-circular [28, 23] transitioning jets, entrainment is governed by the dynamics of the leading vortex ring as well as the trailing shear layer. This motivates the present study to explore the inlet forcing effects on vortex dynamics and entrainment in the leading vortex ring and the trailing shear layer. Large eddy simulation (LES) is conducted and compared with particle image velocimetry (PIV) data to demonstrate the cross-sectional reshaping dynamics of transitioning (starting) rectangular jets. The jet is issued from an aspect ratio 2 ($a \times 2a$) rectangular opening at the Reynolds number of $Re = UD_h/\nu = 17,750$ where U, D_h and ν denote centreline exit velocity, hydraulic diameter and kinematic viscosity, respectively. Spatio-temporal evolution, vortex dynamics and entrainment of the unperturbed (0%) starting rectangular jets are compared with that of sinusoidally forced flow at the fundamental frequency imposed at three amplitude levels of (2%, 4% and 10%).

6.2 Numerical set-up

Non-dimensional form of the filtered unsteady incompressible viscous Navier-Stokes equations governing the dynamics of large-scale structures are given below[109]

$$\frac{\partial \tilde{u_i^*}}{\partial x_i^*} = 0 \tag{6.1}$$

$$\frac{\partial \tilde{u_i^*}}{\partial t^*} + \frac{\partial \tilde{u_i^*}\tilde{u_j^*}}{\partial x_j^*} = -\frac{\partial \tilde{p^*}}{\partial x_i^*} + \frac{1}{Re_a}\frac{\partial^2 \tilde{u_i^*}}{\partial x_j^* x_j^*} - \frac{\partial \tau_{ij}^r}{\partial x_j^*} \tag{6.2}$$

where $x_i^*(i = 1, 2, 3)$ represent the non-dimensional coordinates x/a, y/a and z/a. Non-dimensional time is defined as $t^* = (Ut)/a$ and $Re_a = Ua/\nu$ is the Reynolds number. The dimensionless filtered velocity components and pressure are presented as $\tilde{u_i^*} = u_i/U$ and $\tilde{p^*} = P/\rho U^2$. For large eddy simulation (LES), flow quantities are decomposed into the resolved (filtered) and sub-grid scale (residual) fields, denoted respectively as $(\tilde{u_i^*}, \tilde{p^*})$ and $({u'}^{*}_{i}, {p'}^{*})$ for velocity and pressure. Above system of equations are solved using the dynamic Smagorinsky-Lilly subgrid-scale (SGS) model in Ansys Fluent 14 solver [113].

The residual or the SGS stress tensor is defined as $\tau_{ij}^R = \widetilde{u_i u_j} - \tilde{u}_i\tilde{u}_j$ from which the anisotropic residual stress $\tau_{ij}^r = \tau_{ij}^R - \frac{2}{3}k_r\delta_{ij}$ can be extracted. The isotropic content within the residual kinetic energy $k_r = \frac{1}{2}\tau_{ii}^R$ can be accounted for in the pressure correction term

$\widetilde{p_m} = \widetilde{p} + \frac{2}{3}k_r$. Evaluation of the anisotropic component of the residual stress tensor τ_{ij}^r requires extra effort through the dynamic Smagorinsky-Lilly model where the Smagorinsky model constant is continuously updated based on the resolved field calculations [110]. In present large eddy simulation (LES), filtered Navier-Stokes equations are solved using the coupled solver with a second-order fully implicit time marching scheme [113]. Finite volume approach is implemented to spatially discretize the equations with second-order central differencing of the diffusion terms and third-order MUSCL (Monotonic Upwind Scheme for Conservation Laws [125]) scheme for convective terms in momentum equations.

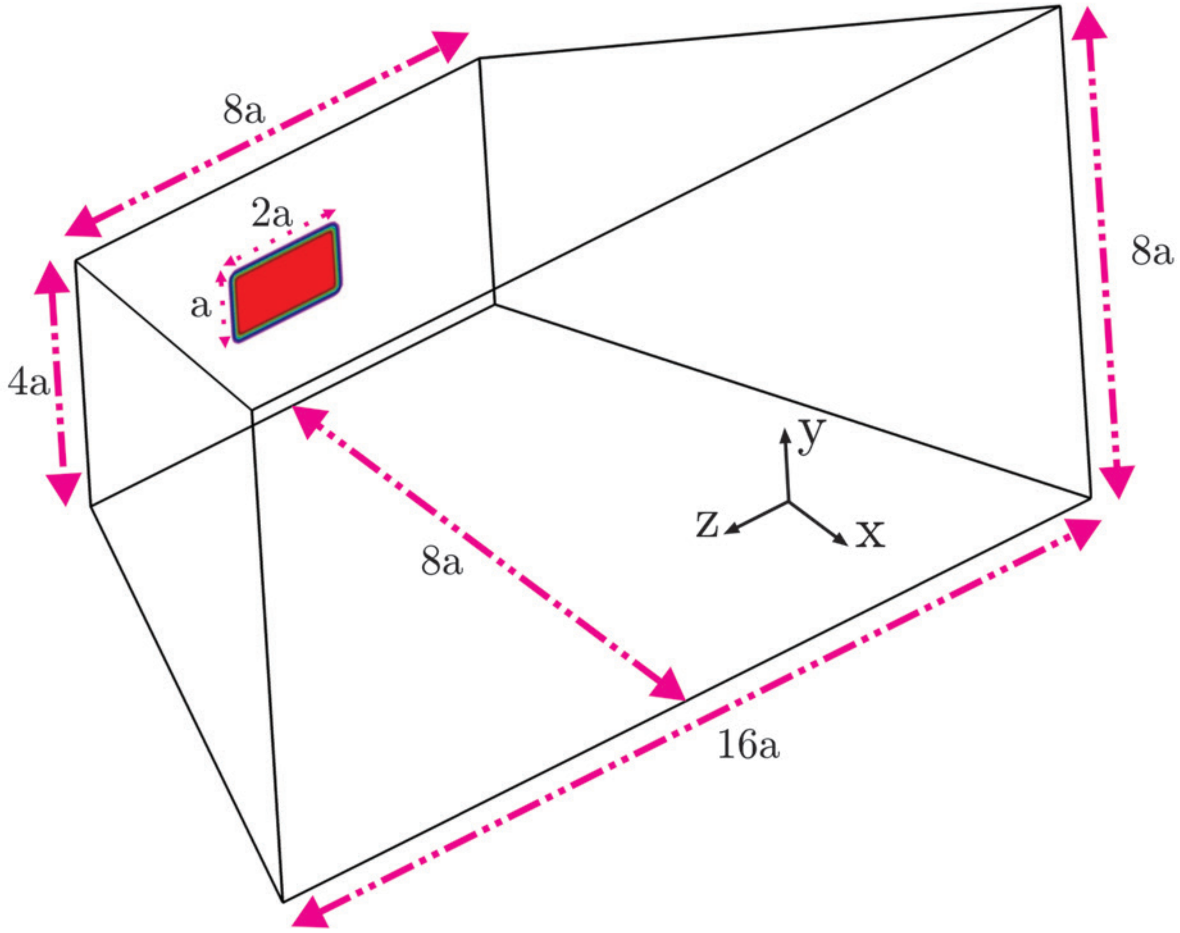

Figure 6.1: Characteristic dimensions of the computational domain. Origin of the Cartesian coordinate system is located at the centroid of the $2a$ by a rectangular opening placed flushed with the inlet wall.

6.2.1 Inflow and boundary conditions

Geometrical characteristics of the computational domain constructed for numerical simulations are shown in Figure 6.1. Surrounding boundaries of the flow domain are allowed to diverge along the streamwise distance to conform with the spatial jet (shear layer) growth. The transient jet is issued into the computational domain through the aspect ratio 2 ($a \times 2a$) rectangular opening placed flushed with the $x/a = 0$ inlet wall. Origin of the Cartesian coordinate system $(x, y, z) = (0, 0, 0)$ is located at the centroid of the inlet orifice. The flow exit boundary at $x/a = 8$ is subjected to outflow conditions. Circumferential extents located at the traverse directions of the jet are treated as symmetric boundaries within the range $y/a = \pm 2$ and $z/a = \pm 4$ expanding to $y/a = \pm 4$ and $z/a = \pm 8$. Numerical simulations are carried out using nearly 30 million structured finite volume cells at the Reynolds number of $Re = 17,750$.

Inflow velocity is introduced uniformly and is allowed to oscillate based on the sinusoidal function given below:

$$U^*{}_{in} = 1 + u^{'} \sin(2\pi \times St_a \times t^*) \tag{6.3}$$

where the dimensionless forcing frequency is given by the Strouhal number defined as $St_a = fa/U$. According to the hot-wire (HW) anemometry experiments and linear stability (LST) predictions by [49], the forcing frequency $St_a = 0.7$ is adopted. The selected forcing frequency represents the dominant instability associated with the fundamental mode due to the Kelvin-Helmholtz (KH) instability. In addition, amplitudes of the inlet streamwise velocity oscillations are varied by $u^{'} = 0, 0.02, 0.04, 0.1$, which are referred to as 0%, 2%, 4% and 10% cases in the following sections.

To verify that the inlet sinusoidal oscillations are properly introduced, space-time variation of the centreline ($y/a = 0, z/a = 0$) streamwise velocity is presented in Figure 6.2. The color contour map is being used to show the effect of the amplitude of the sinusoidal oscillations in the near exit region (vertical axis: $0 < x/a < 0.08$) during the simulation time period (horizontal axis: $0 < t^* < 16$). The unperturbed $u^{'} = 0$ (0%) case shows a steady inflow velocity after the time $t^* = 5$ when small transient effects disappear. On the other hand, near-exit streamwise velocity oscillates regularly proportional to the forcing amplitudes of $u^{'} = 0.02$ (2%), $u^{'} = 0.04$ (4%) and $u^{'} = 0.1$ (10%).

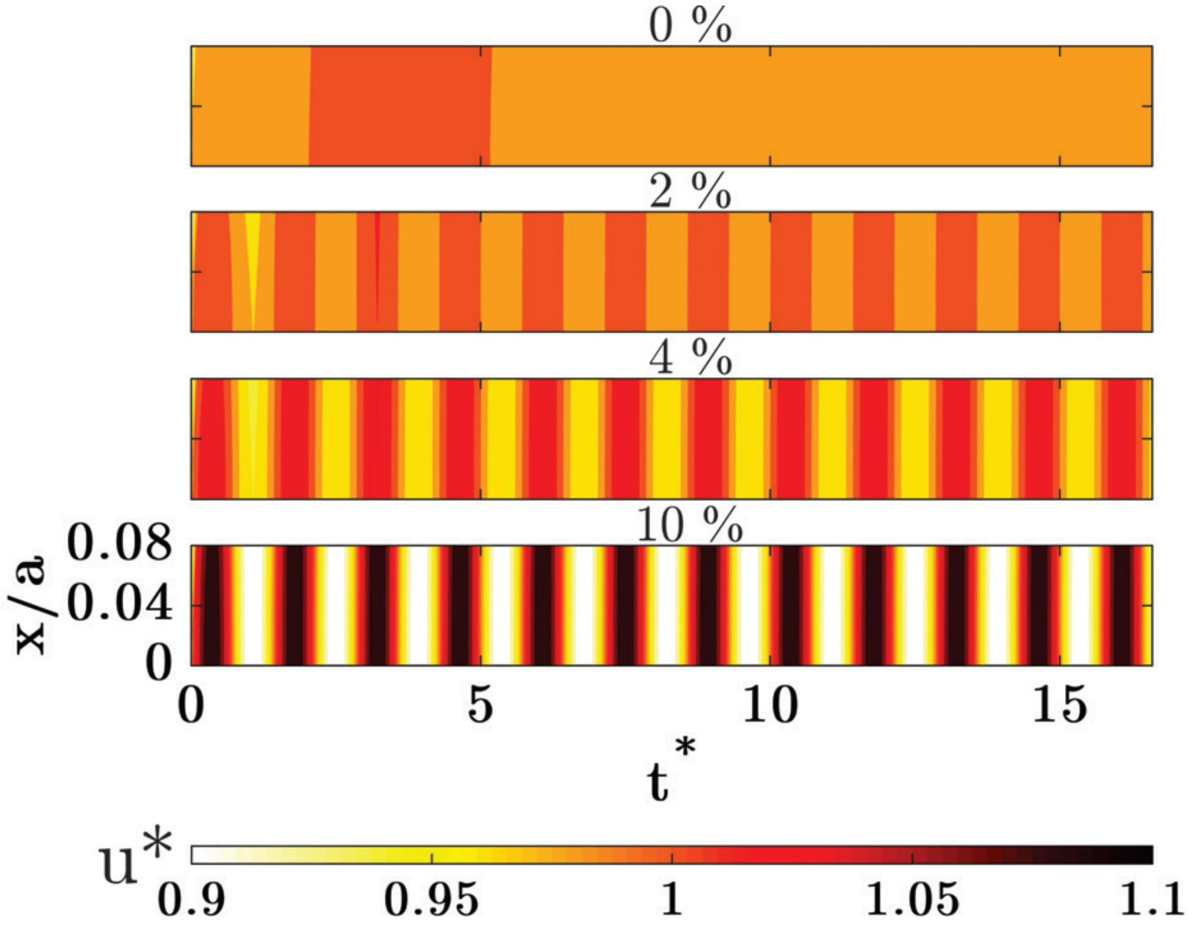

Figure 6.2: Sinusoidal inflow velocity oscillations for: (a) $u^{'} = 0$ (0%), (b) $u^{'} = 0.02$ (2%), (c) $u^{'} = 0.04$ (4%) and (d) $u^{'} = 0.1$ (10%) amplitudes. Contours show the space-time variations of the centreline ($y/a = 0, z/a = 0$) streamwise velocity near the jet exit ($x/a = 0 - 0.08$) during the dimensionless times $t^{*} = 0 - 16$.

6.2.2 LES grid specifications

It is important to ensure that the LES grid resolves the flow structures down to the smallest possible scales [109]. To this end, integral (λ_I), Taylor (λ_T) and Kolmogorov (λ_K) length scales are evaluated using the HW measurements of the rectangular jet (at the same Reynolds number) by [49]. As seen in Figure 6.3, length scales are compared against the streamwise variation of the local LES filter width Δ. In accordance with the shear layer growth, all the length scales increase in the streamwise direction until attaining a linear trend in fully-developed regions.

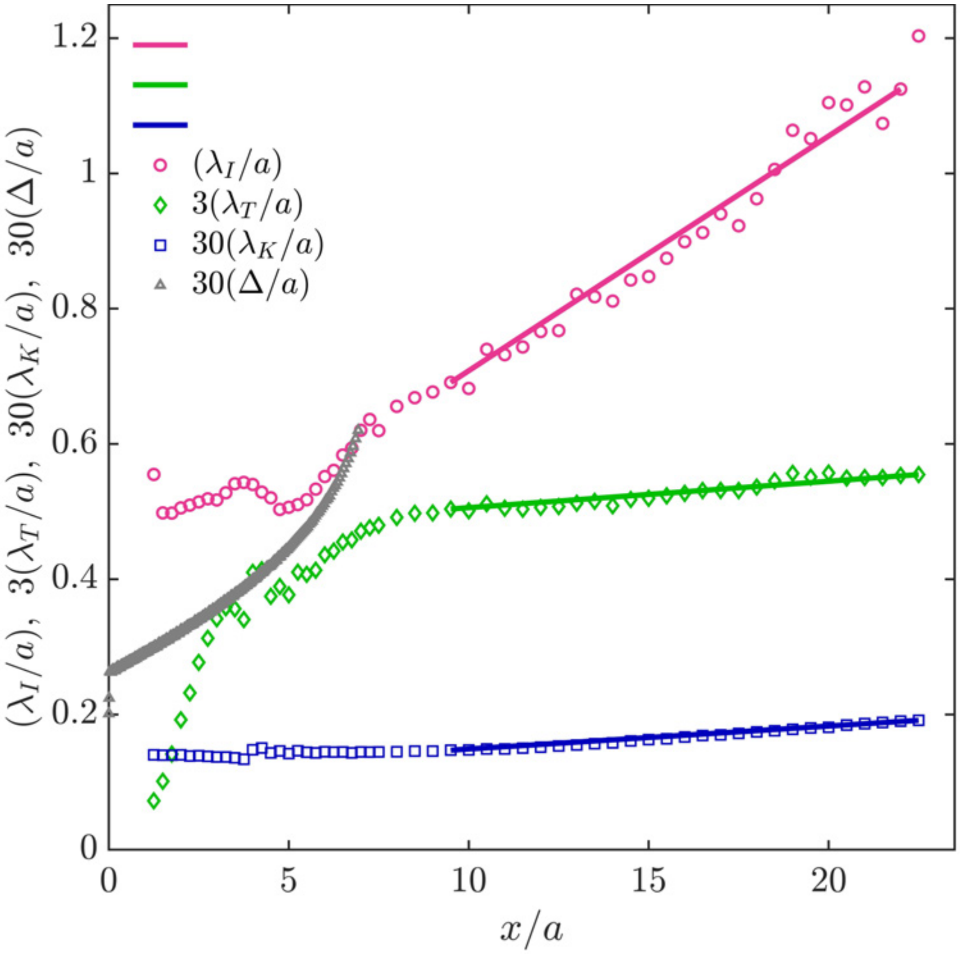

Figure 6.3: Local flow length scales of the rectangular jet evaluated by the HW measurements. The integral (λ_I), Taylor (λ_T) and Kolmogorov (λ_K) length scales are compared against the LES filter width (Δ).

The high inertia large structures (λ_I) that dominate the viscous effects, extract the energy of turbulence from the bulk flow and transfer it to the intermediate scales (λ_T). The Taylor micro-scales (λ_T), which are the largest structures influenced by viscosity, transfer this energy to the low inertia λ_K scales where it is dissipated into heat by strong viscous effects. To achieve an efficient LES, it is recommended that the flow scales up to almost twenty times Kolmogorov scales are resolved to account for majority of the small scales contributing to dissipation [109]. The present model is adopted from the simulations conducted by [28] with enhanced grid resolution and higher order schemes implemented for the lower Reynolds number flows. With the near-field LES filter width evaluated between $1.7\lambda_K$ and $4.3\lambda_K$, simulations are expected to successfully resolve the smallest length scales.

6.3 Results and discussion

In this section, numerical results and experimental data are first compared to introduce the reshaping phenomenon taking place in the cross-section of rectangular jets. Afterwards, effects of the controlled inflow perturbations on reshaping of the three-dimensional jet evolution are discussed. Furthermore, spatio-temporal vortex dynamics are discussed to understand the underlying physics causing the reshaping phenomenon. Finally, effect of the controlled oscillation amplitudes on the instantaneous entrainment of rectangular jets are investigated.

6.3.1 Effect of perturbations on the cross-sectional reshaping of rectangular jets

In figure 6.4, streamwise velocity obtained from the LES and phase-locked particle image velocimetry (PIV) are compared within the cross-sectional ($x/a = 0.7, 1.5, 2.3, 3.1, 3.9$) and side view (SV: $z/a = 0$) planes of the rectangular jet. In figure 6.4a, phase-averaged PIV results are given for the streamwise velocity obtained by [49]. Details of the phase-locked PIV measurement conditions are given in [49]. The presented phase-averaged velocity field demonstrates the mean flow features while maintaining some of the instantaneous dynamics. It should also be noted that the cross-sectional information are obtained by interpolating multiple phase-locked planar measurements [49]. Since it is difficult to conduct PIV measurements for starting jets, PIV of steady jets are compared with arbitrary time instants from LES to elucidate the cross-sectional reshaping behaviour. The near-exit jet cross-section demonstrates the aspect ratio 2 rectangular distribution in accordance with the inlet orifice shape at $x/a = 0$. With increased downstream distance, edges of the jet become distorted due to the onset of instabilities and shear layer formation. Distortions appear to be stronger near the sharp corners of the jet. Farther downstream at $x/a = 3.9$, the jet cross-section reshapes into rather elliptic/circular geometries. It is worth to mention that the measured jet experiences three components of perturbations. The first passive component appears due to the random upstream fluctuations arising from the apparatus imperfections. The second passive perturbation is due to the azimuthal instabilities in

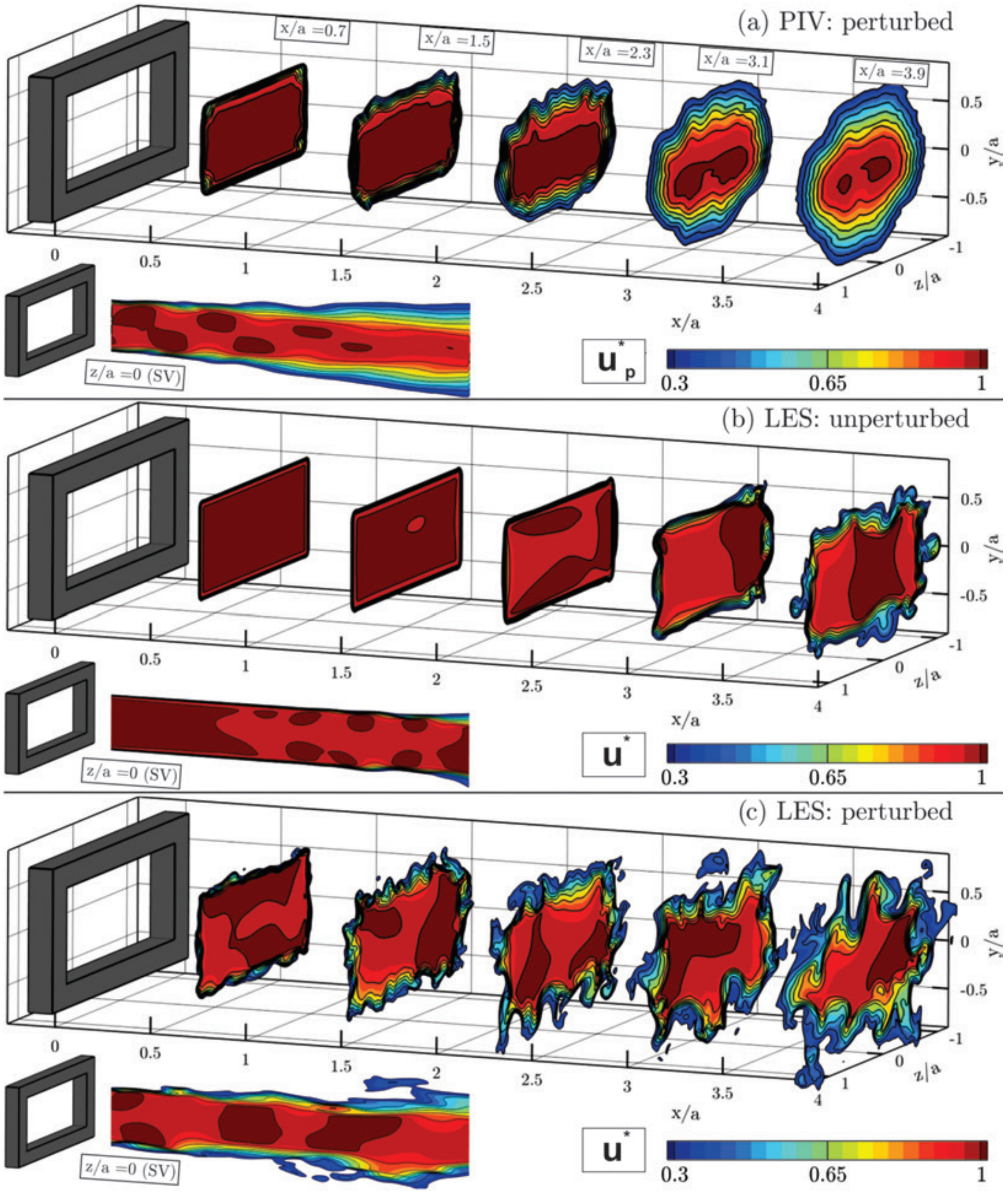

Figure 6.4: Streamwise velocity in the cross-sectional ($x/a = 0.7, 1.5, 2.3, 3.1, 3.9$) and side view (SV: $z/a = 0$) planes: (a) Phase-averaged PIV; (b) Instantaneous LES: unperturbed; (c) Instantaneous LES: randomly perturbed (2%).

non-circular jets. The third element is the active forcing imposed by acoustic excitation to obtain phase-locked planar measurements.

Figure 6.4b presents the instantaneous streamwise velocity obtained from LES. For this case, a uniform velocity profile with negligible momentum thickness is considered. Also, no perturbations are added to the inlet velocity. As a result, a thin shear layer is formed compared to the PIV data. In addition, the edges of the jet are not distorted at all up to $x/a = 3.1$ and the shear layer thickness does not grow. Moreover, the jet cross-section remains fairly rectangular and no reshaping is observed up to the downstream distance of $x/a = 3.9$. On the other hand, jet dynamics are significantly altered when only 2% random perturbations are introduced to the streamwise velocity (figure 6.4c). Unlike the unperturbed case, edges of the jet become distorted shortly after the exit. As a consequence, perturbations grow rapidly and result in the reshaping of the jet cross-section. Even though the presented instantaneous cross-section does not demonstrate a complete reshaping into the more rounded geometries, a clear deviation from the rectangular shape is observed for the perturbed case. It should be noted that the small random perturbations introduced here are merely to compare the reshaping phenomenon with the unperturbed steady jets. The periodic oscillations governed by equation 6.3 are used to perturb the transitioning jets discussed in following sections.

To further elucidate the active forcing effects on rectangular jets, sinusoidal inlet velocity oscillations are introduced at the dimensionless frequency of $St_a = 0.7$. This fundamental forcing frequency represents the Kelvin-Helmholtz (KH) instability mode characterized by the HW-based spectral analysis and linear stability (LST) predictions conducted by [49]. Jet flow is then controlled by introducing perturbation amplitudes of $u' = 0, 0.02, 0.04, 0.1$ (the 0%, 2%, 4% and 10% cases). Near-exit ($x/a = 0.08$) contributions of the forcing amplitudes 0%, 2%, 4% and 10% are characterized using the power spectral density (PSD) of centreline streamwise velocity as seen in figure 6.5. The unperturbed case (0%) demonstrates the lowest PSD energy content and no frequency preference is detected. On the other hand, forced cases exhibit a sharp high-energy peak associated with the dominance of $St_a = 0.7$ frequency. It is evident that the energy content of the peaks are elevated with increased forcing amplitudes. In the following sections, it is shown how different forcing strategies regulate the flow structures and consequently the jet entrainment is affected.

In figure 6.6, instantaneous iso-surfaces of streamwise velocity ($u^* = 0.5$) coloured by the local pressure (p^*) are given during the times $t^* = 1, 3, 5, 9$ for 0%, 2%, 4% and 10% forcing amplitudes. At $t^* = 1$, all cases exhibit similar and rather rectangular shapes. At this stage, the jet has just started to enter the domain resulting in a high-pressure (red) stagnation zone in the front. The surrounding low pressure (dark blue) region is caused by the formation of the leading vortex ring and the consequent rotation-induced pressure

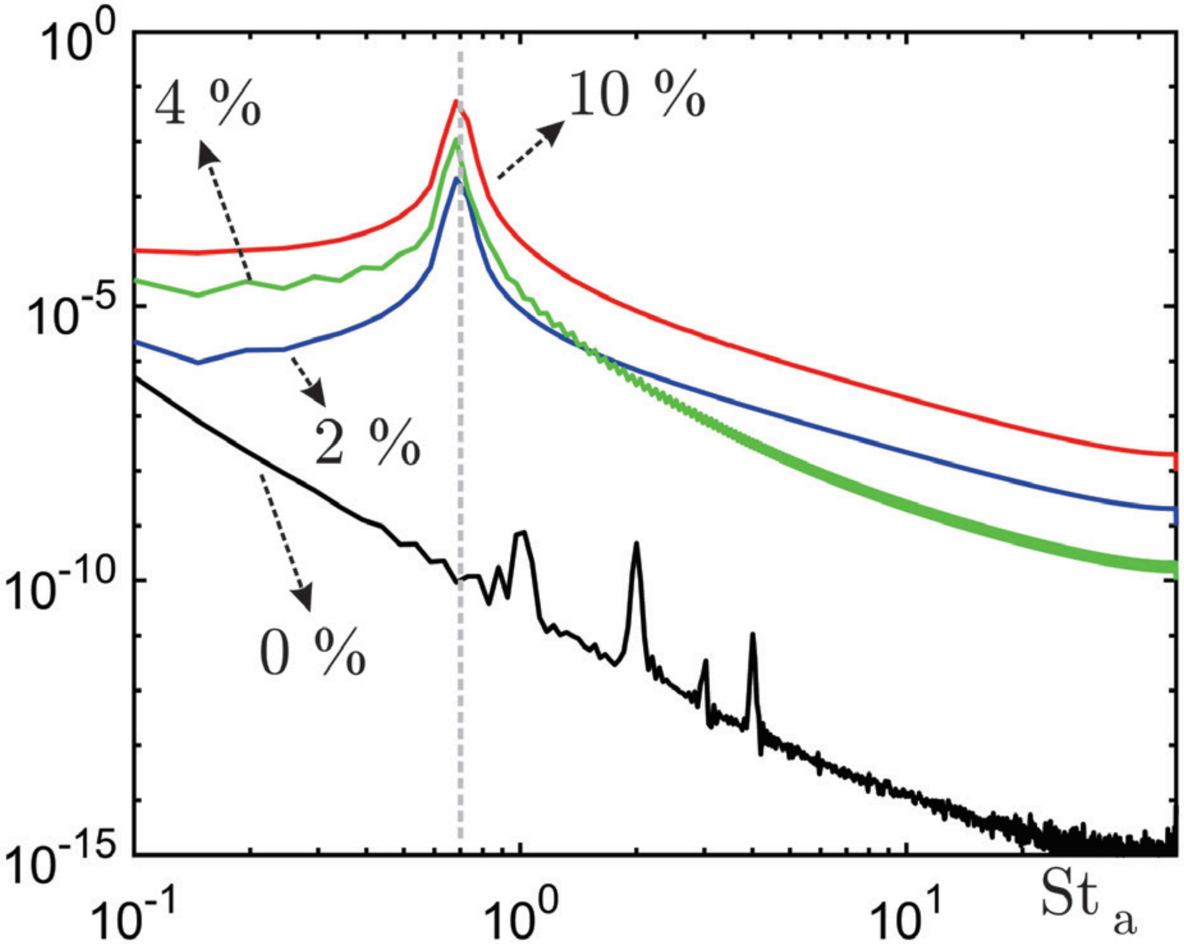

Figure 6.5: Power spectral density (PSD) of the centreline streamwise velocity at $x/a = 0.08$ for the forcing frequency of $St_a = 0.7$ at 0%, 2%, 4% and 10% forcing amplitudes.

drop. From $t^* = 3$ to $t^* = 5$, significant expansion in y-direction and the mild growth in z-direction reduce the aspect ratio of the jet leading tip. Eventually at $t^* = 9$, the leading tip appears to be rotated for 90^o around the x-axis as compared to its $t^* = 1$ orientation. This apparent rotation is attributed to the so-called "axis-switching" phenomenon. Another important aspect of the starting rectangular jet during the times $t^* = 1{-}9$, is the formation of the quasi-steady trailing jet evolving in the wake of the leading tip. In the trailing jet region, alternating high/low pressure zones are observed. These high-pressure and low-pressure regions respectively correspond to the local expansions and contractions in the jet boundaries. The high-pressure expansion zones are formed in the downstream of any

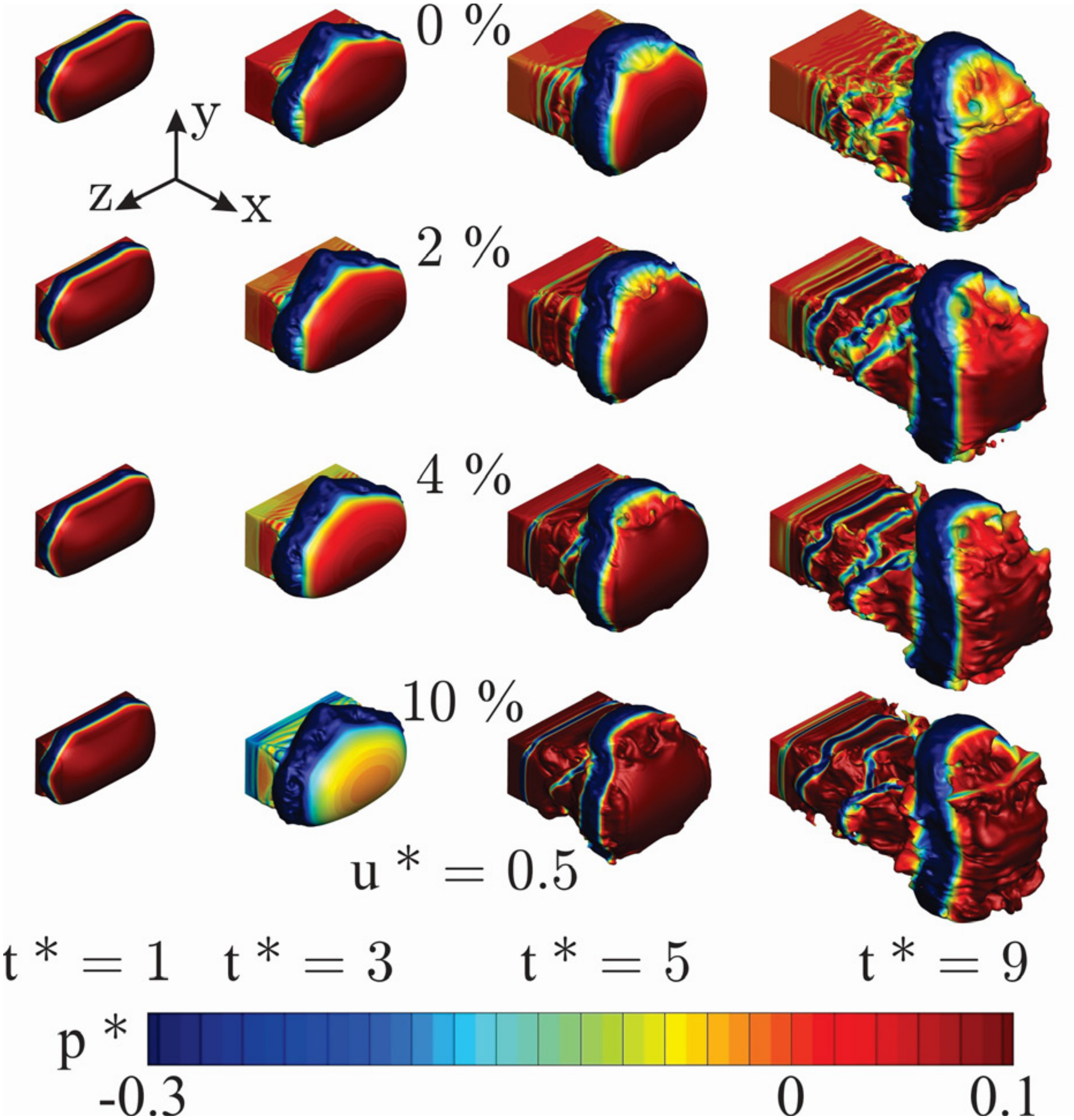

Figure 6.6: Instantaneous iso-surfaces of the streamwise velocity ($u^* = 0.5$) coloured by local pressure (p^*) during the times $t^* = 1, 3, 5, 9$ for 0%, 2%, 4% and 10% forcing amplitudes.

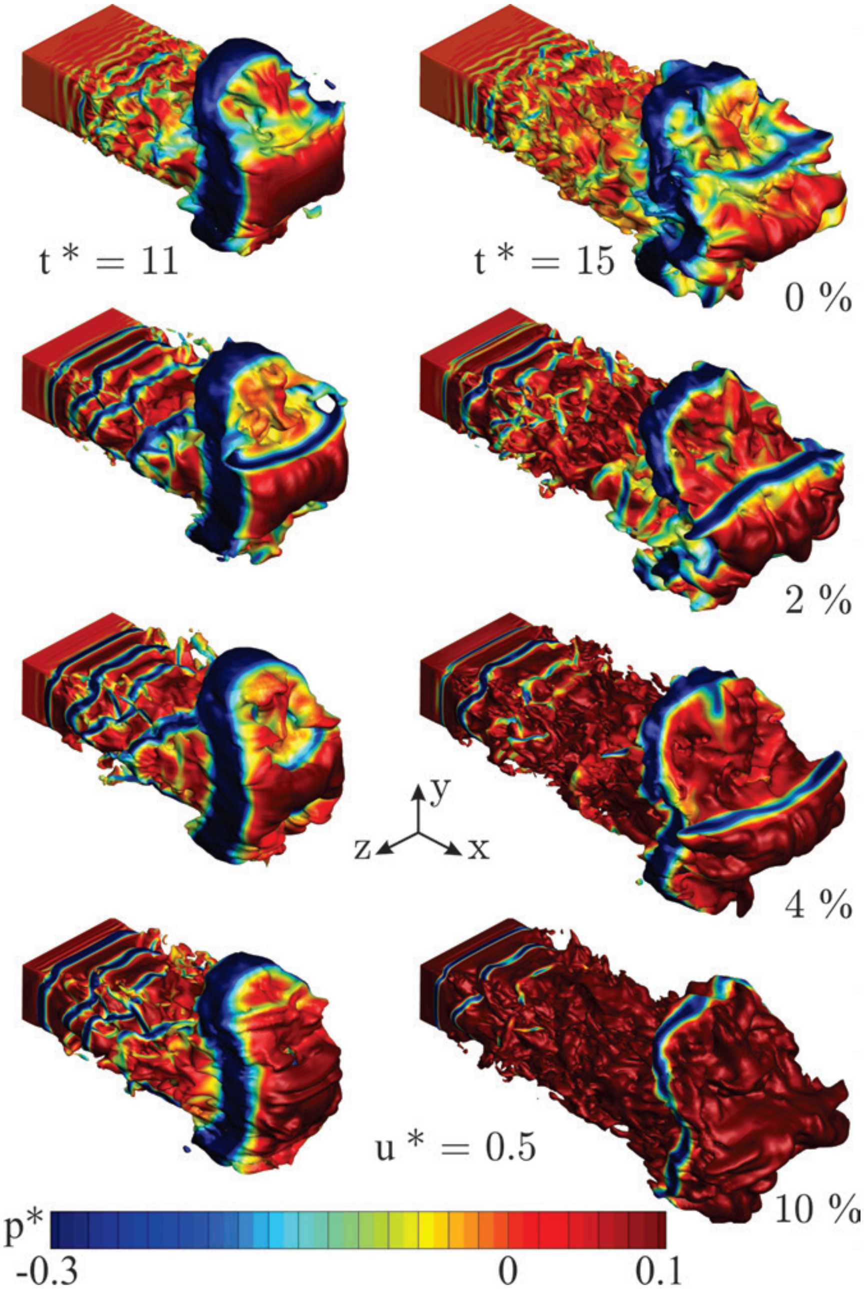

Figure 6.7: Instantaneous iso-surfaces of the streamwise velocity ($u^* = 0.5$) coloured by local pressure (p^*) during the times $t^* = 11, 15$ for 0%, 2%, 4% and 10% forcing amplitudes.

passing vortex ring while its upstream goes through the low pressure contraction. It can be clearly seen that the pressure variations are quite random in the unforced jet. On the other hand, all the forced jets demonstrate a very nice organization of high/low pressure zones. As a result, the forced cases at $t^* = 9$ exhibit the leading vortex followed by the three trailing rings. The organized shedding of the KH vortex rings at $t^* = 9$, clearly promote the downstream vortex pairing proportional to the forcing amplitude.

In figure 6.7, the instantaneous iso-surfaces of streamwise velocity ($u^* = 0.5$) coloured by the local pressure (p^*) are given during the times $t^* = 11, 15$ for 0%, 2%, 4% and 10% forcing amplitudes. With farther jet penetration, more trailing vortex rings appear in the wake of the leading vortex ring at $t^* = 11$. Further in time at $t^* = 15$, low pressure regions due to the trailing vortex ring disappear as they break down in the downstream locations. At this stage, it can be seen that the cross-section of the trailing quasi-steady jet also deviates from the rectangular shape and becomes more round with the downstream distance. However, the 90^o rotation is not observed in the trailing jet unlike the leading tip. The above observations of the rectangular jet reshaping are known as the axis-switching phenomenon. The underlying physical mechanisms, which are associated with the instantaneous vortex dynamics, are explored below.

6.3.2 Effect of the perturbations on spatio-temporal vortex dynamics

To reveal the underlying mechanisms governing the above cross-sectional reshaping, instantaneous dynamics of the vortical structures need to be explored. To this end, the mechanism of the self-induced velocity on a vortex loop should be first explained. Any given point on a curved vortex loop/filament has two velocity components. The first part is due to the advection along with the bulk flow motion, while the second contribution is called the self-induced velocity. The self-induced velocity itself is affected by the vortex core radius and the local curvature of the vortex loop as predicted by the Biot-Savart law [42]. Since the curvature-induced velocity plays the most important role in the dynamics of non-circular vortex rings, figure 6.8 describes the physical mechanism. The isolated yellow-coloured vortex loop located on the longer side of the rectangular ring is viewed from the top. The intersecting horizontal plane is coloured by the instantaneous streamwise velocity in the vicinity of the vortex loop. The qualitative distribution of the low to high velocity regions are coloured from blue to red.

At early stage of $t^* = 1.5$, sharp (high curvatures) corners of the vortex ring (on either side of the loop) induce a pair of high velocity spots. Therefore, high curvature zones move

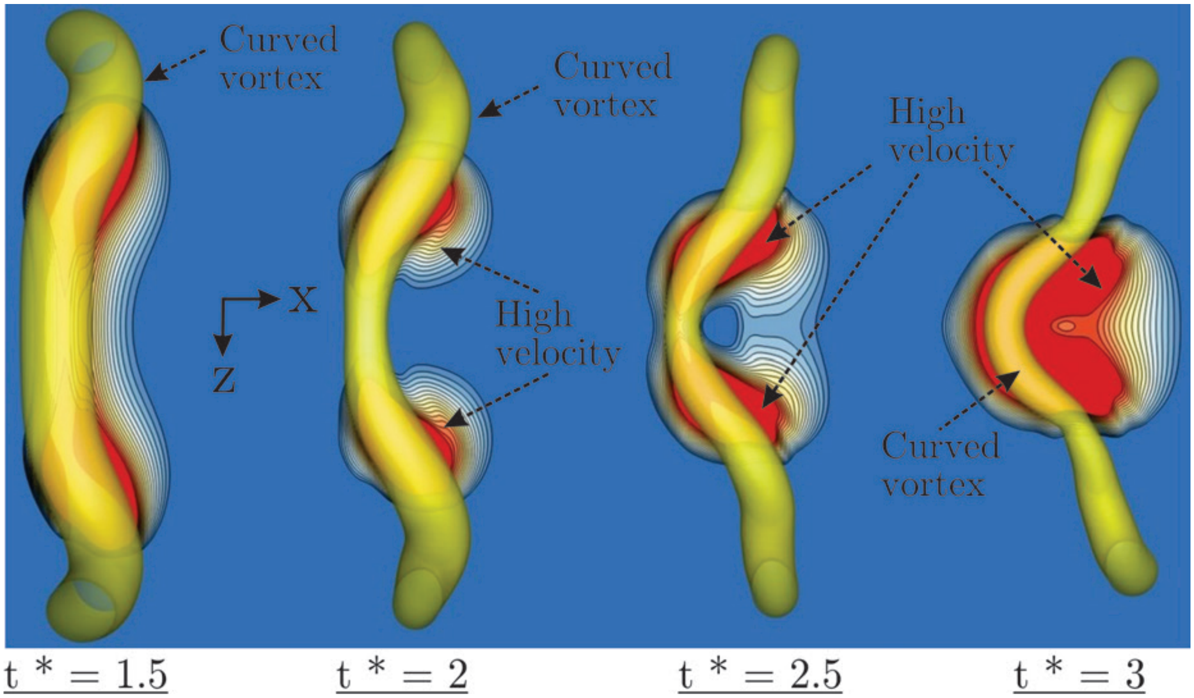

Figure 6.8: Vortex loop (yellow) on the longer side of an isolated rectangular vortex ring viewed from the top. The intersecting horizontal plane displays the curvature-induced velocity coloured qualitatively from blue to red.

forward before the rather flat mid part. As a consequence, the vortex loop is curved and results in the formation of high curvature regions near the mid part. Accordingly, the pair of high velocity spots tend to get closer towards the mid section until they merge at $t^* = 3$. Beyond this time, the high curvature mid part moves faster than edges. This simplified example is the building block to the complex three-dimensional vortex dynamics taking place in non-circular vortex rings explored in the followings.

In figure 6.9, instantaneous vortex structures are identified using the iso-surfaces ($Q = 0.05Q_{max}$) of Q-criterion [61] and coloured by the streamwise component of vorticity (${\omega_x}^*$). Dynamics of the vortices are compared for the unperturbed (0%) and forced (10%) cases during the times $t^* = 1, 3, 5, 7$. At $t^* = 1$, both the unperturbed and perturbed cases form a single rectangular leading vortex ring (LVR). The curved corners of the rectangular ring have slightly moved forward due to the increased curvature-induced velocity. At $t^* = 3$, LVR becomes more distorted and reshapes into more three-dimensional geometries. Also, hairpin vortex (HPV) structures appear near the corners of the LVR. Each of the counter-

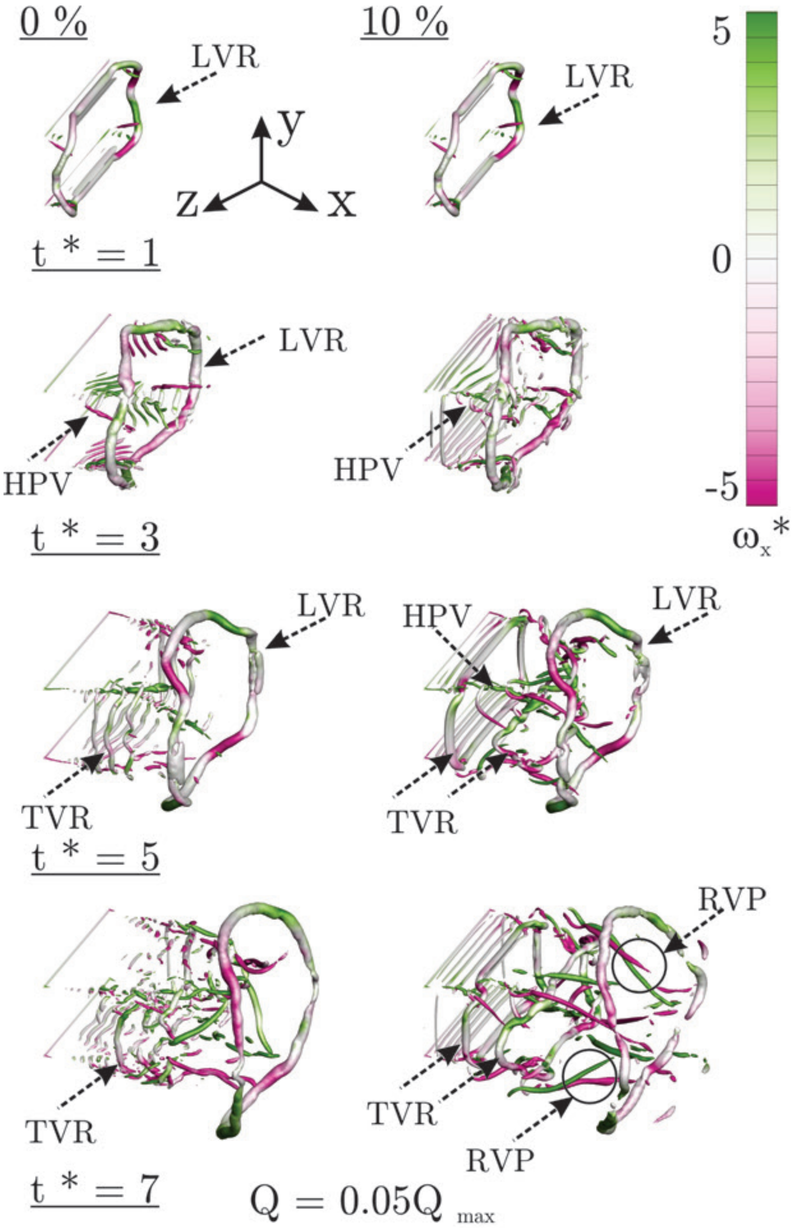

Figure 6.9: Instantaneous vortex structures identified by the iso-surfaces ($Q = 0.05Q_{max}$) of Q-criterion and coloured by the streamwise component of vorticity ($\omega_x{}^*$) during the times $t^* = 1, 3, 5, 7$ for 0% and 10% forcing amplitudes.

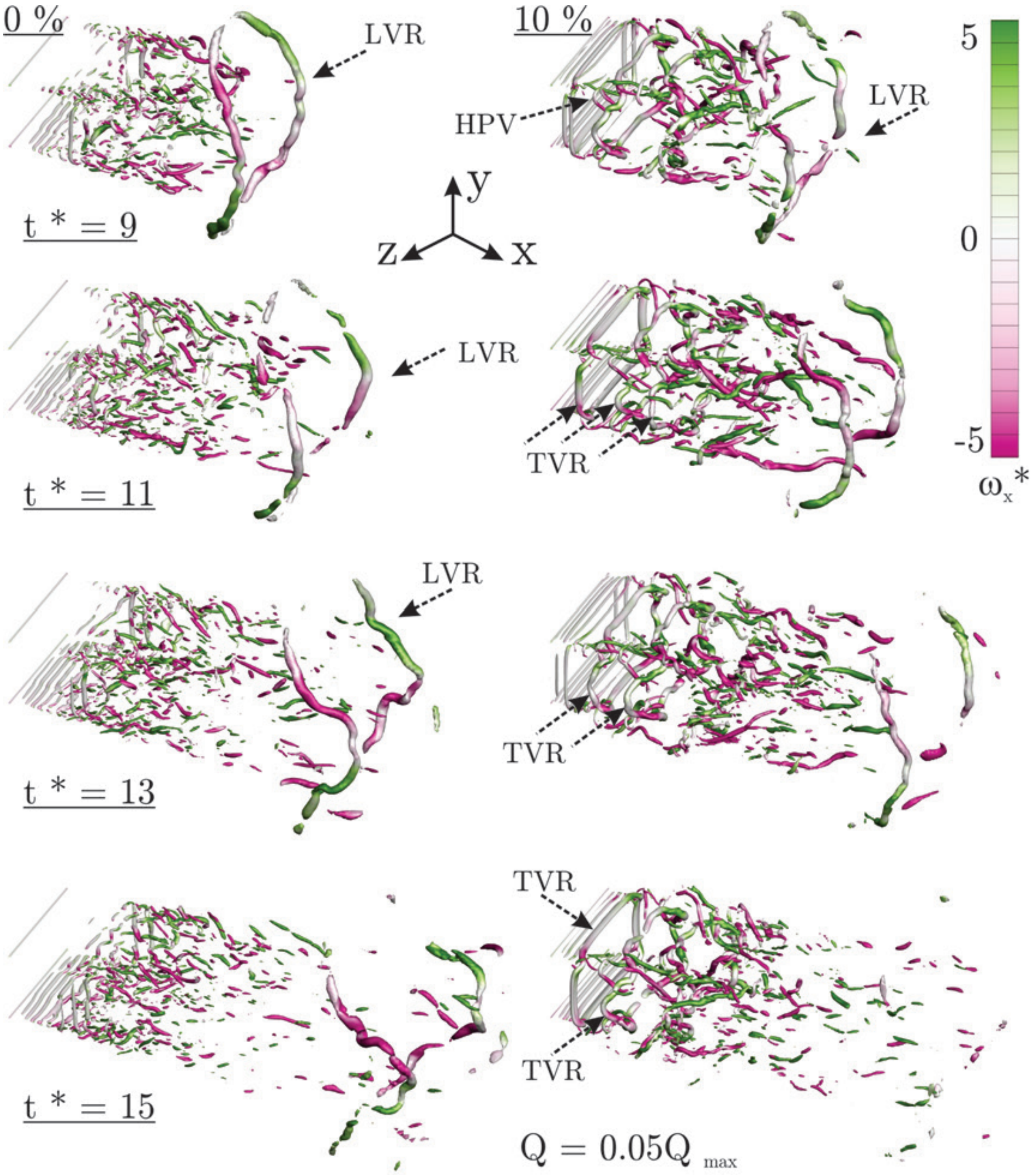

Figure 6.10: Instantaneous vortex structures identified by the iso-surfaces ($Q = 0.05Q_{max}$) of Q-criterion coloured by the streamwise component of vorticity ($\omega_x{}^*$) during the times $t^* = 9, 11, 13, 15$ for 0% and 10% forcing amplitudes.

rotating arms of the hairpin vortex portray the pair of streamwise longitudinal vortex loops coloured by the opposite signs of streamwise vorticity. While the trailing vortex rings (TVR) have not emerged for the unperturbed jet, they start to form due to the augmentation of the KH instability in the forced jet.

Later at $t^* = 5$, thin trailing vortex rings weakly appear for the unperturbed jet. On the other hand, stronger TVRs appear in the more organized trailing shear layer of the forced jet. At $t^* = 7$, the leading vortex ring has completed the axis-switching process as it seems to have rotated for 90^o degrees; that is, the long side appears in the vertical direction while its short side is in the horizontal direction, opposite to the ring orientation at earlier time of $t^* = 1$. On the other hand, self-induced deformations of the trailing vortex rings does not demonstrate a complete axis-switching. It is rather the reshaping of the rings before they break down into smaller scales. Such differences bwetween the reshaping of non-circular steady jets and the axis-switching of isolated or leading vortex rings are also observed in [47, 49]. Another interesting observation is the formation of streamwise vortex loops. These counter-rotating rib vortex pairs (RVP) exhibit opposite signs of streamwise vorticity. At the early stage, rectangular ring dynamics are mostly affected by curvature-induced deformations. With increased time, distortions are also influenced by the interaction among hairpins, ribs and the primary vortex ring.

Instantaneous vortical structures obtained by the iso-surfaces ($Q = 0.05Q_{max}$) of Q-criterion and coloured using the streamwise vorticity (${\omega_x}^*$) are presented in figure 6.10 for the unperturbed (0%) and forced (10%) cases during the times $t^* = 9, 11, 13, 15$. It can be seen that both the trailing (TVR) and leading (LVR) vortex rings start to break down during this stage. Break-down of the LVR occurs earlier for the forced jet. On the other hand, weaker TVRs formed in the unperturbed shear layer tend to disintegrate faster into the smaller scales. Unlike steady jets, dynamics of transitioning/starting jets are significantly affected by the presence of the leading vortex ring and its interaction with the trailing shear layer. Self-induced vortex dynamics increase the complexity of the patio-temporal evolution of non-circular starting jets.

6.3.3 Effect of the perturbations on instantaneous entrainment

Earlier sections show that non-circular jets can be used to passively alter the jet dynamics and control the mixing and entrainment. In addition to the passive control, it would be beneficial to actively regulate the behaviour of the transitioning (starting) rectangular jets. This is particularly important since starting jets are implemented in many practical applications to optimize the processes such as mixing, heat/mass transfer and combustion. Entrainment of the stagnant ambient fluid into the jet core is evaluated to better understand the practical importance of active forcing. The radial mass flow rate passing through the jet interface from the low-speed ambient to the high-speed core is known as entrainment. However, integrating the mass flow in the radial direction is difficult. Because a properly identified interface forms an irregular three-dimensional boundary, it is challenging to integrate the radial component of the velocity. Alternatively, the entrained mass flow rate can be evaluated by integrating the streamwise velocity component passing through the cross-sectional planes. This approach is justified by the conservation of mass as the radially entrained flow balances with the increased streamwise flow rate between two cross sectional planes.

To this end, two arbitrary cross-sectional planes located at the streamwise locations of x and $x + \delta x$ are considered. The corresponding streamwise mass flow rates in each of the planes can be denoted as M_x and $M_{x+\delta x}$, respectively. The streamwise mass flow rate M can be evaluated within each cross-sectional plane using the integration:

$$M = \int \rho u dy dz \tag{6.4}$$

which can be normalized by the inlet mass flow rate (M_o). According to the conservation of mass, the radial mass flow rate (the local entrainment) into the jet core should balance with the differential value $M_{x+\delta x} - M_x$ evaluated in the streamwise direction. This method of quantification is found more convenient and is expected to provides more accurate entrainment values. Therefore, the downstream variation of the streamwise mass flow rate provides valuable information on the local entrainment.

Variation of $\frac{M}{M_o}$ along the downstream distance is presented in figure 6.11 to quantify the instantaneous entrainment during the times $t^* = 1, 3, 5, 7$ for 0%, 2%, 4% and 10% amplitudes. In order to evaluate the entrainment, several cross-sectional $y - z$ planes with the spatial spacing of $\delta x = 0.05a$ are extracted along the streamwise direction. The interior jet boundaries are defined as the regions where $u^* < 0.03$ determines the integration limit. This is to ensure that the integration boundaries do not cut through the recirculation zones which may lead into the miscalculation of the entrainment. These recirculation zones are formed due to the rotation of vortex cores inside the shear layer [1]. As seen in figure 6.11, variation of the instantaneous $\frac{M}{M_o}$ with the downstream direction exhibits a single major peak at $t^* = 1$. As shown in earlier sections, there is only a single leading vortex ring (LVR) at this time for all the 0%, 2%, 4% and 10% amplitudes of the oscillations. The curves starts from the inlet value of $\frac{M}{M_o} = 1$ in the upstream of the LVR and grow to a peak value farther downstream. After this increased local entrainment along the leading vortex ring, the $\frac{M}{M_o}$ values and the corresponding entrainment decline in the downstream of the LVR. The large scale rotation of the leading vortex ring engulfs the surrounding fluid

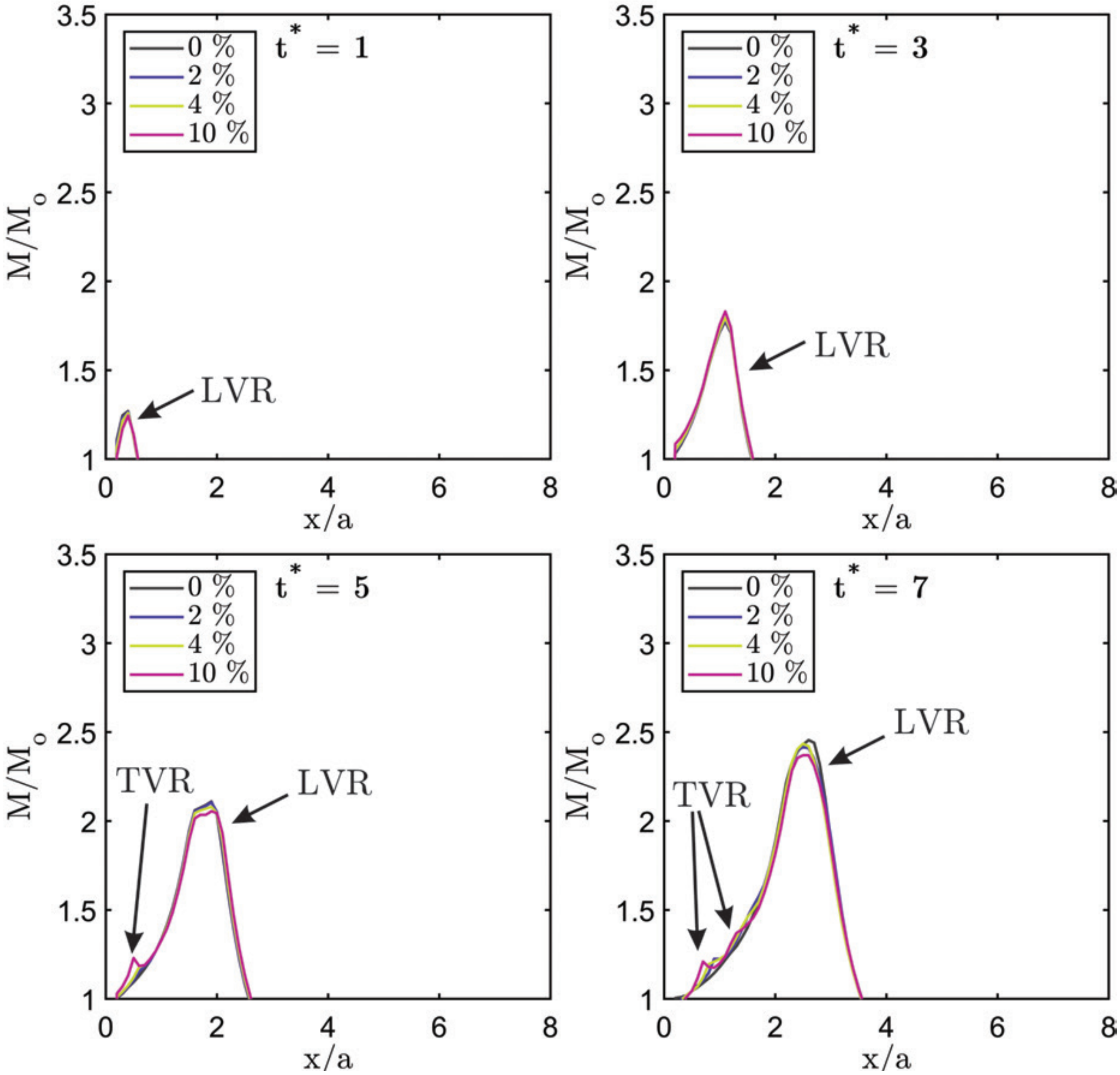

Figure 6.11: Variation of instantaneous entrainment with downstream distance during the times $t^* = 1, 3, 5, 7$ for 0%, 2%, 4% and 10% forcing amplitudes.

inward. In addition the low pressure caused by the rotational core of the vortex draws the ambient flow inward.

A similar major peak pattern is observed for the entrainment at the dimensionless time

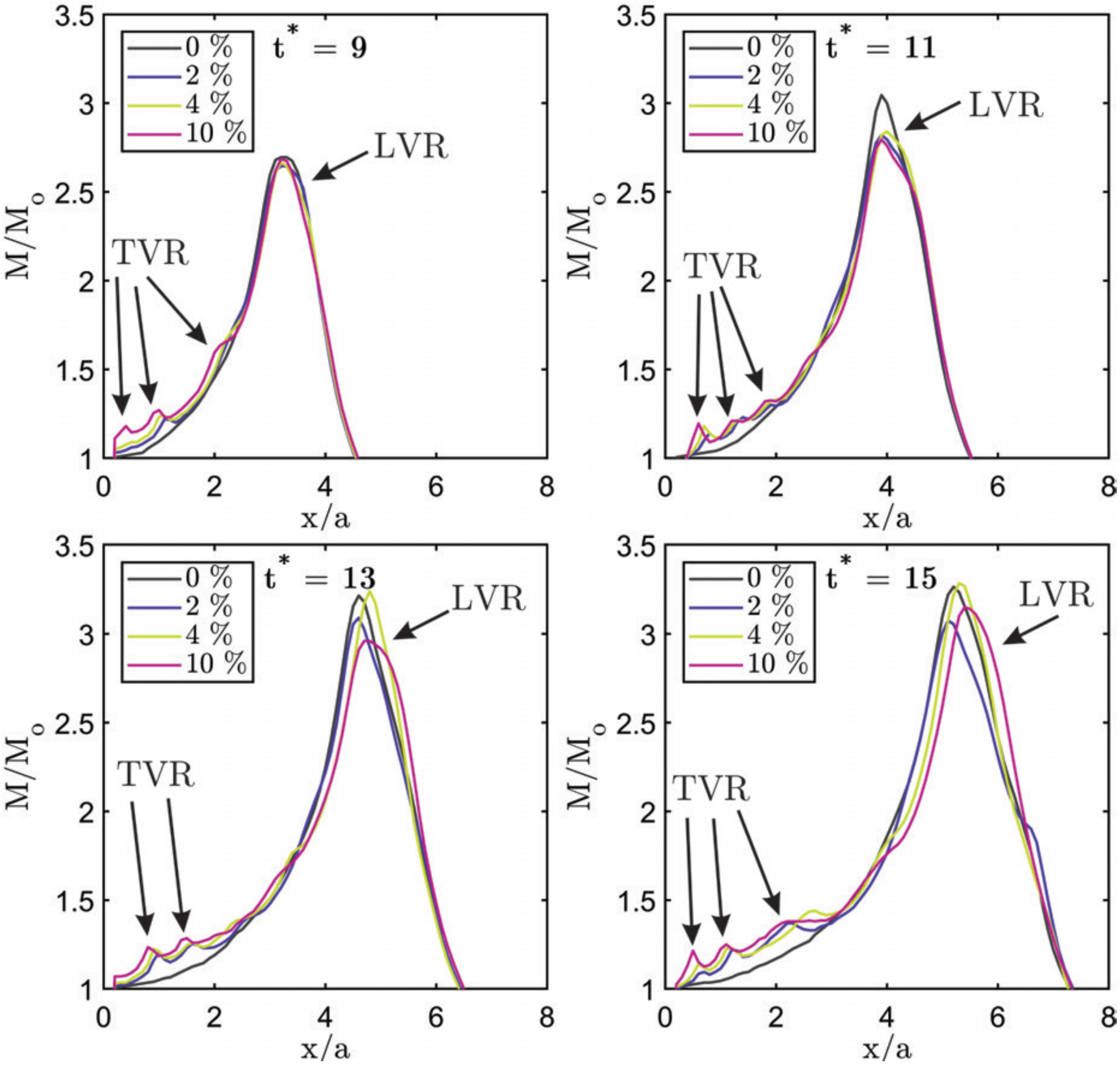

Figure 6.12: Variation of instantaneous entrainment with downstream distance during the times $t^* = 9, 11, 13, 15$ for 0%, 2%, 4% and 10% forcing amplitudes.

$t^* = 3$. It can be seen that the magnitude of the major peak grows at this time as a result of enhanced entrainment. Furthermore, the spatial width of the entrainment peak extends in accordance with the size of the leading vortex ring. In addition to the major peak, minor entrainment peaks appear near the jet exit during the times $t^* = 5 - 7$. The minor peaks show up due to the shedding of trailing vortex rings (TVR) and demonstrate their contribution to local entrainment. The minor peaks and valleys of entrainment can also be associated with the local contractions/expansions described in the earlier sections. During the early stage of $t^* = 1 - 7$, large scale entrainment of the starting rectangular jet is found to be dominated by the presence of the leading vortex ring. It can also be seen that the entrainment due to the leading vortex ring is not significantly affected by forcing the jet during this time.

In general, three different entrainment mechanisms take place in the near-field, developoing and the fully-developd regions of shear flows [1]. The large scale "engulfment" mechanism entrains the flow due to the vortex ring roll-ups. The second large scale entrainment is due to the "flow induction" caused by the low pressure induced within the rotational vortex cores. The third mechanism is the small scale "nibbling" of the non-turbulent fluid patches near the edges of the jet. The entrainment peaks observed here are mainly due to the two large scale mechanisms described above. In figure 6.12, the streamwise distribution of the instantaneous entrainment is presented during the times $t^* = 9, 11, 13, 15$ for 0%, 2%, 4% and 10% forcing amplitudes. At $t^* = 9$, the entrainment zone due to the trailing vortex rings is extended in accordance with the evolution of the trailing shear layer. Also, the contribution of the trailing vortices to the local entrainment increases proportional to the amplitude of the controlled oscillations.

During the dimensionless times $t^* = 9$ to $t^* = 15$, it can be clearly seen that the near-field instantaneous entrainment of the unperturbed jet does not exhibit the contributions from the orderly vortex ring structures appearing for the forced jets. From $t^* = 11$ to $t^* = 15$, the forcing effect also appears in the leading vortex ring. Since the strength of the leading vortex ring starts to decay during its break-down into smaller scales, the corresponding entrainment peak declines for the forced cases compared to the unperturbed jet. For sufficiently large times when the LVR is completely diffused, the entrainment curve is expected to continually grow with the downstream distance in accordance with the shear layer expansion. At that stage, the jet loses its transitioning behaviour and approaches the steady state. In addition to influencing the near-field vortices, controlled forcing of the jet may affect the vortex pairing, break-down and the far-field spread rate of steady jets.

6.4 Summary

Large eddy simulation (LES) is carried out to study the cross-sectional reshaping of transitioning rectangular jets starting from the aspect ratio 2 orifice at the Reynolds number of $Re = UD_h/\nu = 17,750$. The study focuses on the spatio-temporal dynamics of the jets under the simultaneous effects of the active/passive forcing.

Comparison of the LES with phase-locked particle image velocimetry (PIV) data demonstrates that the initially rectangular cross-section of the jet deforms into the rounder shapes with increased downstream distance. The reshaping phenomenon occurs due to the shear layer instability which is more significantly observed near the high-curvature corners. The non-circular (rectangular) cross-section of the jet passively introduces azimuthal perturbations resulting in the different expansion rates in the longer and shorter edges of the jet. Furthermore, small levels of random inlet perturbations are shown to advance the reshaping phenomenon.

In addition to passive perturbations, active sinusoidal velocity oscillations of different amplitudes are introduced at the jet inlet. In accordance with the spectral analysis of the hot-wire (HW) data as well as linear stability (LST) predictions, oscillations are associated with the fundamental frequency due to the Kelvin-Helmholtz (KH) instability. Compared to the unperturbed jet, the controlled sinusoidal oscillations develop a more organized trailing shear layer where stronger vortex rings go through the curvature-induced deformations. While curvature-induced deformations result in the 90^o axis-switching of the leading vortex ring, the trailing vortex rings only go through the mild reshaping before breaking down.

Spatio-temporal vortex dynamics of transitioning rectangular jets are also correlated with the instantaneous variation of local entrainment. At early stage, inlet forcing does not influence the entrainment induced by the leading vortex ring. In later time where the leading vortex ring at the highest forcing amplitude starts to break down, the corresponding entrainment declines. In general, evolution of the leading vortex ring dominates the entrainment process of the transitioning jets. In addition, controlled forcing of the inlet improves the near-field entrainment caused by the trailing vortex rings. The local entrainment of trailing vortex rings are increased proportional to the amplitude of the active forcing.

Chapter 7

Conclusions and Future Work

7.1 Summary and Conclusions

The present thesis has explored the shear layer and vortex dynamics at the exit of an aspect ratio 2 rectangular duct using experimental characterization and numerical simulations. Hot-wire (HW) anemometry and conventional/phase-locked particle image velocimetry (PIV) measurements as well as large eddy simulations (LES) reveal different aspects of the underlying mechanisms involved in rectangular jet vortex dynamics.

The HW anemometry and PIV measurements carried out within the near-exit region of the naturally developing as well as acoustically actuated shear layers separating from the longer edge of the rectangular opening reveal important information on the underlying physicist associated with the initial roll-up. Out of the measurements conducted within a wide range of Reynolds numbers, the transitioning nature of the shear layer is nicely demonstrated for $Re_{\theta_0} = 85, 135, 276, 470, 616, 713, 780, 860, 945$. It is found that the competing effects between the shear and rotation mechanisms further describe the Kelvin-Helmholtz (KH) roll-ups and how they affect the downstream vortex pairing. In addition, the peculiar double-peaking phenomenon of the RMS of the streamwise velocity fluctuations (u_{RMS}) is better understood. Along with the major u_{RMS} peak commonly observed on the high-speed (HS) side of the shear layer, a second minor peak may or may not emerge leaning towards the low-speed (LS) region. It is found that the minor peak develops within the range $276 \leq Re_{\theta_0} \leq 860$, and vanishes for lower or higher limits. While the minor peak generally appears at a certain streamwise location, grows and ultimately decays, its transitioning character is found passively controllable through the grid-induced turbulence, incoming boundary layer characteristics and Reynolds number by altering the near-exit shear/rotation counteraction. On the other hand, the vortex shedding/pairing and consequently the double-peaking phenomenon can be actively controlled using the acoustic excitation at the fundamental (f_n) and its subharmonic ($f_n/2$) frequency. Fluctuations surrounding the vortex core suggest a four-arrow arrangement that illustrates the coupling between the shear/rotation zones and elucidates the phase-reversal phenomenon.

The rectangular jet formed at the exit of the duct demonstrates cross-sectional reshaping due to the curvature-induced vortex ring deformations. Naturally evolving and acoustically excited jets at the Reynolds number of $Re = UD_{\mathrm{h}}/\nu = 17,750$ are issued from the rectangular duct of aspect ratio 2. The initially rectangular jet cross-section reshapes into more elliptic/circular geometries with increased downstream distance. The reshaping mechanism, commonly known as the axis-switching, contracts the jet diagonal and mildly expands the longer and shorter edges. The axis-switching characteristics can be controlled using the acoustic forcing to alter the relative expansion/contraction of the jet in the top (TV), side (SV), and diagonal (DV) planes. The near-field self-induced deformations result in the increased anisotropy and intermittency levels not commonly seen for round jets. The phase-locked PIV measurements allow for the study of rectangular vortex rings as they appear owing to the KH instability, reshape due to the curvature-induced velocity and eventually break-down due to the increased azimuthal perturbations. The downstream propagation of the azimuthal perturbations is found to be symmetric/non-symmetric depending on the direction of the acoustic source. The curvature-induced velocity spots first appear near the corners of the ring. With increased downstream distance an additional spot is observed near the mid part. Farther downstream, the resulting perturbations propagate from the corners and dominate in the mid part.

Large eddy simulation (LES) of the isolated rectangular vortex rings reveal the viscous diffusion effects on the self-induced distortions. It is found that the reshaping or axis-switching of isolated vortex rings lead into different dynamics from those of rectangular jets. The reason is that the vortex rings generated in the rectangular jet shear layer strongly interact with each other and also with other secondary structures such as the rib and hairpin shape vortices. Formation of larger vortex cores under increased viscous diffusion effects resulted into the more diffused rotational region and consequently reduced self-induced velocity. While curvature-induced velocity deforms the rectangular vortex ring, strong viscous effects diffuse the ring and prevents it from switching. The proposed space-time mapping technique revealed a correlation between the high-velocity spots and the number of completed axis-switchings. Also, the vortex core trajectories in the side (SV), top (TV) and the diagonal (DV) planes demonstrate symmetric contractions/expansions that are found similar to the varicose mode of instability. It is suggested that the axis-switching phenomenon can be described based on the interaction between the two orthogonal planes going through the varicose type of instability with a phase difference of quarter of a cycle.

In transitioning rectangular jets, the leading vortex ring demonstrates a complete axis-switching similar to that of isolated rings. On the other hand, the trailing vortex rings deform/reshape into rounder geometries with increased downstream distance. Small levels of random inlet perturbations are found to advance the reshaping of the jet cross-section. Introducing the controlled sinusoidal oscillations resulted into the more organized vortex shedding within the trailing shear layer. In addition, curvature-induced deformations occur more significantly for the vortex rings generated under controlled perturbations. The entrainment of transitioning rectangular jets at initial stage is mostly dominated by the leading vortex ring and is not significantly affected by the inlet perturbations. With increased jet penetration, the contribution of the trailing shear layer to entrainment increases accordingly. It is found that the controlled inlet perturbations can increases the entrainment in the trailing shear layer.

7.2 Proposed future work

The findings in the present thesis shed more light on the vortex dynamics at the exit of a rectangular duct. In addition, present research can open the direction for many future experimental/numerical studies, namely:

- *Shear/rotation competition and the double-peaking in shear layers*:

  The proposed shear/rotation mechanism for the peculiar double-peaking phenomenon of the streamwise turbulence intensity can be followed by both experimental and numerical studies to further elucidate the underlying physics. The future experimental work could implement high-speed particle image velocimetry (PIV) measurements to generate time-resolved information for the shear/rotation dynamics and their correlation with the double-peaking phenomenon. In addition, high-order direct numerical simulations (DNS) can be carried out to extract high-resolution flow field in time and space for different inlet conditions.

- *Curvature-induced velocity of the vortex rings in rectangular jets*:

  The correlation between the vortex curvature, the locally induced velocity on the vortex rings and the resulting deformations can be further understood using different experimental/numerical techniques. The PIV experiments can be extended to Tomographic (Tomo) measurements to enable the instantaneous characterization of the three velocity components to be used for 3D volumetric analysis. Furthermore, accurate DNS calculations can provide detailed information on the complex dynamics of the vortex deformations. Another important study proposed by the present thesis is to conduct a detailed analysis of the directional effect of the acoustic source on the vortex dynamics in rectangular jets.

- *Isolated rectangular vortex rings*:

  Study of the isolated vortex rings can provide detailed information on the self-induced deformation mechanisms. However, it is very difficult to extract the three dimensional vortex structures for several appropriate time instants. Therefore, the space-time mapping technique proposed in the present thesis can be used conveniently for experimental (e.g. time-resolved PIV) and numerical analysis. This allows for studying a wide range of inflow regimes and nozzle geometrical configurations. Another future study to be proposed is to further identify the role of varicose mode of instability and the suggested phase lagging/leading mechanism for the vortex rings of different shapes (circular, square, rectangular, elliptic, triangular diamond, etc.) and aspect ratios.

- *Transitioning/starting jets*:

  Transitioning/starting jets have many practical application in which the entrainment and mixing play important roles. Therefore, it is suggested that a complete future study is dedicated to the entrainment in starting jets issued from the non-circular openings of different shapes. From the fundamental point of view, starting jets simultaneously demonstrate the small and large scale entrainment mechanisms with their own interesting dynamics.

References

[1] AJ Yule. Large scale structure in the mixing layer of a round jet. *J. Fluid Mech.*, 89(3):413–432, 1978.

[2] Martin Schmitt, Rennan Hu, Yuri Martin Wright, Patrik Soltic, and Konstantinos Boulouchos. Multiple cycle les simulations of a direct injection natural gas engine. *Flow, Turbulence and Combustion*, 95(4):645–668, 2015.

[3] Asok K Sen, Jianjun Zheng, and Zuohua Huang. Dynamics of cycle-to-cycle variations in a natural gas direct-injection spark-ignition engine. *Applied Energy*, 88(7):2324–2334, 2011.

[4] V Vuorinen, J Yu, S Tirunagari, O Kaario, M Larmi, Christophe Duwig, and BJ Boersma. Large-eddy simulation of highly underexpanded transient gas jets. *Physics of Fluids*, 25(1):016101, 2013.

[5] Iman Chitsaz, Mohammad Hassan Saidi, Ali Asghar Mozafari, and Alireza Hajialimohammadi. Experimental and numerical investigation on the jet characteristics of spark ignition direct injection gaseous injector. *Applied energy*, 105:8–16, 2013.

[6] Ville Vuorinen, Armin Wehrfritz, Christophe Duwig, and BJ Boersma. Large-eddy simulation on the effect of injection pressure and density on fuel jet mixing in gas engines. *Fuel*, 130:241–250, 2014.

[7] A Ghasemi, RM Barron, and R Balachandar. Spray-induced air motion in single and twin ultra-high injection diesel sprays. *Fuel*, 121:284–297, 2014.

[8] V Sepret, R Bazile, M Marchal, and G Couteau. Effect of ambient density and orifice diameter on gas entrainment by a single-hole diesel spray. *Experiments in fluids*, 49(6):1293–1305, 2010.

[9] S Cj Crow and FH Champagne. Orderly structure in jet turbulence. *J. Fluid Mech.*, 48(3):547–591, 1971.

[10] AKM Fazle Hussain and KBMQ Zaman. The preferred mode of the axisymmetric jet. *J. Fluid Mech.*, 110:39–71, 1981.

[11] RA Petersen and MM Samet. On the preferred mode of jet instability. *J. Fluid Mech.*, 194:153–173, 1988.

[12] Fernando F Grinstein. Vortex dynamics and entrainment in rectangular free jets. *J. Fluid Mech.*, 437:69–101, 2001.

[13] Jungwoo Kim and Haecheon Choi. Large eddy simulation of a circular jet: effect of inflow conditions on the near field. *J. Fluid Mech.*, 620:383–411, 2009.

[14] Frederick Kent Browand. An experimental investigation of the instability of an incompressible, separated shear layer. *J. Fluid Mech.*, 26(2):281–307, 1966.

[15] Hiroshi Sato. Experimental investigation on the transition of laminar separated layer. *J. Phys. SOC. Japan.*, 11(6):702–709, 1956.

[16] Hiroshi Sato. Further investigation on the transition of two-dimensional separated layer at subsonic speeds. *J. Phys. SOC. Japan.*, 14(12):1797–1810, 1959.

[17] Hiroshi Sato. The stability and transition of a two-dimensional jet. *J. Fluid Mech.*, 7(1):53–80, 1960.

[18] Peter A Monkewitz. On the nature of the amplitude modulation of jet shear layer instability waves. *Phys. Fluids*, 26(11):3180–3184, 1983.

[19] Tadashi Matsuda and Jun Sakakibara. On the vortical structure in a round jet. *Phys. Fluids*, 17(2):025106, 2005.

[20] Christophe Bogey and Christophe Bailly. Large eddy simulations of transitional round jets: influence of the reynolds number on flow development and energy dissipation. *Phys. Fluids*, 18(6):065101, 2006.

[21] D Oster and I Wygnanski. The forced mixing layer between parallel streams. *Journal of Fluid Mechanics*, 123:91–130, 1982.

[22] J Mi and GJ Nathan. Statistical properties of turbulent free jets issuing from nine differently-shaped nozzles. *Flow. Turbul. Combust.*, 84(4):583–606, 2010.

[23] Jiao Jian Ai, SCM Yu, Adrian Wing-Keung Law, and LP Chua. Vortex dynamics in starting square water jets. *Phys. Fluids*, 17(1):014106, 2005.

[24] Trushar B Gohil, Arun K Saha, and K Muralidhar. Direct numerical simulation of free and forced square jets. *International Journal of Heat and Fluid Flow*, 52:169–184, 2015.

[25] A Bejan, S Ziaei, and S Lorente. Evolution: Why all plumes and jets evolve to round cross sections. *Sci. Rep.*, 4:4730, 2014.

[26] Fernando F Grinstein and CR DeVore. Dynamics of coherent structures and transition to turbulence in free square jets. *Phys. Fluids*, 8(5):1237–1251, 1996.

[27] EJ Gutmark and FF Grinstein. Flow control with noncircular jets. *Annu. Rev. Fluid Mech.*, 31(1):239–272, 1999.

[28] A Ghasemi, V Roussinova, RM Barron, and R Balachandar. Large eddy simulation of the near-field vortex dynamics in starting square jet transitioning into steady state. *Phys. Fluids*, 28(8):085104, 2016.

[29] A Ghasemi, V Roussinova, Ram Balachandar, and RM Barron. Reynolds number effects in the near-field of a turbulent square jet. *Exp. Therm. Fluid Sci.*, 61:249–258, 2015.

[30] M Xu, A Pollard, J Mi, F Secretain, and H Sadeghi. Effects of Reynolds number on some properties of a turbulent jet from a long square pipe. *Phys. Fluids*, 25(3):035102, 2013.

[31] Adel Hashiehbaf and GP Romano. Particle image velocimetry investigation on mixing enhancement of non-circular sharp edge nozzles. *Int. J. Heat Fluid Flow*, 44:208–221, 2013.

[32] KBMQ Zaman. Spreading characteristics of compressible jets from nozzles of various geometries. *J. Fluid Mech.*, 383:197–228, 1999.

[33] Chih-Ming Ho and Ephraim Gutmark. Vortex induction and mass entrainment in a small-aspect-ratio elliptic jet. *J. Fluid Mech.*, 179:383–405, 1987.

[34] A Krothapstarting squaalli, D Baganoff, and K Karamcheti. On the mixing of a rectangular jet. *J. Fluid Mech.*, 107:201–220, 1981.

[35] WR Quinn and J Militzer. Experimental and numerical study of a turbulent free square jet. *Phys. Fluids*, 31(5):1017–1025, 1988.

[36] Abbas Ghasemi, Vesselina Roussinova, and Ram Balachandar. A study in the developing region of square jet. *J. Turbul.*, 14(3):1–24, 2013.

[37] Y Tsuchiya and C Horikoshi. On the spread of rectangular jets. *Exp. Fluids*, 4(4):197–204, 1986.

[38] Alexandros P Vouros, Thrassos Panidis, Andrew Pollard, and Rainer R Schwab. Near field vorticity distributions from a sharp-edged rectangular jet. *Int. J. Heat Fluid Flow*, 51:383–394, 2015.

[39] WR Quinn. On mixing in an elliptic turbulent free jet. *Physics of Fluids A: Fluid Dynamics*, 1(10):1716–1722, 1989.

[40] PG Saffman and GR Baker. Vortex interactions. *Annu. Rev. Fluid Mech.*, 11(1):95–121, 1979.

[41] PG Saffman. Vortex dynamics (cambridge monographs on mechanics and applied mathematics). *Cambridge University Press, Cambridge*, 311:368, 1992.

[42] D Margerit and J-P Brancher. Asymptotic expansions of the biot-savart law for a slender vortex with core variation. *J. Eng. Math.*, 40(3):297–313, 2001.

[43] AJ Callegari and Lu Ting. Motion of a curved vortex filament with decaying vortical core and axial velocity. *SIAM J. Appl. Math.*, 35(1):148–175, 1978.

[44] GN Abramovich. On the deformation of the rectangular turbulent jet cross-section. *Int. J. Heat Mass Transfer*, 25(12):1885–1894, 1982.

[45] Christopher KW Tam and Andrew T Thies. Instability of rectangular jets. *J. Fluid Mech.*, 248:425–448, 1993.

[46] FF Grinstein, E Gutmark, and T Parr. Near field dynamics of subsonic free square jets. a computational and experimental study. *Phys. Fluids*, 7(6):1483–1497, 1995.

[47] Abbas Ghasemi, Aaron Pereira, and Xianguo Li. Large eddy simulation of compressible subsonic turbulent jet starting from a smooth contraction nozzle. *Flow Turbul. Combust.*, 98(1):83–108, 2017.

[48] Abbas Ghasemi, Burak Ahmet Tuna, and Xianguo Li. Shear/rotation competition during the roll-up of acoustically excited shear layers. *Journal of Fluid Mechanics*, 844:831854, 2018.

[49] Abbas Ghasemi, Burak Ahmet Tuna, and Xianguo Li. Curvature-induced deformations of the vortex rings generated at the exit of a rectangular duct. *Journal of Fluid Mechanics*, 864:141180, 2019.

[50] Abbas Ghasemi, Burak Ahmet Tuna, and Xianguo Li. Viscous diffusion effects on the self-induced distortions of rectangular vortex rings. *Physics of Fluids*, 30(12):124101, 2018.

[51] Abbas Ghasemi and Xianguo Li. Cross-sectional reshaping of perturbed/unperturbed rectangular jets. *International Journal of Numerical Methods for Heat and Fluid Flow*, (In Press)(NN):AA–BB, 2019.

[52] A-M Shinneeb, JD Bugg, and R Balachandar. Quantitative investigation of vortical structures in the near-exit region of an axisymmetric turbulent jet. *Journal of Turbulence*, 9(9):N19, 2008.

[53] Jimmy Philip and Ivan Marusic. Large-scale eddies and their role in entrainment in turbulent jets and wakes. *Phys. Fluids*, 24(5):055108, 2012.

[54] R Andriani, A Coghe, and GE Cossali. Near-field entrainment in unsteady gas jets and diesel sprays: A comparative study. volume 26, pages 2549–2556. Elsevier, 1996.

[55] Paul S Krueger and Morteza Gharib. The significance of vortex ring formation to the impulse and thrust of a starting jet. *Physics of fluids*, 15(5):1271–1281, 2003.

[56] L Gao and SCM Yu. Development of the trailing shear layer in a starting jet during pinch-off. *Journal of Fluid Mechanics*, 700:382–405, 2012.

[57] Mouhammad El Hassan and Amina Meslem. Time-resolved stereoscopic particle image velocimetry investigation of the entrainment in the near field of circular and daisy-shaped orifice jets. *Physics of Fluids*, 22(3):035107, 2010.

[58] Abbas Ghasemi, Vesselina Roussinova, Ronald Barron, and Ram Balachandar. Analysis of entrainment at the turbulent/non-turbulent interface of a square jet. In *ASME 2013 International Mechanical Engineering Congress and Exposition*, pages V07AT08A048–V07AT08A048. American Society of Mechanical Engineers, 2013.

[59] Gi E Cossali, A Coghe, and L Araneo. Near-field entrainment in an impulsively started turbulent gas jet. *AIAA journal*, 39(6):1113–1122, 2001.

[60] Geno Pawlak, Carolina Marugan Cruz, Carlos Martínez Bazán, and Pedro García Hrdy. Experimental characterization of starting jet dynamics. *Fluid dynamics research*, 39(11-12):711, 2007.

[61] Jinhee Jeong and Fazle Hussain. On the identification of a vortex. *J. Fluid Mech.*, 285:69–94, 1995.

[62] JE Broadwell and RE Breidenthal. A simple model of mixing and chemical reaction in a turbulent shear layer. *Journal of Fluid Mechanics*, 125:397–410, 1982.

[63] Jean-Luc Aider, Alexandra Danet, and Marcel Lesieur. Large-eddy simulation applied to study the influence of upstream conditions on the time-dependant and averaged characteristics of a backward-facing step flow. *J. Turbul.*, 8(8):N51, 2007.

[64] Alfred Ayoub and K Karamcheti. An experiment on the flow past a finite circular cylinder at high subcritical and supercritical reynolds numbers. *J. Fluid Mech.*, 118:1–26, 1982.

[65] Dorian Liepmann and Morteza Gharib. The role of streamwise vorticity in the near-field entrainment of round jets. *J. Fluid Mech.*, 245:643–668, 1992.

[66] Jennifer Hamelin and Amy E Alving. A low-shear turbulent boundary layer. *Phys. Fluids*, 8(3):789–804, 1996.

[67] Albert A Townsend. *The structure of turbulent shear flow.* Cambridge university press, 1980.

[68] Daniel I Meiron, Gregory R Baker, and Steven A Orszag. Analytic structure of vortex sheet dynamics. part 1. kelvin–helmholtz instability. *J. Fluid Mech.*, 114:283–298, 1982.

[69] Scott C Morris and John F Foss. Turbulent boundary layer to single-stream shear layer: the transition region. *J. Fluid Mech.*, 494:187–221, 2003.

[70] Peter Freymuth. On transition in a separated laminar boundary layer. *J. Fluid Mech.*, 25(4):683–704, 1966.

[71] Hyder S Husain and Fazle Hussain. Experiments on subharmonic resonance in a shear layer. *J. Fluid Mech.*, 304:343–372, 1995.

[72] KBMQ Zaman and AKMF Hussain. Vortex pairing in a circular jet under controlled excitation. part 1. general jet response. *Journal of fluid mechanics*, 101(3):449–491, 1980.

[73] AKMF Hussain and KBMQ Zaman. Vortex pairing in a circular jet under controlled excitation. part 2. coherent structure dynamics. *Journal of Fluid Mechanics*, 101(3):493–544, 1980.

[74] Jerry Westerweel and Fulvio Scarano. Universal outlier detection for piv data. *Exp. Fluids.*, 39(6):1096–1100, 2005.

[75] Andrea Sciacchitano, Douglas R Neal, Barton L Smith, Scott O Warner, Pavlos P Vlachos, Bernhard Wieneke, and Fulvio Scarano. Collaborative framework for piv uncertainty quantification: comparative assessment of methods. *Meas. Sci. Technol.*, 26(7):074004, 2015.

[76] Michael Amitay, Burak A Tuna, and Haley DellOrso. Identification and mitigation of ts waves using localized dynamic surface modification. *Phys. Fluids*, 28(6):064103, 2016.

[77] JC Vassilicos, J-P Laval, J-M Foucaut, and Michel Stanislas. The streamwise turbulence intensity in the intermediate layer of turbulent pipe flow. *Journal of Fluid Mechanics*, 774:324–341, 2015.

[78] Ivan Marusic and Gary J Kunkel. Streamwise turbulence intensity formulation for flat-plate boundary layers. *Physics of Fluids*, 15(8):2461–2464, 2003.

[79] Julian CR Hunt, Alan A Wray, and Parviz Moin. Eddies, streams, and convergence zones in turbulent flows. In *Studying Turbulence Using Numerical Simulation Databases, 2. Proceedings of the 1988 Summer Program*, pages 309–321. 1988.

[80] MD Slessor, CL Bond, and PE Dimotakis. Turbulent shear-layer mixing at high reynolds numbers: effects of inflow conditions. *Journal of Fluid Mechanics*, 376:115–138, 1998.

[81] AKMF Hussain and KBMQ Zaman. An experimental study of organized motions in the turbulent plane mixing layer. *Journal of Fluid Mechanics*, 159:85–104, 1985.

[82] Chih-Ming Ho and Patrick Huerre. Perturbed free shear layers. *Annual Review of Fluid Mechanics*, 16(1):365–422, 1984.

[83] Alfons Michalke. The instability of free shear layers. *Progress in Aerospace Sciences*, 12:213–216, 1972.

[84] Robert Betchov. *Stability of parallel flows*. Elsevier, 2012.

[85] Philip G Drazin and William Hill Reid. *Hydrodynamic stability*. Cambridge university press, 2004.

[86] Paolo Dini, Michael S Seligt, and Mark D Maughmert. Simplified linear stability transition prediction method for separated boundary layers. *AIAA journal*, 3(8), 1992.

[87] Peter A Monkewitz and Patrick Huerre. Influence of the velocity ratio on the spatial instability of mixing layers. *The Physics of Fluids*, 25(7):1137–1143, 1982.

[88] Peter J Schmid and Dan S Henningson. *Stability and transition in shear flows*, volume 142. Springer Science & Business Media, 2012.

[89] Serhiy Yarusevych and Marios Kotsonis. Steady and transient response of a laminar separation bubble to controlled disturbances. *Journal of Fluid Mechanics*, 813:955–990, 2017.

[90] Olaf Marxen, Rupesh B Kotapati, Rajat Mittal, and Tamer Zaki. Stability analysis of separated flows subject to control by zero-net-mass-flux jet. *Physics of Fluids*, 27(2):024107, 2015.

[91] TJ Bridges and PJ Morris. Differential eigenvalue problems in which the parameter appears nonlinearly. *Journal of Computational Physics*, 55(3):437–460, 1984.

[92] Steven A Orszag. Accurate solution of the orr–sommerfeld stability equation. *Journal of Fluid Mechanics*, 50(4):689–703, 1971.

[93] AMO Smith and Nathalie Gamberoni. Transition, pressure gradient, and stability theory. report no. es. 26388, douglas aircraft co. *Inc., El Segundo, CA*, 1956.

[94] JL Van Ingen. A suggested semi-empirical method for the calculation of the boundary layer transition region. *Technische Hogeschool Delft, Vliegtuigbouwkunde, Rapport VTH-74*, 1956.

[95] JL Van Ingen. *The eN method for transition prediction: Historical review of work at TU Delft*, volume 3830. AIAA, 2008.

[96] Clinton D Winant and Fred K Browand. Vortex pairing: the mechanism of turbulent mixing-layer growth at moderate reynolds number. *Journal of Fluid Mechanics*, 63(2):237–255, 1974.

[97] Alfons Michalke. On spatially growing disturbances in an inviscid shear layer. *Journal of Fluid Mechanics*, 23(3):521–544, 1965.

[98] Laurent Graftieaux, Marc Michard, and Nathalie Grosjean. Combining piv, pod and vortex identification algorithms for the study of unsteady turbulent swirling flows. *Measurement Science and technology*, 12(9):1422, 2001.

[99] NJ Zabusky and GS Deem. Dynamical evolution of two-dimensional unstable shear flows. *Journal of Fluid Mechanics*, 47(2):353–379, 1971.

[100] Hassan Aref and Eric D Siggia. Vortex dynamics of the two-dimensional turbulent shear layer. *Journal of Fluid Mechanics*, 100(4):705–737, 1980.

[101] KBMQ Zaman. Axis switching and spreading of an asymmetric jet: the role of coherent structure dynamics. *J. Fluid Mech.*, 316:1–27, 1996.

[102] Aaron Towne, André VG Cavalieri, Peter Jordan, Tim Colonius, Oliver Schmidt, Vincent Jaunet, and Guillaume A Brès. Acoustic resonance in the potential core of subsonic jets. *J. Fluid Mech.*, 825:1113–1152, 2017.

[103] Chih-Ming Ho and Nagy S Nosseir. Dynamics of an impinging jet. part 1. the feedback phenomenon. *Journal of Fluid Mechanics*, 105:119–142, 1981.

[104] Chih-Ming Ho and Lein-Saing Huang. Subharmonics and vortex merging in mixing layers. *Journal of Fluid Mechanics*, 119:443–473, 1982.

[105] Fazle Hussain and Hyder S Husain. Elliptic jets. part 1. characteristics of unexcited and excited jets. *Journal of Fluid Mechanics*, 208:257–320, 1989.

[106] Uriel Frisch. *Turbulence: the legacy of AN Kolmogorov.* Cambridge university press, 1995.

[107] C Bogey, C Bailly, and D Juvé. Noise investigation of a high subsonic, moderate reynolds number jet using a compressible large eddy simulation. *Theoretical and Computational Fluid Dynamics*, 16(4):273–297, 2003.

[108] Christophe Bogey and Christophe Bailly. An analysis of the correlations between the turbulent flow and the sound pressure fields of subsonic jets. *Journal of Fluid Mechanics*, 583:71–97, 2007.

[109] Stephen B Pope. Turbulent flows, 2001.

[110] Joseph Smagorinsky. General circulation experiments with the primitive equations: I. the basic experiment. *Mon. Weather Rev.*, 91(3):99–164, 1963.

[111] Massimo Germano, Ugo Piomelli, Parviz Moin, and William H Cabot. A dynamic subgrid-scale eddy viscosity model. *Phys. Fluids*, 3(7):1760–1765, 1991.

[112] Douglas K Lilly. A proposed modification of the germano subgrid-scale closure method. *Phys. Fluids*, 4(3):633–635, 1992.

[113] Ansys Fluent 14.0 theory guide. *ANSYS inc*, 2011.

[114] Hachimi Fellouah and Andrew Pollard. The velocity spectra and turbulence length scale distributions in the near to intermediate regions of a round free turbulent jet. *Physics of Fluids*, 21(11):115101, 2009.

[115] M Cheng, J Lou, and TT Lim. Evolution of an elliptic vortex ring in a viscous fluid. *Physics of Fluids*, 28(3):037104, 2016.

[116] Fernando F Grinstein. Self-induced vortex ring dynamics in subsonic rectangular jets. *Physics of Fluids*, 7(10):2519–2521, 1995.

[117] Jongil Han, Yuh-Lang Lin, David G Schowalter, S Pal Arya, and Fred H Proctor. Large eddy simulation of aircraft wake vortices within homogeneous turbulence- crow instability. *AIAA journal*, 38(2):292–300, 2000.

[118] I Hennemann and F Holzäpfel. Large-eddy simulation of aircraft wake vortex deformation and topology. *Proceedings of the Institution of Mechanical Engineers, Part G: Journal of Aerospace Engineering*, 225(12):1336–1350, 2011.

[119] Takashi Misaka and Shigeru Obayashi. Numerical study on jet-wake vortex interaction of aircraft configuration. *Aerospace Science and Technology*, 70:615–625, 2017.

[120] Thomas Leweke and Charles HK Williamson. Experiments on long-wavelength instability and reconnection of a vortex pair. *Physics of Fluids*, 23(2):024101, 2011.

[121] T Misaka, Frank Holzäpfel, I Hennemann, T Gerz, M Manhart, and F Schwertfirm. Vortex bursting and tracer transport of a counter-rotating vortex pair. *Physics of Fluids*, 24(2):025104, 2012.

[122] Victor Kozlov, Genrich R Grek, and Yury Litvinenko. *Visualization of conventional and combusting subsonic jet instabilities.* Springer, 2016.

[123] Juan Lasheras, Katherine Prestridge, Juan Lasheras, and Katherine Prestridge. Three-dimensional vorticity dynamics in coflowing jets subjected to axial and azimuthal forcing. In *4th Shear Flow Control Conference*, page 1880, 1997.

[124] Ionut Danaila and Bendiks Jan Boersma. Direct numerical simulation of bifurcating jets. *Physics of fluids*, 12(5):1255–1257, 2000.

[125] Bram Van Leer. Towards the ultimate conservative difference scheme. v. a second-order sequel to godunov's method. *Journal of computational Physics*, 32(1):101–136, 1979.

[126] KW Bedford and WK Yeo. Conjunctive filtering procedures in surface water flow and transport. *Large eddy simulation of complex engineering and geophysical flows*, pages 513–537, 2010.

[127] François Charru. *Hydrodynamic instabilities*, volume 37. Cambridge University Press, 2011.

[128] Gordon Erlebacher, M Yousuff Hussaini, Charles G Speziale, and Thomas A Zang. Toward the large-eddy simulation of compressible turbulent flows. *Journal of fluid mechanics*, 238:155–185, 1992.

[129] H Fellouah, CG Ball, and A Pollard. Reynolds number effects within the development region of a turbulent round free jet. *International Journal of Heat and Mass Transfer*, 52(17-18):3943–3954, 2009.

[130] Philip G Hill and Patric Ouellette. Transient turbulent gaseous fuel jets for diesel engines. *Journal of fluids engineering*, 121(1):93–101, 1999.

[131] Raad I Issa. Solution of the implicitly discretised fluid flow equations by operator-splitting. *Journal of computational physics*, 62(1):40–65, 1986.

[132] KH Lie and DN Riahi. Numerical solution of the orr-sommerfeld equation for mixing layers. *International journal of engineering science*, 26(2):163–174, 1988.

[133] Anthony Leonard. Computing three-dimensional incompressible flows with vortex elements. *Annual Review of Fluid Mechanics*, 17(1):523–559, 1985.

[134] Hans J Lugt. The dilemma of defining a vortex. In *Recent developments in theoretical and experimental fluid mechanics*, pages 309–321. Springer, 1979.

[135] Thomas Morel. Comprehensive design of axisymmetric wind tunnel contractions. *Journal of Fluids Engineering*, 97(2):225–233, 1975.

[136] David Munday, Mihai Mihaescu, and Ephraim Gutmark. Experimental and numerical study of jets from elliptic nozzles with conic plug. *AIAA journal*, 49(3):554–564, 2011.

[137] Eric Pomraning. *Development of large eddy simulation turbulence models.* PhD thesis, University of Wisconsin–Madison, 2000.

[138] CM Rhie and W Li Chow. Numerical study of the turbulent flow past an airfoil with trailing edge separation. *AIAA journal*, 21(11):1525–1532, 1983.

[139] KJ Richards, PK Senecal, and E Pomraning. Converge (version 2.2. 0) manual, convergent science. *Inc., Madison, WI*, 2014.

[140] Stephen K Robinson. A review of vortex structures and associated coherent motions in turbulent boundary layers. In *Structure of Turbulence and Drag Reduction*, pages 23–50. Springer, 1990.

[141] SK Robinson, Stephen Jay Kline, and PR Spalart. A review of quasi-coherent structures in a numerically simulated turbulent boundary layer. 1989.

[142] K Sengupta, GB Jacobs, and F Mashayek. Large-eddy simulation of compressible flows using a spectral multidomain method. *International journal for numerical methods in fluids*, 61(3):311–340, 2009.

[143] Kyle D Squires. Dynamic subgrid-scale modeling of compressible turbulence. In *Annual Research Briefs, 1991*, 1991.

[144] N Soulopoulos, Y Hardalupas, and AMKP Taylor. Mixing and scalar dissipation rate statistics in a starting gas jet. *Physics of Fluids*, 27(12):125103, 2015.

[145] AH Syed and Hyung Jin Sung. Propagation of orifice-and nozzle-generated vortex rings in air. *Journal of visualization*, 12(2):139–156, 2009.

[146] Shuling Tian, Yisheng Gao, Xiangrui Dong, and Chaoqun Liu. Definitions of vortex vector and vortex. *Journal of Fluid Mechanics*, 849:312–339, 2018.

[147] Burak Ahmet TUNA, Serhiy Yarusevych, and Xiangou Li. Investigation of the effect of inlet turbulence on transitional wall-bounded flows. *Fluids Engineering Division Summer Meeting*, -:1–12, 2017.

[148] Bert Vreman, Bernard Geurts, and Hans Kuerten. Large-eddy simulation of the turbulent mixing layer. *Journal of Fluid Mechanics*, 339:357–390, 1997.

[149] Akira Yoshizawa. Statistical theory for compressible turbulent shear flows, with the application to subgrid modeling. *The Physics of fluids*, 29(7):2152–2164, 1986.

[150] KBMQ Zaman and AKMF Hussain. Turbulence suppression in free shear flows by controlled excitation. *Journal of Fluid Mechanics*, 103:133–159, 1981.

[151] Michel Goossens, Frank Mittelbach, and Alexander Samarin. *The LaTeX Companion*. Addison-Wesley, Reading, Massachusetts, 1994.

[152] Donald Knuth. *The TeXbook*. Addison-Wesley, Reading, Massachusetts, 1986.

[153] Leslie Lamport. *LaTeX — A Document Preparation System*. Addison-Wesley, Reading, Massachusetts, second edition, 1994.

APPENDICES

Appendix A

The Biot-Savart integral and its correlation with the curvature-induced velocity

The experimental observations presented in the main body of the present manuscript demonstrate the formation of high velocity spots near the high-curvature regions of the vortex rings. In order to expand the relevant theoretical discussions, we consider the velocity U_{T} of a given point P at the vicinity of a three-dimensional curved vortex line of the form $\mathbf{X}(s,t)$ subjected to the inviscid flow condition. Here, s is the arc length along the line and $\mathbf{P}$ denotes the position vector. The total velocity U_{T} at a given point on the vortex is comprised of the two components:

$$U_{\mathrm{T}} = U_{\mathrm{F}} + U_{\mathrm{I}} \tag{A.1}$$

The U_{F} component of the velocity is due to the bulk flow which is finite along the vortex line. The U_{I} part of the velocity is induced by the presence of a vorticity field. Such a velocity/vorticity relationship can be investigated by taking the curl of the momentum equation to obtain the vorticity transport equation [133]. Further calculations [133] result in the Biot-Savart integral along the vortex line curve $\mathtt{C}$ [40, 41]:

$$U_{\mathrm{I}}(P,t) = -\frac{\Gamma}{4\pi}\int_{\mathtt{C}} \frac{\left[\mathbf{P}-\mathbf{X}(s',t)\right]\times ds'}{|\mathbf{P}-\mathbf{X}(s',t)|^3} \tag{A.2}$$

where Γ is the circulation of the vortex line considered positive in the direction of s. It can be noticed that $U_{\mathrm{I}}(P,t)$ diverges as $|\mathbf{P}-\mathbf{X}(s',t)| \to 0$. In order to deal with the singularity issue of the Biot-Savart integral, the techniques such as the Method of Matched Asymptotic Expansion of Singular Integrals (MAESI) are implemented [42]. It should be noted that the time t appears due to the motion of the curved vortex line. For convenience, the position vector $\mathbf{P}$ can be represented in the curvilinear coordinate system of (r, θ, s) corresponding to the point $\mathbf{P}(s, t)$ located on the vortex line:

$$P(x, y, z) = \mathbf{X}(s, t) + r\hat{r}(\theta, y, z) \tag{A.3}$$

where r defines the minimum distance between the points P and $\mathbf{X}(s, t)$ on the vortex line. The expansion of the Biot-Savart integral yields [43]:

$$U_{\mathrm{I}}(P, t) = U_{\mathrm{I}}(r, t) = \frac{\Gamma}{2\pi r}\hat{\theta} + \frac{\kappa\Gamma}{4\pi}\left[\ln(\frac{R}{r})\right]\hat{b} + \frac{\Gamma}{4\pi R}(\cos\phi)\hat{\theta} + \mathbf{Q}_{\mathrm{f}} \tag{A.4}$$

Here, $\hat{\theta}$ and $\hat{b}$ introduce the local unit vectors in the circumferential and bi-normal directions, respectively. As inferred from the second term on the right hand side, $\kappa = \frac{1}{R(s,t)}$ accounts for the local curvature of the vortex filament. Accordingly, the local self-induced velocity $U_{\mathrm{I}}(P, t)$ varies proportional to the curvature κ as also observed by the present measurements.

Appendix B

Characterization of the sound pressure levels (SPL) for the acoustic excitation

As explained in the main body of the manuscript, the fundamental (f_n) and its subharmonic ($f_\mathrm{n}/2$) mode respectively referred to as the high-frequency (HF) and the low-frequency (LF) are detected using the HW-based spectra and then verified by the PIV-based stability analysis. Afterwards, they are used to acoustically excite the rectangular jet. The characteristics of the low (LA), mid (MA) and high (HA) excitation amplitudes and the corresponding sound pressure levels (SPL) are presented in table B.1. The pressure levels are measured using a Brüel and Kjær 4192 free-field condenser microphone. The SPL level is evaluated using the root-mean-square (RMS) of the pressure (p_rms) in the equation:

$$L_i = \mathrm{SPL_i} = 10\log(\frac{p_\mathrm{rms,\ i}}{p_\mathrm{ref}})^2 = 20\log(\frac{p_\mathrm{rms,\ i}}{p_\mathrm{ref}}) \tag{B.1}$$

where $p_\mathrm{ref} = 20\ \mu Pa$ is the reference pressure used for the calculations in air. Summation of the n different SPLs can be achieved using the equation:

$$L_\mathrm{sum} = 10\log(\frac{{p^2}_\mathrm{rms,\ 1} + {p^2}_\mathrm{rms,\ 2} + \dots + {p^2}_{\mathrm{rms},n}}{{p^2}_\mathrm{ref}}) \tag{B.2}$$

Considering the equation

$$(\frac{p_\mathrm{rms,\ i}}{p_\mathrm{ref}})^2 = 10^{\frac{L_\mathrm{i}}{10}} \tag{B.3}$$

	Tunnel-OFF SPL (dB)	Tunnel-ON excitation amplitude SPL (dB)
Natural	76.33	91.2
Low amplitude (LA)	79.11	91.5
Mid amplitude (MA)	88.04	92.9
High amplitude (HA)	95.55	96.87

Table B.1: Characterization of the sound pressure level (SPL) for the low (LA), mid (MA) and high (HA) amplitudes for the acoustic excitations at the fundamental (f_n) and subharmonic frequencies ($f_n/2$).

the summation of the SPLs can be obtained as

$$L_{\mathrm{sum}} = 10\log(10^{\frac{L_1}{10}} + 10^{\frac{L_2}{10}} + ... + 10^{\frac{L_n}{10}}) \tag{B.4}$$

First, the ambient noise level of SPL = 76.3 (dB) is characterized when the tunnel air flow and the acoustic source are OFF. Afterwards, the SPL levels due to the LA, MA and HA amplitudes are characterized as 79.1 (dB), 88.1 (dB) and 95.5 (dB) when the tunnel air flow and the acoustic source are ON. The Tunnel-OFF SPL values are given in the left column of the table B.1. In order to obtain the SPL levels of the natural (NAT) jet, measurements conducted at the center of the channel exit yield SPL = 91.2 (dB). In order to obtain the Tunnel-ON values in the right column ($\mathrm{SPL_R}$) of the table B.1, the Tunnel-OFF levels in the left column ($\mathrm{SPL_L}$) are added to the SPL of the natural case ($\mathrm{SPL_{NAT}} = 91.2(dB)$) using the equation below:

$$\mathrm{SPL_R} = 10\log(10^{(\frac{\mathrm{SPL_L}}{10})} + 10^{(\frac{\mathrm{SPL_{NAT}}}{10})}) \tag{B.5}$$

For example, $91.5(dB) = 10\log(10^{(\frac{79.11}{10})} + 10^{(\frac{91.2}{10})})$ is the SPL level of the LA excitation of the jet given in the right column of the second row of the table B.1.

Appendix C

Spatial analysis of the linear stability (LST) modes

In linear stability (LST) analysis, the hydrodynamic theory of stability treats the shear layer in terms of the dynamics of the group of waves which may propagate, amplify or decay in the space/time medium [84, 85]. The transport and dynamics of the waves are analysed in the Fourier space instead of the conventional physical time/space. In order to predict the stability criteria, the Orr-Sommerfeld equation is solved which can be derived from the incompressible Navier-Stokes equations [88]:

$$\boldsymbol{\nabla} \cdot \vec{\boldsymbol{V}} = 0 \tag{C.1}$$

$$\rho \frac{D\vec{\boldsymbol{V}}}{Dt} = -\nabla P + \mu \nabla^2 \vec{\boldsymbol{V}} \tag{C.2}$$

Here, $\vec{V}$, P, μ and ρ denote the velocity vector, pressure, dynamic viscosity and density, respectively. The velocity and pressure perturbations $V_x = U+u'$, $V_y = V+v'$ and $p = P+p'$ are introduced to the above continuity and momentum equations:

$$\frac{\partial u'}{\partial x} + \frac{\partial v'}{\partial x} = 0 \tag{C.3}$$

$$\frac{\partial u'}{\partial t} + U\frac{\partial u'}{\partial x} + V\frac{\partial u'}{\partial y} + u'\frac{\partial U}{\partial x} + v'\frac{\partial U}{\partial y} = -\frac{1}{\rho}\frac{\partial p'}{\partial x} + \frac{\mu}{\rho}(\frac{\partial^2 u'}{\partial x^2} + \frac{\partial^2 u'}{\partial y^2}) \tag{C.4}$$

$$\frac{\partial v'}{\partial t}+U\frac{\partial v'}{\partial x}+V\frac{\partial v'}{\partial y}+u'\frac{\partial V}{\partial x}+v'\frac{\partial V}{\partial y}=-\frac{1}{\rho}\frac{\partial p'}{\partial y}+\frac{\mu}{\rho}(\frac{\partial^2 v'}{\partial x^2}+\frac{\partial^2 v'}{\partial y^2}) \tag{C.5}$$

Using the parallel flow assumption as $U = U(y)$ and $V = 0$, above equations are reduced to:

$$\frac{\partial u'}{\partial x}+\frac{\partial v'}{\partial x}=0 \tag{C.6}$$

$$\frac{\partial u'}{\partial t}+U\frac{\partial u'}{\partial x}+v'\frac{\partial U}{\partial y}=-\frac{1}{\rho}\frac{\partial p'}{\partial x}+\frac{\mu}{\rho}(\frac{\partial^2 u'}{\partial x^2}+\frac{\partial^2 u'}{\partial y^2}) \tag{C.7}$$

$$\frac{\partial v'}{\partial t}+U\frac{\partial v'}{\partial x}=-\frac{1}{\rho}\frac{\partial p'}{\partial y}+\frac{\mu}{\rho}(\frac{\partial^2 v'}{\partial x^2}+\frac{\partial^2 v'}{\partial y^2}) \tag{C.8}$$

The following form of the normal instability modes can be introduced to the above perturbation equations [88]:

$$\psi=\phi(y)e^{i(\alpha x-\omega t)} \tag{C.9}$$

$$u'=\frac{\partial \psi}{\partial y}=\frac{\partial \phi}{\partial y}e^{i(\alpha x-\omega t)} \tag{C.10}$$

$$v'=-\frac{\partial \psi}{\partial x}=-i\alpha\phi e^{i(\alpha x-\omega t)} \tag{C.11}$$

In the spatial theory of the LST, α is considered as a complex wave number to account for the exponential growth/decay of the perturbations in space [88, 83]. On the other hand, ω is a real frequency parameter to allow for the purely convective oscillations of the perturbations in time without any amplification/damping [88, 83]. After the calculation and substitution of the corresponding derivatives as well as the elimination of the pressure terms, we obtain:

$$-i\omega\frac{\partial^2\phi}{\partial y^2}+i\alpha U\frac{\partial^2\phi}{\partial y^2}-i\alpha\phi\frac{\partial^2 U}{\partial y^2}+\frac{\mu}{\rho}(-\frac{\partial^4\phi}{\partial y^4}+2\alpha^2\frac{\partial^2\phi}{\partial y^2}-\alpha^4\phi)+i\alpha^2\omega\phi-i\alpha^3U\phi=0 \tag{C.12}$$

Further simplifications result in a fourth-order linear differential equation which is known as the Orr-Sommerfeld equation and describes the linear two-dimensional modes of the perturbations in a viscous parallel flow [88]:

$$(U - \frac{\omega}{\alpha})(\frac{\partial^2 \phi}{\partial y^2} - \alpha^2 \phi) - \phi \frac{\partial^2 U}{\partial y^2} + \frac{i\nu}{\alpha}(\frac{\partial^4 \phi}{\partial y^4} - 2\alpha^2 \frac{\partial^2 \phi}{\partial y^2} + \alpha^4 \phi) = 0 \tag{C.13}$$

It should also be noted that the Orr-Sommerfeld equation can be simplified to the Rayleigh equation for inviscid flow [88]. By defining the scaling variables below

$$c = \frac{\omega}{\alpha} \quad \xi = \frac{y}{\delta} \quad \overline{\phi} = \frac{\phi}{\delta U_\infty} \quad \overline{c} = \frac{c}{U_\infty} \quad \overline{\alpha} = \alpha\delta \quad Re_\delta = \frac{U_\infty \delta}{\nu} \tag{C.14}$$

the dimensionless form of the Orr-Sommerfeld equation can be derived as

$$(\overline{U} - \overline{c})(\overline{\phi}'' - \overline{\alpha}\overline{\phi}) - \overline{U}''\overline{\phi} + \frac{i}{\overline{\alpha} Re_\delta}(\overline{\phi}'''' - 2\overline{\alpha}^2 \overline{\phi}'' + \overline{\alpha}^4 \overline{\phi}) = 0 \tag{C.15}$$

where $c = \frac{\omega}{\alpha}$, δ, α, ω, ν and Re_δ denote the phase velocity, displacement thickness, complex wave number, real frequency, kinematic viscosity and the Reynolds number, respectively.

Since the coefficients are not constant, the exact solutions can only be obtained for very specific conditions. For instance, when the second spatial derivative of the velocity is zero as seen in the case of the piecewise-linear profiles [127]. Therfore, a numerical solution approach needs to be implemented for a more realistic base flow. Prior to the solution of the Orr-Sommerfeld equation, the base velocity $U(y)$ around which the flow is perturbed needs to be determined. For each of the natural or acoustically excited cases, different base flows are considered. To this end, the corresponding time-averaged velocity profiles obtained from the particle image velocimetry (PIV) measurements are extracted for differenet streamwise locations. It is worth mentioning that the spatial LST is previously carried out for the excited flows, namely the studies by [89] and [90]. For the convenience of the numerical implementations, the velocity profiles are fitted to the hyperbolic tangent (Tanh) profile using the method of the least squares [86]:

$$U(y) = c_5 \big\{ (\frac{1 - c_1}{2}) + (\frac{1 + c_1}{2}) \tanh \big[c_2 (\frac{y - c_3}{c_4}) \big] \big\} \tag{C.16}$$

For each of the downstream locations, using the time-averaged streamwise velocity profile as the base flow describes the local LST analysis of the spatial perturbations [87]. The Orr-Sommerfeld equation defines an eigenvalue problem which is numerically solved by applying the proper homogeneous boundary conditions. The nonlinearity issue in the eigenvalue system is resolved by means of the companion matrix according to [91]. In comparison to the conventional numerical techniques such as the finite difference schemes, the spectral methods based on the expansion of the Chebyshev polynomials are preferred as they provide higher accuracy with less demanding computational resources. The eigenfunction $\phi(y)$ in the Orr-Sommerfeld equation is obtained by the spectral colocation solution method in which the expansion in the form of the Chebyshev polynomial approximations are considered:

$$\phi(y) = \sum_{n=0}^{\infty} a_n T_n(y) \tag{C.17}$$

The n^{th}-degree Chebyshev polynomial of the first kind, $T_n(x)$ is defined as

$$T_n(\cos\theta) = \cos(n\theta) \tag{C.18}$$

where the positive integers $n = 0, 1, 2, 3, ..$ recursively yield $T_0(x) = 1$, $T_1(x) = x$ and $T_{n+1}(x) = 2xT_n(x) - T_{n-1}(x)$. The coefficients a_n are obtained from the integration

$$a_n = \frac{2}{\pi c_n} \int_{-1}^{1} v(y) T_n(y) (1 - y^2)^{-\frac{1}{2}} dy \tag{C.19}$$

in which $c_0 = 2$ for $n = 0$ and we have $c_n = 1$ for $n > 0$. For further details on the numerical implementation see [132].